University of Alberta

Adsorption and Decomposition of Pyridine, Pyrrole, and Ethylamine on Mo(110): Experiment and Modeling

by

Wa'el Abdallah Abdallah ©

A thesis submitted to the Faculty of Graduate Studies and Research in
partial fulfillment of the requirements for the degree of *Doctor of Philosophy*

in

Chemical Engineering

Department of *Chemical and Materials Engineering*

Edmonton, Alberta

Fall 2005

Library and
Archives Canada

Published Heritage
Branch

395 Wellington Street
Ottawa ON K1A 0N4
Canada

Bibliothèque et
Archives Canada

Direction du
Patrimoine de l'édition

395, rue Wellington
Ottawa ON K1A 0N4
Canada

0-494-08602-5

Your file Votre référence
ISBN
Our file Notre reference
ISBN

NOTICE:
The author has granted a non-exclusive license allowing Library and Archives Canada to reproduce, publish, archive, preserve, conserve, communicate to the public by telecommunication or on the Internet, loan, distribute and sell theses worldwide, for commercial or non-commercial purposes, in microform, paper, electronic and/or any other formats.

The author retains copyright ownership and moral rights in this thesis. Neither the thesis nor substantial extracts from it may be printed or otherwise reproduced without the author's permission.

AVIS:
L'auteur a accordé une licence non exclusive permettant à la Bibliothèque et Archives Canada de reproduire, publier, archiver, sauvegarder, conserver, transmettre au public par télécommunication ou par l'Internet, prêter, distribuer et vendre des thèses partout dans le monde, à des fins commerciales ou autres, sur support microforme, papier, électronique et/ou autres formats.

L'auteur conserve la propriété du droit d'auteur et des droits moraux qui protège cette thèse. Ni la thèse ni des extraits substantiels de celle-ci ne doivent être imprimés ou autrement reproduits sans son autorisation.

In compliance with the Canadian Privacy Act some supporting forms may have been removed from this thesis.

While these forms may be included in the document page count, their removal does not represent any loss of content from the thesis.

Conformément à la loi canadienne sur la protection de la vie privée, quelques formulaires secondaires ont été enlevés de cette thèse.

Bien que ces formulaires aient inclus dans la pagination, il n'y aura aucun contenu manquant.

Canada

To My Parents, My Wife, Rima, And My Two Angels, Zina and Judy

ABSTRACT

The adsorption and decomposition of pyridine, pyrrole, and ethylamine on Mo(110) were studied using temperature-programmed desorption (TPD), Auger electron spectroscopy (AES), high-resolution electron energy loss spectroscopy (HREELS), and density functional theory (DFT). Low pyridine surface exposures (0.5 L) indicated one desorption peak at 375 K (E_{ads} = 23.5 kcal mol^{-1}), while at 1 L surface exposure two desorption peaks at temperatures of 370 and 530 with adsorption energy of 23.2 and 33.6 kcal mol^{-1}, respectively, were observed. Using DFT and EELS at low surface exposures, it was determined the preferred adsorption mode is pyridine in a parallel configuration coordinated to three surface Mo-sites as μ_3,η^6-Py-0°, while the second desorption feature results from a configuration with a bond to the surface through the nitrogen atom coordinated to one Mo-site as η^1(N)-Py-90°. Pyrrole showed only one desorption feature for all surface exposures at an approximate temperature of 351 K with adsorption energy of 21.9 kcal mol^{-1}, which suggests pyrrole adsorption on Mo(110) is not surface coverage dependent as the case for pyridine. Pyrrole is suggested to adsorb in a parallel mode with respect to the Mo(110) surface through its π orbital similar to μ_3,η^5-Pyr-0° with the possible coexistence of a second adsorption mode with the molecular plane slightly tilted as μ_3,η^4(N,C2,C3,C4)-Pyr-5°, which is suggested to arise from the lateral interactions of adsorbed pyrrole on Mo(110). Both pyridine and pyrrole adsorb reversibly and irreversibly on Mo(110) indicating the surface is active for denitrogenation. This is indicated by the presence of surface carbon and nitrogen following TPD. Pyridine also showed desorbed hydrogen upon decomposition. Ethylamine adsorption showed irreversible reaction behavior, as hydrogen and acetonitrile were observed desorbing from the surface during TPD. Based on the DFT relative adsorption energies of ethylamine adsorption on Mo(110), ethylamine adsorbs molecularly on Mo(110) through the nitrogen atom with the ethyl group pointing away from the surface and CH_2 interacting with the metal surface with an adsorption energy of 20.6 kcal mol^{-1}. This research provides fundamental information regarding the energetics and mechanism of catalytic hydrodenitrogenation (HDN) on a model hydrotreating catalyst surface.

ACKNOWLEDGEMENT

I sincerely appreciate Dr. Alan Nelson unlimited support, his guidance, and being positive all the way. His efforts and discussion were priceless, his positive attitude whenever I get frustrated with the instruments kept me going. I thank you for everything you have done.

I would like to acknowledge Dr. Murray Gray for his positive discussion and inputs, Dr. Gray is a great person to know and I'm blessed to be one of his students. Along these four years, so many wonderful people in the department of chemical and materials engineering assisted me to complete my thesis, specifically, Andrée Koenig and Walter Boddez.

I acknowledge and appreciate the financial support from Syncrude Canada Ltd., Natural Science and Engineering Research Council (NSERC), and Canada Foundation for Innovation.

My group (Martina, Joyce, Brian, Zhenhui, Claudia), it provided irresistible environment that I hate to leave, we became friends more than colleagues, and I thank each one of you for that. Mingyong Sun, thank you for all the technical discussion and sharing the office, it was great. Dr. Maham, thank you for being there and being supportive, the morning coffee will be missed.

My wife, Rima Shana'a, what can I say, you put up with me all along and it wasn't easy for you, but, you were there all the way, thank you.

TABLE OF CONTENTS

1. INTRODUCTION.. 1
    - 1.1 Crude Oil.. 1
    - 1.2 Catalytic Hydrotreating. 2
    - 1.3 Importance of Nitrogen Removal... 6
    - 1.4 Organonitrogen Compounds... 7
    - 1.5 Hydrotreating Catalysis.. 9
    - 1.6 Surface Science and Catalysis... 10
    - 1.7 Density Functional Theory (DFT)... 15
    - 1.8 Summary.. 16

2. LITERATURE REVIEW... 17
    - 2.1 Hydrodenitrogenation (HDN) Process. 17
    - 2.2 Pyridine... 21
        - 2.2.1 Introduction. 21
        - 2.2.2 Pyridine Adsorption on Single Crystal Surfaces 22
        - 2.2.3 Summary.. 29
    - 2.3 Pyrrole... 31
        - 2.3.1 Introduction... 31
        - 2.3.2 Pyrrole Adsorption on Single Crystal Surfaces..................... 31
        - 2.2.3 Summary.. 35
    - 2.4 Ethylamine.. 36
        - 2.4.1 Introduction... 36
        - 2.4.2 Ethylamine Adsorption on Single Crystal Surfaces................ 36
        - 2.4.3 Summary.. 40
    - 2.5 Summary.. 40

3. EXPERIMENTAL AND MODELING... 42
    - 3.1 Experimental... 42
        - 3.1.1 Methods and Materials.. 44

3.1.2 Temperature Programmed Desorption (TPD)........................ 44
3.1.3 Auger Electron Spectroscopy (AES)........................ 48
3.1.4 Low Electron Energy Spectroscopy (LEED)........................ 52
3.1.5 High-Resolution Electron Energy Loss Spectroscopy (HREELS)........................ 53
3.2 Molecular Modeling and Simulation........................ 59
3.2.1 Introduction........................ 59
3.2.2 Development of Density Functional Theory (DFT)........................ 61
3.2.2.1 Solids and Their Structures........................ 61
3.2.2.2 Waves and Particles........................ 62
3.2.2.3 The Schrödinger Equation........................ 63
3.2.2.4 Hartree Model and Hartree-Fock Theory........................ 66
3.2.2.5 Density Functional Theory (DFT)........................ 70
3.2.3 Research Calculations........................ 73
3.2.3.1 Setting up a Project in CASTEP........................ 73
3.2.3.2 Setting up The Electronic Options in CASTEP........................ 74

4. PYRIDINE ADSORPTION AND REACTION ON Mo(110) AND C/N-Mo(110): EXPERIMENT AND MODELING........................ 78
4.1 Introduction........................ 78
4.2 Experimental Results........................ 79
4.2.1 Pyridine Adsorption and Decomposition on Mo(110)........................ 79
4.2.2 Pyridine Adsorption and Decomposition on C/N-Mo(110)........................ 84
4.2.3C/N Surface Accumulation........................ 84
4.2.4 High-Resolution Electron Energy Loss Spectroscopy........................ 87
4.3 Molecular Simulation........................ 93
4.3.1 Pyridine Electronic Structure........................ 93
4.3.2 Pyridine Adsorption on Mo(110)........................ 95
4.3.3 Calculated Vibrational Frequencies of Pyridine Adsorption on Mo(110)........................ 103
4.4 Discussion........................ 104

4.4.1 Chemisorption of Pyridine on Mo(110)............................ 104
4.4.2 Orientation and Adsorption Energy Calculations of Pyridine on Mo(110)............................ 107
4.4.3 Adsorption of Pyridine on C/N-Mo(110)............................ 110
4.5 Conclusions............................ 112

5. PYRROLE ADSORPTION AND REACTION ON Mo(110) AND C/N-Mo(110): EXPERIMENT AND MODELING............................ 113
5.1 Introduction............................ 113
5.2 Experimental Results............................ 114
5.2.1 Pyrrole Adsorption and Decomposition on Mo(110)............................ 114
5.2.2 Pyrrole Adsorption and Decomposition on C/N-Mo(110)............................ 117
5.2.3 C/N Surface Accumulation............................ 119
5.2.4 High Resolution Electron Energy Loss Spectroscopy............................ 121
5.3 Molecular Simulation............................ 127
5.3.1 Pyrrole Electronic Structure............................ 127
5.3.2 Parallel Pyrrole Adsorption on Mo(110)............................ 128
5.3.3 Perpendicular and Inclined Pyrrole Adsorption on Mo(110)............................ 132
5.3.4 Coverage Dependent Pyrrole Adsorption on Mo(110)............................ 139
5.3.5 Calculated Vibrational Frequencies of Pyrrole Adsorption on Mo(110)............................ 141
5.4 Discussion............................ 142
5.4.1 Chemisorption of Pyrrole on Mo(110)............................ 142
5.4.2 Orientation of Pyrrole on Mo(110)............................ 144
5.4.3 Adsorption Energy Calculations of Pyrrole on Mo(110)............................ 146
5.4.5 Adsorption of Pyrrole on C/N – Mo(110)............................ 149
5.5 Conclusions............................ 150

6. ETHYLAMINE ADSORPTION AND REACTION MECHANISM ON Mo(110)............................ 152
6.1 Introduction............................ 152

6.2 Experimental Results 153
  6.2.1 Temperature Programmed Desorption 153
  6.2.2 Surface Composition Analysis 157
6.3 Molecular Simulation 157
  6.3.1 Ethylamine Electronic Structure 157
  6.3.2 Ethylamine Adsorption on Mo(110) 160
  6.3.3 Ethylamine Reaction on Mo(110) 162
  6.3.4 Calculated Vibrational Frequencies of Ethylamine Adsorption on Mo(110) 165
6.4 Discussion 167
  6.4.1 Chemisorption of Ethylamine on Mo(110) 167
  6.4.2 Orientation of Ethylamine on Mo(110) 168
6.5 Conclusions 170

7. CONCLUDING REMARKS 171
7.1 Summary 171
7.2 Implications to Hydrotreating 173
7.3 Future Studies 174
  7.3.1 Molybdenum Dichalcogenides 174
  7.3.2 Transition Metal Phosphides 176

REFERENCES 178

LIST OF FIGURES

FIGURE 1.1 Crude oil refining process flow sheet (Leach, 1983)............. 3

FIGURE 1.2 Simplified flow diagram of a hydrodenitrogenation process unit (Katzer and Sivasubramanian, 1979)......................... 5

FIGURE 1.3 The above image shows a structure of MoS_2 commercial catalyst that consists of sheets of S-Mo-S, while the lower image shows a hexagonal basal plane of MoS_2.................... 11

FIGURE 1.4 The above structure represents a cluster of body centre cube of Mo crystal, while the lower image represents a Mo-surface with (110) crystallographic orientation.......................... 14

FIGURE 2.1 Reaction mechanisms for pyridine HDN (Hanlon, 1987)......... 19

FIGURE 2.2 Reaction mechanism for pyrrole HDN (Satterfield et al., 1980).. 20

FIGURE 2.3 Summary of pyridine bonding modes (Sanchez-Delgado, 2002) (a) η^1(N)-Py-90°; (b) η^6-Py-0° (c) η^1(C2)-Py-90°; (d) η^2(C2,C3)-Py-90°; (e) η^2(N,C2)-Py-90°; (f) η^2(N,C2)-pyridyl; (g) μ_2,η^1(N)-Py-90°; (h) μ_2,η^2(N,C2)-Py-90........................ 24

FIGURE 2.4 Schematic of the reaction of pyridine with various metal surfaces as reported in the literature; a: (Demuth et al., 1980), b: (Avouris and Demuth, 1981), c: (Avouris et al., 1984), d: (Bader et al., 1986), e: (Grassian and Muetterties, 1987), f: (Johnson et al., 1985), g: (Grassian and Muetterties, 1986), h: (Serafin and Friend, 1989), i: (Mate et al., 1988), j: (Mack et al., 1985), k: (Cohen and Merrill, 1990)............................ 30

FIGURE 2.5 Summary of pyrrole bonding modes (Sanchez-Delgado, 2002). (a) Gas-Phase Pyrrole; (b) η^2(C,C)-2H-Pyl; (c) η^2(C,C)-H-Pyl; (d) η^4-Pyr; (e) η^5-Pyr; (f) η^1(N)-Pyl; (g) η^1(C)-Pyl; (h) η^3, η^2-Pyl; (j) η^5-Pyl.. 32

FIGURE 2.6 Schematic of the reaction of pyrrole with various metal surfaces as reported in the literature; Rh(111) (Netzer et al., 1988), Ni(100) (Schoofs and Benziger, 1987), Pd(111) (Baddeley et al., 1996; Futaba and Chiang, 1997), Cu(100) (Sexton, 1985), Pt(111) (Tourillon et al., 1987).................... 37

FIGURE 2.7 Schematic of the reaction of ethylamine with various metal surfaces as reported in the literature; W(100), W(100)-(5 x 1)-C, and W(100)-(2 x 1)-O (Pearlstine and Friend, 1986), Ni(111) (Gardin and Somorjai, 1992)................................ 41

FIGURE 3.1 Schematic diagram of ultrahigh vacuum chamber setup.......... 43

FIGURE 3.2 Experimental set-up of temperature programmed desorption studies in UHV environment.. 47

FIGURE 3.3 Energy level diagram in an Auger process. Electron from L_1 drops into the K level with the emission of an L_2 electron....... 49

FIGURE 3.4 Auger spectrum from Mo(110) single crystal, E_P= 1.5 keV and I_P= 1.2 A.. 51

FIGURE 3.5 The principle of LEED is that a beam of monoenergetic electrons scattered elastically from a surface. Because of the periodic order of the surface atoms, electrons show constructive interference in directions for which the path lengths of the electrons differ by an integral number of times the electron wavelength. Directions of constructive interference are made visible by collecting the scattered electrons on a fluorescent screen.................................... 54

FIGURE 3.6 A schematic drawing of a High-Resolution Electron Energy Loss Spectrometer experiment....................................... 56

FIGURE 3.7 Schematics of LK2000-14 EELS Model (reprinted with permission form LK2000 Technologies)............................ 57

FIGURE 4.1 Temperature Programmed Desorption (TPD) spectra of pyridine (*m/z* = 79) as a function of pyridine exposure on clean Mo(110)... 81

FIGURE 4.2 Temperature Programmed Desorption (TPD) spectra of hydrogen (*m/z* = 2) as a function of pyridine exposure on clean Mo(110)... 83

FIGURE 4.3 Temperature Programmed Desorption (TPD) spectra of pyridine (*m/z* = 79) for five consecutive pyridine doses on Mo(110). (a) 1 L; (b) 5 L; (c) 10 L.................................. 85

FIGURE 4.4 Atomic percent of surface contamination on Mo(110) as a function of consecutive pyridine TPD experiments. (a) at.% carbon; (b) at.% nitrogen... 86

FIGURE 4.5 Auger spectra of clean Mo(110) and C/N-Mo(110) as a function of consecutive 1 L pyridine TPD experiments. The spectra are normalized to the Mo *MNN* (186 eV) peak, and baseline adjusted to clearly show the C *KLL* (272 eV) and N *KLL* (386 eV) Auger peaks.. 88

FIGURE 4.6 Electron energy loss spectra of pyridine adsorbed on Mo(110) at surface exposure of 0.5 L as a function of temperature 100, 200, and 300 K.. 89

FIGURE 4.7 Electron energy loss spectra of pyridine adsorbed on Mo(110) at surface exposure of 1 L as a function of temperature 100, 200, and 300 K.. 91

FIGURE 4.8 Electron energy loss spectra of pyridine adsorbed on Mo(110) at surface exposure of 2 L as a function of temperature 100, 200, and 300 K.. 92

FIGURE 4.9 Electronic structure properties of pyridine simulated by density functional theory (GGA-PBE pesudo-potential) with 0.02 isosurface, a) Electrostatic Potential Map, b) Electrophilic Fukui function, c) Nucleophilic Fukui function, d) HOMO, and e) LUMO.. 96

FIGURE 4.10 Initial and optimized configurations for adsorption sites of pyridine on Mo(110). Py1, Py2, Py3, and Py4 are structures where the nitrogen atom is directly atop of a Mo atom and the molecular plane is tilted to the surface by 0°, 30°, 45°, and 90°, respectively; Py5 and Py6 are parallel and perpendicular adsorption modes where the nitrogen atom is centered at a bridge location between two Mo atoms; Py7 is parallel adsorption with the aromatic ring centered directly above a Mo atom; Py8 is a perpendicular structure with the nitrogen above a Mo 3-fold center; Py9 is an α-pyridyl structure with both C and N atop of two Mo atoms; and Py10 is an α-pyridyl structure with C atop top of a Mo atom.............................. 100

FIGURE 5.1 Temperature-Programmed Desorption (TPD) spectra of pyrrole (m/z = 67) as a function of pyrrole exposure on clean Mo(110).. 115

FIGURE 5.2 Temperature-Programmed Desorption (TPD) spectra of pyrrole (m/z = 67) for three consecutive pyrrole exposures on Mo(110); 0.5 L, 1 L, 2 L, and 5 L (ordinate scales adjusted).... 118

FIGURE 5.3 Atomic percent (at.%) of surface contamination on Mo(110) as a function of consecutive pyrrole TPD experiments for carbon and nitrogen.. 120

FIGURE 5.4 Auger spectra of clean Mo(110) and C/N-Mo(110) as a function of consecutive TPD experiments at 2 L pyrrole exposure. The spectra are normalized to the Mo MNN (186 eV) peak, and baseline adjusted to clearly show the C KLL (272 eV) and N KLL (379 eV) Auger peaks.......................... 122

FIGURE 5.5 Electron energy loss spectra of pyrrole adsorbed on Mo(110) at surface exposure of 0.5 L as a function of temperature (100, 200, and 300 K)... 123

FIGURE 5.6 Electron energy loss spectra of pyrrole adsorbed on Mo(110) at surface exposure of 1.0 L as a function of temperature (100, 200, and 300 K)... 124

FIGURE 5.7 Electron energy loss spectra of pyrrole adsorbed on Mo(110) at surface exposure of 4.0 L (saturation) as a function of temperature (100, 200, and 300 K)................................. 125

FIGURE 5.8 Electronic structure properties of pyrrole calculated by density functional theory (GGA-PBE pesudo-potential) with 0.025 isosurface, a) Electrostatic Potential Map, b) Electrophilic Fukui function, c) Nucleophilic Fukui function, d) HOMO, and e) LUMO... 129

FIGURE 5.9 Initial and optimized geometries of parallel pyrrole adsorption on Mo(110) and the corresponding adsorption energies.......... 131

FIGURE 5.10 Initial and optimized geometries of perpendicular pyrrole and pyrrolyl adsorption on Mo(110) and the corresponding adsorption energies.. 136

FIGURE 5.11 Initial and optimized geometries of inclined pyrrole and pyrrolyl adsorption on Mo(110) and the corresponding adsorption energies.. 138

FIGURE 5.12 Initial and optimized geometries of parallel pyrrole adsorption on Mo(110) as function of surface coverage........................ 140

FIGURE 6.1 Temperature Programmed Desorption (TPD) spectra of ethylamine (*m/z* = 30) at saturation exposure (4 L) on clean Mo(110)... 154

FIGURE 6.2 Temperature Programmed Desorption (TPD) spectra of acetonitrile (*m/z* = 41) at saturation exposure (4 L) on clean Mo(110)... 155

FIGURE 6.3 Temperature Programmed Desorption (TPD) spectra of hydrogen (*m/z* = 2) at saturation exposure (4 L) on clean Mo(110)... 156

FIGURE 6.4 Auger spectra of ethylamine on Mo(110) at surface exposure of 4 L following TPD. Auger electron signals of molybdenum correspond to 186 eV, carbon to 272 eV, and nitrogen 386 eV.. 158

FIGURE 6.5 Electronic structure of ethylamine calculated by density functional theory (GGA-PBE pesudo-potential) with 0.04 isosurface, a) Electrostatic Potential, b) Electrophilic Fukui function, c) Nucleophilic Fukui function, d) HOMO, and e) LUMO.. 159

FIGURE 6.6 Initial and optimized configurations for ethylamine adsorption on Mo(110) and the calculated adsorption energies.............. 161

FIGURE 6.7 Reaction coordinate diagram ethylamine decomposition on Mo(110. The activation energies associated with each transition state are labeled above the pathway and energies in parenthesis are the calculated adsorption energies. Units of energy are kcal mol^{-1}.. 164

LIST OF TABLES

TABLE 1.1 Typical nitrogen-containing compounds found in petroleum crude and shale oil... 8

TABLE 4.1 Summary of Pyridine TPD Features................................. 82

TABLE 4.2 Vibrational frequencies and assignments for the electron energy loss spectra of pyridine over Mo(110)...................... 94

TABLE 4.3 Summary of Pyridine DFT Adsorption Energies.................. 97

TABLE 4.4 Calculated Pyridine Bond Lengths.................................. 98

TABLE 4.5 Calculated Pyridine Inter-atomic Angles........................... 99

TABLE 4.6 Calculated frequencies of selected pyridine adsorption configurations... 105

TABLE 5.1 Summary of Pyrrole TPD Features.................................. 116

TABLE 5.2 Vibrational frequencies (cm^{-1}) and assignment of pyrrole adsorption on Mo(110) surface using high-resolution electron energy loss spectroscopy.. 130

TABLE 5.3 Calculated Pyrrole Bond Lengths.................................... 133

TABLE 5.4 Calculated Pyrrole Bond Angles...................................... 134

TABLE 5.5 Calculated vibrational frequencies (cm^{-1}) of adsorbed pyrrole configuration models.. 143

TABLE 6.1 Calculated Vibrational Frequencies of ethylamine intermediates... 166

LIST OF ABBREVIATIONS AND NOMENCLATURE

AES	Auger electron spectroscopy
ARUPS	Angle-resolved ultraviolet photoelectron spectroscopy
ATM	Atmospheric
BCC	Body centre cube structure
DFT	Density functional theory
DNB	Did not bond
C_X	Atomic concentration of an element X (AES) – Equation 3.2
CPS	Count per second
E_0	EELS Primary electron energy – Equation 3.3
E_0	Ground state energy – Equation 3.13
E	Auger electron energy – Equation 3.1
E	Energy – Equation 3.13
E_{ads}	Adsorption Energy
E_c	Correlation energy – Equation 3.18
E_k	The corresponding energies (Eigenvalues) of the operator – Equation 3.11
$\mathrm{E_K}$	K shell electron energy (AES) – Equation 3.1
$\mathrm{E_{L1}}$	L1 shell electron energy (AES) – Equation 3.1
$\mathrm{E_{L2}}$	L2 shell electron energy (AES) – Equation 3.1
$\mathrm{E_p}$	Primary electron beam energy (AES) – Equation 3.1
E_s	The detected energy loss (EELS) – Equation 3.3
E_x	Exchange energy – Equation 3.18
E_{xc}	Exchange energy – Equation 3.15
EELS	Electron energy loss spectroscopy
ESDIAD	Electron stimulated desorption ion angular distribution
FWHM	Full width at half maximum
GEA	Gradient expansion approximation
GGA	Generalized gradient approximation
h	The Planck's constant – Equation 3.4

$\hat{H}$	Hamiltonian operator – Equations 3.9-11
hcp	Hexagonal closed packed structure
$h\omega$	The energy of excited transition (EELS) – Equation 3.3
HDM	Hydrodemetalation
HDN	Hydrodenitrogenation
HDO	Hydrodeoxygenation
HOMO	Highest occupied molecular orbital
HREELS	High-resolution electron energy loss spectroscopy
HDS	Hydrodesulphurization
j	Represents the square root of -1 – Equation 3.4
inp	In-Plane vibrational mode
I_P	Peak-to-peak amplitude of the primary surface element (AES)
IRA	Infrared absorbances
I_X	Peak-to-peak amplitude of the element X (AES) – Equation 3.2
L	Langmuir
LDA	Local density approximation
LDF	Local density functional
LEED	Low electron energy diffraction
$\mathrm{LN_2}$	Liquid nitrogen
LSD	Local spin density
LST	Linear synchronous transit
LUMO	Lowest unoccupied molecular orbital
m	Represents a single particle of mass – Equation 3.4
ML	Monolayer
m/z	Mass to charge ratio
NEXAFS	Near-edge x-ray absorption fine-structure
QMS	Quadruple mass spectrometer
QST	Quadratic synchronous transit
oop	Out-of-plane vibrational mode
PBE	Perdew-Burke-Ernzerhof
r	The cartesian coordinates (x, y, z) –Equation 3.11

RAIS	Reflection absorption infrared spectroscopy
RFA	Retarding field analyzer
r_N	Positional coordinates – Equation 3.14
SCF	Self-consistent field
S_i	Relative sensitivity of pure element *i* (AES) – Equation 3.2
$T_0[\rho]$	The kinetic energy of electrons in a system – Equation 3.15
TDS	Thermal decomposition spectroscopy
TPD	Temperature programmed desorption
TPRS	Temperature programmed reaction spectroscopy
TS	Transition state
U	The potential energy – Equation 3.4
$\hat{U}_{cl}$	Pure Coulomb interaction between electrons – Equation 3.15
UHP	Ultra-high purity
UHV	Ultra-high vacuum
UPS	Ultraviolet photoemission spectroscopy
$\hat{V}_{ext}$	External potential – Equation 3.15
XPS	X-ray photoelectron spectroscopy

Greek Letters

δ	Bending in-plane vibrational mode
γ	Bending out-of-plane vibrational mode
ε	The energy of the system – Equation 3.6 and 3.7
ν	Stretching vibrational mode
ρ	Electron density – Equation 3.15
τ	Torsions vibrational mode
ϕ	Single-electron functions – Equation 3.12
ψ	Wavefuntion – Equation 3.4

Subscripts

0	Primary Energy (EELS) – Equation 3.3
0	Ground state – Equation 3.13
Ads	Adsorption energy
c	Correlation – Equation 3.18
ext	External – Equation 3.15
i	Pure element (AES) – Equation 3.2
k	Operator – Equation 3.11
K	Represents an atomic shell in AES process
L1	Represents an atomic shell in AES process
L2	Represents an atomic shell in AES process
N	Operator – Equation 3.11
s	Surface (EELS) – Equation 3.3
x	Exchange – Equation 3.18
X	Surface element (AES) – Equation 3.2

Publications

Parts of the results within this thesis were published during the last two years. The following represents each chapter with its related publication/publications.

Chapter 4	Abdallah, W. A., Nelson, A. E. and Gray, R. M (2004), "Pyridine adsorption and reaction on Mo(110) and C/N–Mo(110): experiment and modeling," *Surf. Sci.*, **569**, 193 – 206.
Chapter 5	Abdallah, W. A. and Nelson, A. E. (2005), "Pyrrole adsorption and reaction on Mo(110) and C/N-Mo(110)," *Surf. Sci.*, **585**, 113 – 122.
	Abdallah, W. A. and Nelson, A. E. (2005), "Density Functional Theory Study of Pyrrole Adsorption on Mo(110)," *J. Phys. Chem. B*, **109**, 10863-10870
Chapter 6	Abdallah, W. A. and Nelson, A. E., "Ethylamine adsorption and reaction mechanism on Mo(110) using TPD, HREELS and DFT," In preparation.
Chapter 7	Abdallah, W. A. and Nelson, A. E. (2005), "Characterization of MoSe$_2$(0001) and ion-sputtered MoSe$_2$ by XPS," *J Mat Sci.*, **40**, 2679 – 2681.

1. INTRODUCTION

1.1 Crude Oil

Water and air are considered the basic needs for humankind to live; similarly, energy is considered the basic need for humankind to survive. The dependence on energy started with wood before the industrial revolution, and gradually developed based on the need of the industrialized societies to the utilization of crude oil. The United States, in 1859, was the first to extract crude oil from the ground on a commercial scale to provide kerosene. Currently, the petroleum industry separates the components of crude oil to produce a wide range of products to meet the high specifications demanded in all industrial and economical applications. With the expansion of petroleum-dependent industries and sectors, coupled with increasing environmental legislation, the demand for lighter (conventional) feedstocks has steadily increased. However, lighter crude oil reserves are rapidly depleting and alternative sources of crude oil, specifically heavy oils and bitumens, must be utilized to meet the increasing demand for petroleum and petroleum distillates.

There are several sources of heavy oils which may be available to mitigate the increasing demand for petroleum distillates, including vacuum residue from conventional oil vacuum distillation processes or the sequestering of natural deposits of shale oil or bitumens. The United States has twice the proven reserves of petroleum in the world as shale oil, while Canada has one-third of the proven world reserve of oil sands (Kabe et al., 1999) and the second largest reserves of oil behind Saudi Arabia if oil sands deposits are included. Alberta's oil sand deposits contain resources that could supply the total world needs for up to 15 years, and present estimates indicate the oil sands contain 1.7 – 2.5 trillion barrels of bitumen. However, before heavy oils and vacuum residue can be refined into transportation and heating fuels, substantial processing, or upgrading, is required.

Petroleum and other fossil fuel feedstocks contain mostly hydrocarbons with a wide range of molecular weights and chemical structures. These feedstocks are also contaminated by variable amounts of organic compounds containing sulfur, nitrogen and oxygen as heterocyclic compounds, with much smaller amounts of inorganic compounds, mainly as trace metals of vanadium and nickel (Bianchini et al., 2001; Bond, 1987) depending on the location of origin. These heterocyclic compounds are distributed over the entire boiling range of the crude oil and typically the concentration increases as the boiling point increases (Wiwel et al., 2000). Although the processing of light feedstocks is approaching mature technology, the utilization of heavy oils and vacuum residues is not without substantial technological and economic challenges. Heavy crude oils are commonly higher in viscosity and include high concentrations of contaminants including sulfur, nitrogen, and metals. Thus, the utilization of heavy oils can become environmentally harmful and expensive to process (Kabe et al., 1999), and consequently the removal of contaminants becomes crucial.

1.2 Catalytic Hydrotreating

Figure 1.1 represents a simplified crude oil refining process flow diagram. The major steps of a refinery process consist of distillation, hydrotreating, cracking and reforming. In the distillation unit, the lightest materials (e.g. propane and butane) vaporize and rise to the top of the first atmospheric column (light ends). Middle distillates and naphtha condense in the centre of the column and are withdrawn. Atmospheric gas oils (heavy materials) condense in the lower portion of the atmospheric column, while the heaviest tar-like material is called atmospheric residue, and is withdrawn at the bottom of the atmospheric distillation column. Atmospheric residue is then processed in a second distillation column that operates at less than atmospheric pressure (vacuum) to lower the temperature at which a hydrocarbon mixture boils.

Examination of this flow diagram (Figure 1.1) illustrates that one repeated process unit follows every stream emanating from the main distillation unit - the hydrotreater. Catalytic hydrotreating is considered one of the most important processes in the petroleum industry since all sour streams require hydrotreating prior to their use. Hydrotreatment mainly consists of hydrodesulphurization (HDS), hydrodenitrogenation (HDN), hydrodeoxygenation (HDO) and hydrodemetalation (HDM) reactions for the removal of sulfur, nitrogen, oxygen and metals compounds, respectively, from a petroleum feedstock by a catalytic reaction as shown in Equations 1.1 –1.4, respectively.

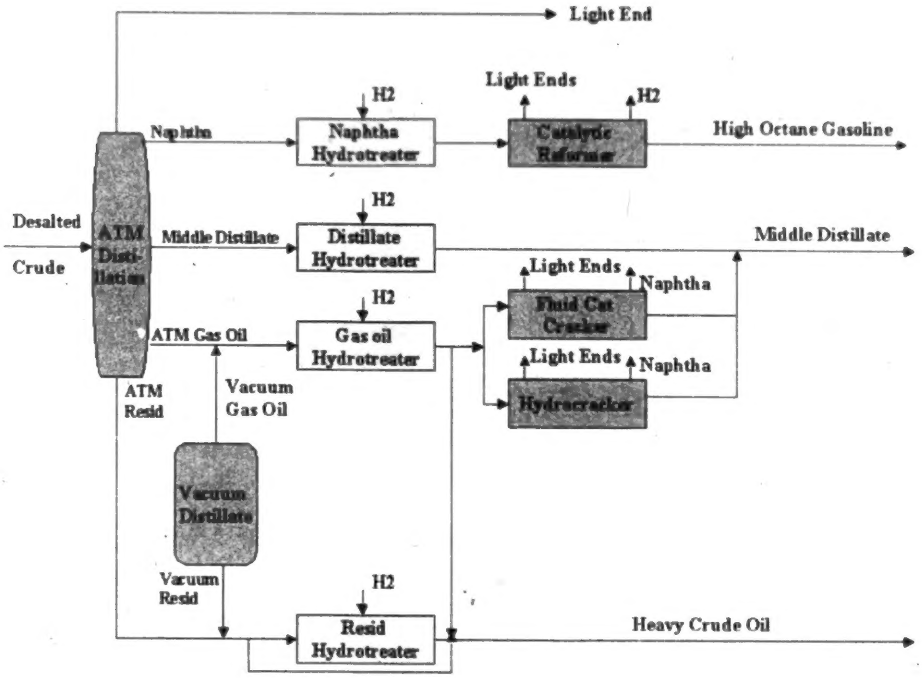

Figure 1.1 Crude oil refining process flow sheet (Leach, 1983).

$$C_xH_yS \xrightarrow{nH_2} H_2S + C_xH_z \qquad (1.1)$$

$$C_xH_yN \xrightarrow{nH_2} NH_3 + C_xH_z \qquad (1.2)$$

$$C_xH_yO \xrightarrow{nH_2} H_2O + C_xH_z \qquad (1.3)$$

$$M-L + aH_2S \xrightarrow{nH_2} MS_a + L-H_z \qquad (1.4)$$

Previous research has been directed toward HDS (Gellman et al., 1987; Gulkova and Zdrazil, 1999; Lewandowski and Sarbak, 2000; Marroqquin et al., 2001; Nagai et al., 1986; Ozkan et al., 1994; Satterfield et al., 1975; Satterfield et al., 1980; Vit, 1993) to reduce sulfur levels to those required for catalytic processing by supported-metals catalysts in order to meet air emission levels when the liquid fuel is burned. Considerably less research effort has been directed toward HDN (Bej et al., 2001; Cocchetto and Satterfield, 1981; Hanlon, 1987; Ledoux and Djellouli, 1990; Lee et al., 1993; Lewandowski and Sarbak, 2000; McIlvried, 1971; Nagai et al., 1988; Nelson and Levy, 1979; Schlatter et al., 1988) because of the comparatively small quantities of nitrogen compounds present in conventional petroleum stocks. In the case of the hydrotreatment of bitumen and vacuum residue, however, hydrodenitrogenation becomes significant. Light crude oil in general contains low levels of organic nitrogen compounds, but vacuum residue bitumen can have up to 0.7 wt% which twice more than the amount of nitrogen in light crude (Wiwel et al., 2000).

Hydrodenitrogenation (Equation 1.2) occurs by mixing crude oil with hydrogen gas in a trickle-bed reactor over conventional hydrotreating catalysts, as shown in Figure 1.2. Hydrogen separated from the product stream is scrubbed to remove ammonia, and light hydrocarbons, and then recycled to the process with added make-up hydrogen. The product stream is then sent to a stripping column to separate the light materials from the heavy fractions. Over conventional hydrotreating catalysts, hydrodenitrogenation proceeds through initial ring saturation (hydrogenation) followed by scission of the

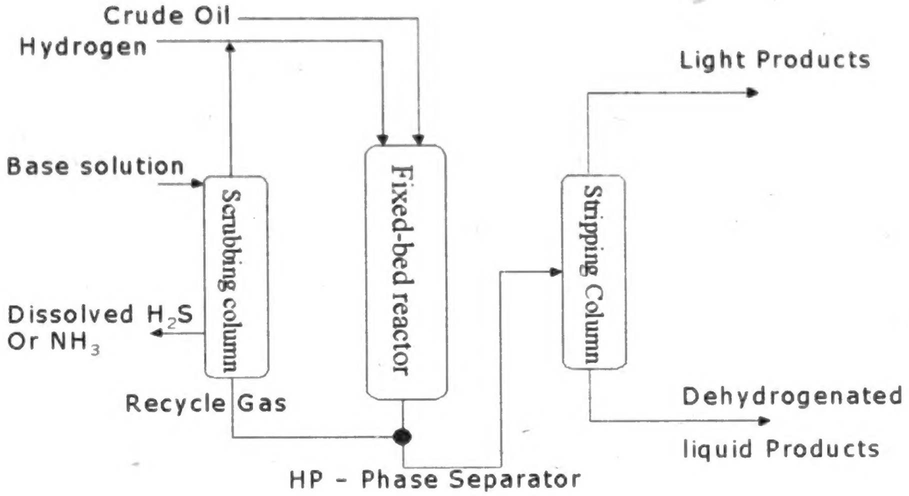

Figure 1.2 Simplified flow diagram of a hydrodenitrogenation process unit (Katzer and Sivasubramanian, 1979).

carbon-nitrogen bond (hydrogenolysis) ultimately leading to the formation of hydrocarbons and ammonia. Ring saturation for nitrogen removal is required in order to cleave the C-N bond, in contrast to HDS where hydrogenation is not always required (Kabe et al., 1999). This saturation requirement can be (partially) explained by the higher C-N bond energy compared to C-S bonds. Thus, hydrodenitrogenation requires significant amounts of hydrogen, which make the process expensive to operate (Alves and Towlerr, 2002; Katzer and Sivasuramanian, 1979; Schlatter et al., 1988). Therefore, a potential approach to improve the efficiency of hydrodenitrogenation would be the development of a denitrogenat~~ion-selectiv~~e catalyst. This requires a fundamental understanding of organonitrogen adsorption and denitrogenation mechanisms on hydrotreating catalyst surfaces.

1.3 Importance of Nitrogen Removal

HDN in general is the most difficult hydrotreating reaction, and little is known about the detailed reaction mechanism and energetics. The hydrodenitrogenation of organonitrogen compounds to ammonia and hydrocarbons also consumes more hydrogen than any other hydrotreating reaction, which makes it the most expensive and most difficult hydrotreating process. The need to remove nitrogen compounds is critical due to several factors, including (1) to meet stiff environmental legislations, (2) to avoid deactivating and poisoning the metal catalysts used in reforming processes. (Nitrogen-containing compounds severely reduce the activity of cracking, reforming, hydrocracking, hydrodesulphurization, hydrodenitrogenation and isomerization catalysts, since the catalysts used in these processes are acidic and thus poisoned by nitrogen compounds, which are strongly basic), (3) nitrogen adversely affects fuel stability during storage as these materials can cause precipitation, (4) nitrogen compounds influence the formation of coke, as many of these molecules are known to be coke precursors, and (5) heavy crude residues and shale oil have high aromatic nitrogen content that can be quite carcinogenic and require HDN (Katzer and Sivasuramanian, 1979; Sanchez-Delgado, 2002; Wiwel et al., 2000). This is further compounded by the fact that there are relatively high concentrations of nitrogen in heavy oils and vacuum residue. Thus, HDN is one of the most important processes in converting oil sands bitumen, shale oil and coal to synthetic fuels (Ho, 1988; Topsøe et al 1996).

Clearly, the environmental and economical impacts of organonitrogen compounds present in petroleum fractions are severe. In order to address the concern of nitrogen removal, hydrodenitrogenation-specific catalysts are required, and unfortunately there is a lack of a detailed understanding of hydrodenitrogenation mechanisms and energetics. Thus, the need to develop a fundamental understanding of nitrogen compound removal from crude oil is crucial and requires further investigations about organonitrogen adsorption and subsequent denitrogenation reaction mechanisms in order to design more efficient catalysts for hydrodenitrogenation of crude oil.

1.4 Organonitrogen Compounds

Nitrogen compounds are present in heavy crude oil primarily as heterocyclic aromatic compounds. Several nitrogen-containing compounds found in petroleum crude and shale oil are presented in Table 1.1. Non-heterocyclic organonitrogen compounds, such as aliphatic amines and anilines are also present but in considerably smaller amounts, and these are denitrogenated much more rapidly than the heterocyclic compounds and are considered less significant in HDN processes (Girgis and Gates, 1991). Despite previous research, the adsorption and subsequent denitrogenation of organonitrogen compounds are still not well understood.

Heterocyclic organonitrogen compounds are classified as basic (six-membered pyridinic ring) and non-basic (five-membered pyrrolic ring) depending on the chemical structure. In the latter (e.g., pyrrole, indole and carbazole), the lone-pair electrons on the nitrogen atom are delocalized around the aromatic ring and, therefore, have a weak tendency to interact with a Lewis acid site on a hydrotreating catalyst. As a result, non-basic organonitrogen compounds would have a tendency to bond with the catalyst surface through the aromatic ring due to the high electron density in the ring rather than the nitrogen atom. In contrast, the basic heterocyclic compounds, such as pyridine, quinoline and acridine have a lone-pair of electrons around the nitrogen atom and most likely will bond to acidic catalytic sites on the catalyst surface. They can also accept Lewis bases to their unoccupied molecular orbitals in the aromatic π-ring structure (Ho, 1988; Katzer and Sivasuramanian, 1979; Laine, 1983).

Table 1.1 Typical nitrogen-containing compounds found in petroleum crude and shale oil

Compound	Formula	Structure
Methylamine	CH_3NH_2	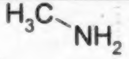
Ethylamine	$CH_3CH_2NH_2$	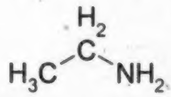
Pyrrole	C_4H_5N	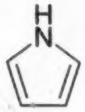
Indole	C_8H_7N	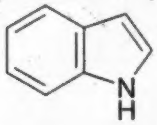
Carbazole	$C_{12}H_9N$	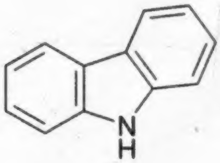
Pyridine	C_5H_5N	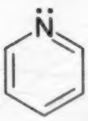
Quinoline	C_9H_7N	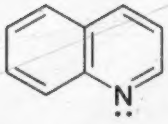
Acridine	$C_{13}H_9N$	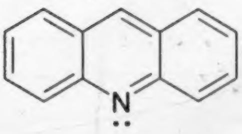

The complexities of these compounds, which are present in crude oil to varying extents, represent a challenge to understand the mechanisms of HDN on hydrotreating catalyst surfaces. As illustrated in Table 1.1, methylamine, pyridine and pyrrole are the essential homologs of nitrogen containing compounds in heavy crude oil. Adding a methyl group to methylamine produces ethylamine, while adding a benzene ring to pyrrole gives indole and adding another ring of benzene to the other side of indole produces carbazole. Similarly for pyridine, the addition of one benzene ring produces quinoline and the further addition of a benzene ring to quinoline produces acridine. In general, these heterocyclic compounds are present in heavy crude oil in relatively high concentrations compared to other nitrogen compounds. Consequently, these molecules are often used as model compounds in understanding HDN reaction kinetics and mechanisms (Katzer and Sivasuramanian, 1979).

In order to understand the fundamental interactions of these compounds with catalyst surfaces, it is required to adopt a model compound with a simple structure to avoid further complexities due to the hydrocarbon structure. The probe compounds most commonly used in HDN studies for comparing the activity of catalysts and studying HDN reaction mechanisms are pyrrole (non-basic) and pyridine (basic) (Bianchini et al., 2001; Glueck et al., 1989; Moravek et al., 1990; Reedijk, 1987; Sanchez-Delgado, 2002). Pyridine and pyrrole, as well as methylamine (or ethylamine) represent the simplest structures of the organnitrogen families, and serve as the building blocks for all other organonitrogen compounds present in crude oils, as mentioned earlier.

1.5 Hydrotreating Catalysts

Commercial hydrotreating catalysts can be described as a transition metal based compounds (molybdenum or tungsten sulfides), promoted by nickel or cobalt and dispersed on a high surface area support such as γ-alumina (Laine, 1983; Ledoux and Djellouli, 1990; Ozkan et al., 1994; Rodiguez et al., 1999; Wexler et al., 1982). In general, industrial HDN is performed using a promoted molybdenum disulfide (MoS_2) catalyst, which is also typically used as a HDS catalyst (Hanlon, 1987; Ledoux and Djellouli, 1990; Marzari et al., 1995; Nagai et al., 1988; Ozkan et al., 1994). As with all heterogeneously catalyzed processes, the activity and selectivity of MoS_2 catalysts are dependent upon the surface properties. Therefore, knowledge of the surface chemistry and morphology is necessary to understand the fundamental relation between structure, electronic states, and reaction dynamics (Byskov et al., 1999; Faye et al., 1999; Kushmerick et al., 2000; Park et al., 1996).

MoS_2 has a *hcp* layered crystal structure consisting of sheets of S-Mo-S, and these sheets are weakly bound to each other by van der Waals interactions. This structure predominantly exposes the relatively inert hexagonal basal planes, and unsaturated (presumably reactive) exposed edge planes, as shown in Figure 1.3. This conclusion is supported by a recent study of thiophene HDS on MoS_2 (Kushmerick et al., 2000). It was reported thiophene HDS activity on MoS_2 basal planes showed negligible activity, however, after sputtering the MoS_2 basal plane thiophene HDS activity increased (Kushmerick et al., 2000). The study is also consistent with the hypothesis that exposed Mo atoms at sheet edges are the active site for HDS (Friend and Chen, 1997; Robert and Friend, 1986; Robert and Friend, 1987; Roe and Schulz, 1998). This level of understanding would not be possible if it were not for atomic-scale studies using modern surface science techniques, as well the use of model catalyst surfaces. These model catalysts can be modified by introducing structural defects or adding promoters on the surface to further reduce the discrepancy between model catalysts and the technical catalysts used in industry. Kinetic information obtained for single crystal models characterized before and after reaction by tools of surface science, provides the standards which work on the corresponding supported catalysts can be assessed (Boudart, 1986).

1.6 Surface Science and Catalysis

Industrial catalysts consist of small solid particles supported on a high surface area support, and these supported particles expose various crystal planes with (typically) poorly defined composition and morphology, which makes them less attractive for atomic-scale type studies. Therefore, the concept of model catalyst surfaces consisting of a simple, well-defined structure is a suitable substitute for industrial catalysts (Boudart, 1986; Campbell, 1989; Ertl and Freund, 1999; Somorjai, 1996).

Indeed, within the last two decades, researchers have utilized the techniques of surface science, heterogeneous catalysis, organometallic chemistry and theoretical

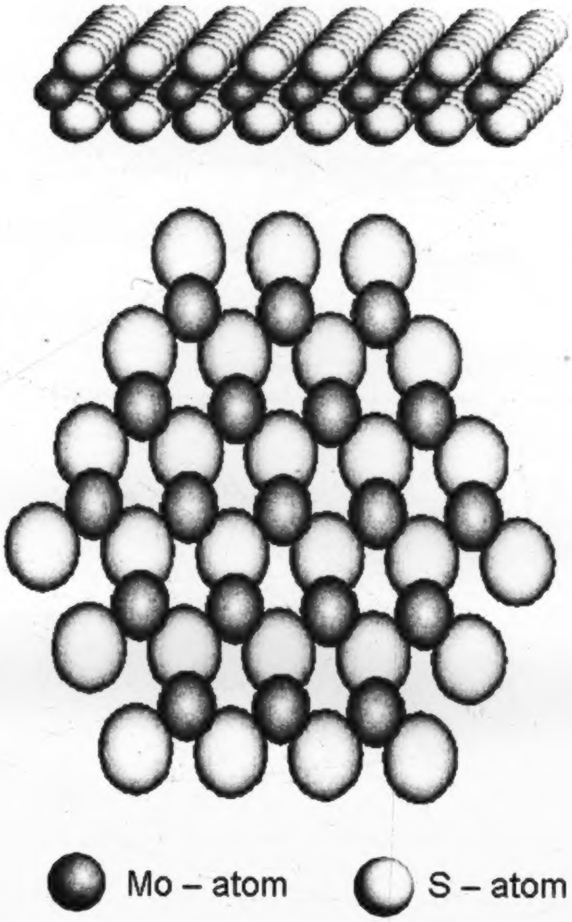

Figure 1.3 The above image shows a structure of MoS_2 commercial catalyst that consists of sheets of S-Mo-S, while the lower image shows a hexagonal basal plane of MoS_2.

chemistry, which have provided new opportunities to elucidate the fundamental understanding of catalytic reaction mechanisms and energetics on model catalyst surface.

Van Santen (1991) identifies three levels of research in catalysis. The macroscopic level is the world of reaction engineering, test reactors and catalyst beds, which addresses questions about activity per unit volume and catalyst mechanical strength. The mesoscopic level comprises kinetic studies, activity per unit surface area and the relationship between the composition and structure of a catalyst and its catalytic behavior. Finally, the microscopic level focuses on fundamental studies to understand the details of adsorption on surfaces, reaction mechanisms, theoretical modeling and surface science. The first two categories have been the subject of considerable research, while considerably less research has been performed at the microscopic level despite the clear potential to develop a fundamental understanding of catalytic phenomena. Surface science and theoretical investigations of surface structure, adsorption, chemisorption and catalytic reactions over well-characterized surfaces have the clear potential to reveal the all-important surface structure-reactivity relationships. That knowledge then would revolutionize the development of tailored, highly product specific catalysts. Indeed, surface science has been very successful by making major inroads in the understanding of the elementary steps of many catalytic reactions, including HDS (Kolasinski, 2002).

Because of the need for atomic level scrutiny of surface properties, many surface specific techniques have been developed. These techniques utilize electrons, ions, and photons to determine surface structure, surface composition, oxidation states of surface atoms, and bonding modes of adsorbates. Recent technological advancements have provided instrumentation with ever increasing spatial resolution, time recalculation, and energy resolution. Most of these techniques can be applied only at fairly low pressures ($1\times10^{-6} - 1\times10^{-11}$ torr), whereas actual catalysis typically function at atmospheric or much higher pressures. The surface science approach, therefore, creates a "pressure gap" in addition to the "materials gap" introduced by the reduction of complex catalyst to single crystal surfaces. There exist various ways to overcome these problems, which always need to be considered (Boudart et al., 1977; Boudart, 1986). One way to overcome the “pressure and material gap” that separate ultrahigh-vacuum (UHV) surface science and technical catalysis has been bridged by coupling an apparatus for the measurement of reaction kinetics at elevated pressures with an ultrahigh-vacuum system for surface analysis. Studies with this combined methodology have provided an atomic-level understanding of various aspects of heterogeneous catalysis such as structure/activity relationships, the role of promoters and inhibitors on catalytic activity, and the nature of the metal-metal bond in mixed-metal catalysts. These investigations have demonstrated the relevance of single crystal studies for modeling the behavior of high surface area supported catalysts as well as the power of surface analytical techniques for characterizing adsorbed reactants and intermediates (Goodman, 1996; Lee et al., 1993). The use of ultrahigh vacuum is in general considered as an advantage since it permits the investigation of surfaces under static and stable conditions. It is required to enable atomically clean surfaces to be prepared for study, and such surfaces need to be maintained in a contamination-free state for the duration of the experiment. Ultrahigh vacuum conditions are also required to permit the use of low energy electron and ion-based experimental techniques without excessive interference from gas phase scattering.

With the difficulty of forming well-ordered stepped surfaces of MoS_2, single-crystal Mo surfaces bare has been suggested as model systems (Wiegand and Friend, 1992). The Mo single crystals have significantly different structures and higher reactivity than MoS_2, nonetheless, with a surface crystallographic orientation of (110), a similar basal plane that correspond to MoS_2 based metal hexagonal structure can be adopted to extrapolate to the industrially relevant MoS_2 catalysts (Figure 1.4). The Mo(110) surface was chosen not only for its industrial applicability in hydrotreating reactions, but also it represents the most thermodynamically stable face limiting the effects of surface reconstruction on the observed adsorption and decomposition of organonitrogen compounds. The Mo(110) single crystal surface has been widely used as a model hydrotreating catalyst as a substitute of MoS_2 catalyst since it is hard to prepare a single crystal of MoS_2 due to its lubricant condition (Liu and Friend, 1988; Serafin and Friend, 1989; Roberts and Friend, 1986; Rodriguez, et al., 2000). As a result, catalyst surface characterization at the microscopic level (atomic level) will be the leading edge in identifying the active sites that are responsible for the HDN activity.

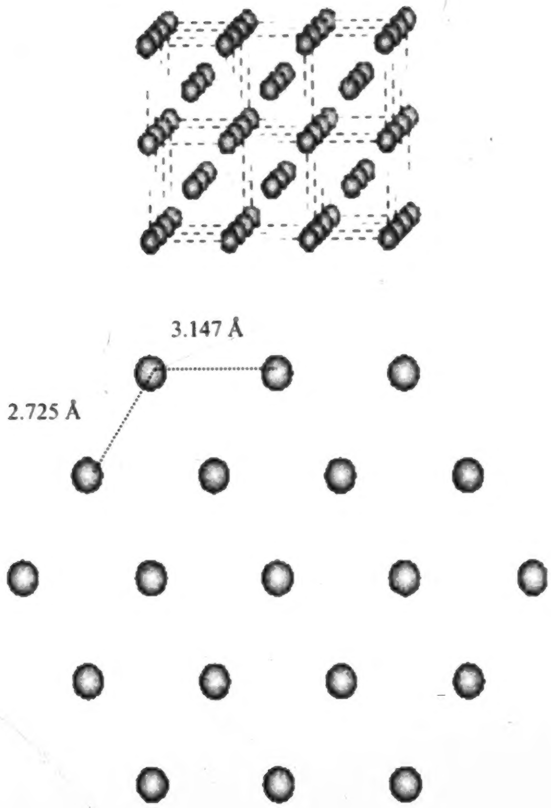

Figure 1.4 The above structure represents a cluster of body centre cube of Mo crystal, while the lower image represents a Mo-surface with (110) crystallographic orientation.

1.7 Density Functional Theory (DFT)

In addition to experiment, quantum mechanics provides an additional basis to study the electronic structure of the molecules and their interaction with a catalyst surface. Starting with a specified molecular geometry, quantum mechanical calculations solve the Schrödinger equation for this arrangement of electrons and nuclei. This yields both the energy of the molecule and the associated wave function from which the electronic properties, such as electron density, can be calculated. The wave function can be used to calculate a range of chemical properties, which can be used in structure-activity studies, which include electrostatic potential, electron density, dipole moment, and the energies and positions of frontier orbitals. In this regard, density functional theory (DFT) has evolved as an important complement to experiment to aid in the interpretation of experimental results and providing complimentary information, which is otherwise difficult to obtain by experiment. Density functional theory, developed in the 1960s by Nobel Prize winner Walter Kohn, is a well-established approach for tackling the quantum mechanics of many-body systems, and has become the standard representation for complex applications in the chemical and materials sciences (Hinchliffe, 2000). DFT is a methodology to solve the Schrödinger equation for the many-body system. In the earlier proposed formulation given by Kohn, Hohenberg, and Sham, the real system is described by an effective one-body and in order to achieve that goal, while the many-body wave function which is the solution of Schrödinger equation is abandoned in favor of the density which only depends on the three spatial coordinates. Thus, the energy is described as a function of the electron density.

Density functional theory studies have provided insights in many areas where surface science techniques are limited. Indeed, density functional theory has provided fundamental information regarding hydrodesulphurization reactions on MoS_2 catalysts by identifying the active sites on the catalyst surface, and how these sites affect hydrogenation, C-S bond scission, and the overall reaction mechanism (Raybaud et al., 2000). Such knowledge furthered the development of HDS catalysts by establishing the fundamental relationships between the structure of the catalyst and the HDS activity (Byskov et al., 1999; Faye et al., 1999). Investigating the adsorption and desorption behavior of organonitrogen compounds on a molecular level using density functional theory can provide energetic and vibrational data that will assist in identifying the adsorption modes and reaction mechanisms. Such studies combined with surface science investigations will serve the development of active and selective HDN catalyst.

1.8 Summary

In recent years, diminishing conventional crude reserves has prompted the utilization of heavy oils and vacuum residue; however, the use of these feeds in not without unique industrial and environmental challenges. With higher contaminant levels, specifically organonitrogen compounds, research is required to develop HDN selective catalysts based on a fundamental understanding of their interaction with catalyst surfaces and subsequent denitrogenation mechanisms. The most promising approach to develop a comprehensive understanding of the energetic and mechanistic features of HDN is using surface science techniques and density functional theory to probe the interaction of representative organonitrogen compounds with model catalyst surfaces. In this research, ethylamine, pyridine, and pyrrole will serve as the representative organonitrogen compounds and Mo(110) as the model hydrotreating catalyst surface.

The remainder of the thesis is organized as follows. Chapter 2 will focus in reviewing previous adsorption and decomposition work of ethylamine, pyrrole and pyridine over the Mo(110) single crystal surface and discuss their results and highlight the significance of previous research results. Chapter 3 presents an experimental summary of the spectroscopic techniques and operational parameters used in this research. Chapter 4 summarizes the experimental and computational results of pyridine adsorption on Mo(110), and presents several important aspects about the energetics and structure of pyridine adsorption on Mo(110). Chapter 5 summaries the experimental results of pyrrole adsorption and decomposition on Mo(110). Chapter 6 summarizes the energetics and mechanism of ethylamine adsorption and decomposition on Mo(110). Chapter 7 summarizes the overall research observations, discusses their implications to catalytic hydrotreating, and future research opportunities extending from this research.

2. LITERATURE REVIEW

2.1 Hydrodenitrogenation (HDN) Process

As previously summarized in Chapter 1, organonitrogen compounds in petroleum and coal is contained in various structural forms, which include five- and six-membered heterocycles, aliphatic and aromatic amines and nitriles. Amines and nitriles are present in lower quantities compared to heterocyclic organonitrogen compounds, and their degradation is efficiently preformed under hydrotreating conditions over molybdenum-based catalysts, such as Co-MoS_2/Al_2O_3 and Ni-MoS_2/Al_2O_3 (Katzer and Sivasubramanian, 1979). The HDN of the aromatic heterocycles is much more difficult to accomplish compared to amines and sulfur removal (hydrodesulfurization or HDS) (Topsøe, et al., 1996). However, as heterocyclic organonitrogen compounds are present in higher concentrations in heavy oil than in the conventional oil, nitrogen removal is an important consideration during the hydrotreating of heavy oil and vacuum residues (Gray, 1994).

In general, HDN takes place through an initial ring saturation (hydrogenation) followed by cleavage of the carbon-nitrogen bond (hydrogenolysis) and then by further reactions leading ultimately to the formation of hydrocarbons and ammonia (Alves and Towlerr, 2002; Katzer and Sivasuramanian, 1979; Schlatter et al., 1988). Ring saturation in nitrogen removal is required to be able to cleave C–N bonds, in contrast to HDS, where hydrogenation is not always required (Kabe et al., 1999). In comparison to HDS, HDN reaction mechanisms and kinetics are quite complex and difficult to analyze since both steps (hydrogenation and hydrogenolysis) are required and either could be rate limiting.

Most of the studies that involved in the hydrogenation reaction network have been concentrated on six-membered nitrogen heterocycles. Among the model compounds studied, pyridine (Guerrerp-Ruiz et al., 1995; Gulkova and Zdrazil, 1999; Hanlon, 1987; Marzari et al., 1995; Satterfield et al., 1980; Satterfield et al., 1985), acridine (Nagai et al., 1986) and quinoline (Cocchetto and Satterfield, 1981; Lee et al., 1993; Rangwala et al., 1990; Satterfield et al., 1985; Schlatter et al., 1988) have received the most attention. Although the amount of information on their HDN kinetics is considerable and several reaction mechanisms have been suggested based on the reactivity of bulk reacting fluids, quantification of the reaction pathway is not complete. The vapor-phase reaction network of pyridine, shown in Figure 2.1, has been reported in several studies using Ni-Mo/Al_2O_3 catalysts (Hanlon, 1987).

In this reaction mechanism, pyridine is hydrogenated to piperidine (irreversible process) of which one C–N bond is cleaved to form n-pentylamine, and n-pentane and ammonia are formed by hydogenolysis of the amine (Hadjiloizou et al., 1992; Hanlon, 1987; Ho, 1988; Laine, 1983; McIlvried, 1971). Several mechanisms of C–N bond scission have been proposed (Kabe et al., 1999) and some of these have been explained based on classical Hofmann-type elimination and nucleophilic substitution, which requires the leaving nitrogen be quaternized before the bond cleavage occurs (Nelson and Ivory, 1979). A different view has been offered, which proposed the C–N bond cleavage in saturated heterocycles may not require acidic sites but rather metal atoms or ions, which gives at least two pathways: one involves a metal alkyl intermediate, and the other involves a metal alkylidene intermediate (Laine, 1983).

Studies with five-membered nitrogen heterocycles have been hindered by the low solubility of most synthetically amenable compounds and their poor stability. Most of the published reaction and kinetic information in this regards is limited to indole (Choi et al., 1995; Goodman, 1982; Lewandowski and Sarbak, 2000; Li et al., 1999; Olive et al., 1985; Schlatter et al., 1988), while considerably less work has been done on pyrrole. Pyrrole has seldom been used in HDN studies since its instability makes handling difficult, and its reactivity is low due to its poor adsorptivity in comparison with the other nitrogen bases (Satterfield et al., 1980); therefore, very little information is available for pyrrole HDN. Satterfield (1980) suggested the kinetic scheme of pyrrole HDN, as summarized in Figure 2.2.

Owing to the higher relative reactivity of pyrrolidine and 1-butylamine, the reaction mechanism at low initial partial pressure can be effectively simplified to a one-step reaction from pyrrole to ammonia and C_4-hydrocarbon.

It is very imperative to understand that the above reaction mechanisms were postulated using similar studies, which focused on the studying the reactivity of bulk

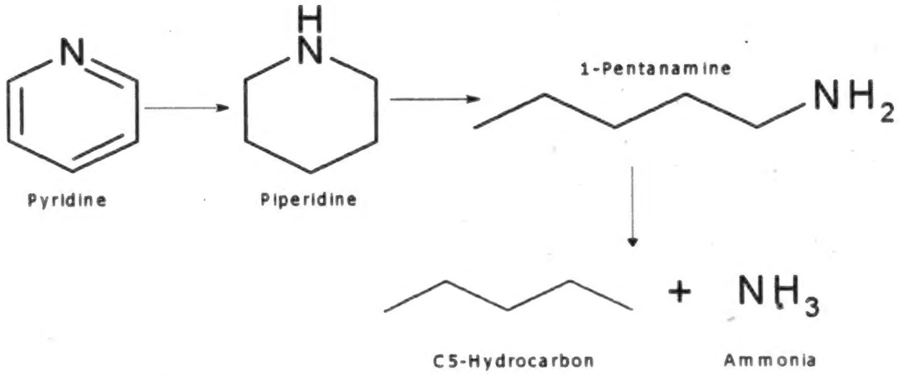

Figure 2.1 Reaction mechanism for pyridine HDN (Hanlon, 1987).

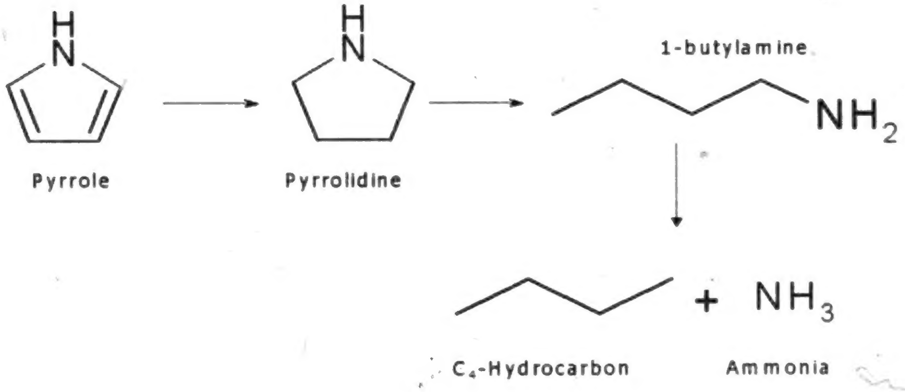

Figure 2.2 Reaction mechanism for pyrrole HDN (Satterfield et al., 1980).

reacting fluids in the presence of a catalyst (e.g. Co-MoS_2/Al_2O_3 and Ni-MoS_2/Al_2O_3) at various reaction conditions. However, these simple conversion studies do not provide the means to develop a fundamental understanding of the HDN of five- and six-membered organonitrogen heterocycles. One of the simplest methods to understand the salient features of HDN is to study the adsorption and desorption behavior of a probe molecule over a model hydrotreating catalyst surface. This approach will also facilitate new insights into the structure-property relationship of HDN catalysis, which is critical for the development of new highly active and selective HDN catalysts.

Therefore, in order to get further understanding of the HDN mechanism, it is important to adopt a suitable probe molecule as well a model catalyst, for example a single crystal. Heterocyclic organonitrogen compounds (Table 1.1) present in heavy crude oil contain either pyridine or pyrrole homologs as the essential nitrogen containing structures for all basic or non-basic heterocyclic organonitrogen compounds. Although studies of organonitrogen adsorption and reaction over model hydrotreating catalyst surfaces are very limited, studies with different single crystals surfaces have been studied for a variety of industrial applications. These studies are summarized in the following sections according to the specific probe molecule studied.

2.2 Pyridine

2.2.1 Introduction

Pyridine (C_5H_5N) is one the most widely adopted molecules for basic organonitrogen adsorption studies, as well as ligands in coordination chemistry. Organometallic chemistry has provided considerable information regarding the possible bonding modes of pyridine to metal centers (Sanchez-Delgado, 2002). Based on these studies, several different bonding configurations have been suggested, as summarized in Figure 2.3. Of these, there are numerous examples of the η^1(N)-Py-90° complex for most transition metals (Reedijk, 1987). The η^1(C2)-Py-90° complex (Selnau and Merola, 1993), obtained by the replacement of a proton (hydrogen atom) by a metal fragment, and the η^6-Py-0° coordination modes are also frequently cited in homogeneous modeling studies of pyridine (Chaudret and Jalon, 1988; Chaudret et al., 1990; Fish et al., 1991a;

Fish et al., 1991b). The η^1(N)-Py-90° mode is preferred for electrophilic metal centers with a single vacant coordination site, and η^6-Py-0° is preferred if three coordination sites are available and the metal centre has filled dπ orbitals. If two free coordination sites are available, the electronic nature of the transition metal determines whether the η^2(C2,C3)-Py-90° or η^2(N,C)-Py-90° mode is prevalent. Specifically, electron-rich transition metals have a tendency to prefer the η^2(C2,C3)-Py-90° mode, while the electrophilic early transition metals effectively stabilize the η^2(N,C2)-Py-90° mode. Unfortunately, while the bonding modes in Figure 2.3 present reasonable models to describe pyridine adsorption on HDN catalyst surfaces, none of them have been found sufficiently reactive for homogeneous phase C–N bond scission (Sanchez-Delgado, 2002).

2.2.2 Pyridine Adsorption on Single Crystal Surfaces

The adsorption and interactions of pyridine on single-crystal surfaces have also been widely studied primarily due to its relevance as a suitable model HDN compound (Andersson and Uvdal, 2001; Avouris and Demuth, 1981; Avouris et al., 1984; Bader et al., 1986; Bandy et al., 1979; Cohen and Merrill, 1990; Davies and Newton, 2003; DiNardo et al., 1984; Gland and Somorjai, 1973; Grassian and Muetterties, 1986; Grassian and Muetterties, 1987; Johnson and Muetterties, 1983; Johnson et al., 1985; Lopinski et al., 1998; Mate et al., 1988; and Mack, 1983a; Netzer and Mack, 1983b; Netzer et al, 1988; Serafin and Friend, 1989; Wexler et al., 1982; Whitten, 2003; Young et al., 2003). In general, these studies concluded that pyridine adsorption geometry is surface coverage dependent, which is supported by three bonding geometries; parallel to the surface at low coverages (η^6-Py-0°) (Avouris and Demuth, 1981; Cohen and Merrill, 1990; Davies and Newton, 2003; DiNardo et al., 1984; Grassian and Muetterties, 1986; Whitten, 2003), perpendicular or inclined at high coverages (η^1(N)-Py-90°) (Avouris and Demuth, 1981; Bader et al., 1986; Cohen and Merrill, 1990; Davies and Newton, 2003; DiNardo et al., 1984; Grassian and Muetterties, 1986; Grassian and Muetterties, 1987; Johnson et al., 1985; Netzer and Mack, 1983a; Serafin and Friend, 1989; Whitten, 2003), and through α-pyridyl species formation, which requires bond formation between the nitrogen and an adjacent carbon with the metal surface (η^2(N,C2)-Pyridyl) mode leading to molecular desorption or surface decomposition on Mo(110) (Davies and Newton, 2003; DiNardo et al., 1984; Grassian and Muetterties, 1986; Johnson et al., 1985; Serafin and Friend, 1989; Wexler et al., 1982).

The molecular adsorption geometry of pyridine was investigated on the Ag(111) surface primarily to study the electronic excitation of the pyridine ring using high-resolution electron energy loss spectroscopy (HREELS) (Avouris and Demuth, 1981). This study concluded that the pyridine adsorption geometry is coverage-dependent. Based on their analysis that involved the comparison of the relative intensities of the in-plane and out-of-plane modes and the structurally averaged infrared absorbances (IRA) of liquid pyridine, it was determined that pyridine at low exposures (< 0.5 L) lies in parallel mode on the surface, while at higher coverages, it changes to inclined phase through the N-atom with ~55° to the surface. This observation is consistent with an earlier study of pyridine chemisorption on the clean Ag(111) surface at ~ 140 K with electron energy loss spectroscopy (EELS) and ultraviolet photoemission spectroscopy (UPS) (Demuth et al., 1980), where they observed a phase transition on the surface at ~ 0.5 L coverage from parallel (π-bonded) phase to an inclined nitrogen bonded phase. This phase transformation has been also confirmed in a later study of pyridine adsorption on the Ag(111) surface using near-edge x-ray absorption fine-structure (NEXAFS) at 100 K (Bader et al., 1986). This study, however, indicated that pyridine adsorbs initially with a tilted mode with an angle of 45° ± 5° between the ring plane and the surface plane at low coverage, in contrast to earlier studies, then coverts sharply at a submonolayer coverage to a phase with an angle of 70° ± 5°.

The electronic energy level structure of pyridine on Pd(111) at room temperature has been studied through angle-resolved ultraviolet photoelectron spectroscopy (ARUPS) in parallel with EELS to determine the electronic excitations of the various adsorbate complexes (Netzer and Mack, 1983a&b). It was suggested that the heteroatom nitrogen has mainly a degeneracy-lifting effect; therefore, the low symmetry of adsorbed pyridine can be interpreted in terms of an inclined adsorbate geometry, with the ring plane tilted with respect to the surface, and bonds through both the nitrogen lone pair and the π orbitals. A different study of pyridine adsorption on the Pd(111) surface at 180 K using

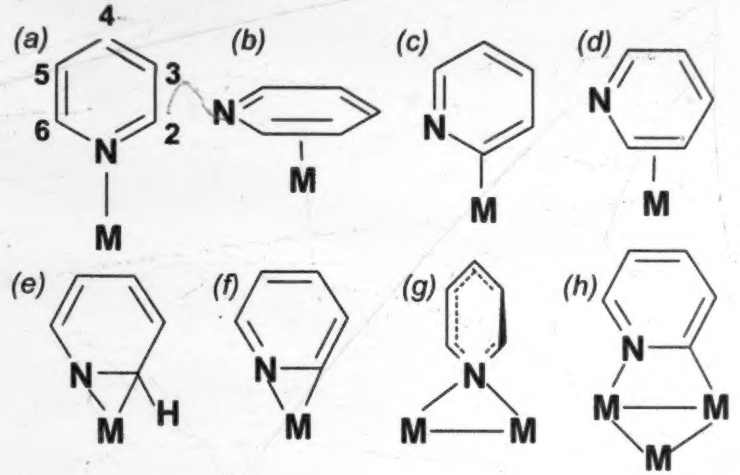

Figure 2.3 Summary of pyridine bonding modes (Sanchez-Delgado, 2002) (a) η^1(N)-Py-90°; (b) η^6-Py-0° (c) η^1(C2)-Py-90°; (d) η^2(C2,C3)-Py-90°; (e) η^2(N,C2)-Py-90°; (f) η^2(N,C2)-pyridyl; (g) μ_2,η^1(N)-Py-90°; (h) μ_2,η^2(N,C2)-Py-90°.

EELS (Grassian and Muetterties, 1987) showed that pyridine bonds weakly to the surface at 180 K with the ring plane oriented parallel to the surface, and at approximately 310 K pyridine bonds predominately to the surface through the nitrogen lone pair. The EELS spectrum showed an increase in the intensity of the in-plane modes relative to the out-of-plane modes, at the specular angle, which correspond to electron donor-acceptor type behavior. Pyridine behaves as a Lewis base, donating electron density via the nitrogen lone pair into the lowest lying unoccupied molecular orbitals of the metal. The results of this study showed consistency with the conclusions made earlier on pyridine adsorption on the Pd(111) surface using UPS and EELS (Netzer and Mack, 1983b). The EELS spectra of adsorbed pyridine on Pd(111) surface at saturation coverage and 170 K was similar to the low coverage EELS spectra of pyridine adsorbed on Ag(111) (Demuth et al., 1980).

Temperature-dependent pyridine adsorption geometry on Pt(111) was studied using NEXAFS (Johnson et al., 1985). Upon surface saturation, pyridine forms a disordered multilayer on clean Pt(111) surface at 90 K. After annealing the multilayer to progressively higher temperatures, the multilayer evaporates and a chemisorbed pyridine monolayer with a tilt angle of 52° between the ring plane and surface was observed. Further surface heating (< 300 K) cleaved the α C–H bond and α-pyridyl species were suggested to form with the ring becoming perpendicular to the surface. In a different study on Pt(111), the chemisorption behavior of pyridine at low temperature (~ 120 K) and room temperature (~ 300 K) at saturation coverage was investigated using EELS and thermal decomposition spectroscopy (TDS) (Grassian and Muetterties, 1986). While at both surface temperatures the most observed modes were characterized as in-plane modes, the relative intensities of the loss peaks differed greatly. Furthermore, two new loss peaks were recorded for pyridine at 120 K and one loss peak disappeared in comparison to 300 K spectrum. At room temperature, they interpreted the spectra as the formation of an α-pyridyl species on the surface, which is bonded to the Pt(111) surface through the nitrogen and one of the α-carbon atoms with the pyridyl plane perpendicular to the metal surface. The thermal desorption spectrum of pyridine at room temperature showed one molecular desorption peak at 473 K, and further analysis indicated partial decomposition of pyridine with an α-hydrogen abstracted, thereby forming a pyridyl surface species. At low temperatures, pyridine bonds through both the nitrogen atom and the π and π^* orbitals of the pyridine ring, and a different bonding arrangement is suggested as indicated by the thermal desorption data. Two molecular desorption peaks were observed at low coverages with temperatures of 347 and 483 K, respectively. As the coverage increases to the saturation level, a third peak at 190 K appears while the 347 K peak shifts to 260 K with a great increase in its intensity. At 260 K, approximately 50% of the pyridine molecularly desorbs, and the remaining surface species partially decompose on the surface to form α-pyridyl fragments.

Pyridine chemistry was studied on Ni(110) at room temperature using TDS (Wexler et al., 1982) at monolayer coverage. On Ni(110), pyridine adsorption proceeds via hydrogen (C–H) abstraction upon adsorption leaving α-pyridyl species adsorbed on the surface, leading to competitive thermal desorption and thermal decomposition as evidenced by molecular hydrogen (H_2) desorption from the surface. Two decomposition mechanisms were proposed for pyridine chemistry on Ni(100) after adsorption; surface heating causes part of the α-pyridyl species to desorb as molecular pyridine, and the remainder decomposes on the surface. In a different study on the same Ni(100) surface using EELS (Avouris et al., 1984), pyridine was noted to adsorb in a parallel configuration at a temperatures < 200 K and surface coverage < 0.5 ML, transformed to a tilted mode at higher coverages. The vibrational and electronic losses of pyridine chemisorbed on Ni(001) using HREELS was carried out to identify the adsorption modes of pyridine on clean surface (DiNardo et al., 1984). The results showed that orientational phase transitions occur as a function of coverage and temperature. While the molecular plane is parallel to the surface at low coverage at approximately 170 K (π-bonded species), at higher coverages and similar adsorption the increase in the intensity of the in-plane molecular modes with respect to the out-of-plane modes indicates that the molecular plane tilts with respect to the surface and bonds through the nitrogen lone pair. However, the exact angle of the tilt was not calculated. In case of room temperature adsorption or momentary heating of the saturation coverage low temperature species to room temperature changes the vibrational spectra, it indicates the presence of nearly vertically oriented species on the surface with some rotation about the nitrogen atom. The electronic loss spectra at room temperature showed these species were α-pyridyl species, and the molecular α-pyridyl species persists up to approximately 493 K before it decomposes, as characteristics electronic losses for C are observed.

Cohen and Merrill (1990) studied the adsorption of pyridine on Ni(111) at 120 and 180 K using HREELS, x-ray photoelectron spectroscopy (XPS) and ARUPS. Changes in the intensity of the in-plane versus out-of-plane vibrational modes show that an orientation phase transition occurs as a function of coverage at low temperature. Low exposures at 120 K exhibit a parallel orientation of the plane with the surface bonding through the π molecular orbitals. At high exposures, this changes to an orientation with the plane of the ring and its 2-fold rotation axis close to the surface perpendicular and bonding now through the nitrogen atom. The vibrational frequencies of this study are in agreement with the reported data on Ni(001) (DiNardo et al., 1984) and Ag(111) ([Demuth et al., 1980) surfaces. Surface heating results in desorption of weakly bonded pyridine at 180 K, and further heating to 520 K indicates substantial decomposition and formation of fragments that may have more highly hydrogenated carbon groups and higher C–C bond order. The decomposition behavior of pyridine on Ni(111) where hydrogen and deuterium evolution from substituted pyridines during thermal desorption is consistent with previous studies of pyridine on Ni(100), Pt(100) and Pt(111) (Wexler et al., 1982) surfaces. The photoemission results for 170 K exposures are also in agreement with the orientation change observed in HREELS. At low coverages, where the parallel adsorption geometry is expected, the data indicate bonding shifts of some of the π molecular orbitals toward higher binding energy. A shift is also seen for the nitrogen lone pair, compared to the gas-phase condition.

Pyridine adsorption on Rh(111) was studied over the 77-450 K temperature range using several spectroscopic techniques (Mate et al., 1988). At 77 K, multilayers of pyridine are observed with a vibrational spectrum similar to that of liquid pyridine. Between 185 and 230 K, HREELS and TDS indicate that both physisorbed and chemisorbed pyridine species are present on the surface. The physisorbed species desorb at 295 K, while the chemisorbed species is stable until it decomposes on the surface at 400 K. It is suggested that the chemisorbed species are α-pyridyl complexes as thermal desorption spectroscopy indicates partial dehydrogenation of this pyridine surface species. Further, the electronic spectroscopy indicates that there is a strong interaction of the π orbitals of the α-pyridyl species with the surface, as well as bonding through the nitrogen and α-carbon atoms. Such interaction of the π orbitals with the surface could account for the molecular ring of the α-pyridyl species being somewhat inclined toward the surface rather than oriented perpendicular to the surface, as observed for the α-pyridyl species on Pt(111) at 300 K (Grassian and Muetterties, 1986). ARUPS has been used in conjunction with electron stimulated desorption ion angular distribution (ESDIAD) to study the molecular structure and orientation of pyridine on Ir(111) (Mack et al., 1985). This study indicated that the pyridine molecules are adsorbed through the nitrogen atom in an upright standing geometry, with a small inclination of the ring plane with respect to the surface normal. The ESDIAD analysis indicated the tilt angle of the ring plane to approximately 20° from the surface normal.

The adsorption and decomposition of pyridine on Mo(110) has been studied only at low surface coverages up to surface saturation (Serafin and Friend, 1989). At 0.85 of saturation, a broad molecular desorption peak at approximately 375 K was observed. Upon increasing pyridine exposure to saturation, a peak centered at 190 K appeared; however, this feature was not discussed further. Increasing the pyridine exposure resulted in two additional low-temperature features at 160 and 175 K. The peak at 160 K was attributed to the sublimination of multilayer of pyridine and the peak at 175 K was attributed to the physisorption of a second layer of pyridine. They also reported dihydrogen gas as the only product to be detected, which is evidenced by a broadening and eventual splitting of two unresolved dihydrogen TPD peaks. At saturation exposures, two dihydrogen desorption peaks were observed at 375 K and 595 K; however, a multitude of peaks from 375 – 595 K were observed depending on pyridine surface coverage. Using additional spectroscopic information from XPS, they concluded pyridine molecularly adsorbs on the surface in more than one configuration, and suggested one possible mode is through the nitrogen atom. While it was reported isotopic studies indicated no H–D exchange in the pyridine temperature-programmed desorption features, no further attempt was made to describe the other possible adsorption modes leading to molecular desorption or surface decomposition on Mo(110).

The adsorption of pyridine on W(110) has also been studied at 90 K using TDS, XPS, UPS, and Kelvin probe work function measurements (Whitten, 2003). Physisorbed pyridine desorbs at a temperature less than 190 K, and the chemisorbed layer dissociatively desorbs as molecular hydrogen at 380 K. UPS showed a similar spectrum for the monolayer and that of multilayer coverages, indicating molecular pyridine adsorbs at 90 K and does not decompose until temperatures > 190 K. Surface analysis using XPS showed a C 1s peak for a pyridine monolayer results in a coverage of $4.5 \pm 0.5 \times 10^{14}$ molecules cm^{-2}, which is consistent with adsorption of pyridine with the plane of its ring tilted presumably bonding to the surface via its nitrogen lone pair electrons. In another study on W(110) using infrared spectroscopy and ab initio electronic structure calculations (Gaussian 98 package using HF/LanL2SZ basis set) (Andersson and Uvdal, 2001), evidence was found for the chemical transformation of pyridine to α-pyridyl species. Pyridine was tilted edge-wise prior transformation, and both pyridine and the α-pyridyl species have their molecular planes perpendicular to the surface.

2.2.3 Summary

In general, and as summarized in Figure 2.4, these studies concluded that pyridine adsorption geometry is surface coverage dependent, which is supported by three bonding geometries and typically consistent with the electronic structural behavior of pyridine molecule; parallel to the surface at low coverages through its π orbital (Avouris and Demuth, 1981; Cohen and Merrill, 1990; DiNardo et al., 1984; Grassian and Muetterties, 1986; Whitten, 2003), perpendicular or inclined at high coverages through its nitrogen atom (Avouris and Demuth, 1981; Bader et al., 1986; Cohen and Merrill, 1990; DiNardo et al., 1984; Grassian and Muetterties, 1986; Grassian and Muetterties, 1987; Johnson et al., 1985; Netzer and Mack, 1983; Serafin and Friend, 1989; Whitten, 2003), and through α-pyridyl species formation, which requires bond formation between the nitrogen and an adjacent carbon with the metal surface (DiNardo et al., 1984; Grassian and Muetterties, 1986; Johnson et al., 1985; Serafin and Friend, 1989; Wexler et al. 1982). While this information presents fundamental insight regarding pyridine adsorption and decomposition behavior, none managed to connect the adsorption/desorption behavior to bonding configurations that are responsible for the adsorption and decomposition on molybdenum-based model hydrotreating catalyst surfaces.

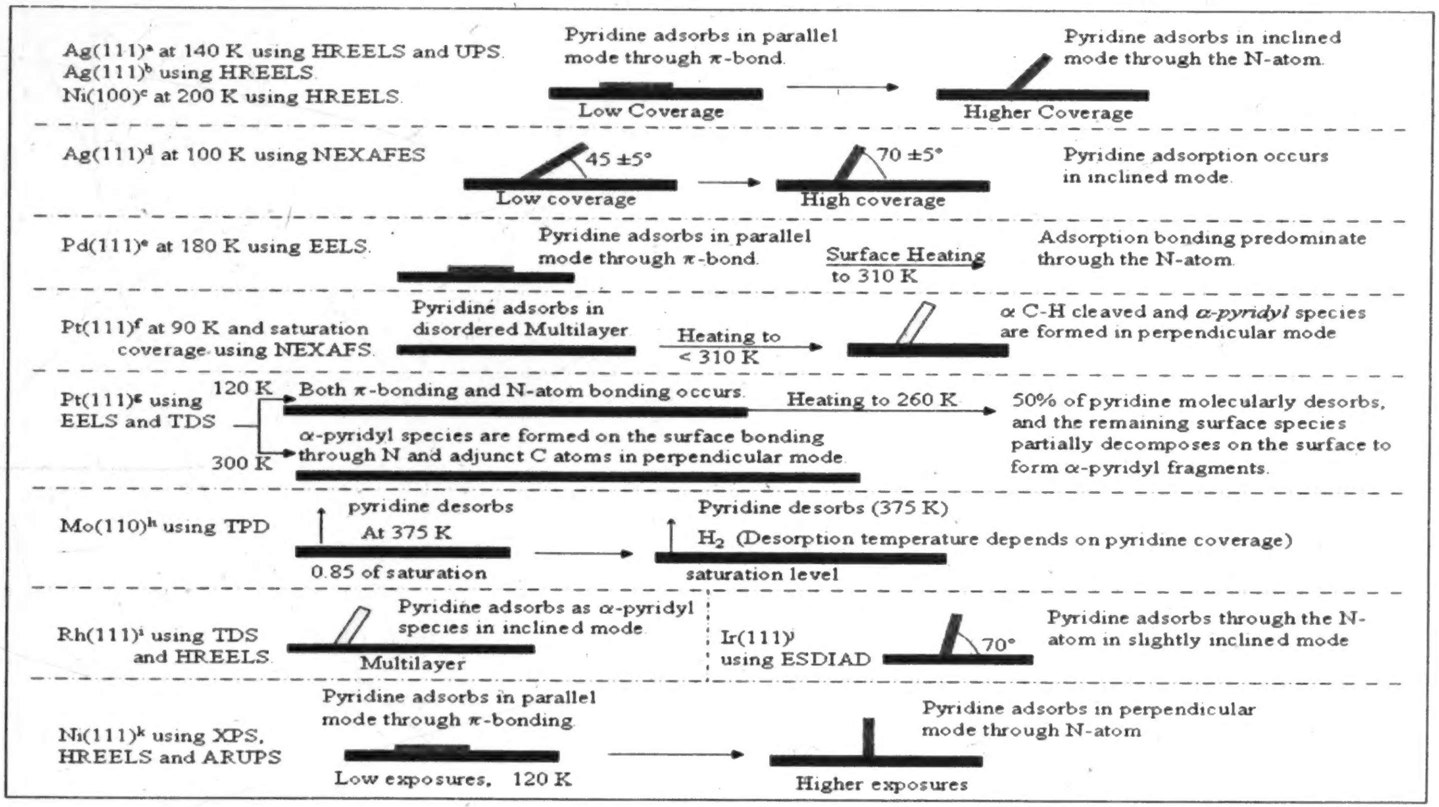
Ag(111)^a at 140 K using HREELS and UPS.
Ag(111)^b using HREELS.
Ni(100)^c at 200 K using HREELS.
Pyridine adsorbs in parallel mode through π-bond.
Low Coverage
Pyridine adsorbs in inclined mode through the N-atom.
Higher Coverage
Ag(111)^d at 100 K using NEXAFES
45 ±5°
Low coverage
70 ±5°
High coverage
Pyridine adsorption occurs in inclined mode.
Pd(111)^e at 180 K using EELS.
Pyridine adsorbs in parallel mode through π-bond.
Surface Heating to 310 K
Adsorption bonding predominate through the N-atom.
Pt(111)^f at 90 K and saturation coverage using NEXAFS.
Pyridine adsorbs in disordered Multilayer
Heating to < 310 K
α C-H cleaved and α-pyridyl species are formed in perpendicular mode
Pt(111)^g using EELS and TDS
120 K
Both π-bonding and N-atom bonding occurs.
Heating to 260 K
50% of pyridine molecularly desorbs, and the remaining surface species partially decomposes on the surface to form α-pyridyl fragments.
300 K
α-pyridyl species are formed on the surface bonding through N and adjunct C atoms in perpendicular mode.
Mo(110)^h using TPD
pyridine desorbs
At 375 K
0.85 of saturation
Pyridine desorbs (375 K)
H_2 (Desorption temperature depends on pyridine coverage)
saturation level
Rh(111)^i using TDS and HREELS.
Pyridine adsorbs as α-pyridyl species in inclined mode.
Multilayer
Ir(111)^j using ESDIAD
70°
Pyridine adsorbs through the N-atom in slightly inclined mode
Ni(111)^k using XPS, HREELS and ARUPS
Pyridine adsorbs in parallel mode through π-bonding
Low exposures, 120 K
Pyridine adsorbs in perpendicular mode through N-atom
Higher exposures

Figure 2.4 Schematic of the reaction of pyridine with various metal surfaces as reported in the literature; a: (Demuth et al., 1980), b: (Avouris and Demuth, 1981), c: (Avouris et al., 1984), d: (Bader et al., 1986), e: (Grassian and Muetterties, 1987), f: (Johnson et al., 1985), g: (Grassian and Muetterties, 1986), h: (Serafin and Friend, 1989), i: (Mate et al., 1988), j: (Mack et al., 1985), k: (Cohen and Merrill, 1990).

2.3 Pyrrole

2.3.1 Introduction

Pyrrole (C_4H_5N) is a non-basic organonitrogen heterocycle in which the lone electron pair of nitrogen is delocalized over the π system of the ring (Jorgebsen and Salem, 1973; Jones and Bean, 1977). The lone-pair electrons of the nitrogen atom and the two C=C bonds form a six-electron conjugated π-electron system. This electronic configuration is suggested to result in a possible pyrrole adsorption on molybdenum-based sulfided hydrotreating catalysts, but very little is known about the modes of adsorption (DuBois et al., 2000).

Organometallic chemistry has provided some information regarding the possible bonding modes of pyrrole to metal complexes (Sanchez-Delgado, 2002). Based on these studies, several different bonding configurations have been suggested, as summarized in Figure 2.5. The most numerous metal complexes of pyrrole are the η^5-Pyr type, which are known for Cr, Mn, Fe, Co, Ru, Rh, Re and Ir surfaces (Efraty et al., 1982; Felkin and Zakrzewski, 1985; Fish et al., 1991a&b; Kvietov et al., 1994). The η^4-Pyr type has been observed in one case, where the pyrrole ligand clearly bonded through the two C=C bonds, while the nitrogen atom is bent away from the ring to a non-bonding distance from the metal ion (Glueck et al., 1989). While there are no records of η^1(N)-Pyl ligand, metal derivatives containing an olefin-like ligand, in either one of the tautomeric forms η^2(C,C)-H-Pyl or η^2(C,C)-2H-Pyl, have been characterized for osmium (II) complexes (Cordone et al., 1989; Myers et al., 1991). Metal complexes containing the anionic pyrrolyl ligands are much more frequent throughout the periodic table, and the η^1(N)-Pyl and η^5-Pyr bonding modes are dominant in the coordination chemistry of such anions (Bianchini et al., 2001; Kvietov et al., 1994). Depending on the degree of electronic unsaturation of the reacting metal containing fragment, the incoming pyrrolyl ligand binds through the N-atom only, or through the entire π-ring.

2.3.2 Pyrrole Adsorption on Single Crystal Surfaces

The adsorption of pyrrole on metal surfaces has been studied to provide some insight into five-membered heterocyclic bonding characteristics; however, these surfaces

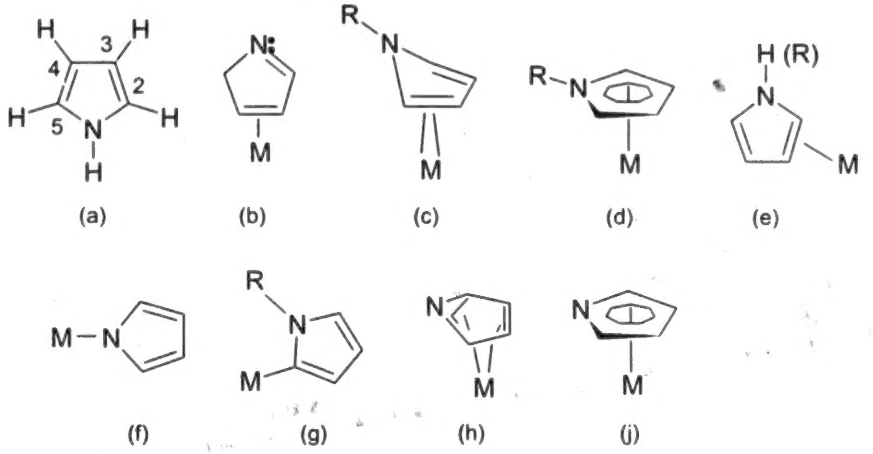

Figure 2.5 Summary of pyrrole bonding modes (Sanchez-Delgado, 2002). (a) Gas-Phase Pyrrole; (b) η^2(C,C)-2H-Pyl; (c) η^2(C,C)-H-Pyl; (d) η^4-Pyr; (e) η^5-Pyr; (f) η^1(N)-Pyl; (g) η^1(C)-Pyl; (h) η^3, η^2-Pyl; (j) η^5-Pyl.

are not representative of hydrotreating catalysts. While these studies highlight pyrrole adsorption and energetics at low coverages and temperatures on several metal surfaces, there have been no studies reported on pyrrole adsorption and reaction on model molybdenum hydrotreating catalyst surfaces. Figure 2.5 summaries the reaction of pyrrole with various metal surfaces.

The structure of pyrrole on the Rh(111) surface has been investigated using low electron energy diffraction (LEED), TDS, and ARUPS techniques (Netzer et al., 1988), pyrrole interacts with the surface via the aromatic π electron system. At 150 K, adsorption appears in the parallel mode, but slightly inclined configuration can coexist. The adsorption may also involve the nitrogen lone pair orbital in the interaction after loss of N–H, which occurs at a temperature range of 150-300 K. Surface heating showed competitive molecular desorption with decomposition of the ring. It also resulted in the molecular desorption of pyrrole at a maximum temperature of 360 K. Hydrogen gas also started desorbing at approximately 350 K in a complex pattern and further heating to 420 K produced the evolution of HCN from the surface. ARUPS of pyrrole on Rh(111) reveals strong modifications of the aromatic π electron system as a result of mixing with metal states. The π electrons constitute, therefore, an important contribution to the surface chemical bond.

Reaction of pyrrole on Ni(100) was studied using temperature programmed reaction spectroscopy (TPRS), reflection absorption infrared spectroscopy (RAIS) and Auger electron spectroscopy (AES) (Schoofs and Benziger, 1987). Two TPRS experiments were conducted at an adsorption temperature of 175 K with heating rates of 8 K s^{-1} and 45 K s^{-1}, respectively. At the lower heating rate, pyrrole desorbs at 235 K, while hydrogen gas desorbs just above room temperature leaving carbon and nitrogen on the surface. At the higher heating rate, similar observations were reported with additional light product gas, including HCN and NH_3, desorption due to complete reaction. RAIS results suggest that pyrrole adsorbs with its ring parallel or nearly parallel to the surface at 200 K, while the infrared spectra of adsorbed pyrrole after surface heating at a rate of 45 K s^{-1} to 400 K showed weak features of C–H and N–H stretching, suggesting the surface species that gives rise to them is at low concentration or oriented with most of the bonds parallel to the surface.

On Pd(111), pyrrole chemisorbs intact on the surface at 200 K with low coverages in an almost flat-lying configuration (Baddeley et al., 1996). Increasing surface coverage led to tilting of the adsorbed molecules, accompanied by some N–H cleavage to yield adsorbed pyrrolyl species. Once the surface saturation is attained, the molecular orientation is close to vertical position. Increasing surface temperature leads initially to desorption of some pyrrole from the mixed pyrrole + pyrrolyl overlayers, with reorientation of the remaining molecules to flat geometry. At higher temperatures, extensive stepwise decomposition of flat-lying pyrrole occurs, triggered by cleavage of the H bond at temperatures < 300 K. The principle gaseous products are H_2 that desorbs at temperatures of 350 and 475 K, and HCN at an approximate temperature of 475 K. Approximately 65% of the initial adsorbed carbon is retained on the surface as indicated by surface analysis using XPS. Vibrational frequencies were collected for pyrrole adsorption on Pd(111) as a function of surface coverage at 200 K. For parallel pyrrole adsorption, the most intense features observed were the ones involving atomic displacements perpendicular to the aromatic ring, which are γ(C–H) and γ(N–H) modes. With increasing coverage the C–H stretch and the ring-stretches increase in intensity relative to the γ(C–H) loss. Overall, the vibrational data indicated that increasing coverage leads to considerable relative intensity changes in the vibrational spectrum.

Pyrrole adsorption on Cu(100) surface was studied using electron EELS and TDS techniques (Sexton, 1985). Adsorption starts at 85 K with exposure sufficient to generate multilayer coverage, and the adsorption appeared to be molecularly reversible and weakly bonded to the surface in parallel mode at low coverage. Pyrrole desorbs at 170 K (sublimation), 200 K and 250 K, respectively with equal integrated area and no other masses observed desorbing off the surface. The observed vibrational modes combined with TDS peaks are strong evidence for formation of a bi-layer of pyrrole. In the bi-layer, the pyrrole ring in the second layer must be oriented with the ring planes non-parallel to the monolayer, if the surface dipole selection rule is obeyed.

On Pt(111), NEXAFS spectra were obtained above the N-K-edge after initial pyrrole adsorption and at 84 K, and following a variety of annealing (up to 181 K) treatments (Tourillon et al., 1987). Pyrrole molecules become oriented with the molecular plane normal to the surface following a brief anneal, then with further heat treatments begin to become orietationally disordered and to dissociate into nitrogen containing products which do not desorb. Furthermore, hydrogen gas was not observed desorbing off the surface. They indicated that the β - β carbon bond and the two carbon heteroatom bonds are stronger than simple single bonds and the α - β carbon bonds are weaker than the simple double bonds.

In a different study of pyrrole adsorption, the binding energy for pyrrole adsorbed on oxidized iron was determined to be negative, which implies that electron transfer from carbon to the surface is greater than from nitrogen. This is consistent with known chemistry of pyrole (Pan and Stair, 1986). The electron pair from nitrogen in pyrrole is not localized in a non-bonding orbital, but participates in the aromatic π-electron system. Indeed, pyrrole achieves the required six π-electrons necessary for aromatic stabilization because of the contribution of two electrons from nitrogen. Since the six π-electrons are delocalized over five annular atoms, pyrrole is classified as "π-electron excessive" aromatic system and is susceptible to electrophilic attack (Walker and Stair, 1980). In particular, the highest occupied molecular orbital, which would be the most susceptible to electrophilic attack, is a π-orbital associated with the carbon atoms. The conclusion for pyrrole adsorption on metal iron oxide on the basis of negative binding energy measured for C 1s and N 1s combined with the electronic structure and the known chemistry of pyrrole is the chemisorption bond is of the acid-base type formed by electron donation from the carbon atoms to acidic (electrophilic) sites on the surface.

2.2.3 Summary

A summary of these studies is presented in Figure 2.6. In general, these studies concluded that pyrrole adsorption geometry and decomposition are surface coverage and temperature dependent. At low coverages and temperatures, pyrrole adsorbs molecularly with a flat-lying geometry via π bonding with the metal surface. Increasing surface coverage leads to a change of the adsorption mode from parallel adsorption to a tilted geometry relative to the metal surface plane. At elevated temperatures, Cu(100) (Sexton, 1985) and Pt(111) (Tourillon et al., 1987) surfaces did not show any decomposition behavior, while Pd(111) (Baddeley et al., 1996) and Rh(111) (Netzer et al., 1988) surfaces catalyzed pyrrole decomposition as a result of N–H bond cleavage and the formation of pyrrolyl species in a tilted configuration relative to the metal surface. While these studies highlight pyrrole adsorption and energetics at low coverages and temperatures on several metal surfaces, there have been no studies reported on pyrrole adsorption and reaction on model molybdenum hydrotreating catalyst surfaces.

2.4 Ethylamine

2.4.1 Introduction

Amines are used to improve and to control the selectivity in hydrogenation and catalytic reactions, which can lead to different reaction products (Bond, 1962; Valyon et al., 1984). It is also widely used as a corrosion inhibitor, where it is generally accepted that the organic inhibitors act through adsorption at the metal-solution interface and forms a complete protective hydrophobic film on the surface (Yao, 1963). Nonetheless, investigations of organic amine (e.g. $R\text{-}NH_2$) adsorption on metal surfaces have not been thoroughly studied in the past, despite its considerable importance in surface catalysis. Amines are intermediate products in all heterocyclic organonitrogen hydrodenitrogenation reactions; 1-pentanamine in pyridine hydrogenolysis and 1-butylamine in pyrrole hydrogenolysis, therefore, it is quite important to understand how these molecules behave and interact on a molecular level over the catalyst surfaces. This fundamental understanding should provide key information regarding the adsorption and reaction behavior of amines, and facilitate the determination of the activation energy for C–H, N–H, C–N, or C–C bond scission that is/are responsible for its decomposition.

2.4.2 Ethylamine Adsorption on Single Crystal Surfaces

An early study by measuring heat of adsorption of amines on reduced and oxidized iron surfaces (Yao, 1963) indicated the authenticity of the general belief that amines chemisorb on transition metals through donating the lone pair electrons to the metal to form a predominantly covalent bond. Unfortunately, ethylamine adsorption studies are scarce in the literature. Only two transition metals were investigated for ethylamine adsorption and decomposition behavior; W(110) (Pearlstine and Friend, 1986), which is the second most important hydrotreating based metal, and Ni(111)

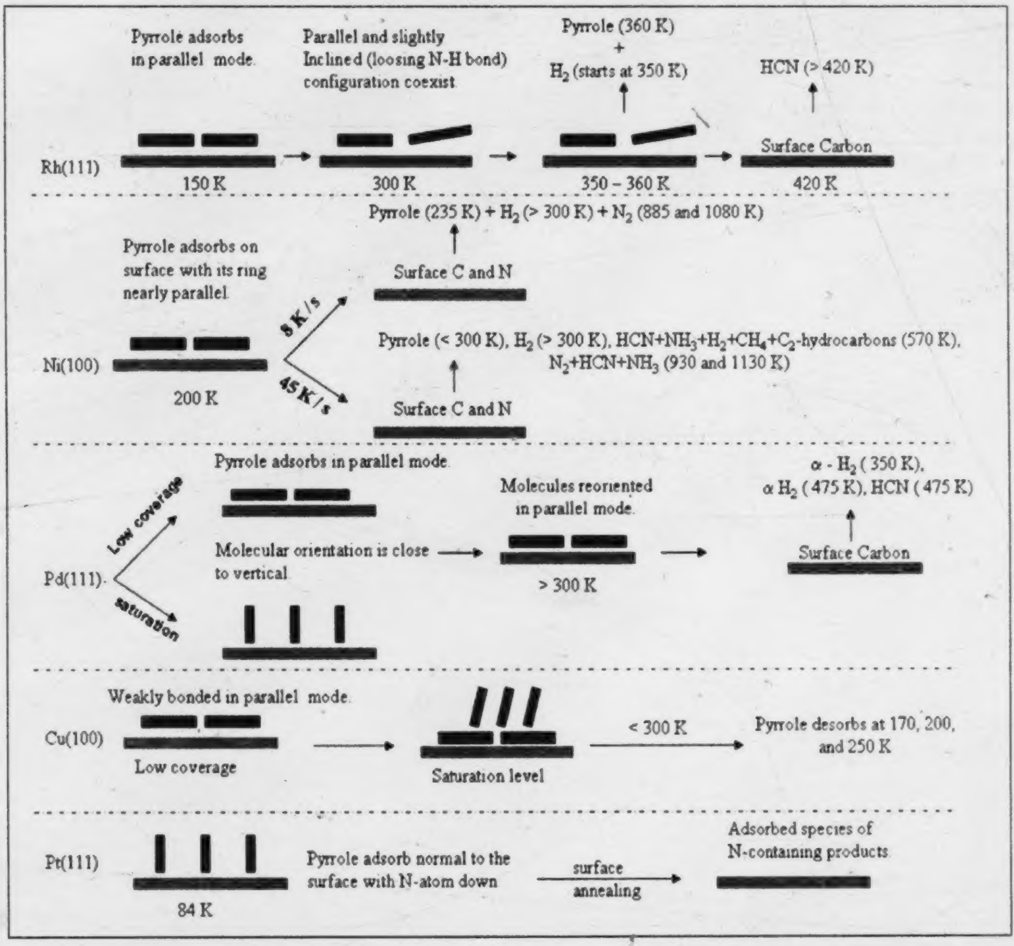
Pyrrole adsorbs in parallel mode.
Parallel and slightly Inclined (loosing N-H bond) configuration coexist
Pyrrole (360 K) + H_2 (starts at 350 K)
HCN (> 420 K)
Surface Carbon
Rh(111)
150 K
300 K
350 – 360 K
420 K
Pyrrole (235 K) + H_2 (> 300 K) + N_2 (885 and 1080 K)
Pyrrole adsorbs on surface with its ring nearly parallel.
Surface C and N
8 K/s
45 K/s
Ni(100)
200 K
Pyrrole (< 300 K), H_2 (> 300 K), $HCN+NH_3+H_2+CH_4+C_2$-hydrocarbons (570 K), $N_2+HCN+NH_3$ (930 and 1130 K)
Surface C and N
Pyrrole adsorbs in parallel mode.
Low coverage
Saturation
Pd(111)
Molecular orientation is close to vertical.
Molecules reoriented in parallel mode.
> 300 K
α - H_2 (350 K), α H_2 (475 K), HCN (475 K)
Surface Carbon
Weakly bonded in parallel mode.
Cu(100)
Low coverage
Saturation level
< 300 K
Pyrrole desorbs at 170, 200, and 250 K
Pt(111)
84 K
Pyrrole adsorb normal to the surface with N-atom down
surface annealing
Adsorbed species of N-containing products

Figure 2.6 Schematic of the reaction of pyrrole with various metal surfaces as reported in the literature; Rh(111) (Netzer et al., 1988), Ni(100) (Schoofs and Benziger, 1987), Pd(111) (Baddeley et al., 1996; Futaba and Chiang, 1997), Cu(100) (Sexton, 1985), Pt(111) (Tourillon et al., 1987).

(Ditlevsen et al., 1993; Gardin and Somorjai, 1992).

Pearlstine and Friend conducted an adsorption study of ethylamine on W(100), W(100)-(5 x 1)-C, and W(100)-(2 x 1)-O surfaces using TPD (Pearlstine and Friend, 1986). Surface exposure of 5 L results in desorption of ethylamine, methane, ammonia, molecular nitrogen and hydrogen. At surface exposures less than 2 L, desorbing hydrogen and nitrogen in the gaseous phase at 400 K and higher than 1000 K were observed. Carbon remains on the surface following temperature programmed reaction up to 1500 K, as determined by AES, while nitrogen is quantitatively removed by thermally induced atom recombination above 1000 K. Ethylamine desorption begins at 325 K at low exposures then decreases as the exposure increases up to 150 K at exposures above 4 L. An isotopic labeling study at W(100) using deuterium indicated that methane formation proceeds via hydrogenation of the methyl group in ethylamine with surface hydrogen (deuterium) (Pearlstine and Friend, 1986). Furthermore, in a co-adsorption of deuterium with ethylamine, the absence of CD_4 production renders re-hydrogenation of adsorbed carbon an unlikely reaction pathway. Ethylamine adsorption on W(100)-(5 x 1)-C surface with 3.3 L exposure showed ethylamine, acetonitrile, ammonia, molecular hydrogen and nitrogen as reaction products. At low exposures (less or equal 0.25 L), irreversible decomposition of ethylamine occurs, producing exclusively hydrogen and nitrogen gases at 450 and ≥ 1300 K, respectively. Exposures above 4 L results in sublimation of the ethylamine multilayer at 150 K. While on the W(100)-(2 x 1)-O surface, the only observed desorption products were mainly ethylamine, molecular hydrogen (>500 K), nitrogen (>1250 K), and CO. Ethylamine desorption from the W(100)- (2 x 1)-O surface is observed even below 0.1 L initial exposure, centered at 550 K, increasing ethylamine exposure results in molecular desorption at temperatures below 500 K, with essentially continuous desorption observed in the range of 150 – 550 K above 0.6 L. The above study clearly indicates that ethylamine undergoes C–C and C–N bond cleavage on clean W(100) resulting in production of methane and ammonia, which is not the case on W(100)-(5 x 1)-C that produces mainly acetonitrile. Initial adsorption suggests a selective α-C–H bond activation without any C–C or C–N bond cleavage that causes acetonitrile to evolve, while the W(100)-(2 x 1)-O surface did not have high reactivity with respect to ethylamine.

Ethylamine adsorption on Ni(111) was studied using vibrational frequency (HREELS) and thermal decomposition techniques (Gardin and Somorjai, 1992), followed by molecular modeling of the reaction pathway to complement the previous study (Ditlevsen et al., 1993). Thermal adsorption and decomposition of ethylamine after exposing the surface with 3 L at 150 K resulted with desorption of ethylamine (≈ 200-320 K), acetonitrile (≈ 350 K), hydrogen (≈ 380 K), and nitrogen (≈ 800 K) as reaction products. At exposures greater than 3 L, a low-temperature peak at 180 K indicated the presence of a second layer of ethylamine on the nickel surface, which clearly results from reaching surface saturation. HREELS data suggest ethylamine binds to the metal surface through its nitrogen lone pair. The methyl-group points away from the surface, and due to the lower activation energy of α-C–H bonds, a hydrogen atom from the CH_2 group interacts with the nickel surface atoms. When the surface is heated up to 270 K, thermal desorption spectroscopy indicated a significant amount of ethylamine desorbs from the surface. When the temperature is raised above 330 K, acetonitrile starts to desorb as further indicated by an HREELS spectrum of acetonitrile. The low intensity of the 1650 cm^{-1} band, assigned to the C–N stretching mode, and the large intensity of the CCN bending mode at 540 cm^{-1} leads to similar previous interpretation on the Ni(111) surface (Sexton and Avery, 1983), who concluded that acetonitrile is adsorbed parallel on Ni(111), in a η^2(N,C) state.

As a result of their findings of ethylamine decomposition, a reaction mechanism was proposed for ethylamine adsorption and decomposition on Ni(111) surface. This mechanism was confirmed a year after by calculating the binding energies of adsorbed species as well the activation energies of reaction intermediates using a semiemprical model based on the extended-Hückel theory. The reaction pathway indicates an initial molecular adsorption of ethylamine (-39.4 kcal mol^{-1}), then followed by α-C–H bonds cleavage to form aminomethylcarbene species, and then breaking N–H bonds to form the acimidoyl species (-102.4 kcal mol^{-1}) and finally the desorption of acetonitrile (-54.7 kcal mol^{-1}). Two molecular hydrogen (30.2 kcal mol^{-1}) species were the only products resulting from ethylamine decomposition on the surface. According to their calculations, three different species are found to be stable on the surface; these are acetonitrile (CH_3CN), the acimidoyl (CH_3CNH), and the alkylidenimido (CH_3CHN) species.

2.4.3 Summary

Unfortunately, the literature on ethylamine adsorption and decomposition on metal surfaces is very limited. As summarized in Figure 2.7, the reaction of ethylamine on two different surfaces showed different reactivity as a result of the decomposition process. Furthermore, surface reaction product showed surface coverage dependency. The adsorption configuration of ethylamine on Ni(111) showed bonding through the nitrogen and this is important to know for further analysis of its decomposition behavior.

2.5 Summary

Given the importance of hydrotreating, there is a fundamental need to understand the adsorption and reaction of organonitrogen compounds on catalyst surfaces. Based on the pervious literature review, probe molecules have been identified to assist in the fundamental interpretation of such reaction; ethylamine (non-heterocyclic), pyridine (heterocyclic basic model) and pyrrole (heterocyclic non-basic model) on Mo(110). Identification of the bonding configuration and the corresponding binding energies can provide a thorough insight of how these molecules approach the surface and how much energy is required for reaction and decomposition.

The unique features of our proposed research in comparison with other studies are the consideration of modified surfaces and studying the adsorption behavior as a function of surface exposures (surface coverage). Therefore, the objective of the present study is to investigate the molecular adsorption and surface reaction of ethylamine, pyridine and pyrrole on Mo(110) and C/N-Mo(110) using TPD, AES and HREELS. By investigating both molecules adsorption over a range of surface coverages, the effect of overlayers on adsorption energetics and reactivity will provide fundamental information regarding the structure-reactivity relationship. Furthermore, the effect of carbon/nitrogen overlayers will be studied to determine the effect of surface modification on molecular adsorption and reactivity. First-principles quantum mechanical calculations using density-functional theory are used to study the molecular adsorption of pyridine and pyrrole on Mo(110) in an attempt to identify the adsorption configurations resulting in molecular desorption and surface decomposition, and to gain further insight about the structure-reactivity relationship.

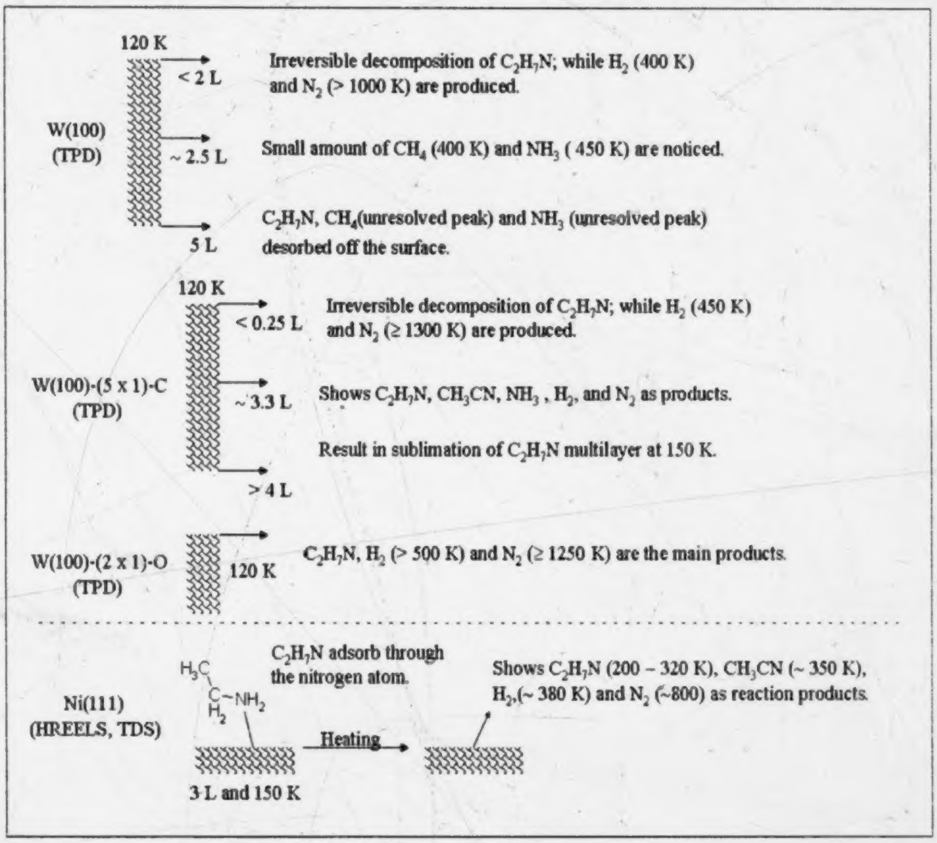
120 K
< 2 L
Irreversible decomposition of C_2H_7N; while H_2 (400 K) and N_2 (> 1000 K) are produced.
W(100)
(TPD)
~ 2.5 L
Small amount of CH_4 (400 K) and NH_3 (450 K) are noticed.
5 L
C_2H_7N, CH_4(unresolved peak) and NH_3 (unresolved peak) desorbed off the surface.
120 K
< 0.25 L
Irreversible decomposition of C_2H_7N; while H_2 (450 K) and N_2 (≥ 1300 K) are produced.
W(100)-(5 x 1)-C
(TPD)
~ 3.3 L
Shows C_2H_7N, CH_3CN, NH_3 , H_2, and N_2 as products.
> 4 L
Result in sublimation of C_2H_7N multilayer at 150 K.
W(100)-(2 x 1)-O
(TPD)
120 K
C_2H_7N, H_2 (> 500 K) and N_2 (≥ 1250 K) are the main products.
Ni(111)
(HREELS, TDS)
H_3C
$C-NH_2$
H_2
C_2H_7N adsorb through the nitrogen atom.
Heating
Shows C_2H_7N (200 – 320 K), CH_3CN (~ 350 K), H_2,(~ 380 K) and N_2 (~800) as reaction products.
3 L and 150 K

Figure 2.7 Schematic of the reaction of ethylamine with various metal surfaces as reported in the literature; W(100), W(100)-(5 x 1)-C, and W(100)-(2 x 1)-O (Pearlstine and Friend, 1986), Ni(111) (Gardin and Somorjai, 1992).

3. EXPERIMENTAL AND MODELING

3.1 Experimental

All experiments were performed in a stainless steel ultrahigh vacuum chamber operating at a base pressure $\leq 1\times10^{-09}$ torr (Figure 3.1). Vacuum conditions were achieved initially with two sorption pumps to a level of 1×10^{-03} torr, and then ultrahigh vacuum (UHV) was achieved and maintained by a combination of a Thermionics TTS-240N 240 $L.s^{-1}$ ion pump and Leybold TMP-151 turbo-molecular drag pump, which is connected to a rotary mechanical pump. The sorption pump has an aluminium body with internal extruded heat transfer fins, and the pump is filled with a very porous material (molecular sieve). A pressure relief tube is mounted on the connecting flange. This pump is placed in polystyrene container containing liquid nitrogen (LN_2), whereby gases from the chamber are trapped in the molecular sieve by cryocondensation and cryosorption. The advantages of using a turbomolecular pump are that it is a very clean mechanical compression pump, operate smoothly and contribute little vibration to the operating system, and can operate from steady state inlet pressures as high as 1×10^{-02} torr to below 5×10^{-10} torr. A PS-500 titanium sublimation pump is also installed in the chamber to reduce all Ti-gettable gases. A titanium sublimation pump consists of a source of titanium, a source of heat, and surrounding surfaces on which a titanium film can be deposited. To reduce the base pressure further during experiments, a LN_2 cryotrap is installed under the ion pump to condense most gases, which reduces the base operating pressure below 1×10^{-10} torr.

Sample positioning on the vacuum chamber system was performed using Thermionics XYZ-θ manipulator (EC-1275-1-1-2 model) equipped with a Thermionics RNN-150 differentially pumped rotary platform (capable of 360° sample rotation), allowing for sample alignment with each port in the vacuum chamber, and a combination power/thermocouple feedthrough with a power rating (5 kV – 50 A) with a K-type thermocouple mounted on a miniflange (Peterson et al., 1994). A Varian SD300 and Leybold D16A mechanical roughing pump was used to differentially pump the rotary platform of the sample manipulator. The Mo(110) single crystal was mounted inside the

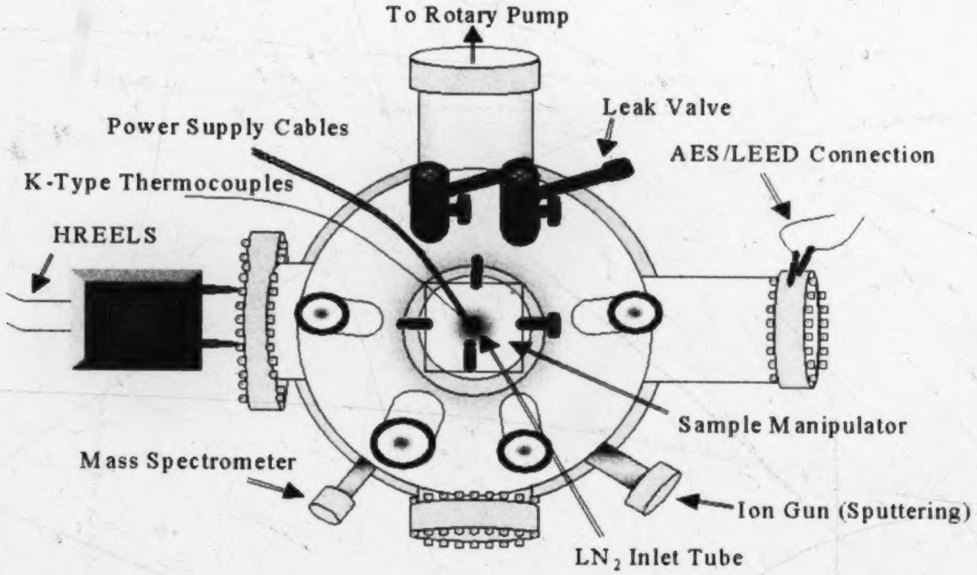

Figure 3.1 Schematic diagram of ultrahigh vacuum chamber setup.

vacuum chamber on 0.5 mm thick tantalum foil and mechanically held to the tantalum.

3.1.1 Methods and Materials

A 99.9% zone refined Mo(110) single crystal was obtained from Alfa Aesar with one side polished to < 0.03 micron and accuracy < 1 deg and was used for all experimental studies. Prior to experiment, the Mo(110) surface was cleaned by a combination of Ar^+ sputtering at 1 keV using a Physical Electronics Model 04-161 Ion Sputter gun. The surface was also annealed in low oxygen partial pressures to remove additional sample impurities. Following the sample cleaning procedure, the sample was characterized to verify the surface was free of contamination and the crystallographic orientation was (110).

Ethylamine (Sigma-Aldrich, 97% purity), pyridine (Sigma-Aldrich, 99.9+% HPLC grade), pyrrole (Sigma-Aldrich, 98%), argon (Praxair, 99.999% purity), oxygen (Praxair, 99.995% purity) were commercially available and used as received. In addition, pyridine and pyrrole were further purified using several freeze-pump-thaw cycles. The purity of pyridine, pyrrole, and ethylamine were verified using the mass spectrometer prior to and during the dosing of each TPD experiment. The mass spectrometer fragment patterns of each pyridine, pyrrole, and ethylamine were compared to spectra found in the NIST mass spectroscopy database (Malard and Linstorm, 1997).

Reactant gases were introduced into the vacuum system through two vacuum pumped dosing lines that were connected to the UHV chamber via variable leak valves. Sample dosing was accomplished by backfilling the vacuum chamber to a desired pressure for a given length of time. All reactant exposures were measured in the units of Langmuir, where $1\ L = 1\times10^{-06}$ torr.s. For all experiments, the sample was initially cooled to ~ 100 K, dosed with the reactant, rotated in front of the mass spectrometer, and linearly heated to approximately 200 K. No corrections were made to the raw TPD spectra for the ion gauge or mass spectrometer sensitivity.

3.1.2 Temperature Programmed Desorption (TPD)

Temperature programmed desorption (TPD) is one of the most common and useful techniques for studying elementary, molecular-level reaction mechanisms of gas-phase species with solid surfaces. It provides information about the heat of adsorption, quantitative coverage information about dissociative and non-dissociative adsorption, energetic information about phase transitions, interadsorbate interaction, multiple adsorption sites, and kinetic information about desorption processes (reaction mechanism). TPD also has some disadvantages, which include catalyst destruction; difficulty to interpret the experimental data (re-adsorption can cause such problems) and sometimes it can be difficult to determine the reaction temperature (Falconer and Schwarz, 1983; Niemantsverdriet, 2000; Pieter et al., 1997).

Fundamentally, TPD relates to physisorption and chemisorption phenomena. Adsorption takes place when an attractive interaction between a particle and a surface is strong enough to overcome the disordering effect of thermal motion. When the attractive interaction is essentially the result of van der Waals forces then physisorption takes place. Physisorptive bonds are characterized by dissociation energies below approximately 12 kcal mol^{-1}, although there are exceptions to this generality. Chemisorption occurs when the overlap between the molecular orbitals of the adsorbed species and the surface atoms permit the formation of chemical bonds, which are characterized by dissociation energies typically exceeding 50 kJ mol^{-1}. It should be noted that chemisorption is often an activated process, i.e., the formation of a chemisorptive bond requires that an activation barrier be overcome. A common feature of molecular chemisorption is the weakening of intramolecular bonds that often lead to the dissociation of the adsorbed molecule.

In practice, the basic TPD experiment is very simple, as illustrated in Figure 3.2. The TPD system consists mainly of a mass spectrometer, power supply, and thermocouples. The transpector, a quadruple partial pressure analyzer, measures the partial pressures of gases in a mixture and up to 12 gases. Controlled by an external computer, the instrument consists of a sensor that functions only in high-vacuum environment (pressure below 1×10^{-4} torr) and the electronics that operate the sensor. The transpector sensor analyzes gases by ionizing some of the gas molecules, separating the ions by mass and measuring the quality of ions at each mass. The masses, unique for each substance, allow you to identify the gas molecules from which the ions were created. The sensor consists of three main parts: the ion source (ionizer), the quadrupole mass filter, and the ion detector. All of these parts are mounted on an electrical feedthrough flange, which is bolted to the vacuum space where the gas analysis measurements are made. Furthermore, the mass spectrometer sensing unit was fitted with a quartz nose cone containing a 1 mm hole, which minimizes the background desorption signals from the manipulator and sample support hardware.

Sample temperature was monitored using a chromel/alumel type K thermocouple spot-welded on the back of the tantalum foil. Both mass spectra data and temperature were recorded using a 486 PC running LabView (Version 3.01) software. The program reads sample temperature using a Lab-PC+ multifunctional I/O board (National Instruments) and a SC-2071 general-purpose termination breadboard (National Instruments). The TPD procedure used in this study is outlines as follows;

1. Prepare a clean Mo(110) sample surface by means of Ar^+ ion sputtering at an acceleration voltage of 1 keV and current of 30 mA at a system backpressure of 3×0^{-05} torr argon. Subsequently, the sample was cooled to approximately 100 K, the chamber backfilled with UHP oxygen at a base pressure of 1 – 2 $\times10^{-08}$ torr, and the sample was annealed at 1200 K for 5 minutes and then thermally flashed to 1500 K. Surface cleanness and crystallographic orientation were verified prior to experiment with AES and LEED.
2. The clean Mo(110) surface was cooled to approximately 100 K by direct thermal contact with LN_2, and the reactant was adsorbed to achieve a predetermined exposure, as measured in units of Langmuir.
3. The sample temperature was linearly increased at a rate of 2 K s^{-1} from 100 to 1200 K using a Hewlett Packard 6672A DC programmable power supply. The desorbed gases were monitored with a Leybold Inficon Transpector H200M quadruple mass spectrometer (QMS) while increasing the substrate temperature in a controlled fashion.

TPD experiments were used in our research over Mo(110) and C/N-Mo(110) single crystal surface to monitor the desorbed gases during sample heating to determine reaction mechanisms, intermediate and final products, heats of adsorption by determining the desorption peak temperatures and combined with Redhead equation (Redhead, 1962), and draw our conclusions about surface activity, selectivity, and reaction pathways that result from the presence of adsorbed carbon and nitrogen.

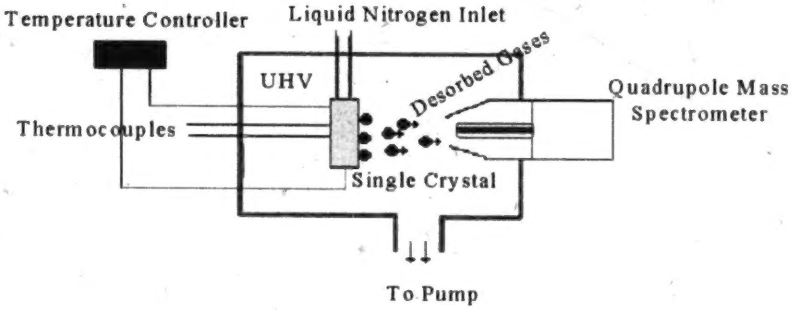

Figure 3.2 Experimental set-up of temperature programmed desorption studies in UHV environment.

3.1.3 Auger Electron Spectroscopy (AES)

Auger electron spectroscopy was developed in the 1960s when UHV technology became commercially available (Harris, 1968a; Harris, 1968b), and has since emerged as one of the most widely used analytical techniques for obtaining the chemical composition of solid surfaces. The basic advantages of this technique are its high sensitivity for chemical analysis at near surface depth of 5 – 20 Å (Czanderna, 1989; Niemantsverdriet, 2000), a rapid data acquisition speed, the ability to detect all elements above helium, and the capability of high-spatial resolution.

The Auger emission process can be understood by considering the ionization process of an isolated atom under electron bombardment. As shown in Figure 3.3, AES is carried out by exciting the sample with a beam of primary electrons with kinetic energy (E_P) between 1 – 25 keV. These electrons create core holes in the atoms of the sample, such as a K level in this illustration. The excited atom relaxes by filling the core hole with an electron from a higher shell L_1. The energy ($E_K - E_{L1}$) is either librated as an x-ray photon (x-ray fluorescence) or transferred to another electron (L_2). This electron is ejected from the atom as an Auger electron. As noted in Figure 3.3, the kinetic energy of the Auger electron is entirely determined by the electron levels involved in the Auger process, and not by the energy of the primary electrons. Thus, the emitted Auger electron will have the energy given by the following expression;

$$E = E_K - E_{L1} - E_{L2} \qquad (3.1)$$

This excitation process is denoted as a KL_1L_2 Auger transition. It is obvious that at least two energy states and three electrons must take part in an Auger process. Therefore, H and He atoms cannot give rise to Auger electrons. Several transitions (KL_1L_1, KL_1L_2, LM_1M_2, etc.) can occur with various transition probabilities. The key aspect of AES it the Auger electron energies are characteristic of the target elements and independent of the incident beam energy.

In this research, an Omicron Vakuumphysik Spectraleed L-A-2000 unit was utilized for Auger electron spectroscopy and low-energy electron diffraction studies. For AES measurements, the sample is irradiated with electrons from a LaB_6 electron gun with

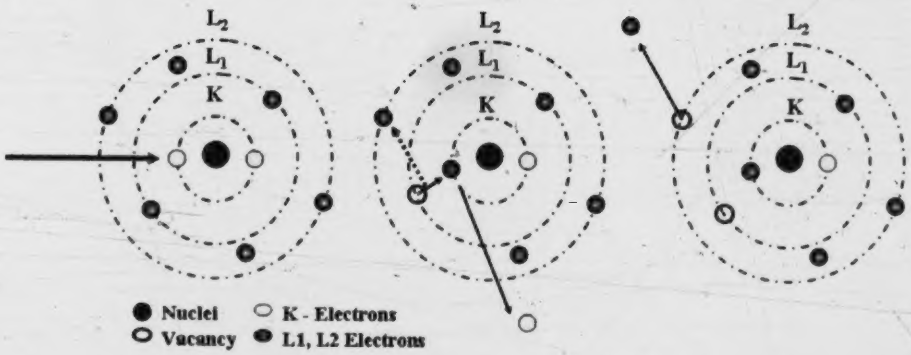

Figure 3.3 Energy level diagrams in an Auger process. Electron from L_1 drops into the K level with the emission of an L_2 electron.

an incident electron beam energy of 1.5 kV, and a resolution of ΔE/E = 0.45%. The emitted Auger electrons are analyzed for energy by a retarding field analyzer (RFA), which is interfaced with a 486-based personal computer running the Omicron Auger control software (ACS Version 4.0). Because the Auger peaks are superimposed on a rather large continuous background, they are more easily detected by differentiating the energy distribution function N(E), and thus the conventional Auger spectrum is the function dN(E)/dE. The experiment is carried out in a UHV environment ($1 - 2 \times 10^{-09}$ torr) because the AES technique is surface sensitive due to the limited mean free path of electrons in the kinetic energy range of 20 to 2500 eV. Figure 3.4, shows AES spectrum of clean a Mo(110) single crystal as obtained for the sample used in this research.

In addition to qualitative analysis, AES can also quantify the composition of a sample surface. In quantitative AES analysis, it is assumed that the composition of the sample in the near surface region is homogeneous. Quantitative analysis involving the use of elemental sensitivity factors is less accurate but is highly useful. The atomic concentration (C) of an element x in a sample is given by

$$C_x = \frac{I_x / S_x}{\sum \left(I_i / S_i \right)} \qquad (3.2)$$

where I_x is the peak-to-peak amplitude of the element X from the unknown specimen and S_i is the relative sensitivity of pure element i (0.257 for carbon, 0.470 for nitrogen, and 0.392 for molybdenum) (Davis, et al., 1978). The summation is for the corresponding ratios for all other elements present in the sample. Because this method neglects variations in the backscattering factor and escape depth with material, this method is semi-quantitative. The main advantages of this method are the elimination of standards and insensitivity to surface roughness. Qualitative analysis of Auger peaks in the spectrum was accomplished through combined use of chart of principle Auger electron energies and the standard spectra (Davis, et al., 1978). In general, this procedure results in rapid and unambiguous interpretation of the spectra. If peaks remain which have not

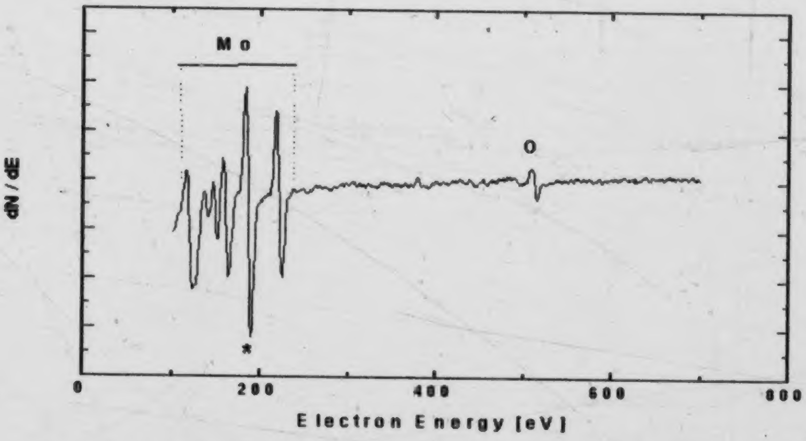

Figure 3.4 Auger spectrum from Mo(110) single crystal, E_P= 1.5 keV and I_P= 1.2 A.

yet been identified, they may be energy loss peaks due to primary electrons, which have lost discrete amount of energy through ionization of core levels. In general, AES experiment proceeds as following:

1. Position the single crystal surface in normal position to the electron gun,
2. Switch on the lock-in amplifier (model 5209), Auger remote control and electron gun units,
3. Set the emission current to 1.2 A and the beam voltage to 1.5 kV in the electron gun unit (try to reach these values in small increments increase and not one jump),
4. Turn on the accompanied Auger control software (version 2.0), which controls the lock-in amplifier and all other scanning parameters.
5. Set the scanning parameters as per the following:
    i. Energy increment : 1 eV
    ii. Sensitivity : 1.0 – 3.0 mV
    iii. Modulation amp. : 1.77 eV
    iv. Dwell time : 300 – 500 msec.
    v. Lock-in-tau : 300 – 500 msec.
6. Read the beam energy from the sample surface to insure good sample position before running AES scanning, this is step is critical and you should read 1.5 kV as set in the electron gun,
7. Once the beam energy is confirmed, run AES between 100 to 600 eV.

3.1.4 Low Electron Energy Spectroscopy (LEED)

Low energy electron diffraction is one of the most powerful methods of surface crystallography (Ertl and Küppers, 1985; Van Hove, et al., 1986). In principle, the LEED experiment is very simple. A monoenergetic electron beam with low energy electrons (25 – 200 eV) impacts the ordered sample surface, and because of the regular arrangement of atoms, electrons are diffracted back in discrete directions determined by the lateral periodicity. Since these electrons can be considered as waves with a certain wavelengths, the scattered electrons are collected with a fluorescent screen, and one can observe a pattern of spots whereby each spot corresponds to a direction in which constructive interference take place. Figure 3.5 shows a schematic diagram of LEED process.

LEED experiments in this research were performed using the Omicron Vakuumphysik Spectraleed L-A-2000 unit as a reverse-view with four grids and LEED optics system. The electron gun filament is held at a current of 1.4 A, and produces an electron beam with an energy that typically ranges from 60 to 70 eV. The LEED image was collected using a Canon Power-shot G5 digital camera.

There are several key advantages to using LEED to characterize a surface. Firstly, strong inelastic scattering caused by plasmon excitations restricts the incoming electrons to penetrating only a few layers near the surface. This makes LEED surface sensitive. Secondly, strong elastic scattering of the outgoing electrons results in multiple scattering by the surface atoms. This provides high precision for the determination of the full surface structure, i.e. all atomic coordinates in the surface. In this way LEED is able to yield the full structure of a certain slab of surface atoms. This surpasses the potential of most other surface sensitive techniques, which provide only a subset of structural information – for example bond lengths or surface corrugation. Additionally, there is high precision and in favourable cases atomic coordinates may be determined with an error limit of only ± 0.01 Å.

3.1.5 High-Resolution Electron Energy Loss Spectroscopy (HREELS)

Vibrational frequency based techniques are one of the most powerful experimental techniques for studying adsorbed systems. In particular, they are extremely useful in identifying the types of bonds that are present in a sample. Shifts in vibrational frequencies can also be used to gain insight into subtle changes in bonding. Vibrational modes are named according to the type of motion involved in the vibration. There are four characteristic types of vibrations; stretching vibrations (ν) which change the bond length, bending in-plane vibrations (δ) which change bond angles but not bond lengths, bending out-of-plane vibrations (γ), and torsions (τ) which change the angle between two planes containing the atoms involved in the motion.

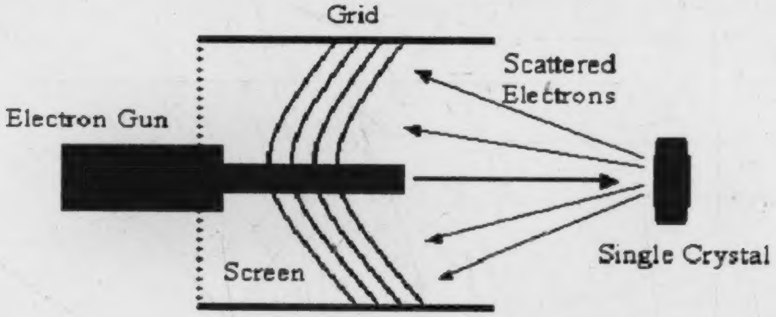

Figure 3.5 The principle of LEED is that a beam of monoenergetic electrons scattered elastically from a surface. Because of the periodic order of the surface atoms, electrons show constructive interference in directions for which the path lengths of the electrons differ by an integral number of times the electron wavelength. Directions of constructive interference are made visible by collecting the scattered electrons on a fluorescent screen.

Electron energy loss spectroscopy (EELS) refers, in a broad sense, to every type of electron spectroscopy in which inelastic electron scattering is used to study excitations of surfaces or thin solid films (Ibach and Mills, 1982). When electrons backscatter from a surface they can lose energy to the various degrees of freedom of the surface and adsorbed layer. EELS relies upon the use of a monochromatic collimated beam of electrons, which is analyzed after it has scattered from the surface. Figure 3.6 presents a schematic representation of the EELS experiment.

When EELS is preformed with high energetic resolution at low primary energies, $E_0 < 20$ eV, it is called high resolution electron energy loss spectroscopy (HREELS). The largest peak in the spectrum is the elastic peak. The absolute energy of the elastically scattered electrons is unimportant as far as the position of peaks in the spectrum is concerned. The centre of the elastic peak, E_0, fixes the origin of the spectrum and is conventional set equal to zero energy. The width of the elastic peak, conventionally expressed as full width at half maximum (FWHM), is a measure of the spectral resolution (Ibach, 1991). The energy at which a peak occurs is given in Equation 3.3

$$E_s = E_0 - h\omega \tag{3.3}$$

where $h\omega$ is the energy of excited transition, and E_s is the detected energy (energy loss). Thus, if we take $E_0=0$, the energy of a peak is the energy of the vibration excited by electron scattering.

Vibrational spectra in this research were collected in an ultrahigh vacuum environment using a LK Technologies LK2000-14 high-resolution EELS mounted on a 14 in. flange and includes all electrical feed-throughs, electron multiplier and magnetic shielding. A schematic of this instrument is shown in Figure 3.7. The spectrometer features a double-pass 127° monochromator of exceptional output and very low spectral background, in combination with a single-pass analyzer. An instrumental resolution of 3 meV (FWHM) and below is combined with very high signal levels, low noise, high-stability power supply and beam energy from 0-240 eV. The spectrometer is operated using computer-based control electronics through menu-driven software that permits setup and optimization of all spectrometer voltages and monitoring of critical current

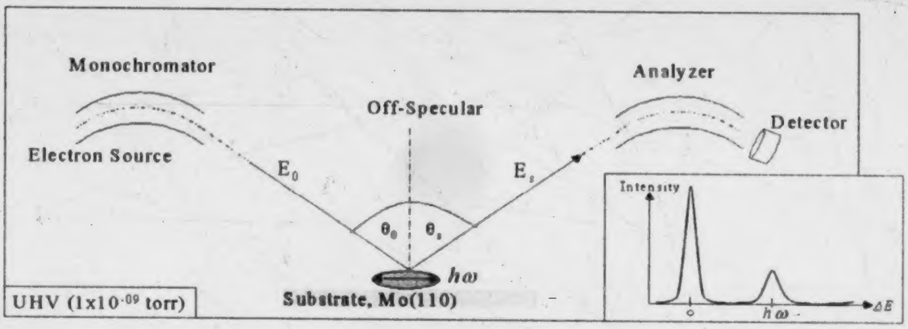

Figure 3.6 A schematic drawing of a High-Resolution Electron Energy Loss Spectrometer experiment.

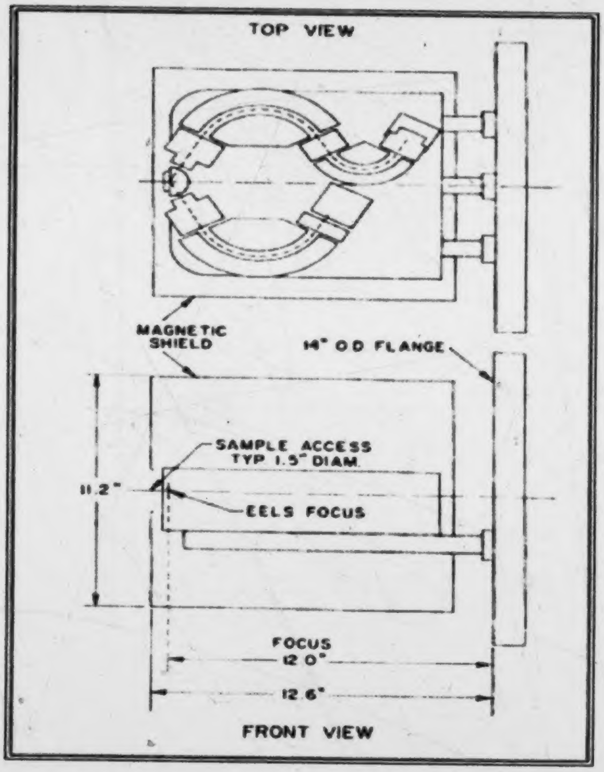

Figure 3.7 Schematics of LK2000-14 EELS Model (reprinted with permission form LK2000 Technologies).

level. The counting electronics includes preamplifier, amp/discriminator, ratemeter (1 MHz), high-voltage power for electron multiplier, and NIM-bin power supply.

It is important at all time to maintain a vacuum of 1×10^{-07} torr or higher while running the EELS. While keeping the EELS's filament off, place the sample surface in a proper location in front of the EELS spectrometer and make sure all instrument cables are connected except the preamp to avoid arcing it. The general EELS operating procedure used in this research is as follows;

1. Turn on the system and set the beam voltage to –3.69 eV, and make sure to measure all lenses voltages using a voltmeter and compare it with readings on computer DAC screen (as an initial check of the system functionality),
2. Turn on the filament to 1.76 A and measure currents of mono1-out current, collimator current, mono2-out current, which should read 0.58, 0.208, and 0.019 μA, respectively.
3. The sample current should read around 97 pA at the above setting. Possible sample current optimization is needed every start-up, and this is done by adjusting the mono2 level and IL1 – IL5 lenses.
4. Once the proper sample current is achieved, turn on the channeltron high voltage supply (to 2.6 kV) and counting electronics. As per the above setting, a count rate of 10^4 – 10^6 cps should be obtained. Tuning is possible by adjusting sample position, delta-D1, delta-D2, delta-Z3, delta-Z4 lenses, analyzer level setting, and beam voltage.
5. A quick scan is preformed to measure the FWHM, which should be 3 – 4 meV (best case).
6. Once the above parameters are obtained, vibrational losses are measured by scanning the analyzer and zoom lens system with the scan control using the computer interface. The usual number of scans are set to 16 and 500 scanning channels are used to scan the entire possible vibrational region.

3.2 Molecular Modeling and Simulation

3.2.1 Introduction

Molecular modeling is a general term that covers a wide range of molecular graphics and computational chemistry techniques used to build, display, manipulate, simulate and analyze molecular structures and to calculate their properties. Molecular modeling is used in several research areas, and therefore the term does not have a rigid definition. Because this is an important foundation for this research, a brief description of molecular modeling, including the development of density functional theory, is provided below to rationalize the methodology and calculation parameters.

When a structure is initially constructed, it needs to be refined to bring it to an energetically stable configuration. This is especially true after building certain structures in three-dimensions when the process of adding fragments can result in atom interactions. The refinement process is known as minimization (or optimization) and is an iterative procedure in which the coordinates of the atoms are adjusted so that the energy of the structure is brought to a minimum. The structure with the lowest energy is considered to have the most stable arrangement and by definition, the optimum geometry. Minimization generally results in a modeled structure with a close resemblance to a real physical structure. The ability to compute the energy of a structure is necessary part of the minimization process and is an extremely important aspect of a modeling system.

Molecular modeling involves molecular mechanics, molecular dynamics and quantum mechanics. Molecular mechanics techniques take a classical approach to calculating the energy of a structure. The molecule is treated essentially as a set of charged point masses, which are coupled together with springs. The total energy of a structure is calculated using an analytical function that sums the individual energy terms. At its simplest level, the function includes bond stretching, valence angle bending, torsion, and non-bond interaction terms that include van der Waals attraction, van der Waals repulsion, and electrostatic interactions), which associate an energetic penalty to the structure based upon deviations from an idealized geometry. The number of non-bond atom pairs rises with the square of the number of atoms, and therefore the non-bond interaction term dominates the computer time required for energy evaluation in calculations on larger structures. For this reason, it is normal to limit the non-bond energy evaluation to atom pairs within a certain cutoff distance, based on the assumption that atom pairs separated by a larger distance make a negligible contribution to the total energy. The idealized reference value of bond lengths and angles, plus the force constants and the van der Waals radii and associated constants required to calculate the non-bond interactions are stored in a file that is referred to when the energy calculation is run. The combination of these parameters with the functional forms of the individual energy terms is known as a force field. It is important to appreciate that the reference values of bonds and angles cannot be based on element type alone. Molecular mechanics gives a great deal of information from the minimized structure energy, nonetheless, these structure are static models, whereas in reality, molecules are flexible structures subject to thermal motion.

The technique molecular dynamics can be used to simulate the thermal motion of a structure as a function of time, using the forces acting on the atoms to drive the motion. Starting with the molecular mechanics energy description of the structure as described above, the forces acting on the atoms can be evaluated. Since the masses of the atoms are known, Newton's second law of motion may be used to compute the accelerations, and thus the velocities, of the atom. The accelerations and the velocities may then used to calculate new positions for the atoms over a short time step (around 1 fs = 1×10^{-15} second), thus moving each atom to a new position in space. This process iterates thousands of times, generating a series of conformations of the structure known trajectory and can been seen as an animated movie, which gives a clear picture of the minimization steps.

For deeper understanding of the chemical reality, quantum mechanics provides a clearer picture for the electronic structure of the molecule and their interaction. Starting with a specified molecular geometry, quantum mechanics calculations solve the Schrödinger equation for this arrangement of electrons and nuclei. This yields both the energy of the molecule and the associated wave function from which the electronic properties, such as electron density, can be calculated. The wave function can be used to calculate a range of chemical properties, which can be used in structure-activity studies, which include electrostatic potential, electron density, dipole moment, and the energies and positions of frontier orbitals.

3.2.2 Development of Density Functional Theory (DFT)

3.2.2.1 Solids and Their Structures

In general, solids are classified into two different categories: those, which possess long-range-order in the position of their atoms (crystals), and those, which do not (amorphous). In a crystal the sites of atoms are determined simply by repeating some sub-unit of the crystal at regular intervals to fill all space. Mathematically we describe a crystal in terms of a regularly arranged set of points whose distribution throughout space looks identical from any point in the set (the lattice), and a prescription telling us how many atoms of each type to associate with each point and where they should go in relation to that point (the basis). Crystals are the most widely studied solids from the theoretical point of view, because we can learn about the behavior of an entire crystal just by studying a very small portion (the structure simply repeats itself at regular intervals). Amorphous materials are less well studied; the lack of a repeating structure means that these materials are much more difficult to deal with from the theoretical point of view.

The atoms, which make up a solid, are made up of a compact heavy core (the nucleus) surrounded by several, much-lighter electron. The nucleus has a positive electric charge, while the electrons have a negative charge. This causes the electrons to be attracted to the nucleus. A neutral atom has just enough electrons to exactly balance the charge of the nucleus. However, some of the electrons are so tightly bound to the nucleus by this attraction that we may as well think of the nucleus plus its core electrons as a single entity. This means that we only have to consider about the behaviour of the remaining loosely bound electrons (known as the valence electrons).

When atoms combine to form a solid, it is the attraction between the positive ion cores and the valence electrons, which holds the material together. While the ion cores occupy fixed positions, the valence electrons move around and between them, forming a kind of electrostatic glue. In some materials this "glue" is piled up into distinct bonds between particular ion cores (so-called covalent bonding), but in others the electrons are more evenly distributed in the space between the ion cores (known as metallic bonding). A third form of bonding occurs when some of the valence electrons from one atomic species are donated wholesale to another atomic species. Atoms of the species, which donates electrons, become positive ions, and atoms of the species, which accepts the electrons, become negative ions. This leads to a direct electrostatic attraction between the oppositely charged ions and is known as ionic bonding.

3.2.2.2 Waves and Particles

At the macroscopic scale we are used to two broad types of phenomena: waves and particles. Briefly, particles are localized phenomena, which transport both mass and energy as they move, while waves are de-localized phenomena (that is they are spread-out in space) that carry energy but no mass as they move. In Quantum Mechanics this distinction is blurred. Entities, which we would normally think of as particles (e.g. electrons) can behave like waves in certain situations, while entities, which we would normally think of as waves (e.g. light) can behave like particles. Thus electrons can create wave-like diffraction patterns upon passing through narrow slits, just like water waves do as they pass through the entrance to a harbour.

Such ideas led DeBroglie to the conclusion that all entities had both wave and particle aspects, and that different aspects were manifested by the entity according to what type of process it was undergoing. This became known as the Principle of Wave-Particle Duality. Furthermore, DeBroglie was able to relate the momentum of a "particle" to the wavelength (i.e. the peak-to-peak distance) of the corresponding "wave". Thus it is possible to calculate the quantum wavelength of a particle through knowledge of its momentum.

This was important because wave phenomena, such as diffraction, are generally only important when waves interact with objects of a size comparable to their wavelength. Fortunately for the theory, the wavelength of everyday objects moving at everyday speeds turns out to be incredibly small. So small in fact that no quantum mechanical effects should be noticeable at the macroscopic level, confirming that Newtonian Mechanics is perfectly acceptable for everyday applications. Conversely, small objects like electrons have wavelengths comparable to the microscopic atomic structures they encounter in solids. Thus a quantum mechanical description, which includes their wave-like aspects, is essential to their understanding.

3.2.2.3 The Schrödinger Equation

The approach suggested by Schrödinger (Hinchliffe, 2000) was to postulate a function which would vary in both time and space in a wave-like manner (the so-called wavefunction) and which would carry within it information about a particle or system. The time-dependent Schrödinger equation (Equation 3.4) allows us to deterministically predict the behavior of the wavefunction over time, once we know its environment. The information concerning environment is in the form of the potential, which would be experienced by the particle according to classical mechanics.

$$-\frac{h^2}{8\pi^2 m}\left(\frac{\partial\psi^2}{\partial x^2}+\frac{\partial\psi^2}{\partial y^2}+\frac{\partial\psi^2}{\partial z^2}\right)+U\psi=\frac{jh}{2\pi}\frac{\partial\psi}{\partial t} \qquad (3.4)$$

In this equation, the wavefunction $\psi(x,y,z,t)$ depends on the spatial and time variable x, y, z and t. j represents the square root of -1, m represents a single particle of mass, h is the Planck's constant, and U is the potential energy. In cases where the potential is time-independent, the wavefunction can be factorized into space- and time-dependent parts (Equation 3.5)

$$\psi(x,y,z,t)=\psi(x,y,z)T(t) \qquad (3.5)$$

which individually satisfy the time-dependent Schrödinger equation (Equation 3.6)

$$-\frac{h^2}{8\pi^2 m}\left(\frac{\partial^2\psi}{\partial x^2}+\frac{\partial^2\psi}{\partial\partial y^2}+\frac{\partial^2\psi}{\partial z^2}\right)+U\psi=\varepsilon\psi \qquad (3.6)$$

and also

$$j\frac{h}{2\pi}\frac{dt}{dt}=\varepsilon T \qquad (3.7)$$

where the quantity ε is equal to the energy of the system. This equation can readily solved to give (Equation 3.8)

$$T = T_0 \exp\left(-j\frac{2\pi\varepsilon}{h}\right) \tag{3.8}$$

Schrödinger's equations are usually written in a briefer manner by invoking the Hamiltonian operator $\hat{H}$ (the operator of the energy for the system), so the time-dependent Equation 3.4 for a single particle becomes

$$\hat{H}\psi = \frac{jh}{2\pi}\frac{\partial\psi}{\partial t} \tag{3.9}$$

and the time-independent Equation 3.6 for a single particle becomes

$$\hat{H}\psi = \varepsilon\psi \tag{3.10}$$

When there are a discrete number of solutions to the equation above, the equation is most generally written as Equation 3.11

$$\hat{H}\psi_k(r_1, r_2, \ldots, r_N) = E_k\psi_k(r_1, r_2, \ldots, r_N) \tag{3.11}$$

The number of solutions can be finite or infinite; the Hamiltonian operator is the quantum-mechanical analogue of the energy, the E_k are the corresponding energies (eigenvalues) of the operator. ψ_k is the wavefunction (eigenvectors or eigenfunctions) of the operator, while $r = (x,y,z)$ is the cartesian coordinates. Whenever we make a measurement on a quantum system, the results are dictated by the wavefunction at the time at which the measurement is made. It turns out that for each possible quantity we might want to measure (an observable) there is a set of special wavefunctions (known as eigenfunctions), which will always return the same value (an eigenvalue) for the observable. Even if the wavefunction happens not to be one of these eigenfunctions, it is always possible to think of it as a unique superposition of two or more of the eigenfunctions. Once the wavefunction has collapsed into one particular eigenfunction it will stay in that state until it is perturbed by the outside world.

The fundamental limitation of quantum mechanics lies in the Heisenberg Uncertainty Principle, which tells us that certain quantum measurements disturb the system and push the wavefunction back into a superposed state once again. For example, consider a measurement of the position of a particle. Before the measurement is made the particle wavefunction is a superposition of several position eigenfunctions, each corresponding to a different possible position for the particle. When the measurement is made the wavefunction collapses into one of these eigenfunctions, with a probability determined by the composition of the original superposition. One particular position will be recorded by the measurement: the one corresponding to the eigenfunction chosen by the particle.

If a further position measurement is made shortly afterwards, the wavefunction will still be the same as when the first measurement was made (because nothing has happened to change it), and so the same position will be recorded. However, if a measurement of the momentum of the particle is now made, the particle wavefunction will change to one of the momentum eigenfunctions (which are not the same as the position eigenfunctions). Thus, if a still later measurement of the position is made, the particle will once again be in a superposition of possible position eigenfunctions, so the position recorded by the measurement will once again come down to probability. What all this means is that one cannot know both the position and the momentum of a particle at the same time because when you measure one quantity you randomize the value of the other.

At any rate, in a macroscopic system the wavefunctions of the many component particles are constantly being disturbed by measurement-like processes, so a macroscopic measurement on the system only ever yields a time- and particle- averaged value for an observable. This averaged value need not, of course, be an eigenvalue, so we do not generally observe quantization at the macroscopic level (the correspondence principle again). If we are to investigate the microscopic behavior of particles we would (in an ideal world) like to know the wavefunctions of any individual particles at any given instant in time.

The time-dependent Schrödinger equation allows us to calculate the wavefunctions of particles, given the potential in which they move. Importantly, all the solutions of this equation will vary over time in some kind of wave-like manner, but only certain solutions will vary in a predictable pure sinusoidal manner. These special solutions of the time-dependent Schrödinger equation turn out to be the energy eigenfunctions, and can be written as a time-independent factor multiplied by a sinusoidal time-dependent factor related to the energy. Because of the simple time-dependence of these functions, the time-dependent Schrödinger equation reduces to the time-independent Schrödinger equation for the time-independent part of the energy eigenfunctions.

That is to say that we can find the energy eigenfunctions simply by solving the time-independent Schrödinger equation and multiplying the solutions by a simple sinusoidal factor related to the energy. It should therefore always be remembered that the solutions to the time-independent Schrödinger equation are simply the amplitudes of the solutions to the full time-dependent equation. One of the most important characteristics of a wavefunction is that the square of its magnitude is a measure of the probability of finding a particle described by the wavefunction at a given point in space. That is, in regions where the square of the magnitude of the wavefunction is large, the probability of finding the particle in that region is also large, and vice versa.

3.2.2.4 Hartree Model and Hartree-Fock Theory

To describe completely the quantum mechanical behavior of electrons in solids it is strictly necessary to calculate the many-electron wavefunction for the system. In principle this may be obtained from the time-independent Schrödinger equation, but in practice the potential experienced by each electron is dictated by the behavior of all the other electrons in the solid. Of course, the influence of nearby electrons will be much stronger than that of far-away electrons since the interaction is electrostatic in nature, but the fact remains that the motion of any one electron is strongly coupled to the motion of the other electrons in the system. To solve the Schrödinger equation directly for all these electrons would thus require us to solve a system of around 1×10^{23} simultaneous differential equations, which is nearly impossible using current computational resources, and thus, we have to use approximations.

One of the earliest attempts to drive approximate wavefunctions for atoms and attempt to solve the problem was made by Hartree (Hartree, 1928). He simplified the problem by making an assumption about the form of the many-electron wavefunction, namely that it was just the product of a single-electron functions ϕ for each of the N electrons as shown in Equation 3.12.

$$\psi(r_1,s_1,r_2,s_2,\ldots,s_N)=\phi_1(r_1)\phi_2(r_2)..\phi_N(r_N) \qquad (3.12)$$

where r_N are the positional coordinates and a spin coordinate for the N^{th} electron.

In a uniform system these wavefunctions would take the form of simple plane waves. Having made this assumption it was possible to proceed using the variational principle. This principle is a very powerful concept in mathematics. In the form most commonly applied to theoretical physics it states that if we take some wavefunction for a system and calculate the expectation value of energy E, this energy will be either higher, or equal to the ground state energy E_0 for this system.

$$E=\frac{\langle\psi|H|\psi\rangle}{\langle\psi|\psi\rangle} \quad \geq \quad E_0=\frac{\langle\psi_0|H|\psi_0\rangle}{\langle\psi_0|\psi_0\rangle} \qquad (3.13)$$

By using the variational method Hartree found the Hamiltonian equation of the many-electron system. In fact, for an N-electron system there are N equations, one for each of the N single-electron wavefunctions, which made up the many-electron product wavefunction. These equations turned out to look very much like the time-independent Schrödinger equation, except the potential (the Hartree potential) was no longer coupled to the individual motions of all the other electrons, but instead depended simply upon the time-averaged electron distribution of the system. This important fact meant that it was possible to treat each electron separately as a single-particle. Consequently the Hartree approximation allows us to calculate approximate single-particle wavefunctions for the electrons in crystals, and hence calculate other related properties.

Unfortunately, the Hartree approximation does not provide us with particularly good results. For example, it predicts that in a neutral uniform system there will be no binding energy holding the electrons in the solid. This, of course, is in direct contradiction to the experimental evidence that electrons must be given a finite amount of energy before they can be liberated from solids.

The most obvious reason for the failure of the Hartree approach lies in the initial assumption of a product wavefunction. The famous Pauli Exclusion Principle (Hinchliffe, 2000) states that no two electrons in an atom can have identical quantum numbers. This principle is manifest as an effective repulsion between any pair of identical fermions possessing the same set of quantum numbers. Mathematically, the Pauli Exclusion Principle can be accounted for by ensuring that the wavefunction of a set of identical fermions is antisymmetric under exchange of any pair of particles. That is to say that the process of swapping any one of the fermions for any other of the fermions should leave the wavefunction unaltered except for a change of sign. Any wavefunction possessing that property will tend to zero (indicating zero probability) as any pair of fermions with the same quantum numbers approaches each other. The Hartree product wavefunction is symmetric (i.e. stays precisely the same after interchange of two fermions) rather than antisymmetric, so the Hartree approach effectively ignores the Pauli Exclusion Principle!

The Hartree-Fock approach is an improvement over the Hartree theory in that the many-electron wavefunction is specially constructed out of single-electron wavefunctions in such a way as to be antisymmetric (McWeeny and Sutcliffe, 1969; Szabo and Ostlung, 1989). The wavefunction is more complicated than the Hartree product wavefunction, but it can be written in a compact way as a so-called Slater determinant similarly to Equation 3.14.

$$\psi(r_1, r_2, \ldots, r_N) = \frac{1}{\sqrt{N!}} \begin{vmatrix} \phi_1(r_1) & \phi_2(r_1) & \ldots & \phi_N(r_1) \\ \phi_1(r_2) & \phi_2(r_2) & \ldots & \phi_N(r_2) \\ \ldots & \ldots & \ldots & \therefore \\ \phi_1(r_N) & \phi_2(r_N) & \ldots & \phi_N(r_N) \end{vmatrix} \tag{3.14}$$

Starting from this assumption it is once again possible to derive the Hamiltonian equation for the system through the variational principle. Just as before, this results in a simple equation for each single-electron wavefunction. However, this time in addition to the Hartree potential (which described the direct Coulomb interaction between an electron and the average electron distribution) there is now a second type of potential influencing the electrons, namely the so-called exchange potential. The exchange potential arises as a direct consequence of including the Pauli Exclusion Principle through the use of an antisymmetrised wavefunction.

We can get a visual impression of the effect of exchange by considering the region surrounding a given electron with a particular quantum mechanical spin. In this context spin is a quantum mechanical property, which is related to magnetism. Electrons can be either in the spin-up state or the spin-down state. In a non-magnetic sample half of the electrons will be spin-up while the other half will be spin-down. If we look at an electron with spin-up, then the Pauli Exclusion Principle means that other nearby spin-up electrons will be repelled. Spin-down electrons will not be affected since they have a different spin quantum number. Thus our spin-up electron is surrounded by a region that has been depleted of other spin-up electrons. Therefore, this region is positively charged. Similarly, if we had considered a spin-down electron from the start, then we would have found a region depleted of other spin-down electrons. The edge of the electron-depleted region is not clearly defined, but nevertheless we call this region the exchange hole.

Notably, the exchange potential contributes a binding energy for electrons in a neutral uniform system, so correcting one of the major failings of the Hartree theory. However, in calculating many other properties the Hartree-Fock approach is actually worse than the Hartree approach. The reason the Hartree-Fock theory gives worse answers than the Hartree theory is simply that there is another piece of physics, which we are still ignoring. To some extent it cancels out with the exchange effect and so when we use the Hartree approach we get reasonable results. On the other hand the Hartree-Fock approach includes the exchange effect but ignores the other effect, which balances it somewhat, completely. This new effect is the electrostatic correlation of electrons.

Ignoring the Pauli Exclusion Principle generated exchange hole for the moment, we can also visualise a second type of hole in the electron distribution caused by simple electrostatic processes. If we consider the region immediately surrounding any electron (spin is now immaterial) then we should expect to see fewer electrons than the average, simply because of their electrostatic repulsion. Consequently each electron is surrounded by an electron-depleted region known either as the Coulomb hole (because of its origin in the electrostatic interaction) or the correlation hole (because of it origin in the correlated motion of the electrons). Just as in the case of the exchange hole the electron-depleted region is slightly positively charged. The effect of the correlation hole is twofold. The first is obviously that the negatively charged electron and its positively charged hole experience a binding force due to simple electrostatics. The second effect is subtler and arises because any entities, which interact with the electron over a length scale larger than the size of the correlation hole will not interact with the bare electron but rather with the electron+correlation hole (which of course has a smaller magnitude charge than the electron alone). Thus any other interaction effects, such as exchange, will tend to be reduced by the correlation hole.

Clearly we can now see why the Hartree-Fock approach fails for solids. Firstly, the exchange interaction should be screened by the correlation hole rather than acting in full, and, secondly, the binding between the correlation hole and electron has been ignored. Although neither of the above methods succeeded in solving the many-body problems of electrons in solids they did at least elucidate the important physical processes, which describe namely exchange and correlation.

3.2.2.5 Density Functional Theory (DFT)

The breakthrough, which revolutionized the field, came in 1964 by Hohenberg and Kohn (Hohenberg and Kohn, 1964). They suggested that the problem really was that the many-electron wavefunction was too complicated an entity to deal with as the fundamental variable in a variational approach. Firstly, it cannot adequately be described without $\sim 1 \times 10^{23}$ parameters, and secondly, it has the complication of possessing a phase as well as a magnitude. They chose instead to use the electron density $\rho(r)$ as their fundamental variable. That is, they considered the ground state of the system to be defined by that electron density distribution which minimises the total energy. Furthermore, they showed that all other ground state properties of the system (e.g. lattice constant, cohesive energy, etc) are functional of the ground state electron density. That is, once the ground state electron density is known all other ground state properties follow.

In 1965, Kohn and Sham (Kohn and Sham, 1965) proposed an ingenious method of marrying wave function and density approach. They worked the total energy functional into the following parts:

$$E[\rho]=T_0[\rho]+\int\left[\hat{V}_{ext}(r)+\hat{U}_{cl}(r)\right]\rho(r)dr+E_{xc}[\rho] \qquad (3.15)$$

where $T_0[\rho]$ is the kinetic energy of electrons in a system which has the same density ρ as the real system, but in which there is no electron-electron interaction.

$$\hat{U}_{cl}(r)=\int\frac{\rho(r')}{|r'-r|}dr' \qquad (3.16)$$

$\hat{U}_{cl}$ is a pure Coulomb interaction between electrons.

$$\hat{V}_{ext}=\sum_{\alpha}\frac{-Z_{\alpha}}{|R_{\alpha}-r|} \qquad (3.17)$$

$\hat{V}_{ext}$ is the external potential, i.e., potential coming from nuclei, and the last functional is called the exchange-correlation energy that includes electron exchange, electron correlation, a portion of the kinetic energy which is needed to correct $T_0[\rho]$ to obtain true kinetic energy of a real system, and correction for self-interaction introduced by the classical coulomb potential.

The first implementations of the Kohn-Sham method used the local approximations to the exchange correlation energy. The appropriate functionals were taken from data for a homogenous electron gas. There were two variants of the method: spin unpolarized (LDF/LDA – Local Density Functional/Approximation) and spin polarized (LSD – Local Spin Density) where arguments require both α and β electron densities, rather than a total density. For historical reasons, the exchange correlation energy was partitioned into 2 parts:

$$E_{xc}[\rho] = E_x[\rho] + E_c[\rho] \tag{3.18}$$

the exchange energy, and the correlation energy.

Early attempts to improve functionals by GEA (Gradient Expansion Approximation), in which $E_{xc}[\rho]$ was expanded in Taylor series versus ρ and truncated at a linear term, did not improve results too much (Langreth and Vosko, 1990). Only GGA (Generalized Gradient Approximation) provided notable improvements by expanding $E_{xc}[\rho]$. The expansion here is not a simple Taylor expansion, but tries to find the right asymptotic behaviour and right scaling for the usually nonlinear expansion. These enhanced functionals are frequently called nonlocal or gradient corrections, since they depend not only upon the density, but also the magnitude of the gradient of density at a given point. There are many different corrections, and it will take some time when their respective merit, accuracy, and best domains of applications will be established. Probably the most frequently in use today is GGA-PBE (Perdew-Burke-Ernzerhof) (Perdew, et al., 1996).

Density functional theory is an extremely successful approach for the description of ground state properties of metals, semiconductors, and insulators. The main idea of DFT is to describe an interacting system of fermions via its density and not via its many-body wave function. For N electrons in a solid, which obey the Pauli principle and repulse each other via the Coulomb potential, this means that the basic variable of the system depends only on three -- the spatial coordinates x, y, and z -- rather than 3*N degrees of freedom. While DFT in principle gives a good description of ground state properties, practical applications of DFT are based on approximations for the so-called exchange-correlation potential. The exchange-correlation potential describes the effects of the Pauli principle and the Coulomb potential beyond a pure electrostatic interaction of the electrons. Possessing the exact exchange-correlation potential means that we solved the many-body problems exactly, which is clearly not feasible in solids.

3.2.3 Research Calculations

In our research, quantum mechanical calculations were performed using an *ab initio* quantum mechanical package with density-functional theory (DFT) plane-wave pseudopotential methods (CASTEP, Accelrys®, San Diego, CA). First principle calculations allow researchers to investigate the nature and origin of the electronic, optical, and structural properties of a system without the need for any experimental input other than the atomic number of mass of the constituent atoms. CASTEP is operated from within the Materials Studio's MS Modeling software environment (version 2.2). MS Modeling provides a user interface that is easy-to-use within Windows®.

CASTEP (Milman, et al., 2000; Segall, et al., 2002) uses a total energy plane-wave pseudopotential method. In the mathematical model of the material it replaces ionic potentials with effective potentials acting only on the valence electrons in the system. Electronic wave functions are expanded through a plane-wave basis set, and exchange and correlation effects in electron-electron interactions can be included within generalized gradient (GGA) approximations. Combining the use of pseudopotentials and plane wave basis sets makes it extremely easy to calculate the forces on the atoms. This enables efficient optimization of ionic configurations of molecules, solids, surfaces, and interfaces. A transition state search scheme has been implemented, which uses a combination of traditional LST/QST methods (Halgren and Lipscomb, 1977) and a subsequent refinement using a conjugate gradient method (Fischer and Karplus, 1992).

3.2.3.1 Setting up a Project in CASTEP

There are a number of steps to performing a calculation using CASTEP, and the general procedure is provided below.

1. Structure definition: A periodic 3D model document containing the structures of interest must be specified. Molybdenum is a body centre cube crystal with lattice parameter of 3.147 Å and cell volume of 31.164 Å^3. The construction of the Mo(110) single crystal was made by cleaving the BCC with (110) crystallographic orientation and then put it in a supercell with a volume of 1369.7 Å^3 and 12.225 Å vacuum slab thickness. Ethylamine, pyrrole, and pyridine

molecules were constructed as well with inter-atomic distance of 1.54 Å in all heterocyclic molecules. The surface and all involved molecules in this study was refined prior to any interaction studies to obtain a stable structure in which the coordinates of the atoms are adjusted so that the total energy of the structure is minimized.

2. Calculation setup: Once a 3D model document has been defined then it is necessary to select the type of calculation and set the associated parameters. Geometry optimization was the main task in our calculations, which allow refining the geometry of the structure to obtain a stable structure. The calculation was then sent to a central server to perform the calculation.
3. Analysis of the results: When the calculation is completed, the files related to that job are returned to the client and viewed in the project explorer.

CASTEP geometry optimization is based on reducing the magnitude of calculated forces and stresses until they become smaller than defined convergence tolerances. BFGS minimization algorithm (Fischer and Almlof, 1992) is adopted in the geometry optimization, which provides the fastest way of finding the lowest energy structure. Furthermore, medium quality was set for all geometry optimization calculations, which set the geometry optimization convergence thresholds for energy change, maximum force, maximum stress and maximum displacement between optimization cycles. The optimization will stop when all these criteria are satisfied. Medium quality indicates energy of 2×10^{-05} eV. atom^{-1}, maximum force of 0.05 eV.Å^{-1}, maximum stress of 0.1 GPa, maximum displacement of 0.002 Å, and a 100 maximum iteration.

3.2.3.2 Setting up The Electronic Options in CASTEP

There are several important adjustable parameters in the CASTEP interface, which affect the quality of the calculations. A description of these parameters and the corresponding settings used in this research are provided below.

1. Quality: Quality determines how accurate and how expensive the calculation will be, and four options are available within the software. Medium quality is set

within our calculation, which automatically sets the SCF tolerance to 2×10^{-06} eV.atom^{-1}, k-point separation to 0.05 Å^{-1} and medium energy cutoff (270 eV).

2. Exchange-correlation functional: The exchange-correlation functional determines the level of DFT description. CASTEP includes one local gradient-corrected exchange-correlation functional (LDA) and three nonlocal gradient-corrected exchange-correlation functionals (GGA). GGA functionals were used in all calculations as it provides a better overall descriptions of the electronic subsystem, while LDA description tends to overbind atoms, so that the bond lengths and the cell volume are usually underestimated by few percent and while the bulk modulus is correspondingly overestimated. GGA corrects this error and can underbind instead, leading to slightly overestimated bond lengths. GGA-PBE (Perdew-Burke-Ernzerhof) exchange in particular was adapted in this research as it is most recommended for studies of molecules interacting with metal surfaces (Perdew, et al., 1996).
3. Pseudopotentials: Pseudopotentials affect both the accuracy and the cost of the calculation. The concept of a pseudopotential is a crucial one for plane-wave total energy methods since the alternative full Coulomb potential of the electron-ion interaction decays too slowly to be accurately represented by a small number of Fourier components. Another way of looking at the problem is to analyze wave functions. Let us consider a solid as a collection of valence electrons and ion cores. The ion cores contain nuclei and tightly bound core electrons. The valence-electron wave functions are orthogonal to core-electron wave functions. All-electron DFT methods treat core and valence electrons on an equal footing. In the pseudopotential approach, ion cores are considered frozen. This means that properties of molecules or solids are calculated on the assumption that the ion cores are not involved in chemical bonding and do not change as a result of structural modifications. All-electron wave functions of valence electrons exhibit rapid oscillations in the core region in order to satisfy the orthogonality constraint. It is impractical to represent such functions using plane waves, as the size of the basis set would be prohibitive. The pseudopotential approximation replaces core electrons and the strong Coulomb potential by a weaker pseudopotential that acts

on a set of pseudo wave functions. This potential can be represented with only a small number of Fourier coefficients. Pseudo wave functions ideally should have no nodes inside the core regions and thus they only require a small basis set. It is now well known that the combination of the power of plane wave technology and the pseudopotential concept is extremely useful for the description of chemical bonding (Srivastava and Weaire, 1987). Two different types of pseudopotential are available: ultrasoft, which is the preferred option as it allows the calculation to be performed at a lower energy cut-off, and Norm-conserving which is typically harder and therefore more computationally expensive than ultrasoft pseudopotentials. In the ultrasoft pseudopotential, introduced by Vanderbilt (Vanderbilt, 1990), pseudo-wave-functions are allowed to be as soft as possible within the core region so that the cutoff energy can be reduced dramatically. Ultrasoft potentials have another advantage besides being much softer than the norm-conserving potentials. The generation algorithm guarantees good scattering properties over a pre-specified energy range, which results in much better transferability and accuracy of the pseudopotential. USP usually also treats shallow core states as valences by including multiple sets of occupied states in each angular momentum channel. This also adds to high accuracy and transferability of the potentials, although at a price of computational efficiency.

4. Basis set: The basis set specifies the quality of the plane wave basis set including the plane-wave energy cut-off, FFT grid specification and finite basis set correction. FFT grid parameters are chosen such that they provide a good representation of the electron density. At the precise level, an exact representation of the density is provided for the given energy-cutoff. At standard level, which has been used in our calculation, a reduced FFT grid is used to speed up the calculation.
5. k-points: The k-points determine the accuracy of the Brillouin zone sampling [Monkhorst-Pack k-points]. The quality of k-point sampling is particular important for metallic system, where rapid changes in the electronic structure may occur along the energy band that crosses the Fermi-level. In our calculations, k-point was set to 2×2×2.

6. SCF: Self-consistent field (SCF) specifies the scheme that is used for electronic minimization. In these calculations, density mixing is recommended for variable occupancy calculations. Mixing schemes specify the method used for mixing the input densities and output densities from the current iteration to obtain the input density for the next iteration in the iterative solution for the SCF. The Pulay mixing method was chosen as the output density is mixed with densities from a number of previous iterations, leading to more rapid convergence.

4. PYRIDINE ADSORPTION AND REACTION ON Mo(110) AND C/N-Mo(110): EXPERIMENT AND MODELING

4.1 Introduction

Pyridine has been widely used as a probe molecule for fundamental studies that involve understanding basic organonitrogen adsorption (and desorption) phenomena, decomposition mechanisms, bonding configurations (number and type of bonds) and chemical transformations on catalyst surfaces (Andersson and Uvdal, 2001; Avouris and Demuth, 1981; Avouris et al., 1984; Bader et al., 1986; Bandy et al., 1979; Cohen and Merrill, 1990; Davies and Newton, 2003; DiNardo et al., 1984; Gland and Somorjai, 1973; Grassian and Muetterties, 1986; Grassian and Muetterties, 1987; Johnson and Muetterties, 1983; Johnson et al., 1985; Lopinski et al., 1998; Mate et al., 1988; Netzer and Mack, 1983a; Netzer and Mack, 1983b; Netzer et al, 1988; Serafin and Friend, 1989; Wexler et al., 1982; Whitten, 2003; Young et al., 2003). Three different adsorption configurations that are coverage dependant were identified through these studies; parallel to the surface at low coverages with an adsorption mode of (η^6-Py-0°) (Avouris and Demuth, 1981; Cohen and Merrill, 1990; Davies and Newton, 2003; DiNardo et al., 1984; Grassian and Muetterties, 1986; Whitten, 2003), perpendicular or inclined at high coverages (η^1(N)-Py-90°) (Avouris and Demuth, 1981; Bader et al., 1986; Cohen and Merrill, 1990; Davies and Newton, 2003; DiNardo et al., 1984; Grassian and Muetterties, 1986; Grassian and Muetterties, 1987; Johnson et al., 1985; Netzer and Mack, 1983a; Serafin and Friend, 1989 ; Whitten, 2003), and through α-pyridyl species formation, which requires bond formation between the nitrogen and an adjacent carbon with the metal surface (η^2(N, C2)-Pyridyl) (Davies and Newton, 2003; DiNardo et al., 1984; Grassian and Muetterties, 1986; Johnson et al., 1985; Serafin and Friend, 1989; Wexler et al., 1982). While these studies have provided information regarding pyridine adsorption on other metal surfaces, pyridine adsorption and denitrogenation on molybdenum-based catalyst surfaces is poorly understood.

In this work, the molecular adsorption and surface reaction of pyridine on Mo(110) is studied using temperature-programmed desorption, Auger electron spectroscopy, high-resolution electron energy loss spectroscopy, and density-functional theory calculations. The Mo(110) surface was chosen because of its industrial applicability in hydrotreating reactions, and it is the most thermodynamically stable face limiting the effects of surface reconstruction on the observed adsorption and decomposition of pyridine (Serafin and Friend, 1989). By investigating pyridine adsorption over a wide range of surface coverages and temperatures, the experimentally determined modes of molecular adsorption and surface decomposition will be compared with *ab initio* calculations to study the structure-reactivity relationship. Additionally, the effect of carbon/nitrogen overlayers will be studied to determine the effect of surface modification on molecular adsorption and reactivity.

4.2 Experimental Results

4.2.1 Pyridine Adsorption and Decomposition on Mo(110)

The Mo(110) surface was cleaned using a combination of argon sputtering and annealing. Low-energy electron diffraction and Auger electron spectroscopy were used to confirm the crystallographic orientation and a contaminant-free surface prior to TPD analysis, respectively. Trace quantities of bulk oxygen were observed, however this has little influence on pyridine adsorption (Davies and Newton, 2003). Temperature programmed desorption spectra for pyridine adsorption on Mo(110) were collected by monitoring and recording the intensity variation of several mass fragments (*m/z* ratios) over the range of 2 to 87 to detect desorption products. The Mo(110) crystal was initially cooled using liquid nitrogen to approx. 100 K and resistively heated to 1000 K with a temperature gradient of 2 K s^{-1}. To clarify the molecular adsorption mode of pyridine on clean Mo(110) and to elucidate adsorption behavior at low and high surface coverages, TPD spectra were collected at 0.5, 1, 2, 5 and 10 Langmiur exposures (1 L $\equiv 1\times10^{-6}$ torr sec). Each TPD experiment was repeated at least twice with several repeated in triplicate, where the quoted uncertainty in the temperature measurement reflects the approximate average desorption temperature differences during repeat analysis. The low temperature physisorption energetics (heat of sublimination) were characterized using leading edge analysis. The adsorption energy for each high temperature molecular desorption feature was calculated using the Redhead equation (Redhead, 1962), assuming first-order desorption behavior and a pre-exponential factor of $\nu = 1\times10^{13}$ s^{-1}. The uncertainties associated with the adsorption energies were calculated based on the average temperature difference of ± 10 K between repeat TPD analyses, and do not reflect the overall uncertainty associated with the Redhead equation (Redhead, 1962). The most significant uncertainty associated with the Readhead equation lies with the value of the pre-exponential factor, and this value was not explicitly determined in this study.

Figure 4.1 shows the TPD spectra for the principal mass-to-charge ratio of pyridine (m/z =79) as a function of pyridine exposure on clean Mo(110). Table 4.1 lists the calculated adsorption energies for each desorption feature. The low coverage TPD spectrum at 0.5 L shows a single pyridine first-order molecular desorption feature at a temperature of 375 ± 10 K (E_{ads} = 23.5 ± 0.6 kcal mol^{-1}). The pyridine TPD spectrum at 1 L suggests two molecular desorption peaks, although additional peaks may be fit to the data depending on the criteria used to describe the features. Assuming two broad first-order desorption features are present, the low temperature peak is centered near 370 ± 10 K (E_{ads} = 23.2 ± 0.6 kcal mol^{-1}) at a temperature similar to that observed at 0.5 L, while the high temperature molecular desorption peak is at approximately 530 ± 10 K (E_{ads} = 33.6 ± 0.6 kcal mol^{-1}). As the pyridine exposure is increased to 2 L, a low temperature physisorption feature at 240 ± 10 K is evident indicating surface saturation, in addition to similar molecular desorption features centered at 330 ± 10 K (E_{ads} = 20.6 ± 0.6 kcal mol^{-1}) and 440 ± 10 K (E_{ads} = 27.7 ± 0.6 kcal mol^{-1}). As the exposure is increased beyond saturation, the pyridine molecular desorption peaks are much less defined as the shoulder of the multilayer physisorption feature begins to convolute with these features. Consequently, no attempt was made to identify the exact temperatures of these molecular desorption peaks at 5 L and 10 L.

The TPD spectra at higher pyridine doses of 5 and 10 L are dominated by a strong pyridine multiplayer physisorption peak at 255 ± 10 K and 260 ± 10 K, respectively. These low-temperature multilayer features clearly exhibit zero-order desorption kinetics. A simple leading edge analysis of all multilayer desorption features (2, 5, and 10 L) yields a pyridine heat of sublimation of 10.3 kcal mol^{-1} assuming $\nu = 1\times10^{24}$. This is in excellent agreement with the literature value of 10.4 kcal mol^{-1}.

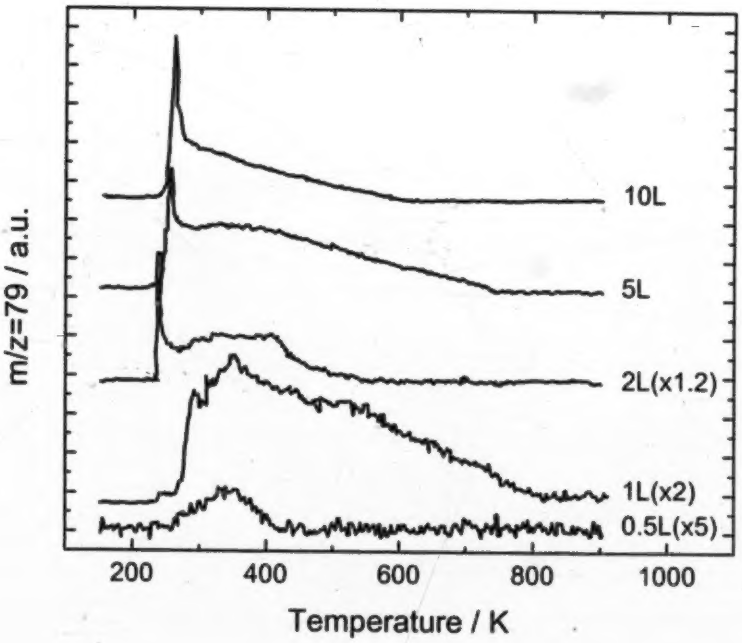

Figure 4.1 Temperature Programmed Desorption (TPD) spectra of pyridine (*m/z* = 79) as a function of pyridine exposure on clean Mo(110).

Additionally, the zero-order analysis is consistent with the slight temperature increase observed as a function of pyridine exposure (240 – 260 K). While the low temperature features are an indication of surface saturation resulting from multilayer desorption, the energetics of multilayer desorption do not provide essential information about pyridine molecular adsorption and surface reaction.

Table 4.1 Summary of Pyridine TPD Features.

Pyridine Dose (Langmiur)	Peak Temperature ± 10 (K)	Adsorption Energy ± 0.6 (kcal mol^{-1})
0.5	375	23.5[a]
1.0	370	23.2[a]
1.0	530	33.6[a]
2.0	240	10.4[b]
2.0	330	20.6[a]
2.0	440	27.7[a]
5.0	255	10.4[b]
10	260	10.4[b]

[a] The adsorption energy (heat of adsorption) was calculated assuming first-order desorption and a pre-exponential factor of $\nu = 1\times10^{13}$.

[b] The adsorption energy (heat of sublimination) was calculated with a leading edge analysis and a pre-exponential factor of $\nu = 1\times10^{24}$.

The only additional gas phase product detected during pyridine TPD on clean Mo(110) was dihydrogen. Figure 4.2 shows temperature programmed desorption spectra for dihydrogen ($m/z = 2$) as a function of pyridine exposure, and includes 1, 5, and 10 L pyridine doses. At low exposures, one desorption peak is observed at 465 ± 10 K, while at 5 L, the desorption peak intensifies and shifts to a lower temperature of 350 ± 10 K. A further increase in pyridine exposure to 10 L suggests two possible desorption peaks for dihydrogen at 375 ± 10 and 540 ± 10 K, respectively. Similar behavior has been previously observed and reported during pyridine TPD (Serafin and Friend, 1989), in

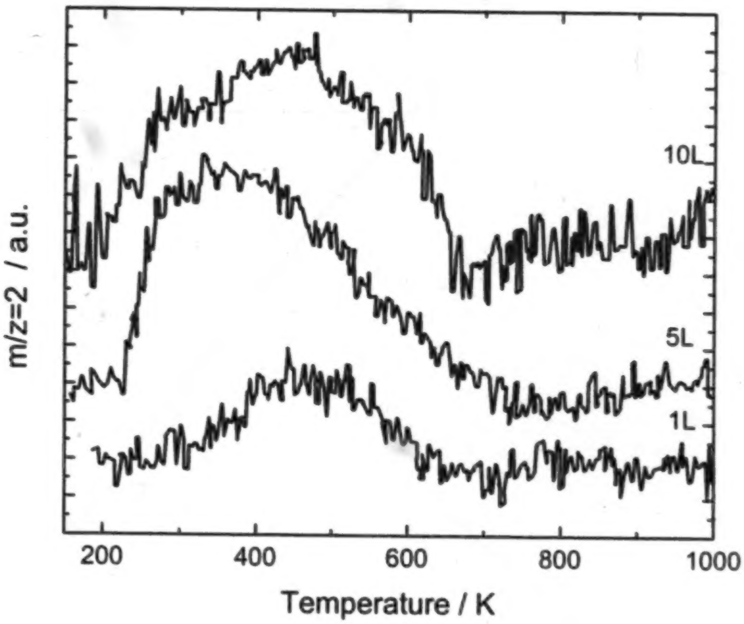

Figure 4.2 Temperature Programmed Desorption (TPD) spectra of hydrogen ($m/z = 2$) as a function of pyridine exposure on clean Mo(110).

which one desorption peak of dihydrogen was observed at low coverages and two unresolved peaks at high coverages are evidenced. The detection of desorbing dihydrogen indicates partial pyridine decomposition on the clean metal surface without the generation of additional desorbing reaction products. While gas phase dihydrogen was detected during TPD, it should be noted the mass spectrometer signal was weak.

4.2.2 Pyridine Adsorption and Decomposition on C/N-Mo(110)

To further study pyridine surface decomposition, a series of sequential TPD experiments were conducted by dosing clean Mo(110) with increments of pyridine, followed by acquisition of TPD spectra. AES measurements were taken between TPD experiments to quantify the residual nitrogen and carbon left behind on the C/N-Mo(110) surface. These experiments were performed to determine the extent of pyridine decomposition on Mo(110), and the subsequent effects of carbon and nitrogen accumulation on adsorption energetics and reaction products.

The effect of multiple pyridine TPD analyses over Mo(110) at 1 L exposures, as shown in Figure 4.3(a), suggest a slight increase in the pyridine TPD peak temperature. However, there was no detection of any decomposition products, including hydrogen, for the TPD experiments on the C/N-Mo(110) surface. A similar TPD spectrum was collected at higher pyridine doses (5 L, 10 L) as a function of consecutive exposure as shown in Figures 4.3(b) and 4.3(c), respectively. The intensity of the low-temperature desorption peak (physisorption) showed an increase as per the measured peak height at 260 ± 10 K. Pyridine molecular desorption on the C/N-Mo(110) surface showed a linear increase as a function of sequential dosage based on the integrated peak area after subtracting the physisorption peak area.

4.2.3 C/N Surface Accumulation

Following each sequential TPD experiment, the surface composition was analyzed by Auger electron spectroscopy to quantify carbon and nitrogen accumulation from the decomposition of pyridine. Figures 4.4a and 4.4b present the percent (atomic) of surface carbon and nitrogen relative to molybdenum. These atomic concentrations were calculated from the AES line intensities using the relative sensitivity factor for each

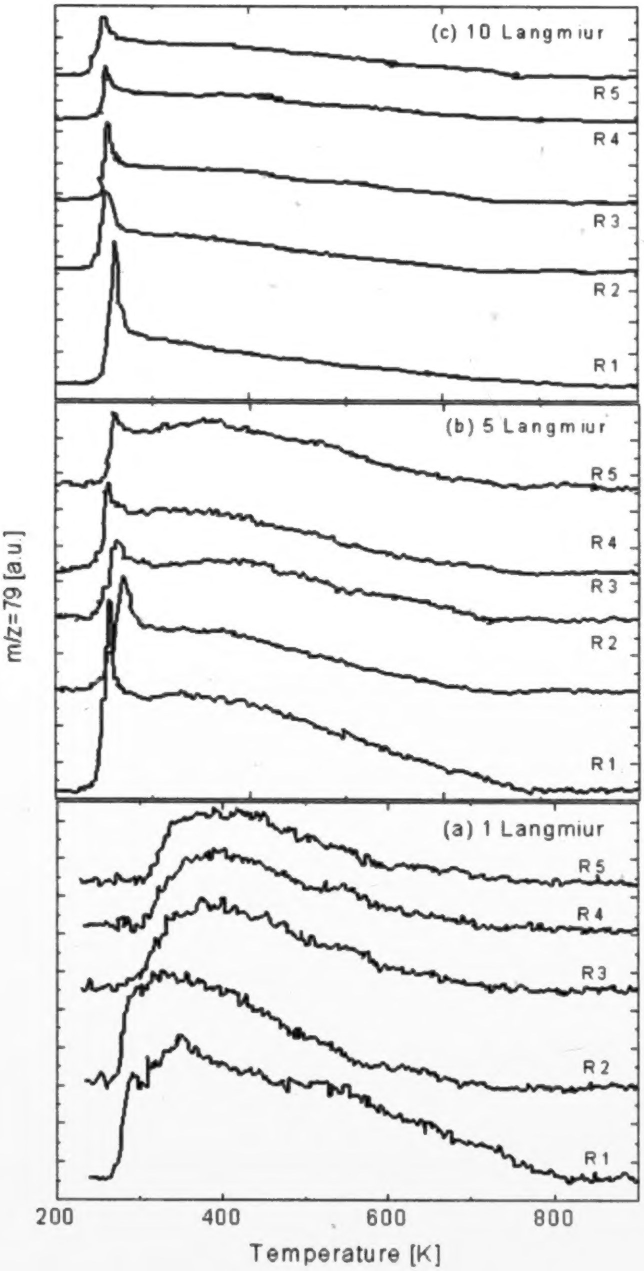

Figure 4.3 Temperature Programmed Desorption (TPD) spectra of pyridine (m/z = 79) for five consecutive pyridine doses on Mo(110). (a) 1 L; (b) 5 L; (c) 10 L.

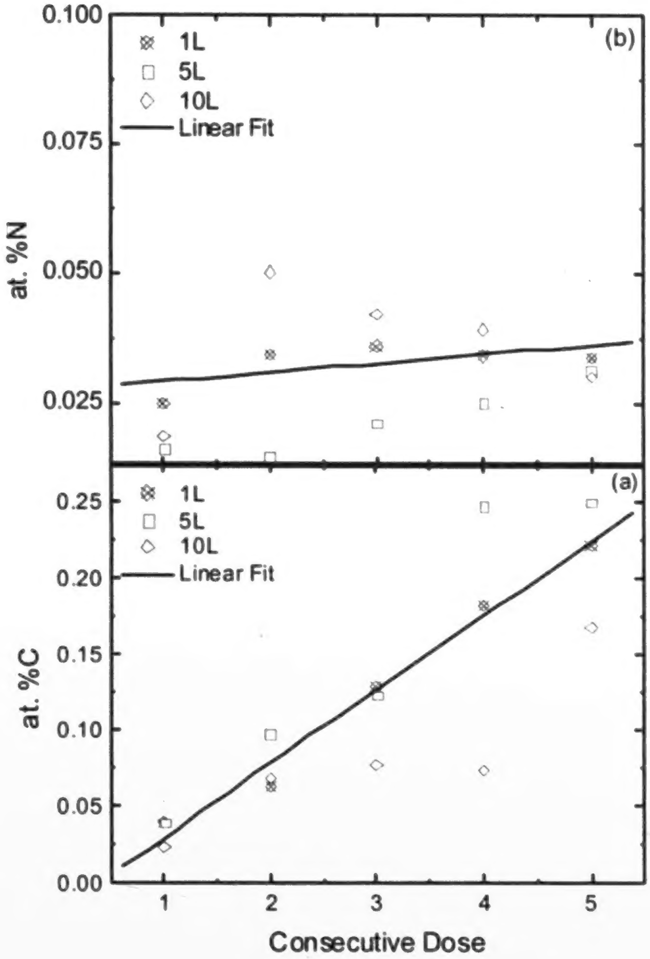

Figure 4.4 Atomic percent of surface contamination on Mo(110) as a function of consecutive pyridine TPD experiments. (a) at.% carbon; (b) at.% nitrogen.

element at 1.5 kV (0.257 for carbon, 0.470 for nitrogen, and 0.392 for molybdenum) (Davis et al., 1978). Surface carbon at 1, 5 and 10 L pyridine exposures showed an overall linear increase as a function of consecutive pyridine dosages. Nitrogen accumulation on the surface initially undergoes a slight increase, and then remains nearly constant for subsequent pyridine doses. Neither ammonia (m/z = 17) nor nitrogen (m/z = 28) were detected as desorbing species (Boudart et al., 1981; Whitten, 2003); therefore, nitrogen either diffused into the bulk (Chen, 1996) or the desorbing nitrogen products were below the sensitivity of the mass spectrometer used in the present study. The local bonding environment of surface carbon may be distinguished by considering AES line shapes (Goodman, 1982), leading to the identification of carbidic or graphitic surface carbon species. Examination at the carbon *KLL* Auger line-shape (Figure 4.5) suggests the surface carbon forms a carbidic surface, similar to the features observed for prepared Mo(110) carbide surfaces (Goodman, 1982; Robbie et al., 2001). LEED patterns of the contaminated surface indicated (1 × 1) hexagonal periodicity with a slight broadening of the spots, and did not suggest an ordered carbidic surface structure, such as a $p(4x4)$ molybdenum carbide surface (He et al., 1992; Jentz et al., 1995; Roe and Schulz, 1998; Roe and Schulz, 2000). These ordered carbidic surfaces often demonstrate higher catalytic activities; however, the increase in pyridine molecular desorption in the subsequent TPD experiments indicates the C/N-Mo(110) surface is less active for pyridine decomposition.

4.2.4 High-Resolution Electron Energy Loss Spectroscopy

Figure 4.6 shows the electron energy loss spectrum of pyridine adsorbed on Mo(110) surface at 0.5 L surface exposure as a function of the surface temperature recorded using a double-pass 127° monochromator. The EELS spectrum is characterized by an elastic peak with 3.2×10^{04} cps and a FWHM (Full Width at Half Maximum) resolution of 65 cm^{-1}, which is larger than the instrumental resolution (30 cm^{-1}). Vibrational frequencies were collected up to 5000 cm^{-1}, however, since there were no features observed beyond 3100 cm^{-1} all EELS figures are truncated at 3500 cm^{-1}.

At low temperature (100 K) the EELS spectrum give loss peaks at 688, 962, 1386, 1447, 1562, 1627, 2962, and 3062 cm^{-1}. As the surface temperature increases to 200 K,

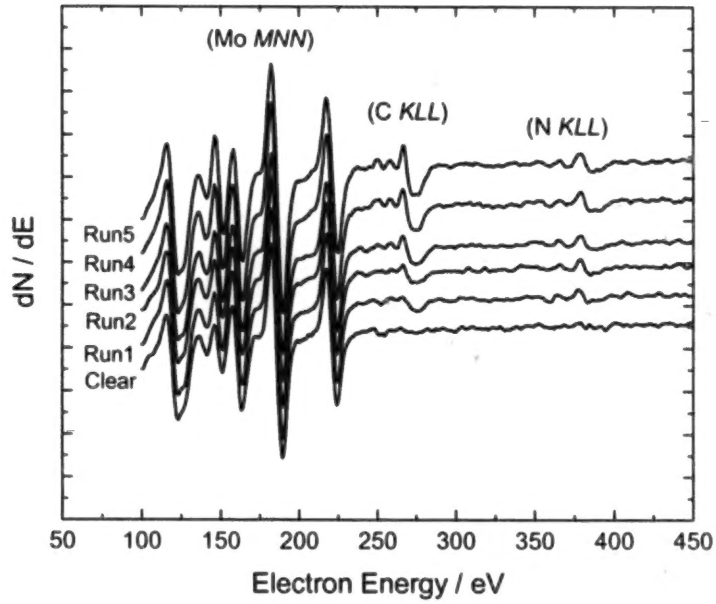

Figure 4.5 Auger spectra of clean Mo(110) and C/N-Mo(110) as a function of consecutive 1 L pyridine TPD experiments. The spectra are normalized to the Mo *MNN* (186 eV) peak, and baseline adjusted to clearly show the C *KLL* (272 eV) and N *KLL* (386 eV) Auger peaks.

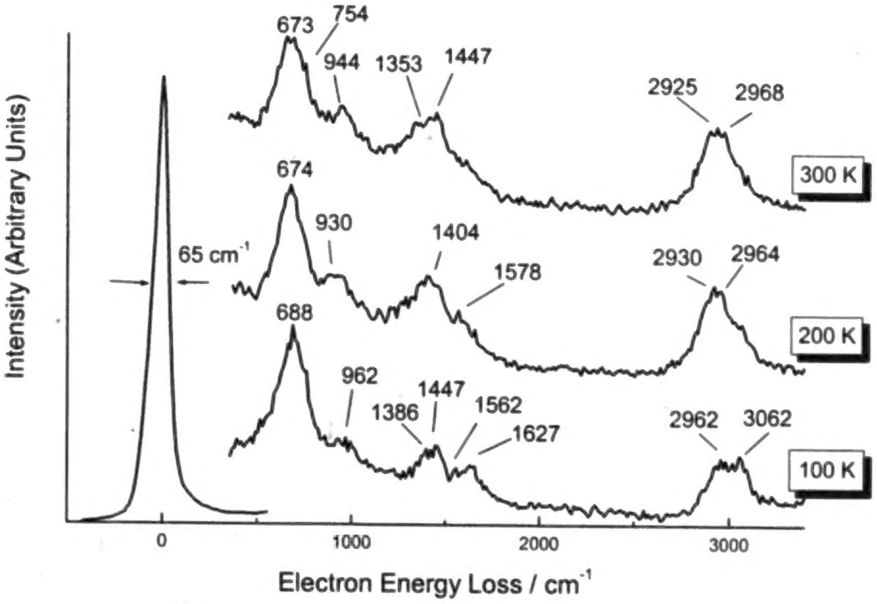

Figure 4.6 Electron energy loss spectra of pyridine adsorbed on Mo(110) at surface exposure of 0.5 L as a function of temperature 100, 200, and 300 K.

the EELS peak intensity decreased, and the frequencies shifted to lower peak losses. The observed loss peaks at 200 K were at 674, 930, 1056, 1219, 1404, 1578, 2930, and 2964 cm^{-1}. Comparing the spectra at 100 and 200 K, the first loss peak at 688 cm^{-1}, which is the predominate peak within the spectrum shifted to 674 cm^{-1}, while the loss peak at 962 cm^{-1} (100K) started to intensify at 200 K and shifted to a lower value of 930 cm^{-1}. At the range of 1386 – 1627 cm^{-1}, four peaks were observed for the 100 K spectrum, while only two loss peaks at 1404 and 1578 cm^{-1} are identified at 200 K. The loss feature at 1404 cm^{-1} is more resolved while the other peak at 1578 cm^{-1} is less pronounced. The last two peaks at higher frequencies showed a reduction in their losses compared to the spectrum obtained at 100 K. The EELS spectrum collected at 300 K showed lower intensity than at 100 or 200 K at the same surface exposures, but with more defined peak losses. The 962 cm^{-1} loss peak at 100 K shifted to 944 cm^{-1} and is more clearly defined at 300 K, while the peak losses over the range of 1404 – 1578 cm^{-1} started to combine forming a broad peak at lower wavenumbers. One additional loss peak started to evolve at 754 cm^{-1} at 300 K, as well.

Figure 4.7 shows electron energy loss spectra of adsorbed pyridine over Mo(110) surface exposure of 1 L at 100, 200, and 300 K. The EELS spectra as a function of increasing temperature did not change from 0.5 L exposure, with the notable exception that the spectrum intensity decreases as the surface temperature increases. The resolution of EELS spectra showed 70 cm^{-1} FWHM with an elastic peak of 2.86 × 10^{04} cps. The peak losses at 100 K were 722, 988, 1155, 1233, 1457, 1639, and 3065 cm^{-1}. Similarly to 0.5 L exposure, the low temperature exposure at 1 L showed four different loss peaks over a range of 1155 – 1639 cm^{-1} that combined to less resolved two peak losses at 1366 and 1446 cm^{-1} at 300 K. The one loss peak at 3065 cm^{-1} at 100 K started to split into several unresolved peaks, which is assigned into two loss peaks at 2924 and 3040 cm^{-1}.

EELS spectra were also collected at saturation exposures of 2 L, as determined by the onset of a physisorbed peak in the previous temperature programmed desorption spectra (Figure 4.1). Figure 4.8 shows the electron energy loss spectra of pyridine over Mo(110) surface at 2 L exposure with an elastic peak resolution of 65 cm^{-1} and intensity of 3.2 × 10^{04} cps. As expected, the loss features at low temperature (100 K) showed further loss peaks comparing to 0.5 and 1 L exposures due to saturation coverage; loss

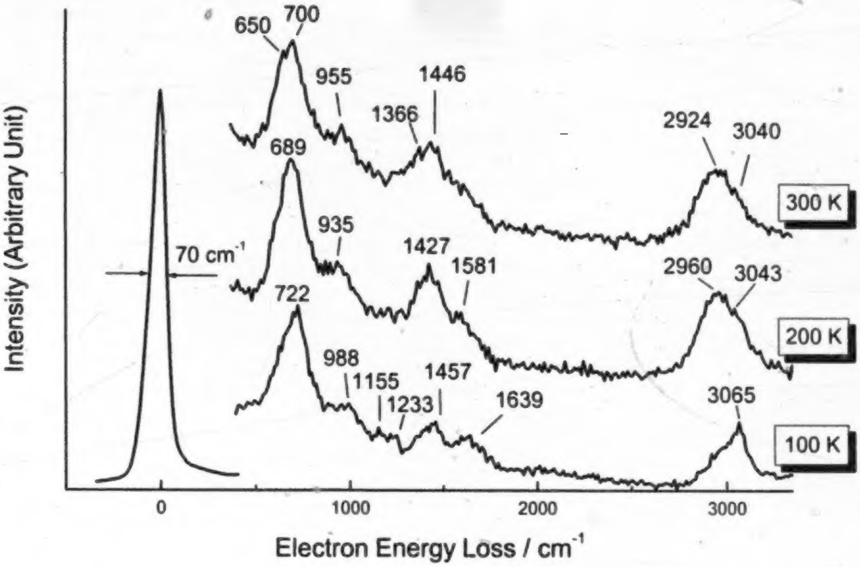

Figure 4.7 Electron energy loss spectra of pyridine adsorbed on Mo(110) at surface exposure of 1 L as a function of temperature 100, 200, and 300 K.

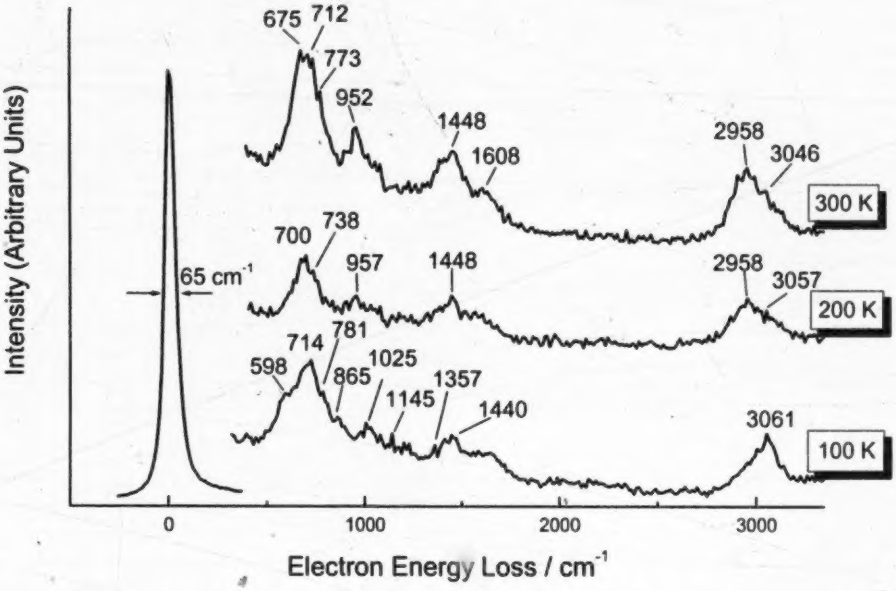

Figure 4.8 Electron energy loss spectra of pyridine adsorbed on Mo(110) at surface exposure of 2 L as a function of temperature 100, 200, and 300 K.

peaks were observed at 598, 714 and 781 cm^{-1} within the low temperature spectra. The general features as a function of increasing surface temperature did not change from the other surface exposures. The 300 K spectrum shows a very distinct peak loss at 955 cm^{-1} compared to other surface exposures (0.5 and 1 L).

The identification of an adsorbed species and the adsorption configuration relies on the knowledge of the vibrational spectrum, as well the dipole selection rules in dipole scattering on surfaces. Only dipole moments normal to the surface give rise to significant dielectric scattering, therefore, the application of these selection rules allows one to draw conclusions about the adsorption geometry of a molecule. In general, there are two distinct classes of molecular vibrations concerning cyclic molecules, stretching and bending. Stretching vibrations change the bond length while bending vibrations change the bond angle. These two classes may be subdivided into different types depending on how the atoms move relative to each other. For pyridine, the possible vibrational modes are represented by out-of-plane (oop) ring distortion, in-plane (inp) ring breathing, C–H oop bending, C–H inp bending, C–C stretching, C–N stretching, and C–H stretching. Vibrations of bonds involving hydrogen are an especially important diagnostic tool because atoms of low mass vibrate faster. Table 4.2 summarizes all of the observed EELS frequencies of pyridine over Mo(110) at 0.5, 1.0, and 2.0 L exposures and their assignment mode corresponding to pyridine liquid phase vibrational frequencies (Corrsin et al., 1953; Wiberg et al., 1984). Due to the limited resolution of the EELS spectra, the observed EELS frequencies of pyridine have been assigned to more than one pyridine vibrational mode.

4.3 Molecular Simulation

4.3.1 Pyridine Electronic Structure

Pyridine adsorption on Mo(110) was modeled to describe the possible adsorption modes giving rise to the molecular desorption features observed in the TPD analysis, and to suggest potential structural and bonding changes during adsorption. The electronic structure of the pyridine molecule was initially analyzed to understand and its chemical reactivity behavior. Figure 4.9a shows the electrostatic potential map of pyridine

Table 4.2 Vibrational frequencies and assignments for the electron energy loss spectra of pyridine over Mo(110)

Description	**$C_5H_5N^a$**	**$C_5H_5N^b$**	**Pyridine-Mo(110) – 0.5 L**			**Pyridine-Mo(110) – 1 L**			**Pyridine-Mo(110) – 2 L**		
	Liquid Phase	Liquid Phase	100 K	200 K	300 K	100 K	200 K	300 K	100 K	200 K	300 K
oop ring distortion	403	405	...	...	...	...	...	...	...	...	...
inp ring breathing	601	604	...	...	...	...	...	...	598	...	...
inp ring breathing	652	653	688	674	673	...	689	650	...	...	675
CH oop bending	700	703	688	674	673	722	689	700	714	700	712
CH oop bending	744	749	...	...	754	722	...	...	781	...	773
oop ring distortion	936	981	962	930	944	...	935	955	865	957	952
inp ring breathing	991	991	962	...	...	988	...	955	...	957	952
oop ring distortion	1007	...	...	...	...	988	...	...	1025	...	...
Inp ring breathing	1032	1030	...	...	...	...	...	...	1025	...	...
CH inp bending	1072	1068	...	...	...	...	...	...	...	...	...
CH inp bending	1079	...	...	...	...	...	...	...	...	...	...
CH inp bending	1143	1148	...	...	...	1155	...	...	1145	...	...
CH inp bending	1218	1217	...		...	1233	...	...	...	...	...
CH inp bending	1227	...	...		...	...	...	...	...	...	...
CC, CN stretch	1362	1357	1386	1404	1353	...	...	1366	1357		...
CC, CN stretch	1442	1441	1447	1404	1447	1457	1427	1446	1440	1448	1448
CC, CN stretch	1483	1482	1447	...	1447	1457	...	1446	1440	1448	1448
CC, CN stretch	1581	1582	1562	1578	...	...	1581	...	...	...	...
CC, CN stretch	1583	1599	1627	1578	...	1639	...	...	...	...	1608
CH stretch	3030	2960	2962	2930	2925	3065	2960	2924	...	2958	2958
CH stretch	3042	3004	3062	2964	2968	3065	3043	3040	3061	3057	3046
CH stretch	3072	3036	3062	2964	2968	3065	3043	3040	3061	3057	3046
CH stretch	3087	3055	3062	2964	2968	3065	3043	3040	3061	3057	3046
CH stretch	3094	3083	3062	2964	2968	3065	3043	3040	3061	3057	3046

[a](Wiberg et al., 1984), [b](Corrsin et al., 1953)

(C_5H_5N). The five hydrogen atoms represent regions that repel a positive ion and are the most electron-poor regions, where the nitrogen atom is the most electron-rich region and is susceptible to positive ion attraction. Intermediate potentials are scattered between these two regions. Electrostatic potential information helps to identify the chemical region or functional group that is most chemically active, and in the case of pyridine the nitrogen atom is the most electron-rich region suggesting a possible location for adsorption.

The electrophilic and nucleophilic Fukui functions of pyridine, which represent the most reactive regions for bond formation with the catalyst active sites on the surface, are shown in Figure 4.9b. Pyridine can act as a nucleophile, forming a bond with the catalyst surface (electrophiles) by donating a pair of electrons by electrophilic attack through the nitrogen lone-pair. In contrast, nucleophilic attack (accepting electrons) can occur above and below the ring plane around the nitrogen and the opposite carbon atoms. In this case, pyridine will accept electrons from a negatively charged species (nucleophiles) on the catalyst surface and form a chemical bond. Thus, two pyridine adsorption modes are possible. The first is directly atop a surface site through the highest occupied molecular orbital (HOMO) where the nitrogen atom has the highest probability to donate electrons and therefore form a bond with the catalyst active site by electrophilic attack. The other possibility, parallel to the surface through the lowest unoccupied molecular orbital (LUMO), can occur when electrons are transferred by nucleophilic attack and form a bond with adsorption site. This is significant since Mo(110) may act as either an electrophile or a nucleophile depending on the nature of the adsorbate molecule (Conrad, et al., 1976; Demuth and Eastman, 1974).

4.3.2 Pyridine Adsorption on Mo(110)

The relative energies of pyridine adsorption on Mo(110) calculated to quantify the adsorption energies of the possible molecular adsorption modes (Table 4.3). The inter-atomic bond lengths and the inter-atomic angles were determined to provide an indication of ring deformation (Table 4.4 and Table 4.5, respectively). Figure 4.10 shows an overview of the initial bonding modes and the optimized configurations. The adsorption modes studied include: parallel adsorption η^1(N)-Py-0° (structure Py1), μ_2,η^1(N)-Py-0°

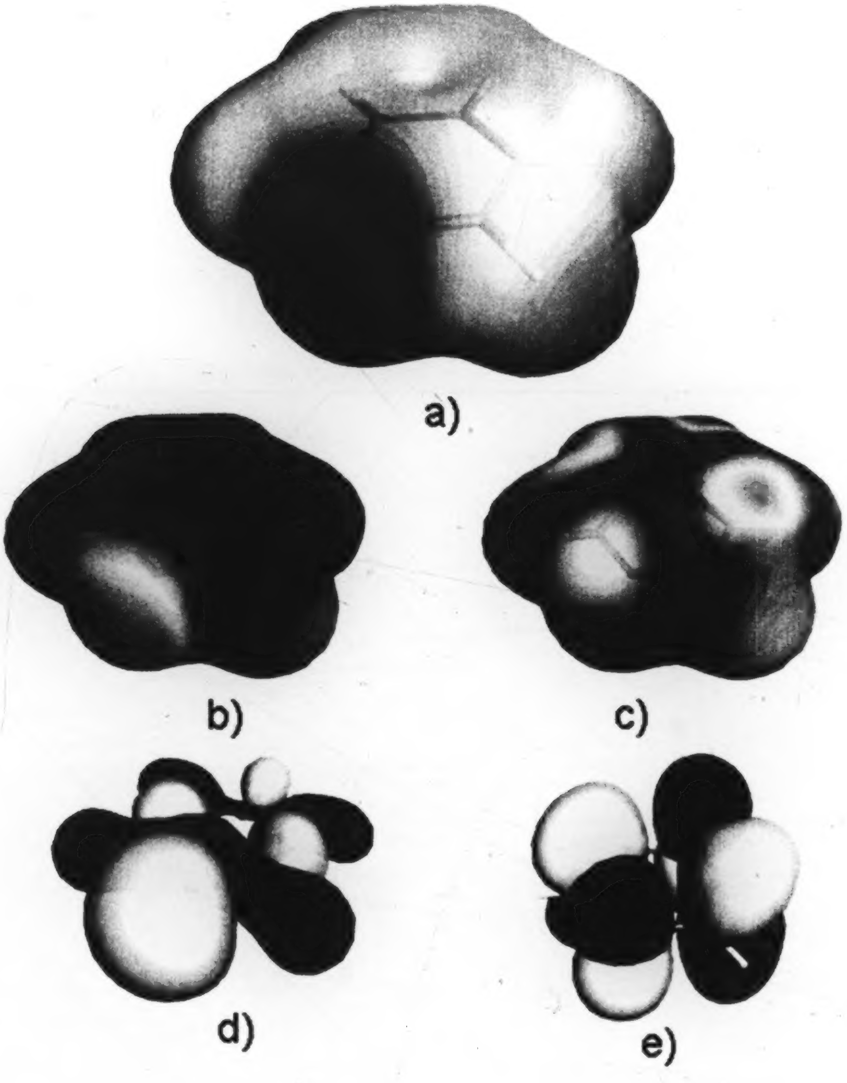

Figure 4.9 Electronic structure properties of pyridine simulated by density functional theory (GGA-PBE pesudo-potential) with 0.02 isosurface, a) Electrostatic Potential Map, b) Electrophilic Fukui function, c) Nucleophilic Fukui function, d) HOMO, and e) LUMO.

(structure Py5), η^6-Py-0° (structure Py7); titled adsorption η^1(N)-Py-30° (structure Py2) and η^1(N)-Py-45° (structure Py3); and perpendicular adsorption η^1(N)-Py-90°(structure Py4), $\mu_{2,}\eta^1$(N)-Py-90° (structure Py6), $\mu_{3,}\eta^1$(N)-Py-90°(structure Py8), $\mu_{2,}\eta^2$(N, C2)-Pyridyl (structure Py9) and η^1(C2)-Pyridyl (structure Py10). These initial geometries reflect the most prevalent pyridine adsorption modes in organometallic chemistry (Sanchez-Delgado, 2002), as well as the many proposed tilted bonding geometries (Avouris and Demuth, 1981; Bader et al., 1986; Netzer and Mack, 1983a; Whitten, 2003) on metal surfaces. Pyridine and the Mo(110) surface were fully optimized prior to adsorption calculations.

Table 4.3 Summary of Pyridine DFT Adsorption Energies

Notation	Optimized Bonding Mode	Adsorption Energy (kcal mol^{-1})
Py1	$\mu_{2,}\eta^2$(N,C4)-Py-0°	-27.2
Py2	η^1(N)-Py-26.5°	-6.9
Py3	η^1(N)-Py-46.2°	-9.1
Py4	η^1(N)-Py-90°	-15.1
Py5	μ_3,η^3(N,C3,C5)-Py-0°	-35.6
Py6	η^1(N)-Py-90°	-12.5
Py7	η^6-Py-0°	-17.4
Py8	η^1(N)-Py-72°	-9.7
Py9	μ_2,η^2(N,C2)-Pyridyl	-21.7
Py10	η^2(N,C2)-Pyridyl	-23.9

Pyridine adsorption as a function of plane angle to the Mo(110) surface was investigated with the N-atom directly atop a Mo-atom. The plane parallel to the Mo(110) surface (structure Py1) indicated the highest adsorption energy with a value of -27.2 kcal mol^{-1}. Following geometrical optimization, the pyridine forms two bonds with the metal surface through the nitrogen atom and a carbon atom ($\mu_{2,}\eta^2$(N,C4)-Py-0°). The aromatic plane structure is partially destroyed during optimization, as indicated by the calculated pyridine bond lengths and inter-atomic angles. Tilted pyridine adsorption, represented by structures Py2 and Py3, indicate bonding with the surface occurs only through the nitrogen atom as η^1(N)-Py-26.5° and η^1(N)-Py-46.2° modes with adsorption energies of -6.9 and -9.1 kcal mol^{-1}, respectively. Neither geometries showed deformation of the aromatic ring or the ability to change plane angle with the metal surface. Perpendicular

Table 4.4 Calculated pyridine bond lengths

Notation	Optimized Bonding Mode	N-C2 (Å)	C2-C3 (Å)	C3-C4 (Å)	C4-C5 (Å)	C5-C6 (Å)	C6-N (Å)
	Free Gas Molecule	1.34	1.40	1.40	1.40	1.40	1.34
Py1	μ_2,η^2(N,C4)-Py-0°	1.39(.05)	1.45(0.05)	1.42(0.02)	1.44(0.01)	1.47(0.07)	1.39(0.05)
Py2	η^1(N)-Py-26.5°	1.35(.01)	1.39(-0.01)	1.38(-0.02)	1.39(-0.01)	1.38(-0.02)	1.35(0.01)
Py3	η^1(N)-Py-46.2°	1.35(0.01)	1.38(-0.02)	1.39(-0.01)	1.39(-0.01)	1.38(-0.02)	1.35(0.01)
Py4	η^1(N)-Py-90°	1.34(0.00)	1.38(-0.02)	1.38(-0.02)	1.38(-0.02)	1.38(-0.02)	1.35(0.01)
Py5	μ_3,η^3(N,C3,C5)-Py-0°	1.40(0.06)	1.44(0.04)	1.43(0.03)	1.45(0.05)	1.43(0.03)	1.37(0.03)
Py6	η^1(N)-Py-90°	1.35(0.01)	1.38(-0.02)	1.38(-0.02)	1.38(-0.02)	1.37(-0.03)	1.35(0.01)
Py7	η^6-Py-0°	1.40(0.06)	1.42(0.02)	1.42(0.02)	1.41(0.010	1.42(0.02)	1.41(0.07)
Py8	η^1(N)-Py-72°	1.36(0.02)	1.36(-0.04)	1.39(-0.01)	1.38(-0.02)	1.38(-0.02)	1.36(0.02)
Py9	μ_2,η^2(N,C2)-Pyridyl	1.35(0.01)	1.38(-0.02)	1.38(-0.02)	1.38(-0.02)	1.38(-0.02)	1.35(0.01)
Py10	η^2(N,C2)-Pyridyl	1.33(-0.01)	1.38(-0.02)	1.39(-0.01)	1.39(-0.01)	1.40(0.00)	1.35(0.01)

Table 4.5 Calculated pyridine inter-atomic angles

Notation	**N-C2-C3** ∠	**C2-C3-C4** ∠	**C3-C4-C5** ∠	**C4-C5-C6** ∠	**C5-C6-N** ∠	**C6-N-C2** ∠
Free Gas Molecule	123.9	118.4	118.5	118.4	123.9	116.9
Py1	121.6(-2.3)	118.4	117.7(-0.8)	119.2(0.8)	119.7(-4.2)	118.7(1.8)
Py2	122.1(-1.8)	118.9(0.5)	119.5(1.0)	118.6(0.2)	122.5(-1.4)	118.3(1.4)
Py3	122.5(-1.4)	118.4	119.4(0.9)	118.8(0.4)	122.2(-1.7)	118.2(1.3)
Py4	123.2(-0.7)	118.8(0.4)	118.8(0.3)	119.0(0.6)	122.8(-1.1)	117.4(0.5)
Py5	122.0(-1.9)	116.3(-2.1)	119.3(0.8)	117.8(-0.6)	123.4(-0.5)	117.2(0.3)
Py6	123.0(-0.9)	119.6(0.9)	118.0(-0.5)	118.9(0.5)	124.2(0.3)	116.3(-0.6)
Py7	120.1(-3.8)	120.6(2.2)	118.8(0.3)	118.9(0.5)	122.1(-1.8)	118.8(1.9)
Py8	123.7(-0.2)	119.2(0.8)	118.5	119.7(1.3)	122.5(-1.4)	116.4(-0.5)
Py9	121.9(-2.0)	119.4(1.0)	118.4(-0.1)	120.5(2.1)	119.8(-4.1)	119.8(2.9)
Py10	119.3(-4.6)	118.4	120.7(2.2)	119.6(1.2)	116.8(-7.1)	125.1(8.2)

Model	Initial Geometry	Optimized Geometry	Model	Initial Geometry	Optimized Geometry
Py1	η^{1}(N)-Py-0° 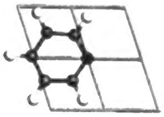	μ_{2},η^{2}(N,C4)-Py-0° 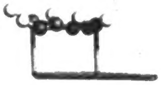	Py6	μ_{2},η^{1}(N)-Py-90° 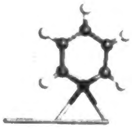	η^{1}(N)-Py-90° 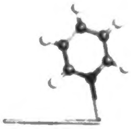
Py2	η^{1}(N)-Py-30° 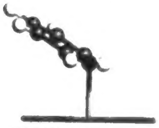	η^{1}(N)-Py-26.5° 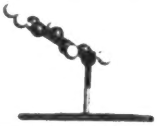	Py7	η^{6}-Py-0° 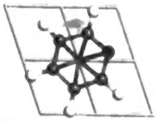	μ_{2},η^{7}-Py-0° 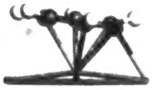
Py3	η^{1}(N)-Py-45° 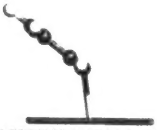	η^{1}(N)-Py-46.2° 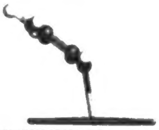	Py8	μ_{3},η^{1}(N)-Py-90° 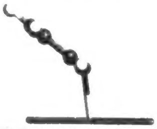	η^{1}(N)-Py-72° 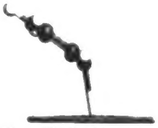
Py4	η^{1}(N)-Py-90° 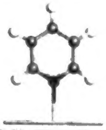	η^{1}(N)-Py-90° 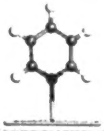	Py9	μ_{2},η^{2}(N,C2)-Pyridyl 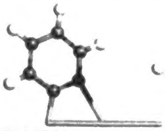	μ_{2},η^{2}(N,C2)-Pyridyl 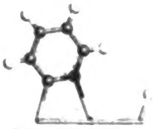
Py5	μ_{2},η^{1}(N)-Py-0° 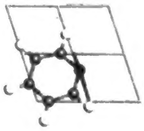	μ_{3},η^{3}(N,C3,C5)- 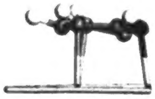	Py10	η^{1}(C2)-Pyridyl-90° 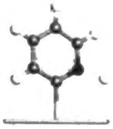	η^{2}(N,C2)-Pyridyl 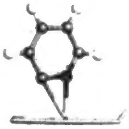

Figure 4.10 Initial and optimized configurations for adsorption sites of pyridine on Mo(110). Py1, Py2, Py3, and Py4 are structures where the nitrogen atom is directly atop of a Mo atom and the molecular plane is tilted to the surface by 0°, 30°, 45°, and 90°, respectively; Py5 and Py6 are parallel and perpendicular adsorption modes where the nitrogen atom is centered at a bridge location between two Mo atoms; Py7 is parallel adsorption with the aromatic ring centered directly above a Mo atom; Py8 is a perpendicular structure with the nitrogen above a Mo 3-fold center; Py9 is an *α*-pyridyl structure with both C and N atop of two Mo atoms; and Py10 is an *α*-pyridyl structure with C atop top of a Mo atom.

adsorption with the pyridine plane 90° to the metal surface (structure Py4) has a higher adsorption energy (E_{ads} = -15.1 kcal mol^{-1}) compared to tilted adsorption.

It was expected the tilted geometries would relax to parallel geometry based on the relative energetics; however, in each case, the angle geometry was confirmed by additional calculations suggesting an energy barrier for the transformation. In order to quantify the energy barrier and identify the possible transition state, the reaction pathway was generated by constructing the minimum energy path between optimized η^1(N)-Py-26.5° (reactant) and $\mu_{2,}\eta^2$(N,C4)-Py-0° (product) geometries using a Linear Synchronous Transit (LST) maximum approach.

The calculation used 10 images along the reaction path, and the convergence tolerance was set to medium quality (0.25 eV/Å). The reaction pathway analysis yielded an apparent energy barrier of 0.37 eV (8.53 kcal mol^{-1}) for the transition from η^1(N)-Py-26.5° to $\mu_{2,}\eta^2$(N,C4)-Py-0°, which quantitatively explains why the tilted geometry does not undergo further relaxation to parallel geometry. At the approximate transition state, the N atom remains directly atop a Mo atom at a bond distance of 2.14 Å and the plane angle is reduced to an apparent critical angle 18.7°. The pyridine η^1(N)-Py-18.7° transition state showed no additional aromatic ring deformation, other than an observed repulsion between the C2 and C6 hydrogen atoms and the Mo(110) surface. It should be noted the calculated energy barrier provides a maximum value for the Mo(110) surface, although lower energy pathways may exist involving other adsorption modes and transition states.

A combination of linear synchronous transit and quadratic synchronous transit (QST) methods were used to find the transition state (TS) for three different reaction pathways starting from complete perpendicular η^1(N)-Py-90° through η^1(N)-Py-46.2° and η^1(N)-Py-26.5° intermediates, followed by further relaxation to $\mu_{2,}\eta^2$(N,C4)-Py-0°. The calculations used 10 images along the reaction path with a convergence tolerance set to fine quality (0.05 eV/Å) with a maximum of 5 QST steps. The activation energies for all three pathways were positive, indicating an activation energy barrier for the transformation. The calculated activation energies were 1.45 eV (33.4 kcal mol^{-1}), 0.36 eV (8.3 kcal mol^{-1}), and 0.19 eV (4.4 kcal mol^{-1}), for 90° to 46.2° then to 26.5° and finally to 0°, respectively. For the last reaction pathway, a difference of 0.18 eV (4.1 kcal mol^{-1}) from the initial calculated value using LST-only approach was observed. Based on these results, it is reasonable to assume small angle tilted adsorbed species might transform to parallel adsorption as the surface temperature is increased.

Pyridine adsorption at a bridging location was studied with the nitrogen initially located equidistant between neighboring Mo atoms and the aromatic ring parallel (structure Py5) and perpendicular (structure Py6) to the surface. During geometry optimization, the nitrogen atom in both geometries relocated on the surface to bond solely to either one of the neighboring Mo atoms. While parallel adsorption showed the aromatic ring structure is weakened and the ring geometry itself is highly deformed leading to the optimized μ_3,η^3(N,C3,C5)-Py-0° bonding mode, perpendicular adsorption forms a bond through the nitrogen atom only and the molecular plane remains perpendicular to the Mo(110) surface. During geometry optimization pyridine rotates and approaches one of the Mo atoms. The calculated adsorption energies for parallel (structure Py5) and perpendicular (structure Py6) adsorption are -35.6 and -12.5 kcal mol^{-1}, respectively. The relatively higher adsorption energy for parallel adsorption at a bridging site is consistent with the previous results obtained for bonding directly atop Mo, and confirms parallel adsorption is energetically favorable in comparison to perpendicular adsorption.

Further comparison between parallel and perpendicular adsorption was studied by modeling the η^6-Py-0° mode with the pyridine ring centered directly atop a Mo atom (structure Py7), and locating pyridine at a three-fold hollow as μ_3,η^1(N)-Py-90° (structure Py8). The adsorption energy of the optimized η^6-Py-0° mode was -17.4 kcal mol^{-1}, and there was also an indication of ring deformation and partial weakening of interatomic bond lengths. Adsorption at a three-fold site was not stable and resulted in the η^1(N)-Py-72° structure with adsorption energy of -9.7 kcal mol^{-1}.

To complete the comprehensive modeling of possible adsorption modes, pyridine adsorption through surface pyridyl species formation was studied perpendicular to the Mo surface. Pyridyl adsorption was modeled using two different initial configurations as μ_2,η^2(C2)-Pyridyl (structure Py9) and η^2(N,C2)-Pyridyl (structure Py10). A proton was abstracted from C2 and bonded on the metal surface adjacent to the pyridyl species. Py9 bonds to the surface as μ_2,η^2(N,C2)-Pyridyl after pyridine rotates as a result of an interaction between carbon and molybdenum, allowing nitrogen to approach the Mo-atom more closely (E_{ads} = -21.7 kcal mol^{-1}). Py10 bonds as η^2(N,C2)-Pyridyl with the surface, resulting in an adsorption energy of -23.9 kcal mol^{-1}. Although the initial position of the N-atom in both Py9 and Py10 was far from the Mo(110) surface, during optimization pyridine rotates to approach the surface to bond through the N-atom in perpendicular geometry. Furthermore, both geometries experienced ring deformation as indicated by the interatomic bond lengths and angles.

Overall, parallel adsorption showed higher adsorption energy in comparison with perpendicular adsorption modes. The calculated adsorption energies were found to increase in the following order; Py2 < Py3 < Py8 < Py6 < Py4 < Py7 < Py9 < Py10 < Py1 < Py5. This observed trend in adsorption energies is primarily the result of increasing interaction through the aromatic ring structure of pyridine with the Mo(110) surface. The relativistic DFT adsorption energietics also suggest two general competitive adsorption modes on Mo(110); namely parallel adsorption (i.e. μ_3,η^6-Py-0°) and perpendicular adsorption (i.e. η^1(N)-Py-90°) depending on surface coverage.

4.3.3 Calculated Vibrational Frequencies of Pyridine Adsorption on Mo(110)

The vibrational frequencies for several of the proposed adsorbed models (Figure 4.10) were calculated and are summarized in Table 4.6. Gas phase pyridine vibrational frequencies were also calculated and are included in the table for further reference. The vibrational frequencies in Table 4.6 are summarized per the assignment mode associated for each calculated frequency. As discussed previously, the first vibrational mode indicates an out-of-plane (oop) ring distortion in a range of 420 – 863 cm^{-1}. For this particular mode (oop ring distortion), parallel configuration (Py5) showed lower frequencies starting at 420 cm^{-1}, while all perpendicular configurations (Py4, Py9, and Py10) showed higher frequencies ranging from 554 – 863 cm^{-1}. For in-plane (inp) ring breathing mode, frequencies were calculated in the range of 605 – 1086 cm^{-1} for all configurations (Py4, Py5, Py9, and Py10). For this particular vibrational mode (inp ring breathing), a clear distinction can be noticed between parallel configuration (Py5) frequencies and perpendicular (Py4, Py9, and Py10) frequencies. While the vibrational frequencies of parallel configuration (Py5) are scattered in the range of 605 – 1025 cm^{-1}, perpendicular models showed no frequencies in the range of 800 – 1000 cm^{-1}. For C–H out-of-plane (oop) bending vibrational mode, parallel configuration (Py5) showed lower frequencies in the range of 1146 – 1317 cm^{-1} in comparison to perpendicular configurations (Py4, Py9, and Py10), which showed frequencies in the range of 1188 – 1455 cm^{-1}. C–H in-plane (inp) bending mode showed a frequency of 1185 and 1181 cm^{-1} for Pyr9 and Py10 configurations, respectively, which were not evident in the Py4 and Py5 configurations. Additionally, parallel configuration (Py5) did not show any C–H inp bending vibrations above 1683 cm^{-1}, while perpendicular configurations (Py4, Py9, and Py10) showed vibrational frequencies up to 1747 cm^{-1}. The C–C and C–N stretching modes within the ring were completely absent in the parallel configuration (Py5) and mostly present in the Py9 model. The final vibrational mode (C–H stretching) was expected to produce five frequencies for a pyridine. Py4 (perpendicular) and Py5 (parallel) models showed five frequencies, while Py9 and Py10 models showed only four frequencies, which is not surprising as one of the carbon atoms lost a hydrogen atom to the surface and bonded to a Mo-atom.

4.4 Discussion

The results from this study indicate that pyridine molecularly adsorbs on Mo(110) and C/N-Mo(110), and decomposes on both surfaces giving rise to surface carbon and nitrogen. Dihydrogen desorption from pyridine decomposition on clean Mo(110) was observed at temperatures below 540 K; however, dihydrogen was not observed desorbing from the C/N-Mo(110) surface and no additional reaction products were detected from either surfaces. The TPD spectra clearly indicate a coverage dependent competitive adsorption process, and this is further supported by the DFT relative energetics and HREELS vibrational frequencies.

4.4.1 Chemisorption of Pyridine on Mo(110)

Serafin and Friend (Serafin and Friend, 1989) studied the adsorption and decomposition of pyridine on Mo(110) at low coverages up to surface saturation. At 0.85

Table 4.6 Calculated frequencies of selected pyridine adsorption configurations

	C_5H_5N	Py4	Py5	Py9	Py10
	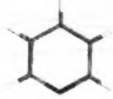	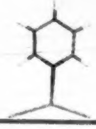	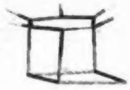	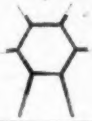	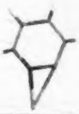
oop ring distortion	406	612	420	554	586
	733	623	755	597	622
	…	863	…	831	828
inp ring breathing.	606	691	605	694	713
	644	705	644	713	739
	977	1011	857	1062	1051
	1041	1086	970	1077	1084
	…	…	1007	…	…
	…	…	1025	…	…
C–H oop bending	675	1188	1146	1220	1252
	838	1211	1201	1283	1384
	940	1339	1246	1341	1408
	969	1375	1280	1357	1430
	…	1418	1317	1398	…
	…	1455	…	…	…
C–H inp bending	1052	1620	1563	1185	1181
	1128	1647	1610	1256	1469
	1209	1710	1635	1647	1637
	1359	1737	1663	1719	1666
	1445	…	1683	1747	1721
C–C, C–N stretching	1304	1277	…	1426	1246
	1478	…	…	1467	…
	1599	…	…	1635	…
	1614	…	…	…	…
C–H stretching	3082	3140	2911	3207	3185
	3084	3156	3097	3262	3217
	3111	3173	3197	3350	3225
	3114	3196	3201	3418	3334
	3148	3232	3247	…	…

of saturation they observed a broad molecular desorption peak at approximately 375 ±10 K. Upon increasing pyridine exposure to saturation, a peak centered at 190 ±10 K appeared; however, this feature was not discussed further. Increasing the pyridine exposure resulted in two additional low-temperature features at 160 ±10 K and 175 ±10 K. The peak at 160 ± 10 K was attributed to the sublimination of multilayers of pyridine and the peak at 175 ± 10 K was attributed to the physisorption of a second layer of pyridine. They also reported dihydrogen gas as the only product to be detected, which is evidenced by a broadening and eventual splitting of two unresolved dihydrogen TPD peaks. At saturation exposures, two dihydrogen desorption peaks were observed at 375 ± 10 K and 595 ± 10 K; however, a multitude of peaks from 375 – 595 ± 10 K were observed depending on pyridine surface coverage. Using additional spectroscopic information from XPS, they concluded pyridine molecularly adsorbs on the surface in more than one configuration, and suggested one possible model is η^1(N)-Py. No further attempt was made to describe the other possible adsorption modes leading to molecular desorption or surface decomposition on Mo(110).

In the present study, pyridine adsorption and decomposition on Mo(110) was studied with TPD from 0.5 to 10 L to quantify the structure-property relationship over a wide range of exposures. At low pyridine exposures (0.5 L), a pyridine desorption feature was observed at 375 ± 10 K (E_{ads} = 23.5 ± 0.6 kcal mol^{-1}), which is in excellent agreement with the previous results of Serafin and Friend (Serafin and Friend, 1989) at 0.85 of saturation. As the exposure is increased to 1 L, a second pyridine desorption feature at 530 ± 10 K (E_{ads} = 33.6 ± 0.6 kcal mol^{-1}) develops, in addition to the first peak at 375 ± 10 K. This high temperature desorption feature is not evident in the 0.5 L TPD spectrum, and was not observed in a previous study at low (below saturation) coverages (Serafin and Friend, 1989). This would suggest that at low pyridine exposures, the high temperature molecular bonding mode undergoes surface decomposition upon heating, as opposed to molecular desorption. The TPD spectra of pyridine exposures over 2 L show a sharp physisorption feature, which is attributed to multilayer desorption (sublimination). As pyridine exposure is increased from 2 L to 10 L, the position of this feature increases from 240 ± 10 K to 260 ± 10 K, which is consistent with zero-order pyridine submimination. The high temperature molecular desorption features are still evident at these higher exposures; however, peak deconvolution at these coverages is subjective and was not performed. As shown in Figure 4.2, dihydrogen gas was observed desorbing from the clean Mo(110) surface over a temperature range of 350 – 540 ± 10 K, depending on pyridine exposure. This is in agreement with several studies indicating the desorption of dihydrogen from the recombination of hydrogen atoms on Mo(110) occurs at 450 ± 10 K in the high coverage region (Roberts and Friend, 1987; Serafin and Friend, 1989).

4.4.2 Orientation and Adsorption Energy Calculations of Pyridine on Mo(110)

The TPD spectra clearly indicate a coverage dependent competitive adsorption and surface reaction process on Mo(110), and the DFT calculations can provide new insight into the nature of the adsorption modes. It is suggested pyridine initially adsorbs molecularly on the surface through the π orbitals (more energetically favorable) followed by adsorption through the nitrogen atom in a perpendicular mode (less energetically favorable) as pyridine coverage increases. Upon sample heating, the less energetically favorable molecularly adsorbed species desorb at 375 ± 10 K (E_{ads} = 23.5 ± 0.6 kcal mol^{-1}), which is attributed to η^1(N)-Py-90° based on the relativistic DFT adsorption energies. At low pyridine exposures (0.5 L), μ_3,η^3(N,C3,C5)-Py-0° surface species are suggested to transform to α-pyridyl species beginning at approximately 250 ± 10 K, forming a bond with the surface through the nitrogen atom and an adjacent carbon atom with the α-pyridyl plane perpendicular or slightly tilted to the Mo(110) surface. This transformation would be essentially complete at low pyridine coverages, giving rise to surface carbon and nitrogen without additional high temperature pyridine desorption. However, at higher pyridine exposures (>1 L), this α-pyridyl species transformation may be competitive with molecular desorption of μ_3,η^3(N,C3,C5)-Py-0° surface species, which explains the lack of the high temperature molecular desorption feature at 0.5 L pyridine exposures. At saturation or higher pyridine coverages, a portion of the μ_3,η^3(N, C3, C5)-Py-0° species desorbs from the surface at higher temperatures within the range of 440 –

530 ± 10 K (E_{ads} = 27.7 – 33.6 ± 0.60 kcal mol^{-1}). The α-pyridyl species then decompose on the Mo(110) surface at higher temperatures resulting in surface nitrogen and carbon accumulation. The adsorbed hydrogen atoms recombine and desorb from the surface as gas phase dihydrogen.

The DFT calculations lend further credence to irreversible α-pyridyl formation and subsequent decomposition on Mo(110). The DFT simulations indicate η^1(N)-Py-90° pyridine would not lead to α-pyridyl formation, as the interaction with the Mo(110) surface is fairly weak and the aromatic ring is not activated. As a result, η^1(N)-Py-90° pyridine on Mo(110) molecularly desorbs at temperatures near 375 ± 10 K. During sample heating it is suggested α C-H bonds of μ_3,η^3(N,C3,C5)-Py-0° pyridine are cleaved as α-pyridyl forms on the Mo(110) surface. The abstracted hydrogen adsorbs on the surface and will eventually recombine with other hydrogen to desorb at temperatures near 465 ± 10 K. Further heating results in the α-pyridyl decomposing to surface carbon and nitrogen, and additional dihydrogen desorption at higher temperatures from the decomposition of α-pyridyl fragments. This transformation is limited by the sample heating rate (2 K sec^{-1} in this study), and consequently a portion of the μ_3,η^3(N,C3,C5)-Py-0° pyridine molecularly desorbs at temperature range of 440 – 530 ± 10 K on the clean Mo(110).

The EELS vibrational frequencies of pyridine over Mo(110) and the calculated vibrational frequencies for the proposed adsorption configurations can provide additional verification of the proposed adsorption mechanism. Obvious differences are noticed between the calculated vibrational frequencies of the Py4 (η^1(N)-Py-90°) and Py5 (μ_3,η^3(N,C3,C5)-Py-0°) adsorption modes. At higher frequencies, the calculated C–H stretching frequencies for model Py5 were at 2911 and 3097 cm^{-1}, whereas Py4 showed a higher frequency at 3140 cm^{-1}. The EELS vibrational frequencies at all surface exposures at low temperature (100 K) had poor resolution and did not show five distinct features for the C–H stretching mode as would have been expected. Nonetheless, the EELS spectra showed vibrational frequencies of 2962 and 3062 cm^{-1} at 0.5 L, 3065 cm^{-1} at 1 L, and 3061 cm^{-1} at 2 L, which is consistent with the calculated frequencies of model Py5 (parallel configuration), and provides further indication that parallel adsorption is preferred at low surface exposures. Vibrational frequencies in the range of 1145 – 1639 cm^{-1} were observed in the experimental EELS frequencies, and assigned to C–H in-plane bending mode (1145, 1155, and 1233 cm^{-1}) and ring stretching (C–C, and C–N) mode (1357, 1386, 1440, 1447, 1457, 1562, 1627, and 1639 cm^{-1}) based on previously reported experimental pyridine frequencies (Corrsin et al., 1953; Wiberg et al., 1984). The calculated vibrational frequencies over a similar range of 1146 – 1737 cm^{-1} for parallel and perpendicular adsorbed configurations (Py4, and Py5) indicated mixed modes of C–H out-of-plane bending, C–H in-plane bending, and ring stretching (C–C and C–N) modes. For the calculated frequencies, it is simple to distinguish which vibrational mode each frequency belongs to, while it is more difficult for the experimental EELS frequencies. The most important observation that should be highlighted is the fact the main vibrational frequencies calculated by DFT are observed in the EELS frequencies. Calculated ring vibrational modes for out-of-plane ring distortion and in-plane ring breathing showed some distinct features between the parallel (Py5) and perpendicular (Py4) configuration. At 0.5 L, EELS showed a frequency of 962 cm^{-1}, which is consistent with parallel adsorption (Py5 at 970 cm^{-1}). At 1.0 L, an EELS frequency of 722 cm^{-1} is comparable to perpendicular adsorption (Py4 at 705 cm^{-1}), while an EELS frequency of 988 cm^{-1} is indicative to parallel adsorption (Py5 at 970 cm^{-1}). At saturation level (2.0 L), EELS vibrational frequencies suggest a combination of parallel (Py5) and perpendicular (Py4) configurations based on a comparison with the DFT calculated vibrational frequencies. Therefore, it is reasonable to suggest that pyridine adsorption mode is surface coverage dependent and that both adsorption modes are possible to occur at high coverages.

The EELS vibrational frequencies at higher surface temperatures (200 – 300 K) show a lower intensity of the vibrational frequencies comparing to 100 K surface temperature. An examination of the calculated vibrational frequencies of α-pyridyl species (structures Py9 and Py10), only four C–H stretching mode frequencies are calculated due to C–H bond cleavage. From the EELS vibrational frequencies, it is difficult to ascertain whether four or five C–H stretching frequencies are present, therefore, it is possible α-pyridyl species transformation takes place above 300 K.

This proposed mechanism is consistent with previous studies of pyridine adsorption on other metal surfaces. A study of pyridine adsorption on Rh(111) (Mate et al., 1988) suggested competitive pyridine adsorption between the electrons in the nitrogen lone pair and the π orbitals as to which will be dominantly responsible for pyridine-metal bonding. It was also proposed that pyridine converts from a relatively flat lying, π-bonded species to a tilted, nitrogen-bonded species with increasing surface coverage. Other work used high-resolution electron energy loss spectroscopy (HREELS) and near-edge x-ray-absorption fine-structure spectroscopy (NEXAFS) to study pyridine adsorption on Ag(111) at 100 K (Bader et al., 1986). This study clearly showed the existence of a phase transition at low coverages where the ring plane of the pyridine is tilted from 45° ± 5° with respect to the surface to 70° ± 5° at high coverages. A similar observation was reported on Ni(111) (Cohen and Merrill, 1990) and Ni(001) (DiNardo et al., 1984) at 170 K, where at low coverages pyridine exhibited η^6-Py-0° adsorption and at high coverages pyridine bonds through the nitrogen atom as η^1(N)-Py-90°. Intermediate α-pyridyl formation on the metal surface while sample heating and its decomposition at temperatures below 530 K has been reported on other metal surfaces. Reversible α-pyridyl species formation has been reported on Pt(111) (Johnson et al., 1985) and Ni(100), (Wexler et al., 1982) and irreversible α-pyridyl species formation on Mo(110) (Serafin and Friend, 1989). In a series of coadsorption studies, Serafin and Friend (Serafin and Friend, 1989) showed there was no H-D exchange in any of the pyridine desorption peaks on Mo(110). Their work indicated a mixture of C_5H_5N and C_5D_5N with compositions in the range of 0.35:0.65 to 0.50:0.5 of pyridine-d_0:pyridine-d_5 at saturated exposures, while there were no mixed isotopes of pyridine formed. Furthermore, the reaction of C_5H_5N in the presence of a saturated layer of deuterium atoms or reaction of C_5D_5N in the presence of a saturated layer of hydrogen atoms showed no isotopic mixing in the molecular desorption peaks.

4.4.3 Adsorption of Pyridine on C/N-Mo(110)

The presence of surface nitrogen and surface carbon on clean Mo(110) indicates non-selective C-C, C-N and C-H bond cleavage, although no gas phase products were detected except for dihydrogen. Auger analysis of the surface after the TPD experiments on clean Mo(110) indicated the presence of a carbidic overlayer based on the line-shape analysis of the carbon Auger peak. A similar observation has been reported for pyridine and ammonia adsorption on clean Al(111) (Davies and Newton, 2003). LEED patterns for the C/N-Mo(110) surface indicate a (1 × 1) hexagonal periodicity with a slight broadening of the spots and an increased diffuse background similar to that previously reported for thiophene decomposition on α-$Mo_2C(0001)$ (Clair et al., 2002). While the LEED results indicate a decrease in the size in surface domains and an increase in surface disorder (Clair et al., 2002), no additional conclusions about the ordering of C and N can be inferred from the LEED data. The surface C/N ratio on the contaminated surface was highly variable with an overall average ratio of 4:1. This is less than the expected ratio of 5 based on the stoichiometry of pyridine. Since there was no products detected desorbing from the surface including dihydrogen, the apparent lack of nitrogen accumulation as a function of consecutive dose suggests nitrogen is possibly diffusing into the bulk. Although this cannot be directly confirmed, this is consistent with the observations during sample cleaning.

The C/N-Mo(110) surface was further studied to determine the adsorption energetics and surface activity as a function of carbon and nitrogen accumulation. Molybdenum nitrides and carbides have shown potential for use as commercial HDN (Choi et al., 1995; Li et al., 1999) and HDS (Markel and Van Zee, 1990; Nagai and Miyao, 1992) catalysts; however, the reactivity of these surfaces depends on surface states and the structure of the reactant molecule. Frühberger and Chen (Frühberger et al., 1996) suggested that the nature of the adsorbed carbon on Mo(110) has a strong effect on catalytic properties. From their studies of hydrocarbons on carbon-modified Mo(110) surfaces, they observed that carbidic carbon produces changes in surface chemistry and graphitic carbon has no effect other than to reduce reactivity. In a series of studies to understand the effect of carbidic overlayers on Mo(110), Roe and Schulz reported carbidic overlayers do not alter the reactivity of ethanethiol (Roe and Schulz, 2000), while 1,2-ethanedithiol (Roe and Schulz, 2000) showed clear changes in selectivity and reaction pathways on both defective and *p*(4x4)-C/Mo(110) surfaces compared to Mo(110). They also noted a shift to lower desorption temperatures on carbided Mo(110) indicating a lowering of the activation energy. In the present study, an increase in pyridine desorption was noted as a function of consecutive exposures. However, carbon accumulation continued to increase approximately linearly indicating that while the surface activity slightly decreases, it does not become inactive towards pyridine decomposition, as C and N continue to accumulate on the Mo(110) surface.

4.5 Conclusions

Pyridine adsorbs reversibly and irreversibly on Mo(110) indicating the surface is active for denitrogenation. TPD analysis of pyridine adsorption at low exposures (0.5 L) indicates a single desorption feature at 375 ± 10 K (E_{ads} = 23.5 ± 0.6 kcal mol^{-1}). At higher pyridine exposures (1 L) two desorption peaks at temperatures of 370 ± 10 K (E_{ads} = 23.2 ± 0.6 kcal mol^{-1}) and 530 ± 10 K (E_{ads} = 33.6 ± 0.6 kcal mol^{-1}) are evidenced on the clean Mo(110) surface. As the pyridine exposure is increased (2, 5, 10 L) similar chemisorption features were observed in addition to a multiplayer physisorption peak at 240 – 260 ± 10 K. The TPD spectra clearly indicate a coverage dependent competitive adsorption and surface reaction process on Mo(110). EELS vibrational frequencies of pyridine at 100 K and the DFT relative energetics along with the calculated vibrational frequencies of these two proposed configuration suggest pyridine initially adsorbs as η^6-Py-0° followed by η^1(N)-Py-90° coordination on clean Mo(110). Surface heating is suggested to result in desorption of η^1(N)-Py-90° and a portion of η^6-Py-0° pyridine, with additional η^6-Py-0° transforming to surface α-pyridyl species (μ_2,η^2(N,C2)-Pyridyl, η^2(N, C2)-Pyridyl) that further decompose to surface carbon and nitrogen and desorbing dihydrogen on clean Mo(110). This transformation is suggested to occur at temperature above 300 K as indicated by the EELS spectra and the calculated vibrational frequencies of α-pyridyl species.

5. PYRROLE ADSORPTION AND REACTION ON Mo(110) AND C/N-Mo(110): EXPERIMENT AND MODELING

5.1 Introduction

Pyrrole (C_4H_5N) represents the essential building block for all non-basic nitrogen compounds present in crude oil, and for this reason is an excellent probe molecule for understanding the adsorption and reactivity behavior of non-basic organonitrogen compounds. Pyrrole is a non-basic organonitrogen heterocycle in which the lone electron pair of nitrogen is delocalized over the π system of the ring, and it is therefore an electron rich molecule that reacts readily with electrophiles but is not susceptible to nucleophilic attack (Jones and Bean, 1977; Jorgebsen and Salem, 1973). The adsorption of pyrrole on metal surfaces, including Cu(100) (Sexton, 1985), iron oxide (Pan and Stair, 1986), Pt(111) (Tourillon et al., 1987), Ni(100) (Schoofs and Benziger, 1987), Rh(111) (Netzer et al., 1988), and Pd(111) (Baddeley et al., 1996; Futaba and Chiang, 1997), has been studied to provide some insight into five-membered heterocyclic bonding characteristics; however, these surfaces are not representative of hydrotreating catalysts. In general, these studies concluded that pyrrole adsorption geometry and decomposition are surface coverage and temperature dependent. At low coverages and temperatures, pyrrole adsorbs molecularly with a flat-lying geometry via π bonding with the metal surface. Increasing surface coverage leads to a change of the adsorption mode from parallel adsorption to a tilted geometry relative to the metal surface plane.

Given the importance of hydrotreating, there is a fundamental need to understand the adsorption and reaction of pyrrole on molybdenum to identify the bonding configuration and energetics as a function coverage and carbon/nitrogen surface contamination. Therefore, the objective of the present study is to investigate the molecular adsorption and surface reaction of pyrrole on Mo(110) and C/N-Mo(110) using temperature-programmed desorption (TPD), Auger electron spectroscopy (AES), and high-resolution electron energy loss spectroscopy (HREELS). The Mo(110) surface orientation was chosen because of its hexagonal (1 × 1) surface structure, which is similar to the *hcp* structure of MoS_2. By investigating pyrrole adsorption over a range of surface coverages, the effect of overlayers on adsorption energetics and reactivity will provide fundamental information regarding the structure-reactivity relationship. Furthermore, the effect of carbon/nitrogen overlayers will be studied to determine the effect of surface modification on molecular adsorption and reactivity. In addition to the experimental studies, first-principles quantum mechanical calculations using density-functional theory (DFT) will be used to study the molecular adsorption of pyrrole on Mo(110) in an attempt to identify the adsorption configurations resulting in molecular desorption and surface decomposition, and gain further insight about the structure-reactivity relationship.

5.2 Experimental Results

5.2.1 Pyrrole Adsorption and Decomposition on Mo(110)

Temperature-programmed desorption spectra for pyrrole adsorption on Mo(110) were collected by monitoring and recording the intensity variation of several mass fragments (m/z ratios) over the range of 2 to 67 to detect desorption products. However, the only desorption product detected was molecular pyrrole. Decomposition products as HCN (m/z = 27), nitrogen (m/z = 28), ammonia (m/z = 17), and H_2 (m/z = 2) were not detected, although it could be these products were below the sensitivity of the mass spectrometer used in the present study.

Figure 5.1 shows the TPD spectra of pyrrole (m/z = 67) on Mo(110) at 0.5, 0.75, 1, 2, 3, 4, and 5 Langmiur exposures and Table 5.1 summaries the peak temperatures with the calculated adsorption energies. At 0.5 L, the TPD spectrum shows one desorption feature centered at 342 ± 10 K with a corresponding first-order adsorption energy of 21.4 ± 0.6 kcal mol^{-1}. Increasing the surface exposure from 0.75 L to 3 L results in a similar desorption feature at a temperature of 345 – 354 ± 10 K and corresponding adsorption energies of 21.6 – 22.1 ± 0.6 kcal mol^{-1}. At 4 L exposure, a second desorption feature at a lower temperature of 248 ± 10 K is observed, in addition to a desorption peak at a temperature of 354 ± 10 K similar to that observed at lower exposures. This low temperature desorption feature increases in intensity at 5 L exposure, and shifts to a slightly higher temperature of 260 ± 10 K. A similar high temperature desorption feature was also noted at 5 L exposure at a temperature of 357 ± 10 K with an adsorption energy of 22.3 ± 0.6 kcal mol^{-1}.

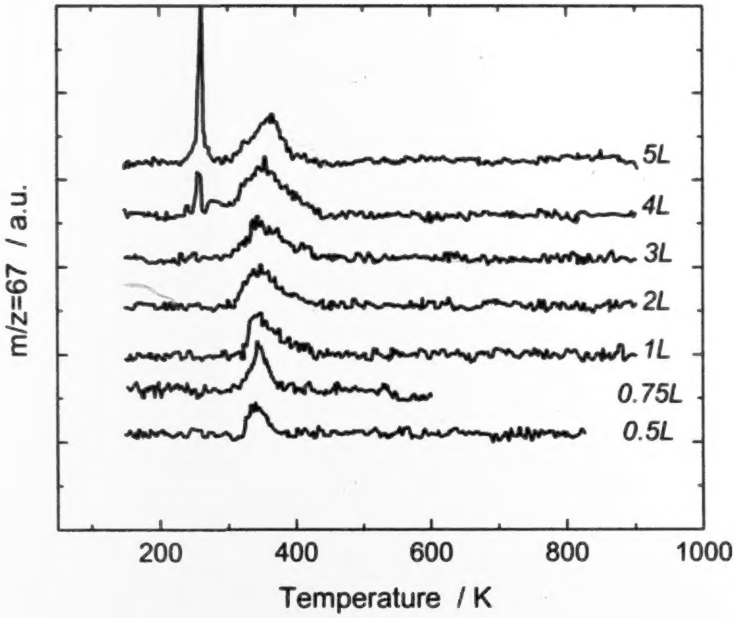

Figure 5.1 Temperature-Programmed Desorption (TPD) spectra of pyrrole (m/z = 67) as a function of pyrrole exposure on clean Mo(110).

Table 5.1 Summary of Pyrrole TPD Features.

Pyrrole Exposure (Langmiur)	Peak Temperature ± 10 K	Adsorption Energy ± 0.6 kcal mol^{-1}	Relative Peak Area a.u.
0.5	342	21.4[a]	7.6×10^{-11}
0.75	345	21.6[a]	1.0×10^{-10}
1	352	22.0[a]	1.5×10^{-10}
2	350	21.9[a]	1.6×10^{-10}
3	354	22.1[a]	1.7×10^{-10}
4	354	22.1[a]	2.6×10^{-10}
5	357	22.3[a]	2.7×10^{-10}
4	248	11.1[b]	2.5×10^{-11}
5	260	11.1[b]	9.8×10^{-11}

[a] The adsorption energy (heat of adsorption) was calculated assuming first-order desorption and a pre-exponential factor of $\nu = 1\times10^{13}$.

[b] The adsorption energy (heat of sublimination) was calculated with a leading edge analysis and a pre-exponential factor of $\nu = 1\times10^{24}$.

The high temperature desorption feature is assigned to a molecularly bound pyrrole species. The adsorption energy was calculated assuming first-order adsorption because the TPD spectra exhibit a characteristic asymmetric peak shape and a constant desorption temperature (approximately) as a function of surface exposure. It should be noted that although the desorption temperature shifts slightly with increasing exposure, this variation is within the repeatability of the TPD experiment. The integrated peak area of the high-temperature desorption feature indicated an overall increase from 0.5 to 5 L pyrrole exposures (Table 5.1), however, the increase in peak area is less than expected based on the increasing pyrrole exposure assuming a uniform sticking coefficient over the entire range of exposures. It is well established that sticking coefficients not only depend on temperature, but also depend on surface coverage. The present data would, therefore, indicate that the sticking coefficient for pyrrole on Mo(110) at exposures at or below 1 L is near unity, and decreases with increasing surface coverage. The origin of the decrease in the sticking coefficient is suggested to be due to incomplete accommodation of pyrrole on Mo(110) at higher surface coverages resulting from adsorbate-adsorbate interactions. The low-temperature peak observed at exposures of 4 L and 5 L is ascribed to multilayer pyrrole desorption, as suggested by the increase in intensity and a shift to slightly higher temperatures with increasing pyrrole exposure. This behavior is consistent with zero-order desorption of physisorbed species. Leading edge analysis of the multilayer desorption features yields a pyrrole heat of sublimation of 11.1 kcal mol^{-1}, which is in excellent agreement with the literature value of 11.2 kcal mol^{-1} (Lide, 2004). While the low temperature features are an indication of surface saturation resulting from multilayer desorption, the energetics of multilayer desorption do not provide essential information about pyrrole molecular adsorption and surface reaction.

5.2.2 Pyrrole Adsorption and Decomposition on C/N-Mo(110)

To further study pyrrole adsorption and surface decomposition, a series of sequential TPD experiments were conducted by dosing clean Mo(110) with increments of pyrrole, followed by acquisition of TPD spectra. AES measurements were taken between TPD experiments to quantify the residual surface carbon and nitrogen on the C/N-Mo(110) surface. These experiments were performed to determine the extent of pyrrole decomposition on Mo(110), and the subsequent effects of carbon and nitrogen accumulation on adsorption energies and reaction products. The details of carbon and nitrogen accumulation are discussed in the following section.

Figure 5.2 shows TPD spectra of pyrrole on clean Mo(110) and C/N-Mo(110) as a function of sequential TPD experiments for several exposures, including 0.5, 1, 2, and 5 L. At 0.5 L, each TPD spectrum showed similar behavior with a single high temperature desorption feature at a constant temperature of (340 – 342) ± 10 K. Further analysis of these peaks by integration indicated a similar amount of pyrrole desorbed as a function of consecutive doses. The TPD spectra for 1 L exposures showed similar behavior to 0.5 L exposure. The first and second exposure at 1 L resulted in a desorption peak at approximately 352 ± 10 K, while the third exposure peak is at a temperature of 374 ± 10 K. The amount of desorbed pyrrole at 1 L slightly increases with each subsequent TPD experiment. The 2 L TPD spectra also indicated one desorption feature as a function of pyrrole exposure, with a slight increase in the peak position; the first exposure peak is at 350 ± 10 K and the second and third exposure peaks are at 360 ± 10 K and 359 ± 10 K, respectively. Above saturation, the 5 L pyrrole TPD spectra showed similar overall

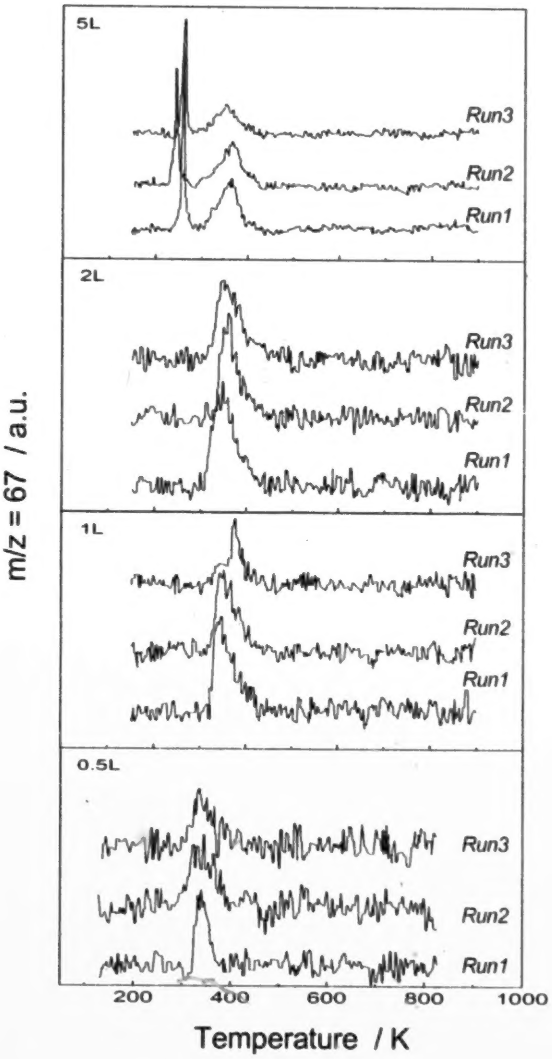

Figure 5.2 Temperature-Programmed Desorption (TPD) spectra of pyrrole (*m/z* = 67) for three consecutive pyrrole exposures on Mo(110); 0.5 L, 1 L, 2 L, and 5 L (ordinate scales adjusted).

behavior with a single chemisorption peak at temperatures of 357 ± 10 K, 361 ± 10 K, and 353 ± 10 K, respectively. The physisorption peak shifted to a lower temperature for the second exposure (248 ± 10 K), while the third exposure (262 ± 10 K) showed approximately the same temperature as the first exposure (260 ± 10 K). With both 2 L and 5 L exposures, similar quantities of pyrrole were desorbed as a function of consecutive exposures.

5.2.3 C/N Surface Accumulation

Surface composition analysis for Mo(110) was performed after each TPD experiment using AES. These measurements showed the presence of carbon and nitrogen confirming the decomposition of pyrrole on Mo(110). The quantitative analysis for each element was based on measuring the Auger peak-to-peak amplitude for C (KLL, 272 eV), N (KLL, 386 eV) and Mo (MNN, 187 eV) Auger features. Figure 5.3 shows the atomic concentration of carbon (at.% C) and nitrogen (at.% N) as a function of consecutive exposure for 0.5, 1, 2, and 5 L. These atomic concentrations were calculated from the AES line intensities using the relative sensitivity factor for each element at a beam energy of 1.5 kV; 0.257 for carbon, 0.470 for nitrogen, and 0.392 for molybdenum (Davis et al., 1978). Surface exposures on clean Mo(110) less than or equal to 2 L indicate an approximate C:N atomic ratio of 4:1, while at higher surface exposures this ratio reduces to a value of 2:1. These ratios suggest that at low surface exposures (approx. ≤2 L), adsorbed pyrrole decomposes completely on the Mo(110) surface, while at higher surface exposures pyrrole tends to react differently to yield other reaction products. While the exact decomposition behavior at high surface exposures is not clear, the difference is possibly due to a different adsorption configuration between low and high surface coverages.

Surface nitrogen accumulation showed a slight increase as a function of consecutive exposures for most surface coverages, except for 0.5 L where surface nitrogen concentration remains nearly constant. While the AES data indicated excellent reproducibility based on repeat analyses, surface carbon showed unsystematic behavior with a dependence on pyrrole exposure. At low exposures (0.5 and 1 L), the second consecutive exposure indicates a reduction in surface carbon while the third consecutive

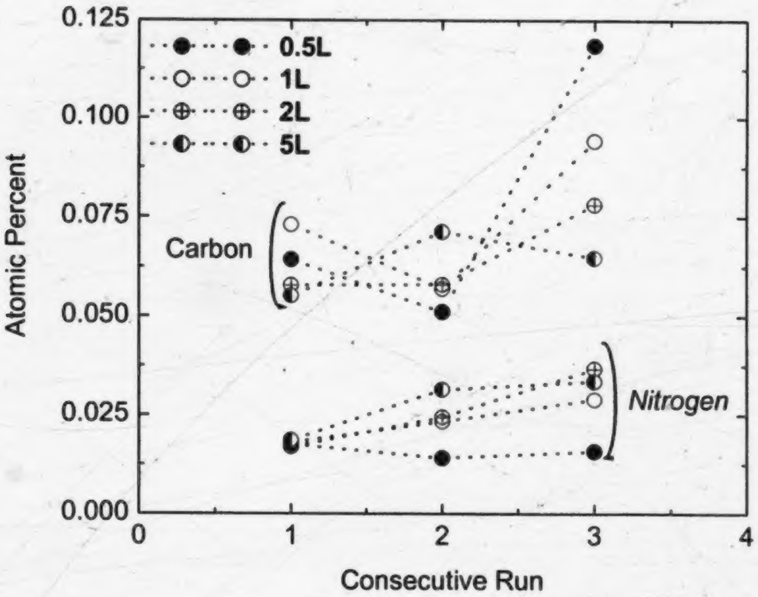

Figure 5.3 Atomic percent (at.%) of surface contamination on Mo(110) as a function of consecutive pyrrole TPD experiments for carbon and nitrogen.

exposure shows a significant increase, although the increase at 1 L is less than 0.5 L. Increasing surface exposure to 2 L showed an overall increase of surface carbon as a function of consecutive exposure. Above saturation levels (5 L), an opposite trend is observed compared to low surface exposures. The second consecutive exposure at 5 L showed an increase in surface carbon, followed by a decrease for the third exposure. The C:N atomic ratio is relatively constant for the first two consecutive exposures at surface exposures less than saturation and increases in the third consecutive exposure, while above saturation levels this ratio decreases in a linear trend. This suggests pyrrole adsorbs and decomposes molecularly on Mo(110) at low surface exposures, while higher exposures alter pyrrole adsorption mode(s) and subsequent decomposition pathways.

The Auger line-shapes of carbon KLL and nitrogen KLL features were examined as a function of surface exposure (Figure 5.4), and the surface structure was studied with LEED to better understand the nature of the C/N-Mo(110) surface. Examination of the C KLL line-shape indicates the formation of a carbidic overlayer on Mo(110) (Goodman, 1982; Robbie et al., 2001; Roe and Schulz, 1998), although the carbon did not form a well-ordered carbidic surface (i.e. $p(4 \times 4)$). LEED patterns of the C/N-Mo(110) surface indicated a (1×1) hexagonal periodicity with a broadening of the spots as a function of consecutive pyrrole exposures and TPD analysis. Ordered carbidic surfaces often demonstrate higher catalytic activities; however, based on the integrated peak area of each subsequent TPD experiment for all exposures, the C/N–Mo(110) surface indicated similar activity for pyrrole desorption as on clean Mo(110) surface.

5.2.4 High Resolution Electron Energy Loss Spectroscopy

Vibrational frequencies of pyrrole adsorption at several surface exposures, including 0.5, 1.0, and 4.0 L, were collected as a function of temperature (100, 200, 300 K), as shown in Figures 5.5, 5.6, and 5.7, respectively. All measured frequencies at surface exposures of 0.5, 1, and 4 L are summarized in Table 5.2.

The electron energy loss spectrum at 0.5 L exposure and an adsorption temperature of 100 K (Figure 5.5) shows frequencies of 633, 990, 1379, 1446, 1585, 2938, and 3097 cm^{-1} with an elastic peak of 3.5×10^4 cps (count per second) and spectral resolution of 55 cm^{-1} FWHM (Full Width at Half Maximum). The sharpest peak and the

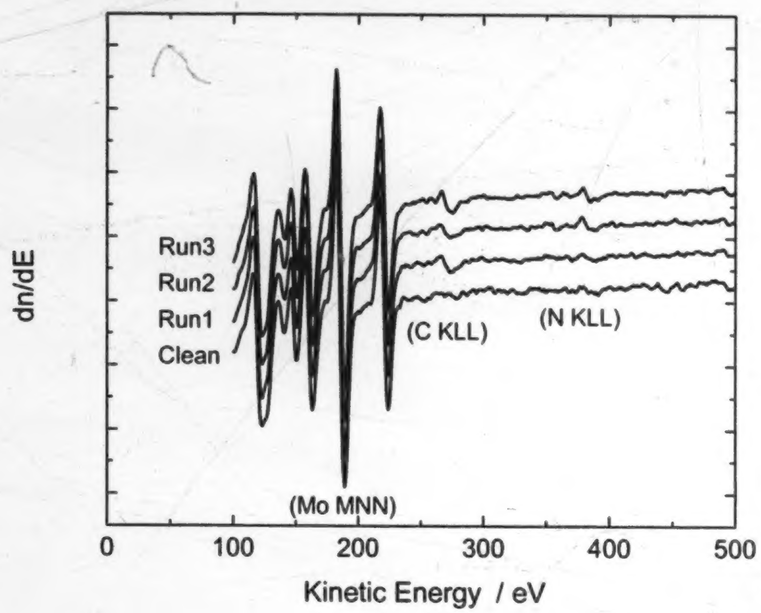

Figure 5.4 Auger spectra of clean Mo(110) and C/N-Mo(110) as a function of consecutive TPD experiments at 2 L pyrrole exposure. The spectra are normalized to the Mo MNN (186 eV) peak, and baseline adjusted to clearly show the C KLL (272 eV) and N KLL (379 eV) Auger peaks.

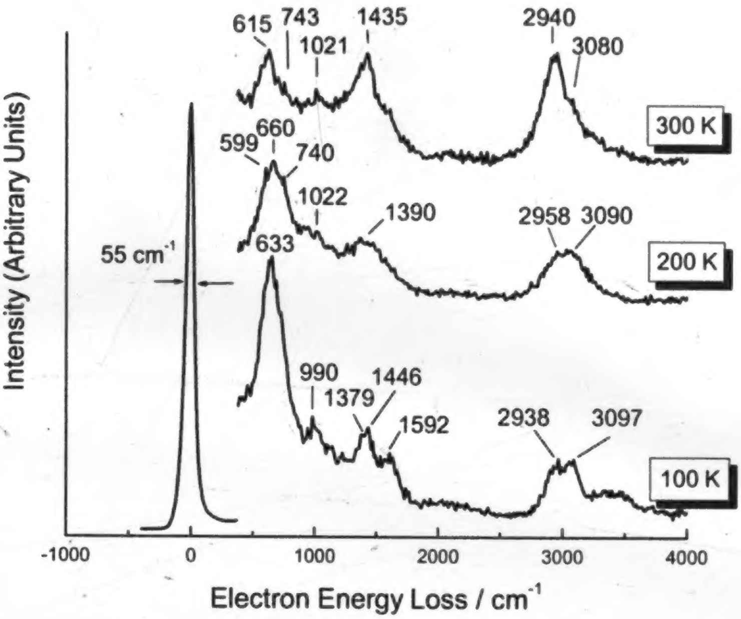

Figure 5.5 Electron energy loss spectra of pyrrole adsorbed on Mo(110) at a surface exposure of 0.5 L as a function of temperature (100, 200, and 300 K).

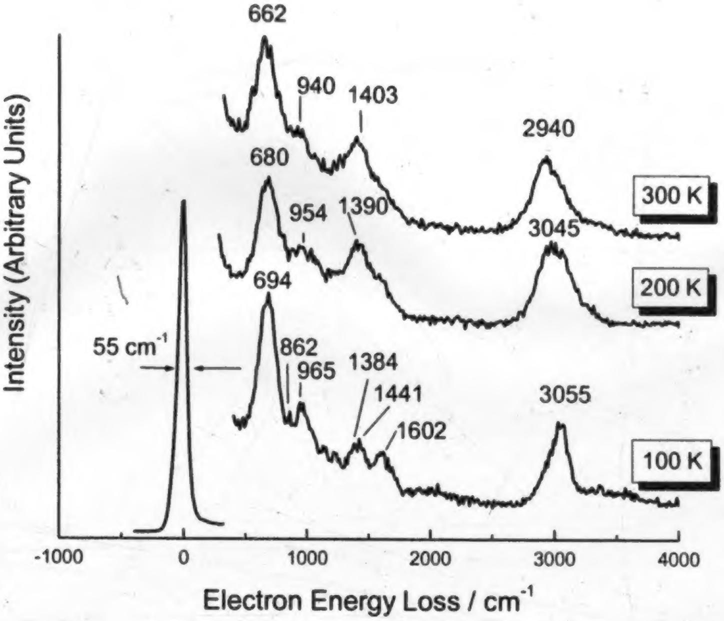

Figure 5.6 Electron energy loss spectra of pyrrole adsorbed on Mo(110) at surface exposure of 1.0 L as a function of temperature (100, 200, and 300 K).

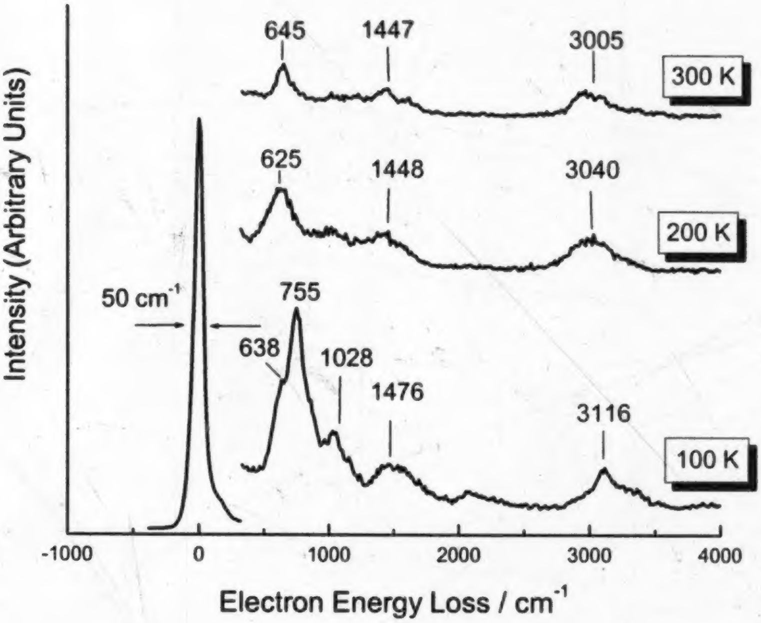

Figure 5.7 Electron energy loss spectra of pyrrole adsorbed on Mo(110) at surface exposure of 4.0 L (saturation) as a function of temperature (100, 200, and 300 K).

strongest frequency signal was at 633 cm^{-1}, while at high frequencies where C–H and N–H stretching vibrational modes are anticipated showed a broad peak with an unresolved number of frequencies. Nonetheless, two vibrational frequencies for C–H stretching were assigned in this region at 2938 and 3097 cm^{-1}. The EELS spectrum at 100 K showed a very broad peak at a range of 3300 – 3500 cm^{-1}, which is consistent with an N–H stretching mode. As the surface temperature increases to 200 K, the intensity of the EELS spectrum decreases. The initial peak position at 633 cm^{-1} splits into three frequencies at 599, 660, and 740 cm^{-1}. Other peak positions recorded at 200 K were not sharp and intense as in the 100 K spectrum; these frequencies are located at 1022, 1390, 2958, and 3080 cm^{-1}. Increasing the temperature to 300 K decreases the intensity of the peak at 633 cm^{-1}, while the other peaks intensified and showed strong signals, specifically at 1435 and 2940 cm^{-1}. Other peak positions were recorded at 615, 743, 1021, and 3080 cm^{-1}.

At a surface exposure of 1.0 L (Figure 5.6), the EELS spectrum had similar resolution with 55 cm^{-1} FWHM and 3.3×10^4 cps. The general spectral features did not change significantly at 1.0 L (100 K) in comparison to 0.5 L exposures; the recorded peak positions at 100 K were 694, 862, 965, 1384, 1441, 1611, and 3080 cm^{-1}. The strongest peak at 694 cm^{-1} and the C–H stretching mode frequency at 3055 cm^{-1} were more resolved than the 0.5 L (100 K) EELS spectrum. As the surface temperature increases to 200 K, some of the reported frequencies at 100 K disappeared and some either shifted to different peak positions or new frequencies emerged. The observed peak positions at 200 K were 680, 954, 1390, and 3045 cm^{-1}. A further increase in surface temperature to 300 K resulted in the entire spectrum shifting to lower peak positions with specific vibrational frequencies at 662, 940, 1403, and 2940 cm^{-1}. In general, the number of recorded frequencies decreases as the surface temperature increases.

The EELS spectra at 4.0 L pyrrole exposure corresponding to surface saturation, as indicted by temperature programmed desorption, is shown in Figure 5.7. The EELS spectra at 4.0 L showed better spectrum resolution than 0.5 and 1.0 L with an overall FWHM of 50 cm^{-1} and 4.2×10^4 cps. At 100 K, the spectrum indicates peak positions at 633, 725, 1035, 1426, 2968, and 3104. Higher frequencies are possible; however, these are not well resolved and difficult to assign specific frequencies to these features. As the surface temperature increases to 200 K, the entire spectrum intensity reduces and the features are less resolved. The low frequency peak recorded at 633 cm^{-1} (100 K) had lower intensity at 200 K with slight shift to 638 cm^{-1}, while the 725 cm^{-1} (100 K) disappeared at 200 K. Additional frequencies were also recorded at 1025, 1409, 2930 and 3080 cm^{-1}. At 300 K, the high frequency C–H stretching mode becomes more resolved at 2930 cm^{-1}, and additional peaks are observed at 638, 1056, and 1438 cm^{-1}.

As previously noted, the identification of an adsorbed species and the adsorption configuration relies on the knowledge of the vibrational spectrum, as well the dipole selection rules in dipole scattering on surfaces. In the case of pyrrole, stretching vibrations include C–H, N–H frequencies, and C–H and N–H bending vibrations, similar to pyridine. For pyrrole, the possible vibrational modes are represented by out-of-plane (oop) ring distortion, in-plane (inp) ring breathing, C–H oop bending, N–H oop bending, C–H inp bending, N–H inp bending, C–C stretching, C–N stretching, C–H stretching, and N–H stretching. All EELS vibrational frequencies observed for adsorbed pyrrole over Mo(110) at all surface exposures (0.5, 1.0, and 4.0 L) were assigned to a vibrational mode based on experimental measured frequencies of pyrrole reported by Mellouki et al., (2001).

5.3 Molecular Simulation

5.3.1 Pyrrole Electronic Structure

The electronic structure of the pyrrole molecule was initially analyzed to understand its chemical reactivity behavior and to get some insights about its favorable adsorption approach on transition metals. Figure 5.8a shows the electrostatic potential map of pyrrole (C_4H_5N) from two different angles (top and side view). The hydrogen atom within the N–H is the most electron-deficient region within the molecule, while other hydrogen atoms within the ring are slightly electron-deficient. The region, which is directly above and below the π-ring, is the most electron-rich region and is susceptible to positive ion attraction suggesting a possible location for initial adsorption. The electrophilic and nucleophilic Fukui functions of pyrrole, which represent the most reactive regions for bond formation with the catalyst surface, are shown in Figures 5.8b and 5.8c. Pyrrole can act as a nucleophile, forming a bond with the catalyst surface (electrophiles) using the π orbitals. In contrast, nucleophilic attack (accepting electrons) can occur above and below the C–H bonds, as well the hydrogen atom of the N–H bond. Figure 5.8d and 5.8e represent the highest occupied molecular orbital (HOMO) and the lowest unoccupied molecular orbital (LUMO) of pyrrole. The HOMO is located on the C=C orbitals and represents the highest probability to donate electrons, thereby forming a bond with the catalyst active site by electrophilic attack. The LUMO is located around the C–H and N–H bonds, which make this region favorable for nucleophilic attack.

5.3.2 Parallel Pyrrole Adsorption on Mo(110)

Parallel adsorption was initially studied, as it is generally believed pyrrole adsorbs on the surface in flat-on geometry at low coverages (Baddeley et al., 1996; Netzer et al., 1988; Schoofs and Benziger, 1987; Sexton, 1985). Figure 5.9 presents initial and optimized parallel adsorption modes with the calculated adsorption energies. Table 5.3 summarizes pyrrole inter-atomic bond lengths and Table 5.4 summarizes the inter-atomic bond angles for all optimized structures. The initial configurations include a flat-centre mode (Pyr1) where the centre of pyrrole is directly atop a Mo atom as η^5-Pyr-0°, flat-hollow mode (Pyr2) where centre of pyrrole is directly atop a hollow site as μ_4,η^6(N,C2,C3,C3,C4,C5)-Pyr-0°, flat-on mode with the pyrrolic nitrogen directly atop a Mo atom (Pyr3) as μ_3,η^5-Pyr-0°, flat-on mode with the pyrrolic nitrogen atop a hollow site (Pyr4) as μ_3,η^4(C2,C3,C4,C5)-Pyr-0°, and flat-on mode with the pyrrolic nitrogen directly atop a Mo bridge (Pyr5) as μ_4,η^6(N,N,C2,C3,C4,C5)-Pyr-0°.

Pyrrole adsorption with the centre of pyrrole directly atop a Mo atom as η^5-Pyr-0° resulted in η^2(C4,C5)-Pyr-23° tilted configuration with an adsorption energy of -9.4 kcal mol^{-1} (Pyr1), the lowest adsorption energy among all studied parallel adsorption geometries. During Pyr1 optimization, pyrrole was slightly repulsed from the Mo(110) surface, and the greatest repulsion came from the nitrogen atom that moved 0.7 Å away from the Mo(110) surface from the initial position. Examination of this adsorption mode indicates possible electrophilic attack, as the C4=C5 π orbital represents the highest occupied molecular orbital (HOMO) and most efficient for donating electrons. The molecule shows an expansion in its inter-atomic bond lengths except for the N–C2 bond,

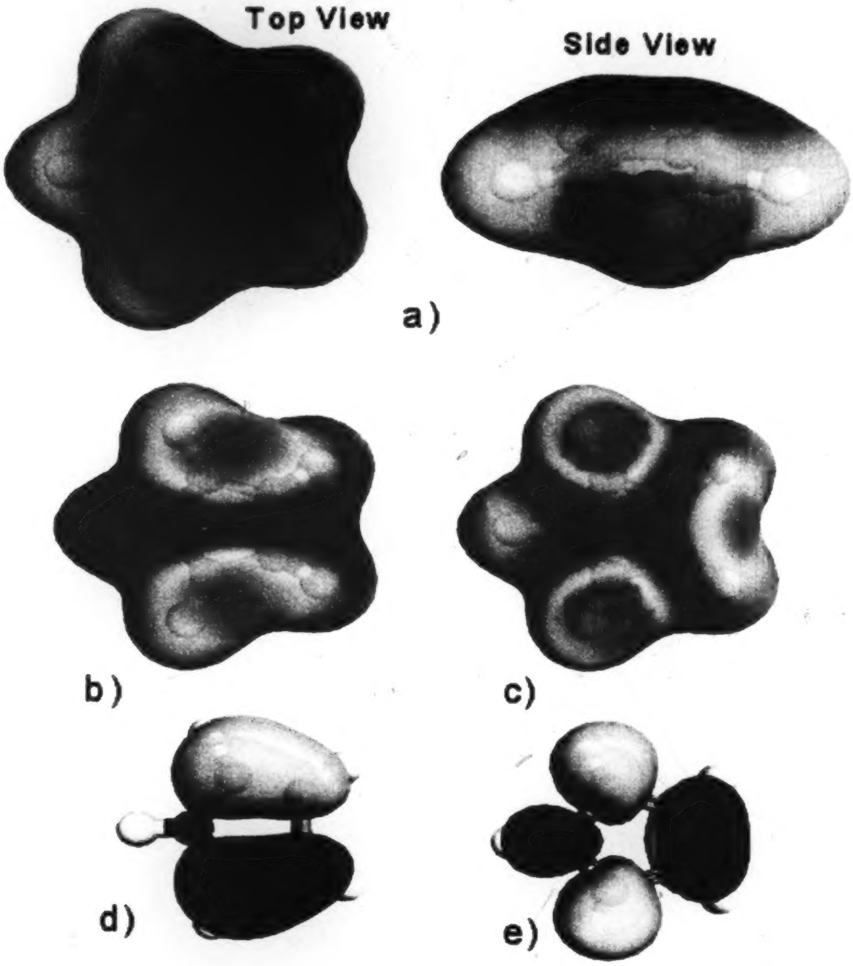

Figure 5.8 Electronic structure properties of pyrrole calculated by density functional theory (GGA-PBE pesudo-potential) with 0.025 isosurface, a) Electrostatic Potential Map, b) Electrophilic Fukui function, c) Nucleophilic Fukui function, d) HOMO, and e) LUMO.

Table 5.2 Vibrational frequencies (cm^{-1}) and assignment of pyrrole adsorption on Mo(110) surface using high-resolution electron energy loss spectroscopy.

Description	C_4H_5N[a]	Pyrrole-Mo(110) – 0.5 L			Pyrrole-Mo(110) – 1 L			Pyrrole-Mo(110) – 4 L		
		100 K	200 K	300 K	100 K	200 K	300 K	100 K	200 K	300 K
NH oop bending	475	...	...	...	...	...	...	...	...	...
oop ring	614	633	599	615	...	...	...	633	638	638
oop ring	621	633	599	615	...	...	...	633	638	638
CH oop bending	629	633	660	615	...	...	662	633	638	638
CH oop bending	722	...	740	743	684	680	662	725	...	...
CH oop bending	827	...	...	...	...	...	...	...	...	...
CH oop bending	864	...	...	...	862	...	...	...	...	...
inp ring	866	...	...	...	862	...	...	...	...	...
Inp ring	882	...	...	...	862	...	940	...	...	...
CH inp bending	1017	990	1022	1021	965	954	940	1035	1025	...
inp ring	1049	990	1022	1021	...	...	...	1035	1025	1056
CH inp bending	1075	...	...	...	...	...	...	1035	...	1056
CH inp bending	1134	...	...	...	...	...	...	...	...	...
inp ring	1148	...	...	...	...	...	...	...	...	...
CH inp bending	1288	...	...	...	...	...	...	...	...	...
inp ring	1401	1379	1390	...	1384	1390	1403	1426	1409	...
NH inp bending	1424	1446	1390	...	1384	1390	1403	1426	1409	1438
inp ring	1472	1446	...	1435	1441	...	...	1426	...	1438
inp ring	1519	1585	...	...	1602	1570	...	...	...	...
CH stretch	3119	2938	2958	2940	3050	3045	2940	2968	2930	2930
CH stretch	3128	3097	3090	3080	3050	3045	...	3104	3080	...
CH stretch	3143	3097	3090	3080	3050	3045	...	3104	3080	...
CH stretch	3149	3097	3090	3080	3050	3045	...	3104	3080	...
NH stretch	3531	...	...	...	...	...	...	...	...	...

[a] (Mellouki et al., 2001)

Model	Adsorption Energy [kcal mol^{-1}]	Initial Geometry	Optimized Geometry
		Top View	*Side View*
Pyr1	*Flat Centre* -9.4	η^5-Pyr-0° 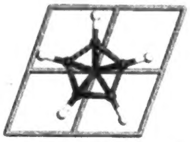	η^2(C4,C5)-Pyr-23° 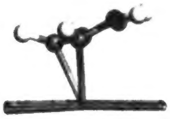
Pyr2	*Flat Hollow* -30.7	μ_4,η^6(N,C2,C3,C3,C4,C5)-Pyr-0° 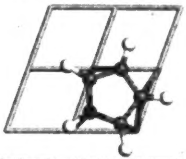	μ_3,η^5-Pyr-0° 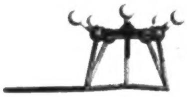
Pyr3	*N-atom atop Mo-atom* -28.7	μ_3,η^5-Pyr-0° 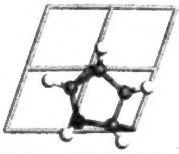	μ_3,η^4(N,C2,C4,C5)-Pyr-0° 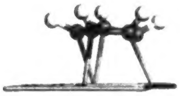
Pyr4	*N-atom in Hollow Site* -31.5	μ_3,η^4(C2,C3,C4,C5)-Pyr-0° 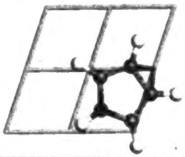	μ_3,η^5 -Pyr-0° 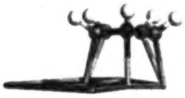
Pyr5	*N-atom in Bridge Site* -19.4	μ_4,η^6(N,N,C2,C3,C4,C5)-Pyr-0° 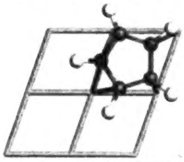	μ_2,η^2(C3,C5)-Pyr-16° 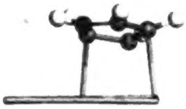

Figure 5.9 Initial and optimized geometries of parallel pyrrole adsorption on Mo(110) and the corresponding adsorption energies.

which showed a reduction by 0.03 Å, while the inter-atomic angles within the ring showed a reduction within C4 and C5 atoms that were involved in bonding with the Mo(110) surface. Additionally, the bond angles centred on the N, C2, and C3 atoms showed a slight expansion from their initial values (Table 5.4).

The Pyr2, Pyr3, and Pyr4 parallel adsorption modes resulted in similar adsorption energies of -30.7, -28.7, and -31.5 kcal mol^{-1}, respectively, all of which are higher in comparison to Pyr1. Both Pyr2 and Pyr4 optimized adsorption modes resulted in optimized geometries of μ_3,η^5-Pyr-0° with the Mo(110) surface. In both geometries, pyrrole shifts from its initial location to a new one with the π-orbital directly atop of a Mo atom. While all of the hydrogen atoms were repulsed away from the surface, the pyrrole molecular plane remained nearly parallel to the Mo(110) surface. It should be noted that in both of these adsorption geometries, although Pyr2 has initially five bonds with the surface through 4-Mo atoms and Pyr4 has four bonds with 3-Mo atoms, both adsorption modes resulted in μ_3,η^5-Pyr-0° optimized geometries with similar adsorption energies. Structure Pyr5 resulted in an optimized geometry of μ_2,η^2(C3,C5)-Pyr-16° titled configuration with an adsorption energy of -19.4 kcal mol^{-1}, which is higher than structure Pyr1 and lower compared to the other optimized parallel adsorption modes. Although during optimization structure Pyr5 showed a similar interaction with the Mo(110) surface as structures Pyr2 and Pyr4, structure Pyr5 bonded through two different HOMO orbitals which contribute to the higher adsorption energy of Pyr5 comparing to Pyr1. During optimization, the Pyr5 structure clearly shifts and rotates from its initial position while the pyrrolic nitrogen is directly atop a Mo bridge site and is slightly repulsed from the surface. The apparent repulsion of the pyrrolic nitrogen would result in a slightly lower adsorption energy, as observed comparing structures Pyr5 to structures Pyr2 and Pyr4.

5.3.3 Perpendicular and Inclined Pyrrole Adsorption on Mo(110)

To elucidate all possible adsorption modes on Mo(110), perpendicular and tilted configurations were also studied. Perpendicular structures were initially modeled with molecular pyrrole approaching the Mo(110) surface from the N–H and all C–H locations (structures not shown). The results clearly indicated these adsorption configurations were

Table 5.3 Calculated Pyrrole Bond Lengths

	Optimized Geometry	*d*(N-C2) (Å)	*d*(C2-C3) (Å)	*d*(C3-C4) (Å)	*d*(C4-C5) (Å)	*d*(C5-N) (Å)
	Gas-Phase	1.38	1.38	1.42	1.39	1.38
Pyr1	η^2(C4,C5)-Pyr-23°	1.35(-0.03)	1.40 (0.02)	1.46 (0.04)	1.47 (0.08)	1.43 (0.05)
Pyr2	μ_3,η^5-Pyr-0°	1.45 (0.07)	1.46 (0.08)	1.47 (0.05)	1.46 (0.07)	1.45 (0.07)
Pyr3	μ_3,η^4(N,C2,C4,C5)-Pyr-0°	1.46 (0.08)	1.48 (0.10)	1.46 (0.04)	1.43 (0.04)	1.45 (0.07)
Pyr4	μ_3,η^5-Pyr-0°	1.45 (0.07)	1.47 (0.09)	1.47 (0.05)	1.46 (0.07)	1.45 (0.07)
Pyr5	μ_2,η^2(C3,C5)-Pyr-16°	1.36(-0.02)	1.39 (0.01)	1.46 (0.04)	1.48 (0.09)	1.43 (0.05)
Pyr6	η^2(C3,C4)-2H-Pyl-88°	1.37(-0.01)	1.37(-0.01)	1.52 (0.10)	1.37(-0.02)	1.37(-0.01)
Pyr7	μ_2,η^2(C4,C5)-2H-Pyl-81°	1.37(-0.01)	1.36(-0.02)	1.45 (0.03)	1.46 (0.07)	1.38
Pyr8	μ_2,η^3(N,C5,C5)-2H-Pyl-86°	1.36(-0.02)	1.39 (0.01)	1.39(-0.03)	1.41 (0.02)	1.42 (0.04)
Pyr9	η^1(N))-H-Pyl-84°	1.38	1.37(-0.01)	1.41(-0.01)	1.37(-0.02)	1.38
Pyr10	μ_2,η^2(C2,C2)-H-Pyl-66°	1.40 (0.02)	1.42 (0.04)	1.40(-0.02)	1.38(-0.01)	1.35(-0.03)
Pyr11	μ_3,η^4(C3,C3,C4,C4)-2H-Pyl-76°	1.36(-0.02)	1.38	1.46 (0.04)	1.39	1.37(-0.01)
Pyr12	μ_2,η^2(C4,C5)-2H-Pyl-84°	1.37(-0.01)	1.37(-0.01)	1.44 (0.02)	1.48 (0.09)	1.37(-0.01)
Pyr13	μ_3,η^3(N,C5,C5)-2HPyl-45°	1.41 (0.03)	1.42 (0.04)	1.40(-0.02)	1.39	1.36(-0.02)
Pyr14	μ_2,η^2(N,C4)-H-Pyl-13°	1.37(-0.01)	1.42 (0.04)	1.42	1.45 (0.07)	1.40 (0.02)
Pyr15	μ_3,η^4(N,C2,C3,C4)-Pyr-5°	1.36(-0.02)	1.38	1.46 (0.04)	1.39	1.37(-0.01)

Table 5.4 Calculated Pyrrole Bond Angles

	C2 N C3 ∠	C3 C2 C4 ∠	C4 C2 C5 ∠	C5 C2 N ∠	N C5 C2 ∠
Gas-Phase	107.48°	107.46°	107.60°	107.39°	110.06°
Pyr1	109.29° (1.81)	108.42° (0.96)	103.79° (-3.81)	105.45° (-1.94)	109.45° (-0.61)
Pyr2	108.69° (1.21)	107.55° (0.09)	107.29° (-0.31)	108.86° (1.47)	107.45° (-2.61)
Pyr3	109.91° (2.43)	106.83° (-0.63)	107.31° (-0.29)	103.56° (-3.83)	111.68° (1.62)
Pyr4	108.80° (1.32)	107.02° (-0.44)	107.37° (-0.23)	108.61° (1.22)	107.52° (-2.54)
Pyr5	105.72° (-1.76)	108.20° (0.74)	106.50° (-1.10)	109.09° (170)	108.02° (-2.04)
Pyr6	108.16° (0.68)	106.84° (-0.62)	104.38° (-3.22)	109.59° (2.20)	111.00° (0.94)
Pyr7	109.83° (2.35)	107.53° (0.07)	106.08° (-1.52)	105.54° (-1.85)	110.91° (0.85)
Pyr8	109.67° (2.19)	107.58° (0.12)	108.24° (0.64)	106.22° (-1.17)	108.27° (-1.79)
Pyr9	107.48°	107.47° (0.01)	107.59° (-0.01)	107.39°	110.06°
Pyr10	102.56° (-4.92)	110.36° (2.90)	106.63° (-0.97)	108.37° (0.98)	112.06° (2.00)
Pyr11	108.12° (0.64)	107.05° (-0.41)	105.79° (-1.81)	108.12° (0.73)	110.59° (0.53)
Pyr12	109.67° (2.19)	108.19° (0.73)	104.90° (-2.70)	105.95° (-1.44)	110.90° (0.84)
Pyr13	109.15° (1.67)	107.04° (-0.42)	108.67° (1.07)	105.49° (-1.90)	109.44° (-0.62)
Pyr14	111.85° (4.37)	106.65° (-0.81)	104.92° (-2.68)	110.23° (2.84)	105.59° (-4.47)
Pyr15	104.53° (-2.95)	109.60° (2.14)	105.85° (-1.75)	108.17° (0.78)	108.92° (-1.14)

unstable and did not result in surface bonding. The observed repulsive effect resulted in all adsorption geometries moving away from the Mo(110) surface an additional 1.5 – 1.7 Å from the initial distance of 2.2 Å. Therefore, perpendicular and tilted adsorption modes were studied by abstracting either one or two hydrogen atoms from pyrrole, with the resulting pyrrolyl fragment and hydrogen atom(s) bonding to the Mo(110) surface.

Figure 5.10 summarizes five different perpendicular configurations where all molecules are located at the same surface position and pyrrolyl approaches the surface from the C3–C4 bond (η^2(C3,C4)-2H-Pyl-90°, structure Pyr6), C4=C5 double bond (η^2(C4,C5)-2H-Pyl-90°, structure Pyr7), and both C5 and N after abstracting two hydrogen atoms and bonding both on the surface (η^2(N,C5)-2H-Pyl-90° , structure Pyr8). Structure Pyr6 resulted in an adsorption energy of -9.6 kcal mol^{-1}, the lowest adsorption energy of all perpendicular pyrrolyl geometries studied. The optimized structure retained its initial adsorption geometry without noticeable changes in its structure or position, although it did bend slightly towards the surface by 2° to form an η^2(C3,C4)-2H-Pyl-88° configuration. Structure Pyr7 resulted in the highest adsorption energy with a value of -55.3 kcal mol^{-1}. During optimization, pyrrolyl shifts from its initial position and bends toward the surface such that the other π-orbital (C2=C3) tries to bond with the surface as μ_2,η^2(C4,C5)-2H-Pyl-81°. The inter-atomic bond lengths showed an increase by 0.07 Å for the C4–C5 bond, and only slight changes to other bonds. The high adsorption energy in this case was the result of a strong interaction between the molecule through its HOMO orbitals and the surface. Structure Pyr8 produced an adsorption energy of -30.3 kcal mol^{-1} with an optimized bonding geometry of μ_2,η^3(N,C5,C5)-2H-Pyl-86°. During optimization, pyrrolyl migrates from its initial position atop a Mo atom to directly above a hollow site. The ring structure showed slight deformation as indicated by the changes in the inter-atomic bond length and angles, as shown in Tables 5.3 and 5.4, respectively.

In addition to the pervious perpendicular adsorption modes, two additional configurations were studied by abstracting the hydrogen atom from the pyrrolic nitrogen initially bonding as η^1(N)-H-Pyl-90° (structure Pyr9), and by abstracting an α-C hydrogen atom initially bonding as η^1(C2)-H-Pyl-90° (structure Pyr10). In both adsorption modes, the pyrrolyl fragment approached the Mo(110) surface directly atop a Mo atom. For structure Pyr9, the number and type of bonds did not change considerably

Model	Adsorption Energy [kcal mol^{-1}]	Initial Geometry	Optimized Geometry
Pyr6	-9.6	η^2(C3,C4)-2H-Pyl-90° 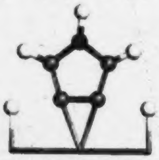	η^2(C3,C4)-2H-Pyl-88° 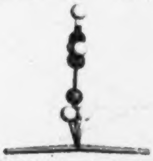
Pyr7	-55.3	η^2(C4,C5)-2H-Pyl-90° 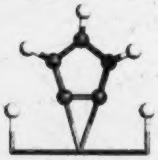	μ_2,η^2(C4,C5)-2H-Pyl-81° 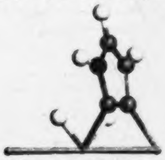
Pyr8	-30.3	η^2(N,C5)-2H-Pyl-90° 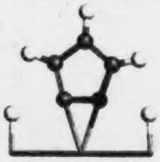	μ_2,η^3(N,C5,C5)-2H-Pyl-86° 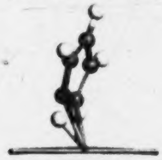
Pyr9	-17.4	η^1(N)-H-Pyl-90° 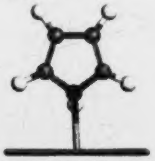	η^1(N))-H-Pyl-84° 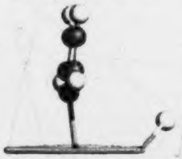
Pyr10	-24.2	η^1(C2))-H-Pyl-90° 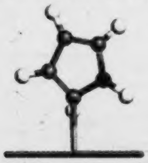	μ_2,η^2(C2,C2)-H-Pyl-66° 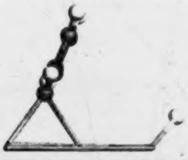

Figure 5.10 Initial and optimized geometries of perpendicular pyrrole and pyrrolyl adsorption on Mo(110) and the corresponding adsorption energies.

following optimization; the optimized structure shows a slight attraction between the molecular plane and the surface forming a slightly tilted configuration as η^1(N)-H-Pyl-84° with an adsorption energy of -17.4 kcal mol^{-1}. However, during optimization structure Pyr10 shifted from the initial position and resulted in an optimized geometry of μ_2,η^2(C2,C2)-H-Pyl-66° with an adsorption energy of -24.2 kcal mol^{-1}.

The initial and optimized pyrrolyl adsorption configurations with the molecular plane inclined with respect to the Mo(110) surface are presented in Figure 5.11. These configurations are similar to the previously discussed perpendicular pyrrolyl adsorption configurations, except the pyrrolyl molecular plane was inclined 45° with respect to the Mo(110) surface as η^2(C3,C4)-2H-Pyl-45° (structure Pyr11), η^2(C4,C5)-2H-Pyl-45° (structure Pyr12), and η^2(N,C5)-2H-Pyl-45° (structure Pyr13). Two additional configurations were studied at inclination angles of 15° to the Mo(110) surface as μ_3,η^5-H-Pyl-15° (structure Pyr14) pyrrolyl adsorption and μ_3,η^5-Pyr-15° (structure Pyr15) molecular pyrrole adsorption. During Pyr11 optimization, the C3-C4 σ-orbital shifts from the initial location directly atop a Mo atom to a hollow site bonding to three Mo atoms. The pyrrolyl plane angle with the Mo(110) surface increases from 45° to 76° forming an μ_3,η^4(C3,C3,C4,C4)-2H-Pyl-76° configuration with an adsorption energy of -31.3 kcal mol^{-1}. Both Pyr12 and Pyr13 configurations showed similar adsorption energies of -37.4 and -36.9 kcal mol^{-1}, respectively. However, while Pyr13 maintained a 45° angle with respect to the Mo(110) surface, structure Pyr12 increased the angle of inclination to 84° and shifted its initial position from atop a Mo atom to a hollow site as μ_2,η^2(C4,C5)-2H-Pyl-84°. Structure Pyr12 also showed an expansion in the inter-atomic bond length involving C4, while the other bonds changed only slightly. This is also reflected in the inter-atomic bond angles, where the angle centred on C4 showed a reduction by 2.7°. During the optimization of Pyr13, pyrrolyl rotates in such a way that the pyrrolic nitrogen positions directly atop a Mo atom. The molecule retains a similar angle with respect to the Mo(110) surface with an optimized configuration of μ_3,η^3(N,C5,C5)-2H-Pyl-45°. Structure Pyr14 did not change considerably upon optimization, and formed an μ_2,η^2(N,C4)-H-Pyl-13° structure with a corresponding adsorption energy of -31.4 kcal mol^{-1}. In the final configuration Pyr15, which is similar

Model	Adsorption Energy [kcal mol^{-1}]	Initial Geometry	Optimized Geometry
Pyr11	-31.3	η^2(C3,C4)-2H-Pyl-45° 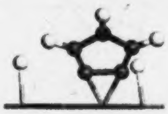	μ_3,η^4(C3,C3,C4,C4)-2H-Pyl-76° 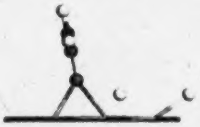
Pyr12	-37.4	η^2(C4,C5)-2H-Pyl-45° 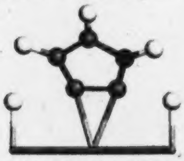	μ_2,η^2(C4,C5)-2H-Pyl-84° 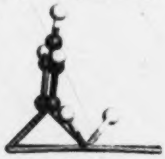
Pyr13	-36.9	η^2(N,C5)-2H-Pyl-45° 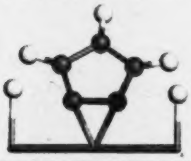	μ_3,η^3(N,C5,C5)-2H-Pyl-45° 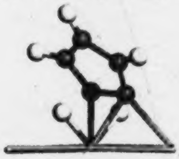
Pyr14	-31.4	μ_3,η^5-H-Pyl-15° 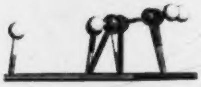	μ_2,η^2(N,C4)-H-Pyl-13° 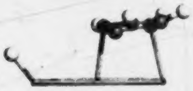
Pyr15	-29.9	μ_3,η^5-Pyr-15° 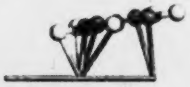	μ_3,η^4(N,C2,C3,C4)-Pyr-5° 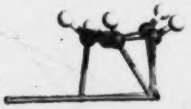

Figure 5.11 Initial and optimized geometries of inclined pyrrole and pyrrolyl adsorption on Mo(110) and the corresponding adsorption energies.

to Pyr14 except the N–H is not cleaved and pyrrole is adsorbed molecularly, the optimized configuration showed lower adsorption energy of -29.9 kcal mol^{-1}. The angle of inclination was also slightly reduced and bonded to the Mo(110) surface as μ_3,η^4(N,C2,C3,C4)-Pyr-5°.

5.3.4 Coverage Dependent Pyrrole Adsorption on Mo(110)

Pyrrole adsorption on Mo(110) was studied as a function of surface coverage to gain additional insight into the effects of lateral interactions between pyrrole molecules during adsorption. Three models including 2, 3 and 4 pyrrole molecules per unit cell were initially constructed in a parallel adsorption configuration as shown in Figure 5.12. In the case of two pyrrole molecules adsorbing on Mo(110) (Pyrrole-2M), both molecules showed a combination of initial nitrogen atom repulsion from the surface and some lateral interaction with a total adsorption energy of -35.7 kcal mol^{-1}. Adsorbate-adsorbate interactions caused the molecules to bond in different configurations; one as η^2(C4,C5)-Pyr-26° and the other as μ_3,η^4(N,C2,C4,C5)-Pyr-0°. In the case of the three pyrrole model (Pyrrole-3M), the optimization showed initial repulsive forces between the Mo(110) surface and the molecules, as well as considerable lateral interactions that result in two pyrrole molecules tilting and interacting with the surface through HOMO orbitals in an opposite molecular plane direction as η^1(C2)-Pyr-tilted and μ_2,η^2(C4,C5)-Pyr-tilted, respectively. The third molecule had less interaction with the other molecules and showed less tilting effect. The bonding mode formed in this case was μ_3,η^4(N,C2,C4,C5)-Pyr-0°, and the nitrogen atom moved up in a higher location than the rest of the ring. The total adsorption energy for the Pyrrole-3M configuration was -34.0 kcal mol^{-1}, and at this coverage all molecules showed significant ring deformation, particularly with the atoms involved with bonding to the Mo(110) surface. In the case of the four pyrrole model (Pyrrole-4M), the optimization resulted in an unstable system that did not bond to the Mo(110) surface, as evidenced by a total bonding energy of +1.0 kcal mol^{-1}. The pyrrole molecules did not show any observable ring deformation, which is also consistent with pyrrole not bonding to the Mo(110) surface. One additional model was constructed (model not shown) using four pyrrole molecules adsorbing in different modes (parallel, perpendicular, and tilted). In this configuration, only one pyrrole

Model		Initial Geometry	Optimized Geometry
Pyrrole-2M E_{ads} = -35.7 kcal mol^{-1}	Top View	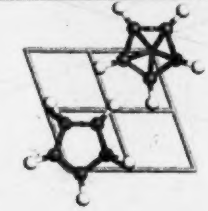	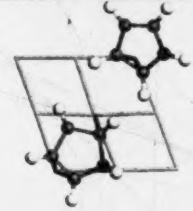
	Side View	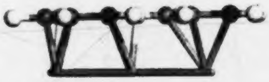	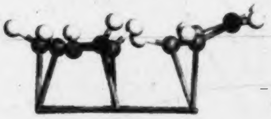
Pyrrole-3M E_{ads} = -34.0 kcal mol^{-1}	Top View	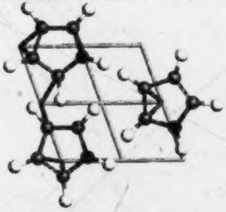	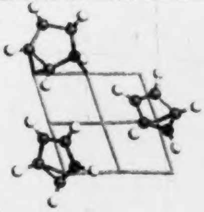
	Side View	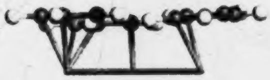	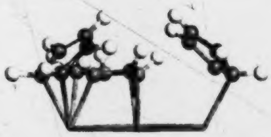
Pyrrole-4M E_{ads} = +1.0 kcal mol^{-1}	Top View	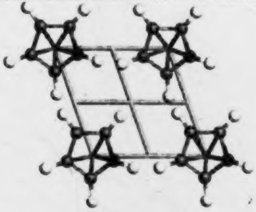	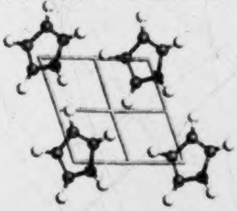
	Side View	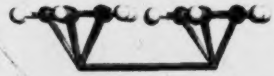	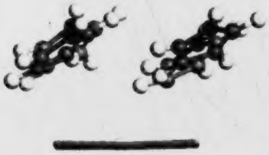

Figure 5.12 Initial and optimized geometries of parallel pyrrole adsorption on Mo(110) as function of surface coverage.

molecule bonded to the surface (initially set to parallel mode) in parallel position, while all other molecules did not form any bonds with the Mo(110) surface.

5.3.5 Calculated Vibrational Frequencies of Pyrrole Adsorption on Mo(110)

The vibrational frequencies of pyrrole-adsorbed configurations were calculated using density functional theory. These calculations were limited to the most stable configurations for each adsorption geometry, as predicted by the adsorption energy calculations. The models studied include structures Pyr 4 (μ_3,η^5-Pyr-0°), Pyr7 (μ_2,η^2(C4,C5)-2H-Pyl-81°, Pyr14 (μ_2,η^2(N,C4)-H-Pyl-13°), and Pyr15 (μ_3,η^4(N,C2,C3,C4)-Pyr-5°). All calculated vibrational frequencies are summarized in Table 5.5 along with the corresponding vibrational mode. The vibrational modes are similar to previously experimentally determined EELS frequencies, which includes out-of-plane ring distortion, in-plane ring breathing, C–H out-of-plane bending, N–H out-of-plane bending, C–H in-plane bending, N–H in-plane bending, C–H stretching, and N–H stretching.

Pyr4 configuration (μ_3,η^5-Pyr-0°) calculated frequencies evidenced all vibrational modes except the N–H oop bending mode, which is probably due to nitrogen atom involvement in forming a bond with the surface. The highest frequency was the N–H stretching mode at 3382 cm^{-1}. In contrast, Pyr7 configuration (μ_2,η^2(C4,C5)-2H-Pyl-81°) showed all possible vibrational modes with two additional vibrational frequencies that are assigned to Mo–H bending modes at 1793 and 2074 cm^{-1}. The stretching mode frequencies for both C–H and specifically N–H for structure Pyr7 were higher than the calculated frequencies in Pyr4. Slightly tilted adsorbed pyrrole configurations similar to Pyr14 (μ_2,η^2(N,C4)-H-Pyl-13°) and Pyr15 (μ_3,η^4(N,C2,C3,C4)-Pyr-5°) were also investigated to understand the effect of tilted geometry on the vibrational frequencies. In general, Pyr14 has similar frequencies to structure Pyr15, with the exception of the vibrational frequencies for N–H inp bending at 1680 cm^{-1} and N–H stretching at 3544 cm^{-1}, which were not evident in structure Pyr14. Furthermore, Pyr14 showed vibrational frequencies for Mo–H bending modes at 690, 1419, and 1981 cm^{-1}. This is due to the fact that one hydrogen atom is bonded to the surface in structure Pyr14.

5.4 Discussion

5.4.1 Chemisorption of Pyrrole on Mo(110)

In the present study, pyrrole adsorption and decomposition on Mo(110) was studied with TPD from 0.5 L to 5 L to quantify the structure-property relationship over a wide range of exposures. The TPD spectra for all surface exposures showed similar desorption features and energetics, except above saturation where a physisorption peak is evident as a result of pyrrole sublimation from the Mo(110) surface. The TPD spectra indicate pyrrole molecular desorption from Mo(110) increases slightly as a function of pyrrole exposure at an average temperature of 351 ± 10 K and a corresponding first-order adsorption energy of 21.9 ± 0.6 kcal mol^{-1}. Carbon and nitrogen accumulation on the Mo(110) surface was also observed in the present study, indicating Mo(110) is active for pyrrole denitrogenation. The carbon and nitrogen surface contamination did not significantly affect pyrrole desorption energetics, or the amount of molecular desorbing pyrrole from Mo(110).

The desorption temperature of pyrrole on Mo(110) is in excellent agreement with similar study on Rh(111) (Netzer et al., 1988). This study reported that intact pyrrole (m/z = 67) desorbs at approximately 360 K at a surface exposure of 3 L. The Rh(111) surface showed slightly different catalytic activity, as pyrrole decomposed on the surface leaving only surface carbon and desorbing H_2 (m/z = 2) and HCN (m/z = 27) at temperatures of 350 and 420 K, respectively. Baddeley et al. (1996) reported that pyrrole desorption on Pd(111) occurs at much lower temperatures (165 K) with H_2 desorption at 350 and 475 K, and HCN at 500 K, with surface carbon accumulation. On Ni(100) (Schoofs and Benziger, 1987), it has been reported pyrrole desorbs at a temperature of 235 K with H_2 desorption above room temperature leaving surface carbon and nitrogen.

Pt(111) (Tourillon et al., 1987) and Cu(100) (Sexton, 1985) surfaces did not show any catalytic activity for pyrrole decomposition, although pyrrole was reported to desorb from Cu(100) at temperatures of 170, 200, and 250 K, respectively. With the exception of Rh(111), all other metal surfaces showed a lower desorption temperature for pyrrole with no apparent trend in surface activity. We would expect these surfaces to react differently based on their coordination chemistry and surface electronic properties. Ni(100) and Cu(100) have a face-centered cubic (*fcc*) crystallographic structure with three different

Table 5.5 Calculated vibrational frequencies (cm^{-1}) of adsorbed pyrrole configuration models.

Mode	Pyr4 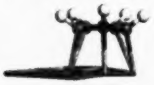	Pyr7 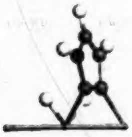	Pyr14 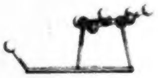	Pyr15 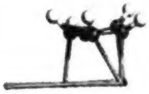
oop ring distortion	523, 675 703	698, 727	467, 514 767	512, 689 704
inp ring breathing	767, 790 914, 971 1044, 1073	858, 901 959, 937 1199	808, 830 1015, 968 1029	785, 798 937, 1013 1057
NH oop bending	…	1037 1068	…	…
CH oop bending	1160, 1221 1248, 1289	1208, 1224 1285, 131614422	1112, 1135 1159, 1186 1249, 1276	1101, 1150 1245, 1262 1294, 1329
CH inp bending	1430, 1507 1528, 1587	1560 1615	1450, 1491 1566, 1608	1460, 1522 1570, 1591
NH inp bending	1675	1659	…	1680
CH stretch	3128, 3135 3148, 3169	3172 3268	3131, 3158 3202, 3223	2960, 3144 3178, 3238
NH stretch	3382	3638	…	3544
MoH bending	…	1793, 2074	1419, 1981	…

bonding sites on the (100) surface (i.e. one-fold, two-fold, and four-fold), while Rh(111), Pd(111), and Pt(111) are also *fcc* but have different surface bonding sites on the (111) surface plane (i.e. one-fold, two-fold, and three-fold). Molybdenum has a body-centered cubic (*bcc*) structure and the (110) orientation has four possible coordination sites; one-fold, two-fold, three-fold, and four-fold. The different possible bonding sites would produce different adsorption energies with the adsorbate, and thus the differences in energetics between these metal surfaces are largely due to the different surface structures.

Based on the above adsorption/desorption behaviour of pyrrole on Mo(110), pyrrole adsorption geometry on Mo(110) can be tentatively discussed. It is reasonable to suggest at low surface coverages (< 50% of saturation), pyrrole does not exhibit strong lateral interactions and adsorbs on Mo(110) through π orbitals in a flat-lying geometry without C–H or N–H bond cleavage. A portion of the flat-lying pyrrole will molecularly desorbs at approximately 351 ± 10 K (E_{ads} = 21.9 ± 0.6 kcal mol^{-1}) and additional adsorbed pyrrole will decompose on the Mo(110) surface. This mechanism is supported by two experimental observations; no reaction products were detected desorbing off the surface, and Auger analysis following TPD indicated a C:N surface atomic ratio of 4:1 consistent with molecular pyrrole. At high surface coverages (> 50% of saturation) pyrrole adsorbs flat-lying as described previously, and as the surface approaches saturation pyrrole adsorbs in a slightly tilted configuration possibly due to lateral interactions between the pyrrole molecules, as suggested by the electron density distribution and HOMOs of pyrrole. With surface heating a portion of these species desorb intact, while the other adsorbed species decompose leaving surface carbon and surface nitrogen. Pyrrole decomposition on Mo(110) would proceed by cleaving C–C bonds followed by N–C bonds, leaving pyrrole fragments on the surface.

5.4.2 Orientation of Pyrrole on Mo(110)

The electronic structure of pyrrole and previously published vibrational data can provide insight into the adsorption mode of pyrrole on Mo(110). The highest occupied molecular orbitals (HOMO) are the π-orbitals associated with the carbon atoms, which would be most susceptible to electrophilic attack if pyrrole approaches a Lewis acid surface. Thus, electrophilic attack should occur preferentially at the α-carbon position (Pan and Stair, 1986). If the molybdenum surface promotes dehydrogenation by cleaving C–H bonds and acts as Lewis acid, then pyrrole would be expected to interact with the Mo(110) surface through its π orbitals in either a perpendicular or tilted mode, taking into consideration adsorbate-adsorbate lateral interactions. If the molybdenum surface does not promote C–H cleavage, pyrrole would interact with the Mo(110) surface via a flat-lying adsorption mode or slightly tilted due to geometrical restrictions. In the present study, hydrogen was not observed desorbing from Mo(110) as a reaction product, which suggests Mo(110) does not promote hydrogen bond cleavage; therefore, pyrrole is suggested to molecularly adsorb intact in a flat-lying and/or slightly tilted adsorption mode.

Studies of the vibrational frequencies of pyrrole adsorption on metal surfaces are limited and only a few reported it on metal single crystals. On Cu(110) (Sexton, 1985) and at a sufficient surface exposure to generate multilayers, pyrrole adsorption appeared to be molecularly reversible with no other products observed desorbing from the surface other than molecular pyrrole and it does not cleave the N–H bond to form pyrrolyl species. It was suggested that at low exposures, each molecule is weakly π-bonded to the Cu(100) surface with the molecular plane parallel to the surface plane. Upon a further increase in surface exposure, a second layer of pyrrole is adsorbed with its molecular ring inclined toward the surface normal. The adsorption of pyrrole on Pd(111) (Baddeley et al., 1996), was suggested that an interaction between the surface and pyrrole occurs through the aromatic π electron system. Pyrrole adsorption at a temperature of 300 K was attributed to parallel adsorption, and a slightly inclined configuration can coexist that involves the nitrogen lone pair orbital after cleaving the N–H bond. A portion of the flat-lying adsorbed species desorbs intact at a temperature of approximately 360 K, while the remainder would undergo C–C bond cleavage and produce H_2 at approximately 350 K and HCN at above 420 K leaving surface carbon.

The electron scattering mechanism in EELS follows the metal surface selection rule (Bunker and Jensen, 1998), which states that only those vibrational modes with dynamic dipole component perpendicular to the surface should be observed (not parallel modes). Therefore, for parallel pyrrole adsorption the most intense features should be those involving atomic displacement perpendicular to the aromatic ring (perpendicular to the metal surface), which represent out-of-plane C–H bending and out-of-plane N–H bending. Other loss features at lower intensities can appear and may assigned to in-plane C–H bending, ring stretching, and C–H stretching. These features can be explained as a result of invoking a small degree of molecular tilt away from the surface. Examining the

EELS vibrational frequencies of pyrrole adsorption on the Mo(110) surface at 100 K at low surface exposure (0.5 L and 1.0 L), the highest intense loss feature belongs to C–H out-of-plane bending while other features (in-plane ring and C–H stretching) are less pronounced. These results were also previously observed on Cu(100) (Sexton, 1985) and Pd(111) (Tourillon et al., 1987) surfaces, and are in excellent agreement with the present study. Increasing the surface exposures shows an increase in the stretching mode intensities (C–H and ring stretch loss), which implies either an increased degree of tilt for all molecules or the coexistence of parallel molecules and strongly tilted adsorption configuration. Increasing the surface temperature shows the disappearance of some lower loss features and the weakening in C–H out-of-plane bending modes with slight intensity changes in the C–H stretching modes. These changes indicate either the orientation of adsorbed pyrrole went through some changes on the surface or pyrrole started to decompose on the surface showing vibrational frequencies of decomposed species on the Mo(110) surface.

5.4.3 Adsorption Energy Calculations of Pyrrole on Mo(110)

The TPD spectra along with the EELS vibrational frequencies indicated that pyrrole adsorbs in parallel mode on the Mo(110) surface with the coexistence of possibly tilted modes at higher surface exposures. Examining all optimized parallel adsorption geometries and calculated adsorption energies, structures Pyr2 and Pyr4 are most likely to occur in comparison to the other parallel structures. Although the initial adsorption geometry in these two models was different, both models resulted in an optimized μ_3,η^5-Pyr-0° configuration. This type of interaction is reflected strongly on the molecular structure of adsorbed pyrrole without destroying its aromaticity or cleaving any hydrogen bonds. The inter-atomic bond lengths within the ring showed relatively uniform bond length and an expansion in the heteroatom angle to an equivalent degree of other carbon atoms within the ring. Structure Pyr3 is initially positioned such that the pyrrolic nitrogen is directly atop a surface Mo atom, and evolves into a structure that is similar to Pyr2 and Pyr4 with slightly lower adsorption energy. However, since the adsorption energies of the Pyr2, Pyr3 and Pyr4 optimized configurations are within the relative uncertainty of the total energy calculations (1.2 kcal mol^{-1}), there is no significant difference between the adsorption energies of these structures. Thus, on the basis of adsorption energies, the preferred adsorption geometry in parallel configuration would be in the following order; Pyr2 ≈Pyr3 ≈Pyr4 > Pyr5 > Pyr1. This would indicate pyrrole adsorbs preferentially on Mo(110) as μ_3,η^5-Pyr-0° , and structures Pyr1 and Pyr5 are local energy minima on the potential energy surface. Furthermore, during parallel pyrrole adsorption the Mo(110) surface acts as a Lewis acid and does not promote hydrogen abstraction. These observations are in agreement with the adsorption energies and apparent lack of gas-phase H_2 from the temperature programmed desorption and Auger electron spectroscopy analysis.

Based on the relative adsorption energies of the perpendicular and tilted adsorption configurations on Mo(110), structure Pyr7 showed the highest stability among the configurations studied. This indicates that the Pyr7 structure is the most energetically favourable if Mo(110) promotes hydrogen abstraction to form pyrrolyl species. This is consistent with the electronic structure of pyrrole whereby pyrrole is an electron rich molecule that reacts readily with electrophiles but is not susceptible to nucleophilic attack. In comparison with the tilted models as shown in Figure 5.10, tilted adsorption did not show similar stability as structure Pyr7. However, tilted adsorption did result in comparable adsorption energies as pyrrolyl adsorption (structures Pyr10, Pyr11, Pyr12, and Pyr13) or as molecular pyrrole adsorption (structure Pyr15). Thus, it is reasonable to suggest that pyrrole may adsorb perpendicular to the surface after abstracting hydrogen atoms from the approaching side, similar to structure Pyr7, since hydrogen was not observed as a reaction product from the TPD spectra. Based on this observation, pyrrole adsorption as pyrrolyl species following hydrogen abstraction is not likely to occur on Mo(110). Therefore, structure Pyr15 with similar adsorption energy as parallel pyrrole adsorption would be the preferred adsorption model for perpendicular and tilted pyrrole adsorption.

The possibility of forming a tilted adsorbed species through phase transformation from parallel adsorption was studied by calculating the activation energy barrier using the optimized models of Pyr2, Pyr3, and Pyr4 as initial geometries. The activation energies were in the range of 160 – 250 kcal mol^{-1}, which are significant compared to the relative adsorption energies for parallel adsorption (28.7 – 31.5 kcal mol^{-1}). Thus, it is clearly not possible for this type of geometrical transformation to occur on Mo(110) during the course of increasing surface temperature.

The coverage dependent adsorption configurations suggest that at high pyrrole coverages on Mo(110), the adsorption energy per pyrrole molecule is significantly reduced and the adsorption geometry is perturbed due to adsorbate-adsorbate interactions. During the adsorption of 2 pyrrole molecules per Mo(110) unit cell, the average pyrrole adsorption energy was -17.9 kcal per adsorbed pyrrole molecule, and this adsorption energy reduces to -11.3 kcal per adsorbed pyrrole molecule for the adsorption of 3 pyrrole molecules. Lateral interactions between the adsorbed pyrrole molecules further destabilize pyrrole adsorption on Mo(110) at a coverage of 4 pyrrole molecules per unit cell, resulting in a system that did not bond to the Mo(110) surface. These results suggest that since the adsorption energy per pyrrole molecule is lowered significantly by repulsive interactions between adsorbed pyrrole molecules, a more stable structure could evolve through the desorption of pyrrole from the surface. It should be noted, however, the calculations use individual gas-phase pyrrole molecules in an infinite vacuum cell as an energetic reference and not a cluster of pyrrole molecules. The optimized geometries at higher pyrrole coverages also indicate that different adsorption modes at higher pyrrole coverages may coexist with parallel pyrrole adsorption, specifically slightly tilted adsorption modes relative to the Mo(110) surface.

The calculated vibrational frequencies of structure Pyr4 (μ_3,η^5-Pyr-0°) showed out-of-plane ring distortion in the range of 675 – 703 cm^{-1}, in-plane ring breathing in the range of 767 – 1073 cm^{-1}, C–H out-of-plane bending in the range of 1160 – 1289 cm^{-1}, C–H in-plane bending in the range of 1430 – 1587 cm^{-1}, and C–H stretching mode in the range of 3128 – 3117 cm^{-1}. Other vibrational modes included N–H in-plane bending at 1675 cm^{-1} and N–H stretching at 3382 cm^{-1}. The vibrational frequencies of the slightly tilted configuration Pyr15 (μ_3,η^4(N,C2,C3,C4)-Pyr-5°) were 512 – 704 cm^{-1} for out-of-plane ring distortion, 785 – 1057 cm^{-1} for in-plane ring distortion, 1101 – 1329 cm^{-1} for C–H out-of-plane bending, 1460 – 1591 cm^{-1} for C–H in-plane bending, a 1680 cm^{-1} for N–H in-plane bending, 2960 – 3238 cm^{-1} for C–H stretching and 3544 cm^{-1} for N–H stretching. The EELS spectra of pyrrole adsorption over Mo(110) surface at 100 K is in good agreement with calculated frequency ranges of the parallel (Pyr4) and the slightly tilted (Pyr15) configurations. The EELS data indicates out-of-plane ring distortion (633 – 725 cm^{-1}), in-plane ring breathing (862 – 1035 cm^{-1}), C–H out-of-plane bending (1379 – 1384 cm^{-1}), C–H in-plane bending (1441 – 1585 cm^{-1}), and C–H stretching (2938 – 3104 cm^{-1}). The slight differences in the frequencies are possibly indicative of a slightly tilted adsorption configuration, which is evidenced by the calculated vibrational frequencies of Pyr15. An increase in the surface temperature to 300 K results in a decrease in intensity of several loss peaks compared to the spectra at 100 K. This suggests that pyrrole adsorption geometry may change to a slightly tilted configuration upon sample heating.

To investigate whether other adsorption configurations of pyrrole are present on the surface, the vibrational frequencies of other stable adsorption configurations similar to Pyr7 and Pyr14 were calculated and examined closely with the EELS spectra. Although, some similarities are observed between EELS vibrational frequencies and structures Pyr7 and Pyr14, a distinct vibrational mode feature assigned to Mo–H bending at 1793 and 2074 cm^{-1} for Pyr7 and 1419 and 1981 cm-1 for Pyr14 makes it clear that hydrogen on the surface is not likely to occur. Thus, adsorption configurations similar to structures Pyr7 and Pyr14 are not possible.

5.4.5 Adsorption of Pyrrole on C/N – Mo(110)

The C/N-Mo(110) surface was studied to determine the adsorption energies and surface activity as a function of carbon and nitrogen accumulation. The amount of pyrrole desorption as a function of consecutive surface exposures increased slightly based on the integrated peak areas. However, carbon accumulation on the surface did not increase linearly as a function of consecutive exposure (Figure 5.3). 0.5 L pyrrole exposure showed an opposite trend compared to 5 L exposure, while other coverages had intermediate values. Surface nitrogen concentration showed a slight increase as a function of consecutive exposures, and was consistent for all exposures studied. This clearly suggests the denitrogenation activity of pyrrole on Mo(110) was not affected by surface carbon and nitrogen after three consecutive exposures of pyrrole and heating to 1000 K.

Transition metal carbides and nitrides, including molybdenum, have demonstrated catalytic activity for hydrotreating reactions, including hydrodesulfurization (Markel and Vanzee, 1990; Nagai and Miyao, 1992) and hydrodenitrogenation (Choi et al., 1995; Li et al., 1999); however, the reactivity of these surfaces depends on the nature of the surface carbides and nitrides. Frühberger et al. (1996) suggested that the nature of the adsorbed carbon on Mo(110) has a strong effect on catalytic properties; they observed that carbidic carbon produces changes in surface chemistry while graphitic carbon has no effect other than to reduce reactivity. Roe and Schulz reported carbidic overlays on Mo(110) do not alter the reactivity of ethanethiol (Roe and Schulz, 2000), but 1,2-ethanedithiol (Roe and Schulz, 2000) showed clear changes in selectivity and reaction pathways on both defective and *p*(4x4)-C/Mo(110) surfaces compared to Mo(110). They also noted a shift to lower desorption temperatures on carbided Mo(110) indicating a lowering of the adsorption energy. Additionally, pyridine adsorption and reaction on the carbidic Mo(110) surface did not show changes in catalytic activity for pyridine decomposition compared to clean Mo(110) as indicated in chapter four. Clearly, carbidic surface carbon alters the nature of the Mo(110) surface and this may alter the catalytic activity and selectivity for a given adsorbate. However, in the case of pyrrole adsorption and decomposition on carbidic Mo(110) surfaces, carbidic carbon did not affect the adsorption energy or extent of surface decomposition. Furthermore, the C/N-Mo(110) surface did not promote additional reaction pathways, as there were no additional reaction products observed.

5.5 Conclusions

The results from this study indicate that pyrrole molecularly adsorbs and decomposes on both Mo(110) and C/N-Mo(110) giving rise to surface carbon (carbidic) and nitrogen with no additional desorbing reaction products. Molecular pyrrole desorption occurs at an average temperature of 351 ± 10 K with a corresponding first order adsorption energy of 21.9 ± 0.6 kcal mol^{-1} for the surface exposures studied. Surface saturation was attained at approximately 4 L exposure, as evidenced by a low-temperature physisorption peak at approximately 250 K that increases in intensity upon 5 L exposure. Auger analysis following TPD indicted a C:N ratio of 4:1 at exposures less than 2 L and 2:1 at higher exposures. Subsequent TPD analysis on the C/N-Mo(110) surface resulted in similar surface activity compared to clean Mo(110). At low surface exposures, EELS vibrational frequencies and DFT calculations suggest pyrrole adsorbs flat-lying through the π orbitals without any bond cleavage, similar to Pyr2, Pyr3 and Pyr4 models with an adsorption energy of -28.7 to -31.5 kcal mol^{-1}. These adsorption models resulted in flat-lying pyrrole bonding to three Mo atoms as μ_3,η^5-Pyr-0° (structures Pyr2 and Pyr4) or μ_3,η^4(N,C2,C4,C5)-Pyr-0° (structure Pyr3). As the surface exposure increases, lateral interactions between pyrrole molecules during adsorption are suggested to cause competitive adsorption resulting in the coexistence of slightly tilted pyrrole molecules bonding to the surface along with parallel adsorption configurations. This slightly tilted configuration can be assigned to a μ_3,η^4(N,C2,C3,C4)-Pyr-5° (structure Pyr15) bonding mode with an adsorption energy of -29.9 kcal mol^{-1}. These slightly tilted adsorption configurations are a result of molecular interaction and not the result of phase transformation on the surface.

6. ETHYLAMINE ADSORPTION AND REACTION MECHANISM ON Mo(110)

6.1 Introduction

Investigations of organic amine (i.e. R-NH_2) adsorption on metal surfaces have not been thoroughly studied despite the considerable importance as a representative intermediate species in heterocyclic organonitrogen hydrodenitrogenation. As discussed previously, following heterocyclic organonitrogen ring hydrogenation one C–N bond is cleaved and C_n-amines form intermediate species bonded to the catalyst surface, which further decompose and desorb as C_n-hydrocarbons and ammonia. The adsorption geometry on the catalyst surface in turn determines the activation energy required for bond scission (i.e. C–H, N–H, C–N, or C–C), which is required for hydrodenitrogenation. It is, therefore, important to gain further insight regarding amine adsorption and decomposition on model hydrotreating catalyst surfaces to understand the salient features of the reaction mechanism (transition states) and energetics. This level of fundamental knowledge should provide key information for understanding of the hydrodenitrogenation reaction network.

The adsorption of amines on transition metal surfaces is generally believed to occur through the amine group toward the surface while the molecular chain is more or less perpendicular to the surface (Ditlevsen et al., 1993; Gardin and Somorjai, 1992; Pearlstine and Friend, 1986). The authenticity of such a hypothesis was validated by measuring the heat of adsorption of amines on reduced and oxidized iron powders at 25 °C (Yao, 1963). This study indicated amines chemisorb on transition metals through donation of the nitrogen lone pair electrons to the metal surface to form a predominantly covalent bond. The steric effect was also shown to play an important role in compensating the effect of higher electron density at the secondary and tertiary amino groups.

The objective of this research is to study the adsorption and decomposition of ethylamine ($CH_3CH_2NH_2$) on Mo(110) using temperature-programmed desorption and Auger electron spectroscopy. In addition to the experimental studies, first-principles quantum mechanical calculations will be used to study the molecular adsorption and surface reaction of ethylamine on Mo(110) in an attempt to gain additional insight about the structure-reactivity relationship for organonitrogen hydrodenitrogenation. An initial adsorption configuration and reaction mechanism is proposed based on the experimental observations and transition state calculations.

6.2 Experimental Results

6.2.1 Temperature Programmed Desorption

Temperature-programmed desorption spectra for ethylamine adsorption on Mo(110) were collected by monitoring and recording the intensity variation of several mass fragments (m/z ratios) over the range of 2 to 45 to detect desorption products. Due to ethylamine sample handling limitations, only exposures at saturation level (4 L) were studied. The only reaction products detected desorbing from the surface were acetonitrile (m/z = 41) and hydrogen (m/z = 2), in addition to ethylamine (m/z = 30).

Figures 6.1, 6.2 and 6.3 show the TPD spectra of ethylamine (m/z = 30) and the observed decomposition products, acetonitrile (m/z = 41) and molecular hydrogen (m/z = 2), on Mo(110) at 4 L pyrrole exposure, respectively. The temperature axis is truncated at 600 K as no additional desorption peaks were observed between 600 and 1000 K. The TPD spectrum clearly indicates the surface was initially saturated with ethylamine, which is indicated by a sharp miltilayer physisorption peak at approximate temperature of 157 ± 10 K. Leading edge analysis of the multilayer desorption features yields an ethylamine heat of sublimation of 7.7 kcal mol^{-1}, which is in excellent agreement with the literature value of 7.4 kcal mol^{-1} (Lide, 2004). Nonetheless, the energy of multilayer desorption does not provide essential information about ethylamine molecular adsorption and surface reaction. The ethylamine TPD spectrum also indicates a possible shoulder peak along with the physisorption peak at an approximate temperature of 184 ± 10 K with an adsorption energy of 9.2 ± 0.6 kcal mol^{-1} based on leading edge analysis and attributed to ethylamine desorption from the second mololayer on the Mo(110) surface. The acetonitrile desorption peak was observed at an approximate temperature of 212 ± 10 K with an approximate adsorption energy (Redhead, 1962) of 13.0 ± 0.6 kcal mol^{-1}. The hydrogen TPD spectrum indicates a main desorption peak at 332 ± 10 K with a

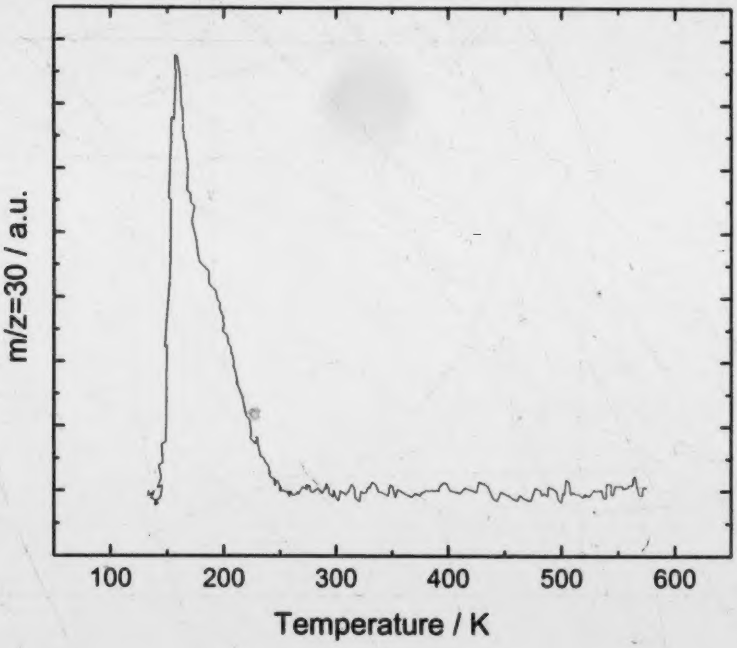

Figure 6.1 Temperature Programmed Desorption (TPD) spectra of ethylamine (m/z = 30) at saturation exposure (4 L) on clean Mo(110).

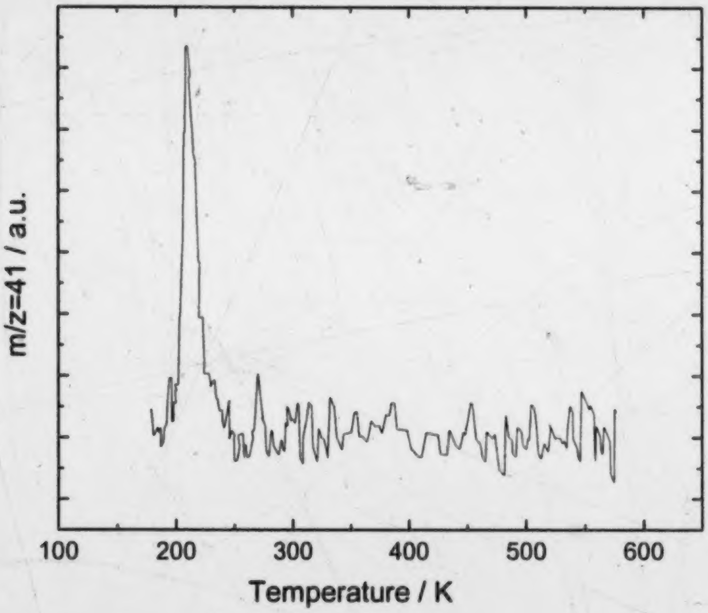

Figure 6.2 Temperature Programmed Desorption (TPD) spectra of acetonitrile (*m/z* = 41) at saturation exposure (4 L) on clean Mo(110).

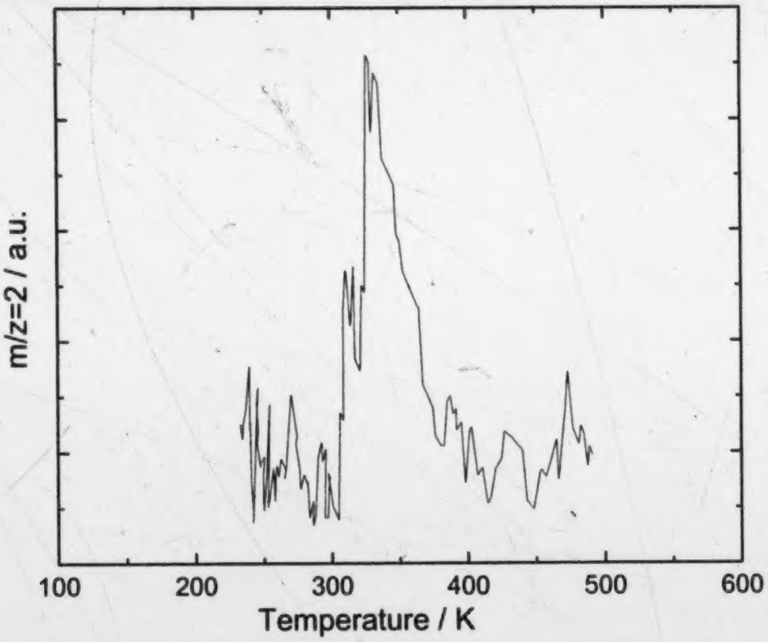

Figure 6.3 Temperature Programmed Desorption (TPD) spectra of hydrogen (*m/z* = 2) at saturation exposure (4 L) on clean Mo(110).

corresponding adsorption energy of 20.7 ± 0.6 kcal mol^{-1}, and a shoulder peak at an approximate temperature of 316 ± 10 K (19.6 ± 0.6 kcal mol^{-1}). No other desorption products were observed, specifically NH_3, CH_4, and N_2.

6.2.2 Surface Composition Analysis

Figure 6.4 shows the Auger electron spectrum of Mo(110) following ethylamine TPD and surface heating to 1000 K. The AES spectrum indicates the presence of surface carbon and nitrogen at an approximate carbon to nitrogen ratio of 4:1. The calculation of the atomic ratio of carbon to nitrogen was based on measuring the Auger peak-to-peak amplitude for C (KLL, 272 eV), N (KLL, 386 eV) and Mo (MNN, 187 eV) using the relative sensitivity factor for each element at a beam energy of 1.5 kV; 0.257 for carbon, 0.470 for nitrogen, and 0.392 for molybdenum (Davis et al., 1978). A carbon to nitrogen ratio of 2:1, which represents molecular ethylamine would be expected since acetonitrile and hydrogen were the only detected desorbing species and neither ammonia nor nitrogen were detected. Therefore, the non-stoichiometric C:N ratio is ascribed to either nitrogen diffusion into bulk Mo (Chen, 1996), or the desorbing nitrogen products were below the sensitivity of the mass spectrometer used in the present study.

6.3 Molecular Simulation

6.3.1 Ethylamine Electronic Structure

The electronic structure of ethylamine ($CH_3CH_2NH_2$) was initially investigated by calculating the electrostatic potential distribution, electrophilic and nucleophilic Fukui function, highest occupied molecular orbital (HOMO), and lowest unoccupied molecular orbital (LUMO) as shown in Figure 6.5. Considering the electrostatic potential distribution (Figure 6.5a), the blue region around the nitrogen is the most electron-rich region and is susceptible to positive ion attraction, while the hydrogen atoms around the amine group (red color region) represent the most electron-deficient region within the molecule. The electrophilic Fukui function of ethylamine (Figure 6.5b) indicates ethylamine can act as a nucleophile forming a bond with the catalyst surface (electrophiles) through the nitrogen atom, while the nucleophilic Fukui function (Figure

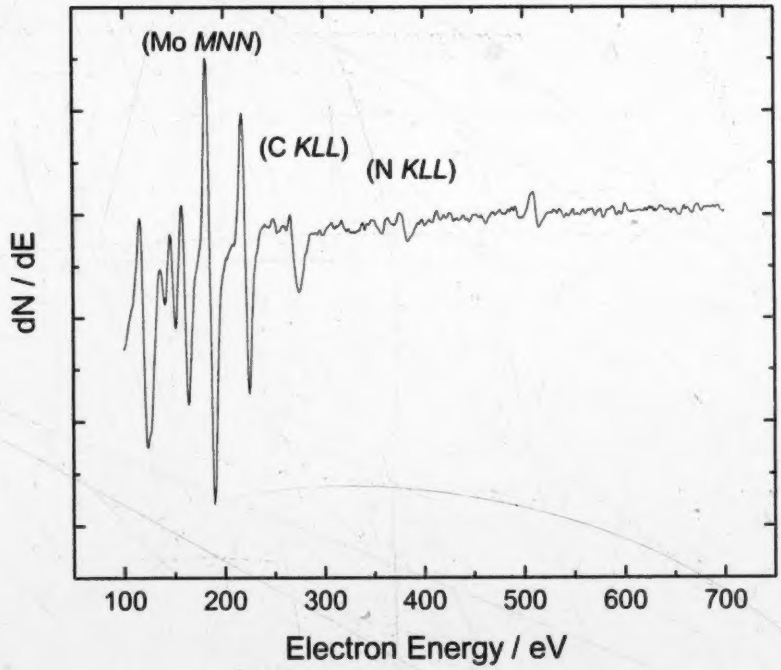

Figure 6.4 Auger spectra of ethylamine on Mo(110) at surface exposure of 4 L following TPD. Auger electron signals of molybdenum correspond to 186 eV, carbon to 272 eV, and nitrogen 386 eV.

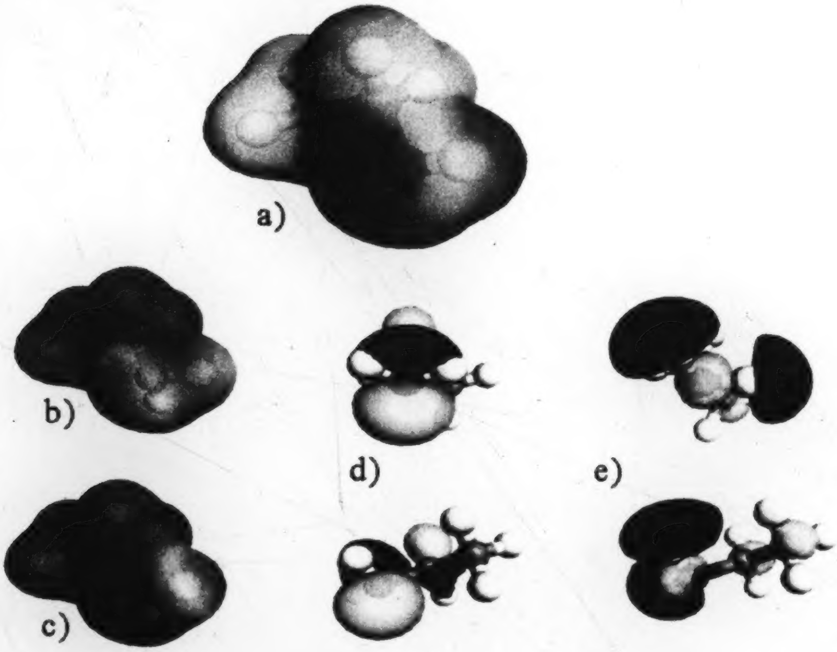

Figure 6.5 Electronic structure of ethylamine calculated by density functional theory (GGA-PBE pesudo-potential) with 0.04 isosurface, a) Electrostatic Potential, b) Electrophilic Fukui function, c) Nucleophilic Fukui function, d) HOMO, and e) LUMO.

6.5c) occurs through the hydrogen atoms within the amine group. The HOMO, which represents the highest probability to donate electrons forming a bond with the catalyst active site by electrophilic attack (Figure 6.5d), is located around the NH_2 group (mostly on the top and the bottom of the nitrogen atom) and slightly around the α-CH_2 group. The LUMO of ethylamine is located mostly around the hydrogen atoms in the amine group, which indicated this region is the most favorable for nucleophilic attack.

6.3.2 Ethylamine Adsorption on Mo(110)

Ethylamine adsorption on Mo(110) was studied with DFT to investigate the initial adsorption mode (or modes) giving rise to the molecular desorption features observed in the TPD analysis, and to suggest potential structural and bonding changes during adsorption. The relative energies of the structures were also calculated to quantify the adsorption energies of the possible molecular adsorption modes. The adsorption modes studied include all possible modes previously cited within the literature (Ditlevse et al., 1993; Gardin and Somorjai, 1992; Pearlstine and Friend, 1986), which indicate ethylamine adsorption primarily occurs through the nitrogen atom. In addition, several additional plausible adsorption configurations were also investigated. Ethylamine and the Mo(110) surface were fully optimized prior to adsorption calculations.

Figure 6.6 shows an overview of the initial proposed bonding modes and the final optimized configurations. The first mode examined, structure $EAI1^1$, was modeled with an initial bond through the nitrogen atom with the surface with the CH_3 group approaching the surface. After geometry optimization, ethylamine moved away from the surface without any bond formation and eventually did not bond (DNB). The second configuration was modeled with ethylamine bonding though the nitrogen atom with the ethyl group parallel to the Mo(110) surface (structure $EAI1^2$). Similar to $EAI1^1$, this configuration showed instability and repulsive forces between the surface and the ethyl group resulting in ethylamine moving away from the surface and eventually did not bond to the surface. The next logical configuration (structure $EAI1^3$) was modeled as a slightly different configuration from EAI^2 with the α-carbon and nitrogen atom approaching nearly parallel to the Mo(110) surface while the ethyl group is tilted 65° with respect to the surface. This configuration again did not bond with the surface, indicating a repulsive

Model	Adsorption Energy [kcal mol^{-1}]	Initial Geometry	Optimized Geometry
EAI1^{1}	DNB	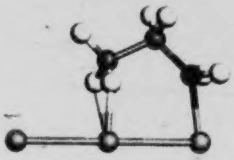	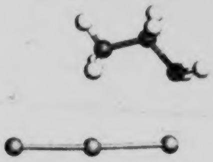
EAI1^{2}	DNB	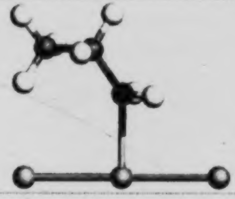	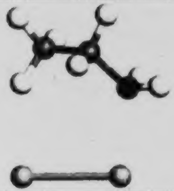
EAI1^{3}	DNB	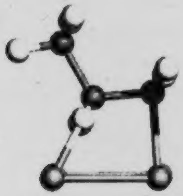	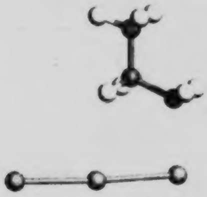
EAI1^{4}	-20.6	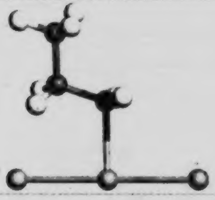	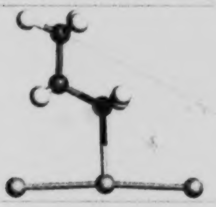
EAI1^{5}	-19.1	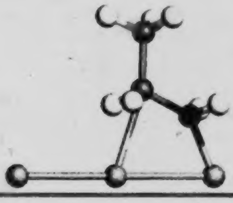	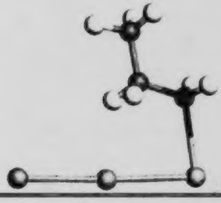

Figure 6.6 Initial and optimized configurations for ethylamine adsorption on Mo(110) and the calculated adsorption energies.

force between the α-carbon and the Mo(110) surface. Moving the ethyl group away from the surface in a perpendicular configuration, while the nitrogen atom is bonded to the surface, and having the α-C–N bond in tilted (20°) position with the surface (structure EAI1^4) resulted in a stable adsorption configuration with a calculated adsorption energy of –20.6 kcal mol^{-1}. In structure EAI1^5, a bonding configuration similar to EAI1^4 was modeled with the C–N bond in a tilted (28°) position with respect to the Mo(110) surface and both the nitrogen and the α-carbon atoms bonded to the surface. During geometry optimization, the α-carbon bond was not stable and the optimized structure bonded only through the nitrogen atom to the Mo(110) surface with an adsorption energy of –19.1 kcal mol^{-1}. It is evident the optimized EAI1^4 and EAI1^5 models are similar in their adsorption geometry and adsorption energies, with the slight difference in the adsorption energies attributed to the convergence quality used in the DFT calculations. Therefore, it can be concluded the preferred adsorption mode of ethylamine on Mo(110) is through the nitrogen atom of the amine group with the hydrocarbon chain (approximately) perpendicular to the surface. This adsorption configuration was used as the initial geometry for studying ethylamine reaction on Mo(110).

6.3.3 Ethylamine Reaction on Mo(110)

Based on the calculated adsorption energies for the most stable initial ethylamine adsorption configuration as discussed in the previous section, the reaction products (hydrogen and acetonitrile) as observed during ethylamine temperature programmed desorption, and previously proposed ethylamine reaction mechanisms on Ni(111) (Ditlevse et al., 1993; Gardin and Somorjai, 1992), a reaction mechanism for ethylamine decomposition on Mo(110) surface was proposed (Figure 6.7). This reaction mechanism includes the most energetically preferred adsorption geometries for each intermediate after intensive adsorption energy calculations for each proposed intermediate. The reaction and activation energies for each elementary step along the reaction pathway were calculated and are included in Figure 6.7. In addition, a combination of Linear Synchronous Transit (LST) and Quadratic Synchronous Transit (QST) methods were used to find the transition state (TS) and to calculate the required activation energy to proceed from one intermediate to another. Transition state calculations used 10 images associate along the reaction path going from one intermediate species to another with a convergence tolerance set to fine quality (0.05 eV/Å) with a maximum of 5 QST steps.

The initial ethylamine adsorption configuration (Figure 6.7) is labeled as structure EAI1 (structure EAI1[4] in the previous section) whereby ethylamine is bonded to the surface though the nitrogen atom and the ethyl group is approximately perpendicular to the Mo(110) surface. The second proposed step would proceed by cleaving an α-C–H bond and adsorbing the hydrogen atom on the surface, and at the same time allowing the α-C atom to interact with the surface by forming another bond with the surface along with the N-atom, as shown in structure EAI2 (CH_3CHNH_2). This process has an activation energy (EAI1 – EAI2) of 35.8 kcal mol^{-1} (TS1) and structure EAI2 has an adsorption energy of –24.8 kcal mol^{-1}. The other α-C–H is then cleaved and allowed to adsorb on the surface while the α-C atom interacts with the surface by forming two bonds. However, following geometry optimization this configuration was not stable and reverted back to structure EAI2. Therefore, a different intermediate was proposed where one of N–H bonds is cleaved and the hydrogen atom is allowed to adsorb on the surface while the C–N bond converted to a double bond. Again this proposed intermediate was not stable upon optimizing. During geometry optimization, this structure translated into a different and more stable configuration, which is referred to as structure EAI3. In this configuration, both α-C–H and one N–H are cleaved and adsorbed on the Mo(110) surface while the α-C–H is converted to a double bond. The calculated adsorption for this intermediate (CH_3CNH) was –50.4 kcal mol^{-1} and the required activation energy from EAI2 – EAI3 was 85.3 kcal mol^{-1} (TS2). Further bond cleavage is proposed as intermediate EAI4 (CH_3CN), where the other N–H bond is cleaved and hydrogen adsorbs on the surface while the nitrogen atom forms two bonds with the surface. This intermediate configuration showed the highest stability among all previous intermediates with calculated adsorption energy of –63.9 kcal mol^{-1} and an activation energy of 31.9 kcal mol^{-1} from EAI3 – EAI4 (TS3). The next proposed intermediate was based on cleaving the α-C-atom bond with the surface and converting the α-C=N to a triple bond while maintaining the four hydrogen atoms on the surface (EAI5), followed by cleaving the N-atom bond with surface and desorbing acetonitrile (CH_3CN) from the surface

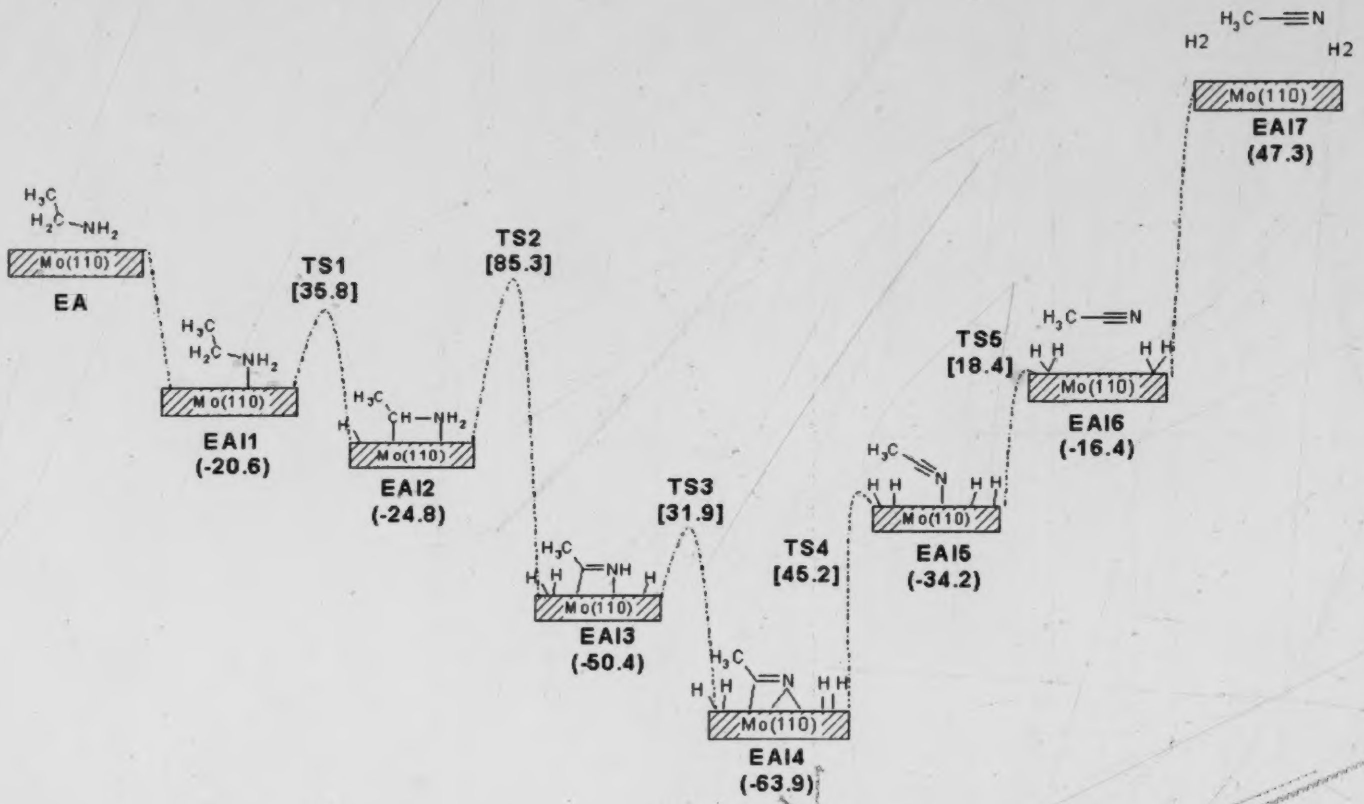

Figure 6.7 Reaction coordinate diagram ethylamine decomposition on Mo(110). The activation energies associated with each transition state are labeled above the pathway and energies in parenthesis are the calculated adsorption energies. Units of energy are kcal mol^{-1}.

(EAI6). The calculated adsorption energies for structures EAI15 and EAI16 were –34.2 and –16.4 kcal mol^{-1}, respectively, while the associated activation energies from EAI4 – EAI5 (TS4) and then from EAI5 – EAI6 (TS5) were 45.2 and 18.4 kcal mol^{-1}, respectively. The last structure is the desorption of hydrogen atoms as molecular hydrogen, as shown in structure EAI7, which has an adsorption energy of 47.3 kcal mol^{-1}.

6.3.4 Calculated Vibrational Frequencies of Ethylamine Adsorption on Mo(110)

Initially the vibrational frequency of a gas phase ethylamine was calculated (Table 6.1) and compared to experimental gas phase ethylamine frequencies (Hamada et al., 1983). Although the experimental frequencies were assigned to specific vibrational modes, the calculated frequencies of the gas phase ethylamine model were analyzed using visualization software, where the actual movement of these frequencies can be observed, described and then compared to experimental frequencies. The calculations identified several additional frequencies that were not observed experimentally; the CH_2 scissor mode at 1470 cm^{-1}, CH_2 asym (asymmetric) stretch at 2821 and 2971 cm^{-1}, the NH_2 asym stretch at 3372 cm^{-1} or CH_2 bend (1238 and 1298 cm^{-1}), and CH_2 wagging (786 cm^{-1}) were noticeably absent in the experimental data. With these exceptions, all other experimental vibrational frequencies of the gas phase ethylamine and its assigned modes are in a good agreement with the calculated gas phase frequencies.

The vibrational frequencies of the EAI1 configuration were calculated and summarized in Table 6.1. Examining the calculated vibrational frequencies of structure EAI1, which is proposed to take place initially on Mo(110) surface by bonding thorough the nitrogen atom and the ethyl group pointing away from the surface, there is good agreement with most experimental and calculated ethylamine gas phase vibrational frequencies. The CH_3 and CH_2 symmetric stretching modes of the experimental gas phase ethylamine are consistent with the calculated vibrational modes of the EAI1 configuration, while the calculated NH_2 symmetric stretching frequency is softened compared to the gas phase frequency indicative of the nitrogen atom bonded to the Mo(110) surface. The vibrational frequencies of the asymmetric stretching modes had different observations; the experimental gas phase had a CH_3 asym stretching frequency at 2977 cm^{-1}, while the EAI1 calculated frequencies indicated a similar frequency at 2979 cm^{-1} and 2949 cm^{-1} for the same mode. The C-N stretching mode at 1040 cm^{-1} for the EAI1 showed a good agreement with the gas phase vibrational frequency of *trans* geometry at 1055 cm^{-1}, while the C-C stretching mode was not observed within EAI1 frequencies. As for the C-C-N stretching mode, the calculated frequency of 467 cm^{-1} showed higher frequency compared to the gas phase ethylamine at 403 cm^{-1}. The CH_2 wagging mode in the gas phase had much higher frequency at 1397 cm^{-1} compared to the calculated frequency at 789 cm^{-1} for EAI1, indicating the CH_2 is interacting with the surface during ethylamine adsorption.

Table 6.1 Calculated Vibrational Frequencies of ethylamine intermediates

Mode	$CH_3CH_2NH_2$ Gas Phase[a]	$CH_3CH_2NH_2$ Gas Phase[b]	EAI1	Ni(111)
CCN bend	403[G]	404	467	...
NH_2 wag	773[G], 789[T]	853, 988	519	760
NH_2 bend	...	...	966, 1005	...
CC stretch	882[T], 892[T]	885	...	880
CH_3 rock	1016[G], 1119[T]	1120	1110	1140
CN stretch	1055[T], 1086[G]	1078	1040	1080
CH_3 bend	1378[G], 1465[G]	1360, 1451	1363	1440
CH_2 wag	1397[G]	786, 1391	789	...
CH_2 bend	1487[G]	1238, 1298, 1490	1215, 1301, 1340	...
NH_2 scissoring	1622[G]	1607	1575	1540
CH_2 scissoring	...	1470	1446	...
CH_3 sym stretch	2880[G]	2947	2875	2960
CH_2 sym stretch	2885[G]	...	2862	2680
CH_3 asym stretch	2977[G]	3017, 3042	2949, 2979	3040
NH_2 sym stretch	3343[G]	3309	3148	3200
CH_2 asym stretch	...	2821, 2971	2930	...
NH_2 asym stretch	...	3372	3215	...

[a](Hamada et al., 1983), [b]DFT calculations, [T]*trans* geometry, [G]*gauche* geometry

The vibrational frequencies of the EAI1 configuration will be discussed in detail in the next section and will be also compared to an experimental study of ethylamine adsorption on Ni(111) using high-resolution electron energy loss spectroscopy.

6.4 Discussion

6.4.1 Chemisorption of Ethylamine on Mo(110)

The results of temperature programmed desorption study indicate that ethylamine molecularly adsorbs and decomposes on the Mo(110) surface giving rise to surface carbon and nitrogen as indicated by the surface composition analysis using Auger electron spectroscopy. The TPD spectrum showed a sharp physisorption peak at 157 ± 10 K (7.7 kcal mol^{-1}) with a shoulder peak at 184 ± 10 K (9.2 kcal mol^{-1}). Similar desorption behavior of ethylamine has been reported on W(100) at a desorption temperature of 170 K with surface exposure of ≥ 4 L, while at higher surface exposures the desorption temperature was approximately at 150 K and attributed to ethylamine sublimation as a result of ethylamine multilayers on the surface (Pearlstine and Friend, 1986). Within the same study and over a modified W(100)-(5 x 1)-C surface at 3.3 L exposure, the ethylamine desorption temperature was within a broad range of 180 – 500 K, while on W(100)-(2 x 1)-O, ethylamine was the only observed desorption product at adsorption temperature of < 700 K. In a different study on Ni(111) and at exposures greater than 3 L, a low temperature peak at 180 K was observed for ethylamine desorption, which was attributed to the growth of a second layer of ethylamine on the nickel surface (Gardin and Somorjai, 1992).

The reaction product distribution of ethylamine decomposition on Mo(110) is consistent with observations on other metal surfaces. In this study, only surface saturation was investigated on the Mo(110) surface, and showed similarity with the reaction products reported for Ni(111) (Gardin and Somorjai, 1992) and W(110) (Pearlstine and Friend, 1986) surfaces. Acetonitrile (CH_3CN) was observed desorbing from the Mo(110) surface at a temperature of 212 ± 10 K (13.0 ± 0.6 kcal mol^{-1}), while over Ni(111) acetonitrile desorbed at a temperature of 350 K (Gardin and Somorjai, 1992), which is higher than the observed temperature on Mo(110). This is possibly due to a lower activation energy required to cleave the N–Mo bond. Ethylamine adsorption on W(100) at an exposure of 5 L did not show any desorbing acetonitrile, only ethylamine, methane, ammonia, molecular nitrogen and hydrogen were observed. However, over W(100)-(5 x 1)-C at 3.3 L exposure, acetonitrile was detected at a temperature of 490 K. The only other desorbed reaction product from Mo(110) was molecular hydrogen at a temperature of 332 ± 10 K (E_{ads} = 20.7 ± 0.6 kcal mol^{-1}) and a shoulder peak at an approximate temperature of 316 ± 10 K (E_{ads} = 19.6 ± 0.6 kcal mol^{-1}). These desorption features are in general agreement with previous studies of hydrogen desorption as a result of ethylamine decomposition on Ni(111) (380 – 450 K) (Gardin and Somorjai, 1992), W(100) (≈ 400 K), W(100)-(5 x 1)-C (450 K), and W(100)-(2 x 1)-O (>500 K) (Pearlstine and Friend, 1986). Molecular hydrogen desorption is also consistent with hydrogen desorption from Mo(110) as a result of pyridine decomposition (Chapter 4).

6.4.2 Orientation of Ethylamine on Mo(110)

The electronic structure of ethylamine suggests the amine group is the preferred molecular region which will interact with the catalyst surface through the nitrogen atom, and this has been confirmed from the initial adsorption calculations searching for the most stable adsorption configuration of ethylamine on Mo(110). All the structures with the ethyl group approaching the surface moved away from the surface during geometry optimization without forming any bonds. Thus, the most probable ethylamine adsorption configuration on Mo(110) is through the nitrogen atom with an approximate adsorption energy of -20.6 kcal mol^{-1} similar to structure EAI1^{4}. Following optimization, structure EAI1^{4} has an inter-atomic C–C–N bond angle of 114.3° and C–N–Mo bond angle of 117.9°, while the inter-atomic bond length is 1.51 and 1.47 Å for C–C and C–N bonds, respectively. This adsorption configuration is also supported by the work of Yao (1963). In this study, the heat of adsorption of amines including ethylamine was calculated and it was concluded that amines chemisorb on transition metals by donating the lone-pair electrons to the metals to form a predominately covalent bond.

HREELS data of ethylamine adsorption on Ni(111) suggested ethylamine bonds to the metal surface through the nitrogen lone pair and the ethyl-group points away from the surface, while the hydrogen atom from the the CH_2 group interacts with the nickel surface due to the lower activation energy of the α-C–H bond. The calculated vibrational frequencies of adsorbed ethylamine on Mo(110) (EAI1 structure) show good agreement with the HREELS frequencies on Ni(111) and with ethylamine gas phase gauche geometry frequencies. This is also supported by the calculated adsorption energies for several proposed initial adsorption configurations, which showed ethylamine molecules can only adsorb through its nitrogen atom while the ethyl group is oriented away from the surface in a perpendicular angle.

Based on the initial adsorption configuration and the reaction product distribution of ethylamine from the temperature programmed desorption, a reaction mechanism was proposed for ethylamine adsorption and decomposition on the Mo(110) surface leading to acetonitrile and hydrogen desorption from the surface. Similarly, Ditlevsen, et al., (1993) proposed a reaction mechanism for ethylamine adsorption and decomposition on Ni(111) based on previous study on Ni(111) (Gardin and Somorjai, 1992) and by calculating the binding energies of adsorbed species as well as the activation energies of reaction intermediates using a semiemprical model based on the extended-Hückel theory.

On Mo(110), the reaction pathway indicates initial molecular adsorption of ethylamine with adsorption energy of –20.6 ± 0.6 kcal mol^{-1} (EAI1), while on Ni(111) surface, the calculated adsorption energy of a similar configuration was –39.4 kcal mol^{-1} (experimental E_{ads} = -18.0 kcal mol^{-1}). This is followed by α-C–H bond cleavage to form CH_3CHNH_2 species (EAI2). The present calculations indicated an adsorption energy of this intermediate of –24.8 kcal mol^{-1}, although this intermediate was not proposed on Ni(111). In contrast, both α-C–H bonds were proposed to break and form a CH_3CNH_2 species on Ni(111) as the next intermediate with calculated adsorption energy of –46.1 kcal mol^{-1} (experimental Eads = -24.0 kcal mol^{-1}). The CH_3CNH_2 intermediate species was not stable on Mo(110). The next intermediate on Mo(110) (EAI3) is formed by breaking both α-C–H bonds and one N–H bond forming CH_3CNH species with adsorption energy of –50.4 kcal mol^{-1}. A similar intermediate was proposed on Ni(111) with calculated adsorption energy of –94.1 kcal mol^{-1} (experimental E_{ads} = -35.7 kcal mol^{-1}). The following intermediate (EAI4) on Mo(110) is a CH_3CN species, which is formed by cleaving the other N–H bond with an adsorption energy of –63.9 kcal mol^{-1}. On

Ni(111), a similar structure was proposed with an adsorption energy of –110.5 kcal mol^{-1} (experimental E_{ads} = -39.7 kcal mol-1). Although a similar intermediate was proposed on both surfaces, the Ni(111) surface had a preceding intermediate (CH_3CHN species) with a calculated adsorption energy of –107.0 kcal mol^{-1}. A similar species was not stable on Mo(110) and no experimental adsorption energy was reported on Ni(111). The last two steps would be the desorption of acetonitrile and hydrogen from the surface. On Mo(110), the adsorption energy of EAI6 configuration (desorbing acetonitrile) is –16.4 kcal mol^{-1}, while on Ni(111) the calculated adsorption energy was –54.7 kcal mol^{-1} (experimental E_{ads} = -18.9 kcal mol^{-1}). The final species, EAI7 (desorption of hydrogen), had an adsorption energy of 47.3 kcal mol^{-1}, while on Ni(111) the calculated adsorption energy was 30.2 kcal mol^{-1} (experimental E_{ads} = 27 kcal mol^{-1}). Thus, the proposed reaction mechanism for ethylamine on Mo(110) shows excellent agreement with the proposed intermediates on Ni(111) with slight adsorption energy differences.

6.5 Conclusions

The adsorption of ethylamine on Mo(110) was studied using temperature programmed desorption and density functional theory. The TPD spectrum at 4 L exposure indicates ethylamine decomposes on Mo(110) producing acetonitrile at 212 ± 10 K (E_{ads} = 13.0 ± 0.6 kcal mol^{-1}), molecular hydrogen at 332 ± 10 K (E_{ads} = 20.7 ± 0.6 kcal mol^{-1}) and a shoulder molecular hydrogen peak at an approximate temperature of 316 ± 10 K (E_{ads} = 19.6 ± 0.6 kcal mol^{-1}), in addition to ethylamine desorption at 157 ± 10 K (7.7 kcal mol^{-1}) and a shoulder peak at 184 ± 10 K (9.2 kcal mol^{-1}). Based on the calculated relative adsorption energies, ethylamine adsorbs molecularly on Mo(110) through the nitrogen atom with the ethyl group perpendicular to the surface with an approximate adsorption energy of –20.6 kcal mol^{-1}. The calculated vibrational frequencies for this model (EAI1) showed good agreement with this adsorption configuration in comparison to *trans* vibrational frequencies. From these results, a reaction pathway for ethylamine decomposition over Mo(110) was proposed, and all intermediate species adsorption energies were calculated. These calculations indicated that the CH_3CN adsorbed intermediate was the most stable species among all other intermediates.

7. CONCLUDING REMARKS

7.1 Summary

The removal of heterocyclic nitrogen compounds through catalytic hydrotreatment proceeds via two key reaction steps; (1) hydrogenation of the heterocyclic ring, which consumes large amounts of hydrogen in comparison to HDS, since HDS does not require hydrogenation, and (2) C–N bond scission, which is suggested to occur through either the Hofmann-type elimination or nucleophilic substitution followed by C–N hydrogenolysis. It is generally believed that basic organonitrogen compounds interact with the active sites over the catalyst surface by two adsorption modes, including parallel adsorption through the π-ring and perpendicular adsorption through the nitrogen atom. In contrast, non-basic organonitrogen compounds cannot interact through the pyrrolic nitrogen due to steric hindrance of the hydrogen atom bonded to the pyrrolic nitrogen, therefore, the interaction occurs predominantly through the π-ring. In the present study, pyridine and pyrrole were adapted as probe molecules for basic and non-basic heterocyclic organonitrogen compounds, respectively, to study their reaction and decomposition behaviour on Mo(110). This was performed using temperature programmed desorption (TPD), and Auger electron spectroscopy (AES), and high resolution electron energy loss spectroscopy (HREELS). In addition, the adsorption geometry and energetics of these molecules on Mo(110) surface was thoroughly investigated using density functional theory (DFT).

Pyridine (C_5H_5N) adsorbs reversibly and irreversibly on Mo(110) indicating the surface is active for decomposition, which is clearly supported by molecular hydrogen desorption and the presence of surface carbon and nitrogen following TPD. More importantly, pyridine adsorption was found to be surface coverage dependent. Only one desorption peak was observed within the TPD spectrum at low surface exposure (0.5 L) at 375 ± 10 K (E_{ads} = 23.5 ± 0.6 kcal mol^{-1}). Using DFT and EELS at low surface exposures, it was determined that the preferred adsorption mode is pyridine in a parallel configuration coordinated to three surface Mo-sites as μ_3,η^3(N,C3,C5)-Py-0°. Although this identified configuration only includes three pyridine atoms bonded to the surface, it is suggested that the entire ring participates in forming the bond similar to μ_3,η^6-Py-0°.

As surface exposure increases (1 L), two desorption peaks at a temperatures of 370 ± 10 K (E_{ads} = 23.2 ± 0.6 kcal mol^{-1}) and 530 ± 10 K (E_{ads} = 33.6 ± 0.6 kcal mol^{-1}) are evidenced on the clean Mo(110) surface. The second desorption feature is indicative of a second adsorption configuration of pyridine on the surface, which is proposed to bond to the surface through the nitrogen atom coordinated to one Mo-site as η^1(N)-Py-90° based on DFT and EELS observations. As the pyridine exposure is increased (2, 5, 10 L), similar chemisorption features were observed in addition to a multilayer physisorption peak at 240 – 260 K; however, these chemisorption features were not well resolved due to strong physisorption peak.

Similar to pyridine, pyrrole (C_4H_5N) was found to adsorb reversibly and irreversibly on Mo(110) indicating the surface is active for denitrogenation of non-basic heterocyclic nitrogen compounds. In contrast to pyridine, pyrrole did not produce any desorption products from the surface; only surface carbon and nitrogen were detected following TPD. Only one desorption feature was observed in the TPD spectra for all surface exposures at an approximate temperature of 351 ± 10 K with an apparent first-order activation energy of 21.9 ± 0.6 kcal mol^{-1}. This suggests that pyrrole adsorption on Mo(110) is not surface coverage dependent as the case for pyridine. An extensive investigation was performed using DFT to study the most probable adsorption configuration of pyrrole on Mo(110) taking into consideration the fact that Mo(110) surface dose not promote hydrogen abstraction. Pyrrole is suggested to adsorb in a parallel mode with respect to the Mo(110) surface through its π orbital similar to μ_3,η^5-Pyr-0° with an adsorption energy of -28.7 to -31.5 kcal mol^{-1}. The calculations also showed the possibility of a coexisting mode where pyrrole adsorbs on the surface with a slightly tilted molecular plane as μ_3,η^4(N,C2,C3,C4)-Pyr-5°, which would begin to populate the surface at higher pyrrole coverages. The slightly tilted configuration is suggested to arise from the lateral interactions of adsorbed pyrrole on Mo(110), and not the result of a phase transformation on the surface since this requires a relatively high activation energy as indicated by additional LST/QST calculations. This adsorption configuration was further supported by EELS vibrational frequency analysis for adsorbed pyrrole on the Mo(110) surface at different surface exposures.

In general, heterocyclic compounds adsorb on the catalyst surface and decompose, eventually desorbing as ammonia (NH_3) and C_n-hydrocarbons. Therefore, it is also of importance to study how these intermediate amine compounds adsorb and decompose on Mo(110) since these compounds are logical intermediates for heterocyclic organonitrogen compound decomposition. In this study, the adsorption and reaction of ethylamine ($CH_3CH_2NH_2$) was studied on Mo(110) to understand the salient features and energetics of amine adsorption and decomposition. Based on the DFT relative adsorption energies of ethylamine adsorption on Mo(110), ethylamine adsorbs molecularly on Mo(110) surface through its nitrogen atom with the methyl group (CH_3) pointing away from the surface with CH_2 interacting with the metal surface with an adsorption energy of –20.6 kcal mol^{-1}. The calculated vibrational frequencies of this model showed good agreement with this adsorption configuration in comparison to *trans* vibrational frequencies. Ethylamine decomposition behaviour showed irreversible reaction behaviour, as hydrogen and acetonitrile were observed desorbing from the surface during TPD. Although ammonia (NH_3) is the ultimate product one would like to observe at the end of HDN reactions, the fact remains that other possible reaction mechanism are possible.

7.2 Implications to Hydrotreating

Hydrotreating is a catalytic process involving the adsorption of reactants on the catalyst surface prior to any reaction. Basic and non-basic organonitrogen adsorption is readily facilitated on Mo(110) due to the long-range order of the surface. However, the active sites on Mo-based hydrotreating catalyst surfaces are limited since these active sites are located on the edge planes on MoS_2 clusters. Although pyridine initially prefers adsorbing through its ring in a parallel configuration similar to μ_3,η^6-Py-0°, which requires three-coordinated Mo-sites, pyridine can reorient its molecular plane depending on surface site availability and competitive adsorption with other adsorbates to adsorb through its nitrogen atom as η^1(N)-Py-90°. In the case of pyrrole, the adsorption configuration was not surface coverage dependent except for adsorbate-adsorbate lateral interactions that could cause the molecules to tilt while adsorbing on the surface. Nonetheless, the preferred adsorption configuration of pyrrole on Mo(110) requires three

Mo-sites and occurs similarly to μ_3,η^5-Pyr-0°. These differences in adsorption modes and the availability of active sites can partly explain the relative differences in activity between basic and non-basic organonitrogen compounds during catalytic hydrotreatment. This represents an interesting point that could be further fully investigated and possibly can be utilized to develop new types of catalysts, which are more active for removing organonitrogen compounds in the hydrotreating process.

7.3 Future Studies

The removal of sulfur and nitrogen compounds from crude oil has been the focus of intensive research due to their negative impact in the processing of oil-derived chemical feedstocks and environmental implications following combustion. Existing commercial hydrotreating catalysts (Ni/Co-MoS_2/γ-Al_2O_3) are active for sulfur and nitrogen removal, although a complete understanding of how organonitrogen compounds are removed is still under investigation. The studies performed in the present study have provided invaluable insights into organonitrogen adsorption and reaction. Based on these studies, the following future research would be a logical extension of the present work.

7.3.1 Molybdenum Dichalcogenides

Molybdenum dichalcogenides (MoS_2, $MoSe_2$, $MoTe_2$) have attracted significant attention because of their primary importance as catalysts (Bastow, 1998; Bolivar et al., 2003) and photovoltaic materials (Kiesewetter er al., 1999; Wada et al., 2001). These materials have a hexagonal closed packed (hcp) structure that results from the stacking of weakly bonded X-Mo-X layers (X = S, Se, Te) and gives rise to highly anisotropic properties. Of these, molybdenum disulfide (MoS_2) has been widely studied primarily due to its relevance as a hydrotreating catalyst to remove sulfur- and nitrogen-containing compounds from various oil fractions. The large basal plane (0001) of MoS_2 is relatively catalytically inactive, while the edge planes (S-edge, $\bar{1}010$; Mo-edge, $10\bar{1}0$) are generally accepted to be the active sites due to the presence of coordinatively unsaturated (*cus*) Mo (or promoter) sites. The MoS_2(0001) surface has been shown to be catalytically inactive toward thiophene (Peterson and Schulz, 1996); however, additional studies with ethanethiol have indicated slight reactivity suggesting the presence of *cus* sites on the freshly cleaved basal surface. Wiegenstein and Schulz (Wiegenstien and Schulz, 1999) demonstrated the density of *cus* Mo sites can be increased using ion bombardment, thereby increasing the reactivity of methanethiol. Their XPS measurements of $MoS_2(0001)$ indicated that the Mo 3d peaks of a (0001) surface are consistent with Mo(IV), and no significant change in binding energy or intensity was observed after annealing to 573 K. However, following ion bombardment the Mo 3d peaks shifted to a higher binding energy consistent with a concentration of additional Mo oxidation states on the defective basal surface. Consequently, the $MoS_2(0001)$ surface can be made reactive using controlled ion bombardment to increase the density of *cus* sites.

In addition to the widespread application in the photovoltaic industry, $MoSe_2$ may also have the potential to be used as a hydrotreating catalyst. For example, the mechanism of C–N bond cleavage in the hydrodenitrogenation (HDN) of aliphatic nitrogen-containing molecules has been suggested to be Hofmann-type elimination or nucleophilic substitution (Laine, 1983; Nelson and Levy, 1979). Both of these mechanisms require a pair of sites: an acid site to react with the nitrogen-molecule through the nitrogen atom, making the amine group ready to leave from the molecule; and a basic site to abstract the β-hydrogen in the elimination mechanism, or a nucleophile to attack the α-carbon in the nucleophilic substitution mechanism. It has been previously suggested that on a promoted (Ni) edge of MoS_2 $(10\bar{1}0)$, the uncovered promoter atoms can accommodate the nitrogen-containing molecules as adsorption sites (Lewis acid sites) and the neighboring sulfur atoms can be the basic sites or the nucleophile (Sun et al., 2004). Consequently, a favorable approach to increasing the reactivity is to increase the nucleophilic strength of the active site to promote the nucleophilic substitution mechanism. Comparing the nucleophilities of several compounds, $RSe^- > RS^- > R_2NH > NH_3 > H_2O$, selenium is the strongest nucleophile (Laine, 1983). Therefore, promoted molybdenum diselenides are ideal materials for highly active and selective hydrodenitrogenation catalysts.

We have done some initial research in this regard by obtaining and interpreting X-ray photoelectron spectroscopy (XPS) data of $MoSe_2(0001)$ and ion-sputtered $MoSe_2(0001)$ to deduce the surface chemistry of well-defined and defective surfaces. This characterization information will not only fill the current information gap, but also provide an indication whether $MoSe_2$ may be a potential candidate as a hydrotreating catalyst. The XPS analysis provided definitive information on the surface chemistry of $MoSe_2$(0001), and the effects of ion sputtering on the preferential removal of selenium and the subsequent change in composition and surface chemistry. It is also apparent that $MoSe_2$(0001) is susceptible to defect site formation through *ex situ* sample handling, or exposure to irradiation or UHV conditions. An acute knowledge of the relative surface chemistry and stability of $MoSe_2$ will support the development of nanocrystalline $MoSe_2$ for increased utilization in the photovoltaic industry and further the development of selenium-based heterogeneous catalysts. Therefore, it would be of a great interest to design such a catalyst and test it for sulfur and nitrogen removal using temperature programmed desorption, Auger electron spectroscopy, high-resolution electron energy loss spectroscopy, and density functional theory.

7.3.2 Transition Metal Phosphides

There is presently active research examining the reactivity of transition metal phosphides using kinetic data obtained from bulk reacting fluids. Among these catalysts, nickel phosphide (Ni_2P) (Layman and Bussell, 2004; Oyama et al., 2002; Oyama, 2004; Rodriguez et al., 2003; Sawhill et al., 2003; Sawhill et al., 2005; Stinner et al., 2002; Wang et al., 2002), molybdenum phosphide (MoP) (Clark and Oyama, 2003; Li et al., 1998; Phillips et al., 2002; Oyama et al., 2001; Rodriguez et al., 2003; Stinner et al., 2000), molybdenum nickel phosphide (MoNiP) (Rodriguez et al., 2003), and tungsten phosphide (WP) (Clark et al., 2001; Clark et al., 2002; Zuzaniuk and Prins, 2003) have received considerable attention.

Within the present research, it has been observed that basic and non-basic organonitrogen compounds have a preference to adsorb on Mo(110) over a three-fold hollow. Although MoS_2 has a hexagonal structure (*hcp*), the basel plane is not active for HDN or HDS due to sulfur coverage on this stuface. Consequently, the edge planes are generally believed to be the active sites for HDS and HDN. However, these edge planes do not provide enough sites for a possible parallel adsorption, specifically for non-basic compounds. Considering the structure of Ni_2P, this structure includes a three-fold hollow coordination site facilitating both non-basic and basic nitrogen compound adsorption in a parallel configuration. Therefore, Ni_2P should be studied using temperature programmed desorption, Auger electron spectroscopy, high-resolution electron energy loss spectroscopy, and density functional theory to understand the adsorption configurations and energetics of basic and non-basic organonitrogen hydrodenitrogenation.

REFERENCES

Alves, J. J. and Towlerr, J. P. (2002), "Analysis of refinery hydrogen distribution systems," *Ind. Eng. Chem. Res.*, **41**, 5759 – 5769.

Andersson, M. P. and Uvdal, P. (2001), "Transformation of pyridine to α-pyridyl on W(110) as probed by vibrational spectroscopy: Experiments and Calculations," *J. Phys. Chem. B*, **105**, 9458 – 9462.

Avouris, Ph. and Demuth, J. E. (1981), "Electronic excitations of benzene, pyridine, and pyrazine adsorbed on Ag(111)," *J. Chem. Phys.*, **75**, 4783 – 4794.

Avouris, Ph., DiNardo, N. J. and Demuth, J. E. (1984), "Electronically excited states of chemisorbed molecules," *J. Chem. Phys.*, **80**, 491 – 502.

Baca, A. G., Schulz, M. A. and Shirley, D. A. (1985), "Electron energy loss spectroscopy (EELS) on CH_3NH_2 adsorbed on Ni(111), Ni(100), Cr(100), Cr(111)," *J. Chem. Phys.*, **83**, 6001 – 6008.

Baddeley, C. J., Hardacre, C., Ormerod, R. M. and Lambert, R. M. (1996), "Chemisorption and decomposition of pyrrole on Pd{ 111 }," *Surf. Sci.*, **369**, 1 – 8.

Bader, M., Haase, J., Frank, K. H. and Puschmann, A. (1986), "Orientational phase transition in the system pyridine/Ag(111): A near-edge x-ray – absorption fine – structure study," *Phys. Rev. Lett.*, **56**, 1921 – 1924.

Bandy, B. J., Lloyd, D. R. and Richardson, N. V. (1979), "Selection rules in photoemission from adsorbates: pyridine adsorbed on copper," *Surf. Sci.*, **89**, 344 – 353.

Bastow T. J. (1998), "Mo-95 NMR: hyperfine interaction in MoO_3, MoS_2, $MoSe_2$, Mo_3Se_4, $MoSi_2$ and Mo_2C," *Solid State NMR*, **12**, 191 – 199.

Bej, S. K., Dalai, A. K. and Adjaye, J. (2001), "Comparison of Hydrodenitrogenation of Basic and Non-Basic Nitrogen Compounds Present in Oil Sands Derived Heavy Gas Oil," *Energy Fuels*, **15**, 377 – 383.

Bianchini, C., Meli, A. and Vizza, F. (2001), "Modeling the hydrodenitrogenation of aromatic N-heterocycles in the homogeneous phase," *Eur. J. Inorg. Chem.*, **1**, 43 – 68.

Bolivar, H., Izquierdo, S., Tremont, R. and Cabrera, C. R. (2003), "Methanol oxidation at Pt/MoO_x/$MoSe_2$ thin film electrodes prepared with exfoliated $MoSe_2$," *J. Appl. Electrochem.*, **33**, 1191 – 1198.

Bond, G. C., Catalysis by Metals, Academic Press, New York, (1962).

Bond, G. C., Heterogeneous Catalysis: Principles and Applications, Clarendon Press, Oxford, NY (1987).

Boudart, M. (1986), "Single crystals: standards for industrial catalysis," *ChemTech.*, **16**, 688 – 692.

Boudart, M., Collins, D. M., Hanson, F. V. and Spicer, W. E. (1977), "Reactions between H_2 and O_2 on Pt at low and high pressures: A comparison," *J. Vac. Sci. Technol.*, **14**, 441 – 443.

Boudart, M., Egawa, C., Oyama, S. T. and Tamaru, K. (1981), "Nitrogen adsorption and ammonia decomposition on polycrystalline molybdenum," *J. Chem. Phys.*, **78**, 986 – 994.

Bunker, P. R. and Jensen, P., Molecular Symmetry and Spectroscopy, NRC Research Press, Ottawa, (1998).

Byskov, L. S., Norskov, J. K., Clausen, B. J. and Topsoe, H. (1999), "DFT Calculations of Unpromoted and Promoted MoS_2-Based Hydrodesulfurization Catalysts," *J. Catal.*, **187**, 109 – 122.

Campbell, C. T., Advances in Catalysis, Academic Press Inc., NY, 1989.

Chaudret, B. and Jalon, F. A. (1988), "Facile preparation of π-arene complexes ofruthenium $[(\eta^5C5Me5)Ru(ARENE)]_x$ including a π-pyridine and the 1st π-furan derivative," *J. Chem. Soc. Chem. Commun.*, **11**, 711 – 713.

Chaudret, B., Jalón, F. A., Pérez-Manrique, M., Plou, J. F. and Sánchez-Delgado, R. A. (1990), "A new and general-method for the preparation of novel π-heterocyclic derivative of ruthenium [C5Me5Ru(η6Arene)]$_x$ (Arene=benzene, thiophene, 3-methylthiophene, benzothiophene, pyridine, 2,6 and 3,5-lutidine, quinoline, acridine) – x-ray crystal-structure of [(C4Me5)2Ru2Cl2(pyridine)2]Pf6," *New J. Chem.*, **14**, 331 – 338.

Chen, J. G. (1996), "Carbide and Nitride Overlayers on Early Transition Metal Surfaces: Preparation, Characterization, and Reactivities," *Chem. Rev.*, **96**, 1477 – 1498.

Choi, J.-G., Brenner, J. R. and Thompson, L. T. (1995), "Pyridine hydrodenitrogenation over Molybdenum Carbide Catalysts," *J. Catal.*, **154**, 33 – 40.

Chorkendorff, I., Russell, Jr.,-N. J. and Yates, Jr.,-J. T. (1987), "Surface reaction pathways of methylamine on Ni(111) surface" *J. Chem. Phys.*, **86**, 4692 – 4699.

Clair, T. P., Oyama, S. T. and Cox, D. F. (2002), "Adsorption and reaction of thiophene on α-Mo$_2$C(0001)," *Surf. Sci.*, **511**, 294 – 302.

Clark, P., Li, W. and Oyama, S. T. (2001), "Synthesis and activity of a new catalyst for hydroprocessing: tungsten phosphide," *J. Catal.*, **200**, 140 – 147.

Clark, P. and Oyama, S. T. (2003), "Alumina-supported molybdenum phosphide hydroprocessing catalysts," *J. Catal.*, **218**, 78 – 87.

Clark, P., Wang, X., Deck, P. and Oyama, S. T. (2002), "Push–pull mechanism of hydrodenitrogenation over silica-supported MoP, WP, and MoS$_2$ hydroprocessing catalysts," *J. Catal.* **210**, 116 – 126.

Cocchetto, J. F. and Satterfield, C. N. (1981), "Chemical Equilibria among Quinoline and its reaction products in hydrodenitrogenation," *Ind. Eng. Chem. Process Des. Dev.*, **20**, 49 – 53.

Cohen, M. R. and Merrill, R. P. (1990), "Adsorption of pyridine on Ni(111): A high resoltion electron energy loss spectroscopy, angular resolved UV photoemission, and x-ray photoelectron spectroscopy study," *Langmiur*, **6**, 1282 – 1288.

Conrad, H., Ertl, G., Küppers, J. and Latta, E. E. (1976), "Adsorption of CO on clean and oxygen covered Ni(111) surfaces," *Surf. Sci.*, **57**, 475 – 484.

Cordone, R., Harman W. D. and Taube, H. (1989), "Synthesis and characterization of a soluble oxide inclusion complex, [CH3CN.cntnd.(v120324-)]," *J. Am. Chem. Soc.*, **111**, 5959 – 5961.

Corrsin, L., Fax, B. J. and Lord, R. C. (1953), "The vibrational spectra of pyridine and pyridine-d_5," *J. Chem. Phys.*, **21**, 1170 – 1176.

Czanderna, A. W., Methods of Surface Analysis, Elsevier Science Publishing Company, Inc., New York, (1989).

Davis, L. E., MacDonald, N. C., Palmberg, P. W., Riach, G. E., and Weber, R. E., Handbook of Auger Electron Spectroscopy, Physical Electronics Industries Inc., Eden Prairie, MN, (1978)

Davies, P. R. and Newton, N. G. (2003), "The chemisorption and decomposition of pyridine and ammonia at clean and oxidised Al(111) surfaces," *Surf. Sci.*, **546**, 149 – 158.

Demuth, J. E., Christmann, K. and Sanda, P. N. (1980), "The vibrations and structure of pyridine chemisorbed on Ag(111): the occurrence of a compressional phase transformation," *Chem. Phys. Lett.* **76**, 201 – 206.

Demuth, J. E. and Eastman, D. E. (1974), "Photoemission observation of π-d bonding and surface reactions of adsorbed hydrocarbons on Ni(111)," *Phys. Rev. Lett.*, **32**, 1123 – 1127.

DiNardo, N. J., Avouris, Ph. and Demuth, J. E. (1984), "Chemisorbed pyridine on Ni(001): A high resolution electron energy loss study of vibrational and electronic excitations," *J. Chem. Phys.*, **81**, 2169 – 2180.

Ditlevse, P. D., Gardin, G. E. Van Hove, M. A. and Somorjai, G. A. (1993), "Molecular modeling of Amine Dehydrogenation on Ni(111)," *Langmuir*, **9**, 1500 – 1503.

DuBois, M. R., Vasquez, L. D., Ciancanelli, R. F. and Noll, B. C. (2000), "Electrophilic Substitution of Nitrogen Heterocycles by Molybdenum sulfide Complexes," *Organometallics*, **19**, 3507 – 3515.

Efraty, A., Jubran, N. and Goldman, A. (1982), "Chemistry of some η^5-pyrrolyl and η^1-N-pyrrolyliron complexes," *Inorg. Chem.*, **21**, 868 – 873.

Ertl, G. and Freund, H.-J. (1999), "Catalysis and Surface Science," *Physics Today*, **52**, 32 – 38.

Ertl G. and Küppers, J., Low Energy Electrons and Surface Chemistry, VCH, Winheim, (1985).

Falconer J. L. and Schwarz, J. A. (1983), "Temperature-programmed desorption and reaction: applications to supported catalysts," *Catal. Rev.-Sci. Eng.*, **25**, 141 – 227.

Faye, P., Payen E. and Bougeard, D. (1999), "Cluster Approach of Active Sites in an MoS_2 Catalyst," *J. Mol. Model.*, **5**, 63 – 71.

Felkin, H. and Zakrzewski, J. (1985), "Regioselective nucleophilic C-alkylation of the pyrrole ring in an (.eta.-pyrrolyl)iodohydridorhenium complex," *J. Am. Chem. Soc.*, **107**, 3374 – 3375.

Fischer, S. and Karplus, M. (1992), "Conjugate peak refinement: an algorithm for finding reaction paths and accurate transition states in systems with many degrees of freedom," *Chem. Phys. Lett.*, **194**, 252 – 261.

Fischer, T. H. and Almlof, J. (1992), "General methods for geometry and wave function optimization," *J. Phys. Chem.*, **96**, 9768 – 9774.

Fish, R. H., Baralt, E. and Kim, H. -S. (1991a), "Bonding of Mono- and Polynuclear Heteroaromatic Nitrgen Ligand to the (η^5-Pentamethylcyclopentadienyl)rhodium Dication: structure-Reactivity Relationshiphs in the Formation of Nitrogen (η^1) versus π (η^5, η^6) Complexes and Competition Studies of the Ligands for the Rhodium Metal Center," *Organometallics*, **10**, 1965 – 1971.

Fish, R. H., Fong, R. H., Than, A. and Baralt, E. (1991b), "Heteroaromatic Nitrogen Ligand Studies with the (η^5-Pentamethylcyclopentadlenyl) ruthenium Cation: η^1(N) and $\eta^6(\pi)$ Bonding Modes and Actors That Influence a Nitrogen to π Rearrangement," *Organometallics*, **10**, 1209 – 1212.

Friend, C. M. and Chen, D. A. (1997), "Fundamental studies of hydrodesulfurization by metal surfaces," *Polyhedron.*, **16**, 3165 – 3175.

Frühberger, B., Chen, J. G., Jr., J. Eng. and Bent, B. E. (1996), "Reactivities of carbon- and nitrogen-modified Mo(110): A comparison of modification effects by surface and interstitial adatoms," *J. Vac. Sci. Technol. A*, **14**, 1475 – 1481.

Futaba, D. N. and Chiang, S. (1997), "Predictions of scanning tunneling microscope images of furan and pyrrole on Pd(111)," *J. Vac. Sci. Technol. A*, **15**, 1295 – 1298.

Gardin, D. E. and Somorjai, G. A. (1992), "Vibrational Spectra and Thermal Decomposition of Methylamine and Ethylamine on Ni(111)," *J. Phys. Chem.*, **96**, 9424 – 9431.

Gellman, A. J., Bussel, M. E. and Somorji, G. A. (1987), "Catalytic hydrodesulfurization over the Mo(100) single crystal surface," *J. Catal.*, **107**, 03 – 113.

Girgis, M. J. and Gates, B. C. (1991), "Reactivities, reaction networks and kinetics in high pressure catalytic hydroprocessing," *Ind. Eng. Chem. Res.*, **30**, 2021 – 2058.

Gland, J. L. and Somorjai, G. A. (1973), "Low energy electron diffraction and work function studies of benzene, naphthalene and pyridine adsorbed on Pt(111) & Pt(100) single crystal," *Surf. Sci.*, **38**, 157 – 186.

Glueck, D. S., Hollander, F. J. and Bergman, R. J. (1989), "Synthesis, structure, and reactivity of a monomeric pentamethylcyclopentadienyliridium(III) imido complex," *J. Am. Chem. Soc.*, **111**, 2719 – 2721.

Goodman, D. W. (1982), "Single crystal as model catalysts," *J. Vac. Sci. Technol.*, **20**, 522 – 526.

Goodman, D. W. (1996), "Correlations between surface science models and 'Real-World' Catalysts," *J. Phys. Chem.*, **100**, 13090 – 13102.

Grassian, V. H. and Muetterties, E. L. (1986), "Electron Energy Loss and thermal desorption spectroscopy of pyridine adsorbed on Pt(111)," *J. Phys. Chem.*, **90**, 5900 – 5907.

Grassian, V. H. and Muetterties, E. L. (1987), "Vibrational Electron Energy Loss Spectroscopic study of bemzene, toluene and pyridine on Pd(111)," *J. Phys. Chem.*, **91**, 389 – 396.

Gray, M. R., Upgrading Petroleum Residues and Heavy Oils, Dekker, New York, (1994).

Guerrerp-Ruiz, A., Sepulveda-Escribano, A., Rodriguez-Ramos, I., Lopez-Agudo, A. and Fierro, J. L. G. (1995), "Catalytic behavior of carbon-supported FeM (M = Ru, Pt) in pyridine hydrodenitrogenation," *Fuel*, **74**, 279 – 283.

Gulkova, D. and Zdrazil, M. (1999), "Synergism between Ni and W in the Ni-W/C sulfide catalyst in hydrodenitrogenation of pyridine and hydrodesulfurization of Thiophene," *Collect. Czech. Chem. Commun.*, **64**, 735 – 746.

Hadjiloizou, G. C., Butt, J. B. and Dranoff, J. S. (1992), "Catalysis and mechanism of hydrodenitrogenation; The piperidine hydrogenolysis reaction," *Ind. Eng. Chem. Res.*, **31**, 2503 – 2516.

Halgren, T. A. and Lipscomb, W. N. (1977), "The synchronous-transit method for determining reaction pathways and locating molecular transition states," *Chem. Phys. Lett.*, **49**, 225 – 232.

Hamada, Y., Hashiguchi, K., Hirakawa, A. Y. and Tsuboi, M. (1983), "Vibrational analysis of ethylamines: Trans and Gauche Forms," *J. Mol. Spect.*, **102**, 123 – 147.

Hanlon, R. T., (1987) "Effects of PH2S, PH2 and PH2S / PH2 on the Hydrodenitrogenation of Pyridine," *Energy Fuels*, **1**, 424 – 430.

Harris, L. A. (1968a), "Analysis of Material by Electron-Excited Auger Electrons," *J. Appl. Phys.*, **39**, 1419 – 1427.

Harris, L. A. (1968b), "Some Observations of Surface segregation by auger Electron Emission," *J. Appl. Phys.*, **39**, 1428 – 1431.

Hartree, D. R (1928), "The wave mechanics of an atom with a non-Coulomb central field Part I theory and methods," *Proc. Cambridge Phil. Soc.*, **24**, 89 – 110.

He, J.-W., Kuhn, W. K. and Goodman, D.W. (1992), "CO adsorption on clean and C-, O- and H-covered Mo(110) surfaces: an IRAS study," *Surf. Sci.*, **262**, 351 – 358.

Hinchiffe, A., Modeling Molecular Structures, John Wiley and Sons, Ltd., England, (2000).

Ho. T. C. (1988), "Hydrodenitrogenation Catalysis," *Catal. Rev.-Sci. Eng.*, **30**, 117 – 160.

Hohenberg, P. and Kohan, W. (1964), "Inhomogeneous Electron Gas," *Phys. Rev. B*, **136**, 864 – 871.

Hwang, S. Y., Seebauer, E. G. and Schmidt, L. D. (1987), "Decomposition of CH_3NH_2 of Pt(111)," *Surf. Sci.*, **188**, 219 – 234.

Jentz, D., Rizzi, S., Barbieri, A., Kelly, D. G., Van Hove, M. A. and Somorjai, G. A. (1995), "Surface structure of sulfur and caron overlayers on Mo(100): A detailed analysis by automated tensor LEED," *Surf. Sci.*, **329**, 14 – 31.

Johnson, A. L. and Muetterties, E. L. (1983), "Orientation of Complex Molecules Chemisorbed on Metal Surfaces: Near-Edge X-ray Absorption Studies," *J. Am. Chem. Soc.*, **105**, 7183 – 7185.

Johnson, A. L., Mutterties, E. L., Stöhr, J. and Sette, F. (1985), "Chemisorption Geometery of pyridine on Pt(111) by NEXAFS," *J. Phys. Chem.*, **89**, 4071 – 4075.

Jones, R. A. and Bean, G. P., The Chemistry of Pyrroles, Academic Press, New York, (1977).

Jorgebsen, W. L. and Salem, L., The Organic Chemist's Book of Orbitals, Academic Press, New York, (1973).

Ibach, H. and Mills, D. L., Electron Energy Loss Spectroscopy and Surface Vibrations, Academic, New York, (1982).

Ibach, H., Electron Energy Loss Spectrometers, Springer, Berlin (1991)

Kabe , T., Ishihara, A. and Qian, W., Hydrodesulfurization and Hydrodenitrogenation: Chemistry and Engineering, Kodansha Ltd., Tokyo (1999).

Katzer, J. R. and Sivasuramanian, R. (1979), "Process and Catalyst Needs for Hydrodenitrogenation," *Catal. Rev.-Sci. Eng.*, **20**, 155 – 208.

Kiesewetter, T., Tomm, Y., Turrión, M. and Tributsch, H. (1999), "Composite materials for photovoltics: A realistic aim?," *Solar Ener. Mat. Solar Cells*, **59,** 309 – 323.

Kohn, W. and Sham, L. J. (1965), "Self-Consistent Equations Including Exchange and Correlation Effects," *Phys. Rev. A*, **140**, 1133 – 1138.

Kolasinski, K. W., Surface Science: Foundations of catalysis and nanoscience, John Wiley and sons, ltd., (2002).

Kushmerick, J. G., Kandel, S. A., Han, P., Johnson, J. A. and Weiss, P. S. (2000), "Atomic-Scale Insights into Hydrodesulfurization," *J. Phys. Chem. B*, **104**, 2980 – 2988

Kvietov, F., Allured, V., Carperos, V. and Dubois, M. R. (1994), "Reactivity of Tetramethylpyrrole Complexes of Ruthenium and Osmium," *Organometallics*, **13**, 60 – 68.

Laine, R. M. (1983), "Comments on the mechanism of heterogeneous catalysis of the hydrodenitrogenation reaction," *Catal. Rev.-Sci. Eng.*, **25**, 459 – 474.

Langreth, D. C. and Vosko, S. H. (1987), "Exact electron-gas response functions at high-density," *Phys. Rev. Lett.*, **59**, 497 – 500.

Layman, K. A. and Bussell, M. E. (2004), "Infrared spectroscopic investigation of thiophene adsorption on silica-supported nickel phosphide catalysts," *J. Phys. Chem. B*, **108,** 15791 – 15802.

Leach, B. E., Applied Industrial Catalysis, Vol. 1, Academic Press Inc., NY (1983).

Ledoux M. J. and Djellouli B. (1990), "Comparative hydrodenitrogenation activity of molybdenum, Co-Mo and Ni-Mo alumina-supported catalysts," *Appl. Catal.*, **67,** 81 – 92.

Lee, K. S., Abe, H., Reimer, J. A. and Bell, A. T. (1993), "Hydrodenitrogenation of Quinoline over High-Surface Area Mo_2N," *J. Catal.*, **139**, 34 – 40.

Lewandowski, M. and Sarbak, Z. (2000), "The effect of boron addition on hydrodesulfurization and hydrodenitrogenation activity of NiMo / Al_2O_3 catalysts," *Fuel*, **79**, 487 – 495.

Li, S., Lee, J. S., Hyeon, T. and Suslick, K. S. (1999), "Catalytic hydrodenitrogenation of indole over molybdenum nitride and carbides with different structures," *Appl. Catal. A: Gen.*, **184**, 1 – 9.

Li, W., Dhandapani, B. and Oyama, S. T. (1998), "Molybdenum phosphide: a novel catalyst for hydrodenitrogenation," *Chem. Lett.*, **27**, 207–208.

Lide, D. R., CRC Handbook of Chemistry and Physics (85th Edition), CRC Press, Cleveland, Ohio, (2004).

Liu A. C. and Friend, C. M. (1988), "The structure and reactivity of chemisorbed aromatics: spectroscopic studies of benzene on Mo(110)," *J. Chem. Phys.*, **89**, 4396 – 4405.

Lopinski, G. P., Forties, T. M., Moffatt, D. J. and Wolkow, R. A. (1998), "Multiple bonding geometries and binding state conversion of benzene/Si.100," *J. Vac. Sci. Technol. A*, **16**, 1037 – 1042.

Mack, J. U., Bertel, E. and Netzer, F. P. (1985), "Structure and orientation of benzene and pyridine on Ir(111): Evidence for molecular distortion of benzene," *Surf. Sci.*, **159**, 265 – 282.

Malard, W. G. and Linstorm, P. J., NIST Standard Reference Database Number 69, National Institute of Standards and Technology, Gaithersburg, MD, (1997).

Markel, E. J. and Van Zee, J. W. (1990), "Catalytic hydrodesulfurization by molybdenum nitride," *J. Catal.*, **126**, 643 – 657.

Marroqquin, G., Ancheyta-Juarez, J., Ramirez-Zuniga, A. and Farfan-Torres, E. (2001), "Effect of crude oil properties on the Hydrodesulfurization of Middle Distillates over NiMo and CoMo Catalysts," *Energy Fuels*, **15**, 1213 – 1219.

Marzari, A., Rajagopal, S. and Miranda, R. (1995), "Bifunctional mechanisum of pyridine hydrodenitrogenation," *J. Catal.*, **156**, 255 – 264.

Mate, C. M., Somorjai, G. A., Tom, H. W., Zhu, X. D. and Shen, Y. R. (1988), "Vibrational and electronic spectroscopy of pyridine and benzene adsorbed on the Rh(111) crystal surface," *J. Chem. Phys.*, **88**, 441 – 450.

McIlvried, H. G. (1971), "Kinetic of the hydrodenitrification of Pyridine," *Ind. Eng. Chem. Process Des. Dev.*, **10**, 125 – 130.

McWeeny, R. and Sutcliffe, B. T., Methods of Molecular Quantum Mechanics, Academic Press, London, (1969).

Mellouki, A.; Liévin, J. and Herman, M. (2001), "The vibrational spectrum of pyrrole (C4H5N) and furan (C4H4O) in the gas phase," *Chem. Phys.*, **271**, 239 – 266

Milman, V., Winkler, B., White, J. A., Pickard, C. J., Payne, M. C., Akhmatskaya, E. V. and Nobes, R. H. (2000), "Electronic Structure, Properies, and phase stability of inorganic crystals: A pseudopotential plane-wave study," *Int. J. Quant. Chem.*, **77**, 895 – 910.

Moravek, V., Duchet, J.-C. and Cornet, C. (1990), "Kinetic study of pyrrole and pyridine HDN on Ni-W and Ni-Mo catalysts," *Appl. Catal.*, **66**, 257 – 266.

Myers, W. H., Sabat, M. and Harman, W. D. (1991), "Enamine character of a 2,3-.eta.2-coordinated pyrrole," *J. Am. Chem. Soc.*, **113**, 6682 – 6683.

Nagai, M., Masunaga, T. and Hana-Oka, N. (1986), "Selectivity of Molybdium Catalyst in hydrodenitrogenation, hydrodesulfurization, and hydrodeoxygenation: Effects of Sulfur and Oxygen Compounds on Acridine hydrodenitrogenation," *J. Catal.*, **101**, 284 – 292.

Nagai, M., Masunaga, T. and Hana-oka, N. (1988), "Hydrodenitrogenation of Carbazole on a Mo/Al2O3 catalysts. Effects of sulfiding and sulfur compounds," *Energy Fuels*, **2**, 645 – 651.

Nagai, M. and Miyao, T. (1992), "Activity of alumina-supported molybdnwum nitride for carbazole hydrodenitrogenation," *Catal. Lett.*, **15**, 105 – 109.

Nelson, N. and Levy, R. B. (1979), "The organic chemistry of hydrodesulphurization," *J. Catal.*, **58**, 485 – 488.

Netzer, F. P., Bertel, E. and Goldmann, A. (1988), "Structure and Surface chemistry of 5-Membered Cyclic Molecules on Rh(111): Pyrrole," *Surf. Sci.*, **199**, 87 - 98.

Netzer, F. P., Bertel, E. and Mattheew, J. A. (1980), "Sensivity of electronic transitions to molecule – surface orientation: ELS of benzene and pyridine on Ir(111)," *Surf. Sci.*, **92**, 43 – 52.

Netzer, F. P. and Mack, J. U. (1983a), "The electronic structure of aromatice molecules adsorbed on Pd(111)," *J. Chem. Phys.*, **79**, 1017 – 1025.

Netzer, F. P. and Mack, J. U. (1983b), "Angle-resolved ultraviolet photoemission of pyridine adsorbed on Pd(111)," *Chem. Phys. Lett.*, **95**, 492 – 496.

Niemantsverdriet, J. W., Spectroscopy in catalysis: an introduction, Weinheim, Chichester: Wiley-VCH, (2000).

Nunney T. S., Birtill, J. J. and Raval, R. (1999), "Infrared studies o sub-monolayer methylamine and trimethylamine adsorption on Ni(111)," *Surf. Sci.*, **427-428,** 282 – 287.

Olive, J. L., Biyoko, S., Moulinas, C. and Genste, P. (1985), "Hydroprocessing of indole and o-ethyl anikine over sulfided CoMo, NiMo and NiW catalysts," *Appl. Catal.*, **19**, 165 – 174.

Oyama, S. T. (2003), "Novel catalysts for advanced hydroprocessing transition metal phosphides," *J. catal.*, **216**, 343 – 352.

Oyama, S. T., Clark, P., Teixeira da Silva, V. L. S., Lede, E. J. and Requejo, F. G. (2001), "XAFS characterization of highly active alumina-supported molybdenum phosphide catalysts (MoP/Al_2O_3) for hydrotreating," *J. Phys. Chem. B*, **105**, 4961 – 4966.

Oyama, S. T., Wang, X., Requejo, f. G., Sato, T. and Yoshimura, Y. (2002), "Hydrodesulphurization of petroleum feedstocks with a new type of nonsulfide hydrotreating catalyst," *J. Catal.*, **209**, 1 – 5.

Ozkan, U. S., Ni, S., Zhang, L. and Moctezuma, E. (1994), "Simultaneous Hydrodesulfurization and Hydrodenitrogenation of model compounds over Ni-Mo / γ-Al2O3 catalysts," *Energy Fuels*, **8**, 249 – 257.

Ozkan, U. S., Zhang, L., Ni, S. and Moctezuma, E. (1994), "Characterization and Activity of Unsupported Ni-Mo Sulfide Catalysts in HDN/HDS Reactions," *Energy Fuels*, **8**, 830 – 838.

Pan, F.–M. and Stair, P. C. (1986), "Chemisorption of pyridine and pyrrole on iron oxide surface studied by XPS," *Surf. Sci.*, **177**, 1 – 13.

Park, K. T., Richards-Babb,†M., Freund, M. S., Weiss, J. and Klier, K. (1996), "Surface Structure of Single-Crystal MoS2(0002) and Cs/MoS2(0002) by X-ray Photoelectron Diffraction," *J. Phys. Chem.*, **100**, 10739 – 10745

Pearlstine, K. A. and Friend, C. M. (1986), "Surface chemistry of Alkyl Amines. 1. Ethyalmine and Triethylamine on W(100), W(100)-(5 x 1)-C, and W(100)-(2 x 1)-O," *J. Am. Chem. Soc.*, **108**, 5837 – 5842.

Perdew, J. P., Burke, K. and Ernzerhof, M. (1996), "Generalized Gradient Approximation Made Simple," *Phys. Rev. Lett.*, **77**, 3865 – 3868.

Peterson, S. L. and Schulz, K. H. (1996), "Ethanethiol Decomposition Pathways on MoS_2(0001)," *Langmuir*, **12**, 941 – 945.

Peterson, S. L; Schulz, K. H.; Schulz Jr., C. A. and Vohs, J. M. (1994), "Inexpensive ultrahigh vacuum heatable/coolable xyz-rotary motion sample manipulator," *Rev. Sci. Inst.*, **66**, 3048 – 3050.

Phillips, D. C., Sawhill, S. J., Self, R. and Bussell, M. E. (2002), "Synthesis, characterization, and hydrodesulfurization properties of silica-supported molybdenum phosphide catalysts," *J. Catal.*, **207**, 266 – 273.

Pieter L. J., Niemantsverdriet, J. W., Ribeiro, F. H. and Somorjai, G. A. (1997), "Surface Science approach to Modeling Supported Catalyst," *Catal. Rev.-Sci. Eng.*, **39**, 77 – 168.

Prins, R. in "Advances in Catalysis" (B. C. Gates, and H. Knözinger, Eds.), **46**, 399 – 464. Academic Press, San Diego, (2001).

Rangwala, H. A., Dalla Lana, I. G., Otto, F. D., Yeniova, H. and Al-Nuaimi, K. (1990), "Influence of catalyst properties and operating conditions on Hydrodenitrogenation of Quinoline," *Energy Fuels*, **4**, 599 – 604.

Raybaud, P., Hafner, J., Kresse, G., Kasztelan, S. and Toulhoat, H. (2000), "Ab Initio Study of the H_2–H_2S/MoS_2 Gas–Solid Interface: The Nature of the Catalytically Active Sites," *J.Catal.*, **189**, 129 – 146.

Redhead, P. A. (1962), "Thermal Desorption of Gases," *Vacuum*, **12**, 203 – 211.

Reedijk, J., in: Comprehensive Coordination Chemistry (Eds. G. Wilkinson, R.D. Gillard, J. McCleverty), Pergamon Press, Oxford, (1987).

Robbie, K., Jemander, S. T., Lin, N., Hallin, C., Erlandsson, R., Hansson, G. V., and Madsen, L. D. (2001), "Formation of Ni-graphite intercalation compounds on SiC," *Phys. Rev. B*, **64**, 155401 – 155412.

Roberts, J. T. and Friend, C. M. (1986), "Model Hydrodesulfurization Reactions: Saturated C4S Molecules on Mo(110)," *J. Am. Chem. Soc.*, **108**, 7204 – 7210.

Roberts, J. T. and Friend, C. M. (1987), "Desulphurisation of saturated C_3S molecules on Mo(110): the effect of ring strain," *J. Am. Chem. Soc.*, **109**, 3872 – 3882.

Rodriguez, J. A., Dvorak, J. and Jirsak, T. (2000), "Chemistry of Thiophene on Mo(110), MoCx and MoSx surface: photoemission studies," *Surf. Sci.*, **457**, L413 – L420.

Rodiguez, J. A., Dvorak, J., Jirsak, T., Li, S. Y., Hrbek, J., Capitano, A. R., Gabelnick, A. M. and Gland, J. L. (1999), "Chemistry of thiophine, pyridine and cyclohexylamine on Ni/MoSx and Ni/S/Mo(110) surfaces: role of nickel in hydrodesulfurization and hydrodenitrogenation processes," *J. Phys. Chem. B.*, **103**, 8310 – 8318.

Rodriguez, J. A. Kim, J- Y., Hanson, J. C., Sawhill, S. J. and Bussell, M. E. (2003), "Physical and Chemical Properties of MoP, Ni2P, and MoNiP Hydrodesulfurization Catalysts: Time-Resolved X-ray Diffraction, Density Functional, and Hydrodesulfurization Activity Studies," *J. Phys. Chem. B*, **107**, 6276 – 6285.

Roe, C. L. and Schulz, K. H. (1998), "Reaction of 1,2-ethanedithiol on clean, sulfur-modified, and carbon-modified Mo .110. surfaces," *J. Vac. Sci. Technol. A*, **16**, 1066 – 1072.

Roe, C. L. and Schulz, K. H. (2000), "Reaction of ethanethiol on clear and carbon-modified Mo(110) surfaces as a function of sulfur coverage," *Surf. Sci.*, **446**, 254 – 266.

Sanchez-Delgado, R.A., Organometalic Modelling of the Hydrodesulfurization and Hydrodenitrogenation Reactions, Kluwer, The Netherlands, (2002).

Satterfield, C. N., Modell, M. and Mayer, J. F. (1975), "Interactions between catalytic hydrodesulfurization of Thiophene and Hydrodenitrogenation of pyridine," *AICHE J.*, **21**, 1100 – 1107.

Satterfield, C. N., Modell, M. and Wilkens, J. A. (1980), "Simultaneous Catalytic Hydrodenitrogenation of Pyridine and Hydrosulfurization of Thiophene," *Ind. Eng. Chem. Process Des. Dev.* **19**, 154 – 160.

Satterfield, C. N., Smith, C. M. and Ingalls, M. (1985), "Catalytic Hydrodenitrogenation of Quinoline. Effect of water and hydrogen sulphide," *Ind. Eng. Chem. Process Des. Dev.*, **24**, 1000 – 1004.

Sawhill, S. J., Layman, K. A., Van Wyk, D. R., Engelhard, M. H., Wang, C. and Bussell, M. E. (2005), "Thiophene hydrodesulfurization over nickel phosphide catalysts: effect of the precursor composition and support," *J. Catal.*, **231**, 300 – 313

Sawhill, S. J., Phillips, D. C. and Bussell, M. E. (2003), "Thiophene hydrodesulphurization over supported nickel phosphide catalysts," *J. Catal.*, **215**, 208 – 219.

Schlatter, J. C., Oyama, S. T., Metcalfe, J. E. and Lambert, J. M. (1988), "Catalytic behavior of selected transition-Metal Carbides, Nitrides and Borides in the hydrodenitrogenation of Quinoline," *Ind. Eng. Chem. Res.*, **27**, 1648 – 1653.

Schoofs, G. R. and Benziger, J. B. (1987), "Reactions of Pyrrole with Ni(100)," *Surf. Sci.*, **191**, 373 – 382.

Segall, M. D., Lindan, P. J., Probert, M. J, Pickard, C. J., Hasnip, P. J., Clark, S. J. and Payne, M. C. (2002), "First –principles simulation: ideas, illustrations ad the CASTEP code," *J. Phys.: Cond. Matt.*, **14**, 2717 – 2744.

Selnau, H. E. and Merola, J. S. (1993), "Reactions of [Ir(COD)(PMe_3)$_3$]Cl with Benzene, Pyridine, Furan, and Thiophene: C-H Cleavage vs. Ring Opening" *Organometallics*, **12**, 1583 – 1591.

Serafin, J. C. and Friend, C. M. (1989), "Reactivity of pyridine on Mo(110): C-H and C-N bond activation," *J. Phys. Chem.*, **93**, 1998 – 2004.

Sexton, B. A. (1985), "A vibrational and TDS study of the adsorption of pyrrole, Furan and thiophene on Cu(100): evidence for π-bonded and included species," *Surf. Sci.*, **163**, 99 – 113.

Sexton, B. A. and Avery, N. R, (1983), " Coordination of acetonitrile (CH3CN) to platinum (111): Evidence for an η^2(C, N) species," *Surf. Sci.*, **129**, 21 – 36.

Somorjai, G. A. (1996), "Modern Surface Science and Surface Technologies: An Introduction," *Chem. Rev.*, **96**, 1223 – 1235.

Srivastava, G. P. and Weaire, D. (1987), "The theory of the cohesive energies of solids," *Adv. Phy.*, **26**, 463 – 517.

Stinner, C., Prins, R. and Weber, Th. (2000), "Formation, structure, and HDN activity of unsupported molybdenum phosphide," *J. Catal.*, **191**, 438 – 444.

Stinner, C., Tang, Z., Haouas, M., Weber, Th. And Prins, R. (2002), "Preparation and ^{31}P NMR characterization of nickel phosphides on silica," *J. Catal.*, **208**, 456 – 466.

Sun, M., Nelson, A. and Adjaye, J. (2004), "On the incorporation of nickel and cobalt into MoS_2-edge structures," *J. Catal.*, **226**, 32 – 40.

Szabo, A. and Ostlund, N. S., Modern Quantum Chemistry, McGraw-Hill, NY, (1989)

Topsøe, H., Clausen, B. S., and Massoth, F. E., Hydrotreating Catalysis, Spinger Verlag, Berlin, (1996).

Tourillon, G., Raaen, S., Skotheim, T. A., Sagurton, M., Garrett, R. and Williams, G. P. (1987), "A near Edge X-Ray Absorption Fine Structure study of the adsorption of pyrrole ans N-methylpyprrole on Pt(111): Orientation and Dissociation of the adsorbed molecules," *Surf. Sci.*, **184**, L345 – L354.

Valyon, J., Schneider, R. L. and Hall, W. K. (1984), "Site selective chemisorption on sulfided molybdena-alumina catalysts," *J. Catal.*, **85**, 277 – 283.

Van Hove, M. A., Weinberg, W. H. and Chan, C.–M., Low Energy Electron Diffraction, Springer Verlag, New York, (1986).

Van Santen, R. A., Theoretical Heterogeneous Catalysis, World Scientific, Singapore, (1991).

Vanderbilt, D. (1990), "Soft self-consistent pseudopotentials in a generalized eigenvalue formalism," *Phys. Rev. B.*, **41**, 7892 – 7895.

Vit, Z. (1993), "Comparison of Carbon and alumina supported Mo, CoMo and NiMo catalysts in parallel hydrodenitrogenation and hydrodesulfurization," *Fuel*, **72**, 105 – 107.

Wada, T., Kohara, N., Nishiwaki, S. and Negami, T. (2001), "Characterization of the Cu(In,Ga)Se_2/o interface in GIGS solar cells," *Thin Solid films*, **387**, 118 – 122.

Walker, B. W. and Stair, P. C. (1980), "Chemical evidence for the formation of an acidic Mo(100) surface by adsorbed oxygen," *Surf. Sci.*, **91**, L40 – L44.

Wang, X., Clark, P., and Oyama, S. T. (2002), "Syntesis, characterization, and hydrotreating activity of everal iron group transition metal phosphide," *J. Catal.*, **208**, 321 – 331.

Wexler, R. M., Tsai, M. C., Friend, C. F. and Muetterties, E. L. (1982), "Pyridine coordination chemistry of Nickel and platinum surfaces," *J. Am. Chem. Soc.*, **104**, 2034 – 2036.

Wiberg, K. B., Walters, V. A., Wong, K. N. And Colson, S. D. (1984), "Azines: Vibrational force field and intensities for pyridine," *J. Phys. Chem.*, **88**, 6067 – 6075.

Wiegand, B. C. and Friend, C. M. (1992), "Model studies of the desulfurization reactions on metal surfaces and in organometallic complexes," *Chem. Rev.*, **92**, 491 – 504.

Wiegenstien, C. G. and Schulz, K. H. (1999), "Methanethiol adsorption on defective $MoSe_2$(0001) surfaces," *J. Phys. Chem. B*, **103**, 6913 – 6918

Wiwel, P., Kundsen, K., Zeuthen, P. and Whitehurst, D. (2000), "Assessing compositional changes of nitrogen compounds during hydrotreating of typical diesel range gas oils using a Novel preconcentration technique coupled with gas chromatography and atomic emission detection," *Ind. Eng. Chem. Res.*, **39**, 533 – 540.

Whitten, J. E. (2003), "Adsorption of thiophene and pyridine on W(1 1 0)," *Surf. Sci.*, **546**, 107 – 116.

Yao, Y. (1963), "Heat of adsorption of amines, hydrocarbons, and water vapour on reduced and oxidized iron surfaces," *J. Phys. Chem.*, **67**, 2055 – 2061.

Young, E. C., Maeng, J. Y. and Sehun, K. (2003), "Formation of Highly Ordered Organic Monolayers by Dative Bonding: Pyridine on Ge(100)," *J. Am. Chem. Soc.*, **125**, 7514 – 7515.

Zuzaniuk, V. and Prins, R. (2003), "Synthesis and characterization of silica-supported transition-metal phosphides as HDN catalysts," *J. Catal.*, **219**, 85 – 96.